Numerical and Experimental Investigations of the Acoustic Standing Wave Resonator, Pump, and Micropump

Majid Nabavi

A Thesis

in

The Department

of

Mechanical and Industrial Engineering

Presented in Partial Fulfillment of the Requirements
for the Degree of Doctor of Philosophy at
Concordia University
Montreal, Quebec, Canada

June 2008

Your file Votre référence
ISBN: 978-0-494-42551-0
Our file Notre référence
ISBN: 978-0-494-42551-0

ABSTRACT

Numerical and Experimental Investigations of the Acoustic Standing Wave Resonator, Pump, and Micropump

Majid Nabavi, PhD.

Concordia University, 2008

The interactions of acoustic waves and thermoviscous fluids in closed cavities lead to some important physical phenomena such as, linear and nonlinear acoustic standing waves, and acoustic streaming which are very important in a wide range of engineering applications. The present dissertation is focused on the detailed investigation of standing wave dynamics in closed cavities. As a part of this research, novel numerical and experimental techniques are developed to analyze different phenomena caused by acoustic-fluid interaction. Using these techniques, the behavior of pressure, acoustic and streaming velocity fields inside the standing wave resonator, as well as the valveless acoustic pump and micropump are investigated.

A new sixth-order accurate compact finite difference method for solving the Helmholtz equation with Neumann boundary conditions is developed. This scheme showed a better performance at higher wave numbers than the finite element method. A new fourth-order numerical scheme is also developed for solving highly nonlinear standing wave equations with no restriction on nonlinearity level and type of fluid. For highly nonlinear waves, the simulation results show the presence of a wavefront that travels along the resonator with very high pressure and velocity gradients. The slopes of the traveling velocity and pressure gradients, and the asymmetry in the pressure waveform are higher for CO_2 than those for air.

The spatial and temporal variations of the nonlinear pressure and particle velocity

fields inside a resonator are experimentally investigated at different frequencies and intensities. The effects of the excitation frequency and displacement on the streaming structure are also studied. It is found that, the classical streaming is not developed for Re_{s1} <6.5, and the irregular streaming patterns are observed at Re_{s2} >50. Acoustic streaming patterns are also found to be significantly affected by transverse temperature gradient

A valveless acoustic standing wave pump is developed and the velocity fields inside this novel pump are analyzed. It is found that, the net flow rate of the pump increases with an increase in the pressure amplitude. The behavior of a novel acoustic micropump is also studied at a high frequency. The effect of the diffuser geometry on the pump performance is investigated. The results show that the maximum diffuser efficiency is achieved at the diffuser-nozzle element's half-angle of approximately 45°.

Dedicated to

my beloved wife, Elham,

whose continual love and support

made this achievement possible

ACKNOWLEDGEMENTS

I would like to thank Dr. Kamran Siddiqui and Dr. Javad Dargahi, my advisors, for the opportunity to work with them, and also for their encouragement, trust and untiring support. I also appreciate the efforts and comments from my examining committee members, Dr. Luc Mongeau, Dr. Ali Dolatabadi, Dr. Wenfang Xie, and Dr. Amir Aghdam.

I am extremely grateful to my parents, for their never-ending support in all my efforts. Lastly, and most importantly, I wish to thank my beloved wife, Elham, for always being there for me, as I went through this journey. I could not have made it through without you by my side.

TABLE OF CONTENTS

LIST OF FIGURES

LIST OF TABLES

Key to Abbreviations

FDM: Finite Difference Method

FEM: Finite Element Method

BEM: Boundary Element Method

SEM: Spectral Element Method

FVM: Finite Volume Method

PIV: Particle Image Velocimetry

LDA: Laser Doppler Anemometry

SWP: Standing Wave Pump

SWR: Standing Wave Resonator

SW: Standing Wave

ASW: Acoustic Standing Wave

ASWP: Acoustic Standing Wave Pump

ASWMP: Acoustic Standing Wave Micropump

FCT: Flux-Corrected Transport

TVD: Total Variation Diminishing

FFT: Fast Fourier Transform

Nomenclature

α	total absorbtion coefficient
χ	Acoustic particle displacement, m
χ_{max}	Maximum acoustic particle displacement, m
Δp_d	time-averaged pressure drop in the diffuser direction
Δp_n	time-averaged pressure drop in the nozzle direction
$\delta_\nu = \sqrt{2\nu/\omega}$	thickness of the viscous acoustic boundary layer
η	The rectification capability of the diffuser-nozzle element
Γ	Cross-sectional area of the resonator
$\gamma = c_p/c_V$	ratio of specific heats
κ	coefficient of thermal conduction
Λ	Eigenvalue
λ	Wavelength, m
μ	Shear viscosity
μ_B	Bulk viscosity
ν	kinematic viscosity
ω	Angular velocity, rad/s
ρ	Density, kg/m^3
ρ'	Perturbation in density, kg/m^3
ρ_0	Static density, kg/m^3
$\wp$	Perimeter of the resonator
b	viscosity number
c	Sound velocity, m/s
c_0	Static sound velocity, m/s

c_p specific heats at constant pressure

c_V specific heats at constant volume

D Diameter of the tracer particles, m

fr Frequency, , s^{-1}

g gravitational acceleration, m/s^2

H Width of the channel, m

k Wave number, m^{-1}

L Length of the channel, m

L_s Characteristic length, m

M Mach number

p Pressure, Pa

p' Perturbation in pressure, Pa

P_0 Static pressure, Pa

P_r Prandtl number

Re Reynolds number

Re_{a1}, Re_{a2} Acoustic Reynolds numbers

$Re_{s1}, Re_{s2}, Re_{s3}$ Streaming Reynolds numbers

T Time period of the wave, s

t Time, s

T_p Particle response time, s

u Axial acoustic velocity, m/s

u_d time-averaged flow velocities in the narrowest part of the diffuser-nozzle element n the diffuser direction

u_n time-averaged flow velocities in the narrowest part of the diffuser-nozzle element n the nozzle direction

U_s Characteristic velocity, m/s

u_T Particle terminal velocity, m/s

u_{max} Maximum axial acoustic velocity, m/s

u_{st} Axial streaming velocity, m/s

v Transverse acoustic velocity, m/s

v_{st} Transverse streaming velocity, m/s

x Axial position, m

X_{max} Maximum vibrational displacement of the vibrator, m

y Transverse position, m

$\mathbf{v} = (u, v, w)$ Acoustic velocity vector

CHAPTER 1
Introduction

1.1 Background

A *standing wave* pattern is a vibrational pattern created within a medium when the vibrational frequency of the source causes reflected waves from one end of the medium to interfere with incident waves from the source. This interference occurs in such a manner that specific points along the medium appear to be standing still. Because the observed wave pattern is characterized by points which appear to be standing still, the pattern is often called a standing wave pattern. Such patterns are only created within the medium at specific frequencies of vibration. These frequencies are known as *resonance frequencies.* At any frequency other than a resonance frequency, the interference of reflected and incident waves leads to a resulting disturbance of the medium which is irregular and non-repeating. To establish the standing wave, we need a chamber and an acoustic driver (see Fig. 1–1). The acoustic driver provides excitation energy to establish a standing wave in the chamber. The frequency of excitation source is matched to the medium and to the length of the excitation chamber so that a traveling wave generated by the excitation source is reflected upon itself within the chamber to create the standing wave. The length of chamber should be equal to an integer times half the wavelength of the acoustic wave ($n\lambda/2, n = 1, 2, ..$). The standing wave results in one or more pressure nodes and pressure anti-nodes within the chamber (see Fig. 1–1). The number of nodes and anti-nodes depend upon the length of the chamber and the frequency of oscillation of the excitation source. Generally, the pressure at a pressure node is relatively constant at approximately the same level as the undisturbed pressure of the fluid while the

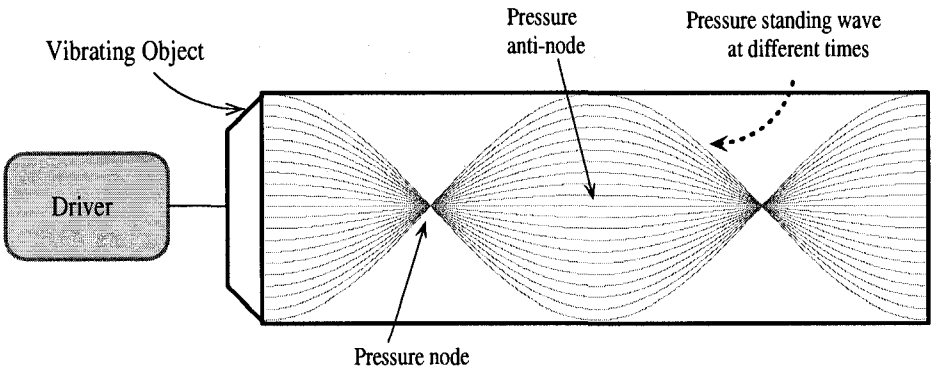

Figure 1–1: Schematic of the standing wave resonator.

pressure at a pressure anti-node fluctuates above and below the undisturbed pressure level.

Acoustic standing waves can be categorized in three groups:

1. *Linear standing wave*: Small amplitude acoustical disturbances (in which the amplitudes of the perturbations are small compared to the static values) in a lossless (inviscid and thermally non-conducting) medium.
2. *Finite-amplitude nonlinear standing wave*: Small amplitude acoustical disturbances in a thermoviscous (viscous and thermally conducting) medium.
3. *Highly nonlinear standing wave*: Large amplitude acoustical disturbances (in which the amplitudes of the perturbations are comparable with the static values) in a thermoviscous medium.

The study of linear and nonlinear acoustic standing waves in closed tubes is very important in designing a wide range of systems such as, thermoacoustic devices [1, 2, 3, 4, 5], high quality resonators [6, 7], high power sonic and ultrasonic equipment [8], standing wave motor [9], standing wave pump [10], particle filtration and levitation [11] and biomedical test and therapy equipment [12, 13, 14].

Interaction of acoustic waves and solid boundaries creates some nonlinear phenomena. One of them is *acoustic streaming.* Acoustic streaming is a stationary flow

which always has rotational character and its velocity increases with the sound intensity. But, even at the high intensity levels, the secondary streaming velocity remains smaller than the primary oscillatory particle velocity in the sound wave. The study of acoustic streaming is very important in different scientific fields such as, thermoacoustic devices [15], heat transfer enhancement [16], convective cooling systems [17], ultrasonic levitators [18], non-contact surface cleaning [19], biosensors [20] and biology [21].

In addition to the above-mentioned applications, acoustic standing waves can be utilized to perform pumping action. Pumps are typically categorized as *displacement pumps* and *dynamic pumps*. Displacement pumps use a volume change to displace the fluid. In a positive-displacement pump a moving boundary forces the fluid along by volume changes. A cavity opens, and the fluid is admitted through an inlet. The cavity is then closed and the fluid is squeezed through an outlet. The classic example is the mammalian heart, but mechanical versions are in wide use which may be classified as rotary pumps and reciprocating pumps. All positive-displacement pumps deliver a pulsating or periodic flow as the cavity volume opens, traps, and squeezes the fluid. Their advantage is the delivery of any fluid regardless of viscosity. Dynamic pumps simply add momentum to the fluid by means of fast moving blades or vanes or certain special designs. There is no closed volume. The fluid momentum increases while moving through open passages and then converts its high velocity into a pressure increase by exiting into a diffuser section. Dynamic pumps can be classified as rotary pumps and jet pumps. Dynamic pumps generally provide a higher flow rate and a much steadier discharge than positive-displacement pumps but they are ineffective in handling high-viscosity liquids. A positive displacement pump is appropriate for high pressure rise and low flow rate, while a dynamic pump provides high flow rate with low pressure rise.

In any event, the majority of conventional pumps use moving parts. The use of

moving parts lowers the pump efficiency through energy losses mainly against the friction. Moving parts also reduce overall pump reliability and increase cost of operation since they are subject to mechanical failure and fatigue, and require maintenance. Moving parts also generally require the application of a lubricant, which needs to be replenished and which must be isolated from the pumped fluid. In recent years, effort has been made to design a pumping apparatus which lacks these traditional moving parts and their associated disadvantages.

The *acoustic standing wave pump (ASWP)* which achieves a pumping action using the properties of standing waves, is a good example of these kinds of pumps [22]. With fewer moving parts, this pump is also typically lighter than moving pumps capable of pumping fluids at the same rates and pressures. The ASWP consists of a chamber defining a pump cavity and an acoustic driver (see Fig. 1–2). The chamber

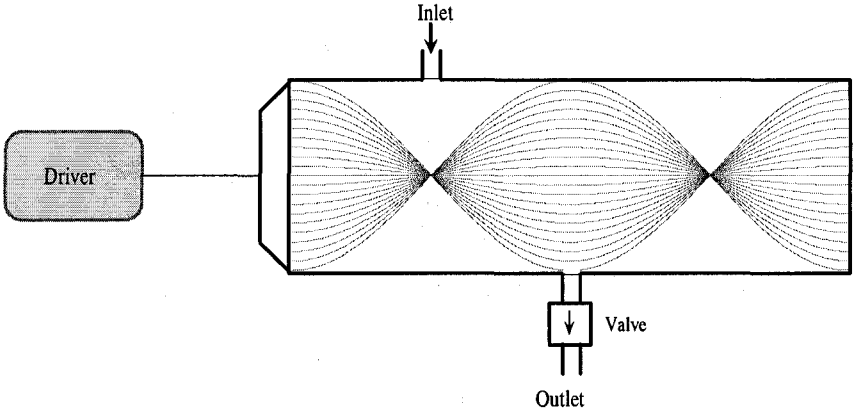

Figure 1–2: Schematic of the standing wave pump.

has a fluid inlet and outlet through which the pumped fluid enters and exits. The excitation driver establishes a standing wave in the chamber. The inlet and outlet could be placed proximate to the pressure nodes and anti-nodes of the chamber, respectively. Due to significantly large pressure inside the cavity at the pressure anti-node, the fluid is discharged through the outlet. As the fluid discharges, there is a reduction in the fluid mass inside the tube which will cause a reduction in the static

pressure. The pressure will now be lower than the pressure of the inlet fluid. As a result the fluid will be sucked into the tube. (see Fig. 1–2). A check valve must be placed at the outlet to prevent the pumped fluid from re-entering the chamber during low pressure portions of the cycle at the pressure anti-node [22]. Refrigeration and air-conditioning compressors [10], thermoacoustic engines [23, 24], micro fluidic pumps [25] and bio-fluid pumps [26] are some examples of a wide range of practical applications where standing wave pump can be used.

1.2 Literature review

In this section, the relevant literature on the different aspects studied in this dissertation is reviewed. The previous studies on the analytical, numerical and experimental analysis of the linear and nonlinear standing waves are given first. The section continues with the review of the acoustic streaming. At the end, the previous works on the ASWP have been reviewed.

1.2.1 Linear standing wave

Linear acoustics is devoted to waves propagate in a lossless medium with amplitude small enough that the small-signal approximation, $|\rho'| \ll \rho_0, |p'| \ll P_0$, is satisfied. The linear wave equation can be written in terms of the axial velocity (u) as,

$$c_0^2 u_{xx} - u_{tt} = 0, \tag{1.1}$$

and in terms of pressure (p) as,

$$c_0^2 p_{xx} - p_{tt} = 0. \tag{1.2}$$

Numerical studies

The time-harmonic linear wave propagation in a lossless medium is governed by the Helmholtz equation . In addition to linear standing wave, the Helmholtz equation governs some important physical phenomena including the potential in time harmonic acoustic and electromagnetic fields [27, 28], acoustic wave scattering from submarines [29], noise reduction in silencers and mufflers [30], water wave propagation [31], membrane vibration [32] and radar scattering [33]. Obtaining an efficient and more accurate numerical solution for the Helmholtz equation has been the subject of many studies in recent years. The numerical solution of the Helmholtz equation has been developed using different approaches such as the boundary element method (BEM) [34, 35], the finite element method (FEM) [36, 37, 38], the spectral element method (SEM) [39] and the finite difference method (FDM) [40, 41, 42].

The BEM is derived through the discretization of an integral equation that is mathematically equivalent to the original partial differential equation. The disadvantages of the BEM are the restriction to linear problems in homogeneous and isotropic media, as well as the large computer storage space and lengthy processing time requirements to solve the inherent problems encountered with characteristic wave numbers [43] .

The FEM is used extensively to solve the Helmholtz equation. In addition to the high computational cost, another disadvantage of the Galerkin FEM for solving the Helmholtz equation is the so-called *pollution effect*, which results in the less accurate solution at higher wave numbers for the given nodes per wavelength. Thus, in order to obtain the same solution accuracy for higher wave numbers, more nodes per wavelength are needed than that for the lower wave numbers [37, 38]. That is, wave resolution (kh) should be kept as even as possible. Although some modifications in the standard Galerkin approximation have been developed to minimize the pollution effect [44, 45, 46, 47, 35], finding an optimal method is still a challenge. The

performance of the BEM and FEM for the Helmholtz equation in two dimensions was investigated by Blyth and Pozrikidis [48]. Their numerical investigations showed that the BEM is generally more accurate than the FEM when the size of the finite elements is comparable to that of the boundary elements, especially for the Dirichlet problem where the boundary values of the solution are specified. Exceptions occur in the neighborhood of isolated points of the Helmholtz constant where eigenfunctions of the boundary integral equation arise and the BEM fails to produce a unique solution.

For the SEM, it is shown that it requires fewer grid nodes per wavelength compared to the FEM for the Helmholtz equation [39]. However, due to the less sparse resultant matrix compared to the resulting finite element matrix, the computational time of both methods are almost the same [39].

For the traditional FDM, in order to increase the order of accuracy of the approximation, the stencil of grid points needs to be enlarged, which is not desirable. Generally, obtaining a more accurate numerical solution means adding more nodes and using smaller mesh size, which requires more computation time and storage space. In order to obtain a more accurate result for constant mesh size, an increase in the order of accuracy of the numerical approximation is required, which in turn, enlarges the stencil of grid points. This, however, leads to some problems including difficult treatments of the boundary conditions and approximation of the points next to the boundaries, and increasing the bandwidth of the stiffness matrix, which makes fast direct solver difficult. Therefore, compact FDMs are desired to solve partial differential equation numerically. A notable work in this field has been performed by Singer and Turkel [40]. They developed a fourth-order compact FDM using two schemes. One scheme was based on the generalization of the Padé approximation and the other used the Helmholtz equation to calculate higher-order correction terms. They implemented these schemes for Dirichlet and/or Neumann boundary conditions.

As the literature review indicates, one of the major disadvantage of the FEM, BEM and SEM is the high computational cost and the disadvantage of the existing FDM is the low accuracy. Thus, development of compact FDM with higher accuracy is necessary. Furthermore, the challenge of efficient computational scheme at high wave numbers has been designated as one of the problems still unsolved by the current numerical techniques [49]. Recently, two sixth-order compact FDMs for solving the Helmholtz equation have been reported by Singer and Turkel [41] and Sutmann [42]. In both studies, the authors implemented their schemes only with Dirichlet boundary conditions. However, most of the practical problems need to be solved with both Dirichlet and Neumann boundary conditions.

Non-standard techniques have also been applied to solve the Helmholtz equation. The polynomial-based differential quadrature (PDQ) and the Fourier expansion-based differential quadrature (FDQ) methods were applied by Shu and Xue to solve the two-dimensional Helmholtz equation [50]. They found that the FDQ approach can generally provide more accurate numerical results than the PDQ approach. El-Sayed and Kaya [51] used the Adomian decomposition method and compared it with the traditional FDM. They argued that the decomposition method provides a more efficient scheme than the FDM to solve the Helmholtz equation. However, they did not comment about the accuracy and the computational cost of the decomposition method.

Experimental studies

Different techniques have been used to measure the linear acoustic standing wave velocity fields. Huelsz and Lopez-Alquicira [52, 53] used hot-wire anemometry (HWA) to measure acoustic velocities in the linear range (maximum velocity of 0.8 m/s). Vignola *et al.* [54] assembled and tested a differential laser Doppler anemometry (LDA) to provide noninvasive measurements of the acoustic velocities of linear

standing waves generated in a water-filled tube. Thompson *et al.* [55] used LDA with burst spectrum analysis (BSA) to study the acoustic velocities of amplitude less than 1.3 m/s (linear range) generated in a cylindrical standing-wave resonator filled with air. Gazengel and Poggi [56] assessed the performances of two LDA systems adapted for measuring the acoustic particle velocities in an enclosed acoustic field. This assessment was performed by comparing the acoustic velocities measured by means of LDA to reference acoustic velocities estimated from sound pressure measurements. In their experiments, the maximum velocity amplitudes were 0.1, 1 and 10 mm/s (linear range) and the corresponding relative errors were 11%, 5% and 3.6%. HWA is an intrusive technique which disturbs the velocity fields inside the resonator. Whereas, LDA is non-intrusive technique where the particle velocity is measured remotely based on the Doppler shift in the frequency of the laser light scattered from small particles. Both HWA and LDA suffer a main drawback. They can only provide velocity measurements at a point in space. As a result, detailed simultaneous two-dimensional flow structure cannot be obtained from these techniques.

Particle image velocimetry (PIV) provides two-dimensional velocity fields with high spatial resolution and measures velocity vectors in a plane simultaneously at many points (e.g. thousands) in a flow field. Very few studies have reported velocity measurements of the standing wave using PIV. Hann and Greated [57, 58] have shown the ability of PIV to measure the amplitude of the sinusoidal sound field and the mean flow. They measured particle velocities of an acoustic standing wave inside a square channel at a frequency of 1616 Hz. However, they did not present detailed velocity characteristics. Campbell *et al.* [59] reported a review of PIV with its application to the measurement of sound. Shin *et al.* [60] studied the velocity field of acoustic standing wave in liquid within small tube using PIV. They conducted study for two different liquid mediums; water and a mixture of glycol and water. The tube was square shaped with the inner dimensions of 3 mm $\times$ 3 mm. A bimorph piezo disk was

used as the acoustic driver at one end, while the other end of the tube was open. The velocity fields were measured at different temporal locations with respect to the driving sinusoidal signal using a set of delay generators. They observed acoustic boundary layer in a very thin region near the wall and flat velocity profiles outside this region. They also observed that the thickness of the acoustic boundary layer decreases with an increase in the frequency. Their experiments were in the linear range of acoustic intensity and they measured the velocity field in a small field of view (190×150 μm) near the wall to investigate the boundary layer effect. Recently, Castrejón-Pita *et al.* [61] used PIV and LDA to measure amplitude and phase velocity on the laminar oscillatory viscous boundary layer produced by acoustic standing wave. They found a good agreement between the experimental data and the predictions made by the Rayleigh viscous boundary layer theory.

Summary

As the above literature review indicates, all the existing numerical solvers for the Helmholtz equation, either have low accuracy (fourth-order or less) or were implemented only with Dirichlet boundary conditions. However, most of the practical problems need to be solved accurately with both Dirichlet and Neumann boundary conditions.

1.2.2 Nonlinear standing wave

When the amplitude of acoustic standing wave is infinitesimal, the acoustic wave can be described by linear laws. However, when the acoustic wave is driven into high amplitude oscillations, the equations of motion are nonlinear and the nonlinear effects could distort originally harmonic waves, shift the resonance frequency, and transform acoustic energy into higher harmonic components [6, 62, 63]. The investigation of nonlinear standing wave in acoustics has a rich history. Several studies dealing with

the analytical, numerical and experimental studies of the finite-amplitude and high-amplitude nonlinear standing waves can be found in the literature.

Analytical and numerical studies

An early analytical study of finite amplitude standing waves was performed by Coppens and Sanders [64]. They presented a perturbation expansion for a second-order one-dimensional nonlinear wave equation. In a later work, they extended their method to a three-dimensional model for lossy cavities [65]. Maa and Liu [66] have shown that the motion of a particle at a point fixed on the waveform of a standing wave is readily soluble from the Riemann equations, and an exact, stable solution of the nonlinear standing wave is obtained. Different resonator shapes and boundary layer effects are studied by Bednařík and Červenka [67].

When nonlinear terms in the conservation equations are retained, great mathematical difficulty is encountered and the analytical solution even in special cases is very difficult or nearly impossible. Therefore, numerical approaches are frequently used. Several numerical algorithms for the solution of finite-amplitude nonlinear standing waves in the frequency and time domains have been reported in the literature. Ilinskii *et al.* [6] developed a one-dimensional model to analyze nonlinear standing waves in an axisymmetric acoustical resonator of arbitrary shape. They presented the results for three geometries: a cylinder, a cone, and a bulb. However, they did not take into account the nonlinear terms with dissipation. A numerical model for nonlinear standing waves, based on a nonlinear differential equation written in Lagrangian coordinates, was presented by Vanhille and Campos-Pozuelo [68]. They presented a numerical formulation to model the standing acoustic wave of finite but moderate amplitude based on the FDM and the finite volume method (FVM). Later, they have extended their methods to two-dimensional nonlinear resonators filled with thermoviscous fluid [69]. Comparison between FDM and FVM for nonlinear standing

ultrasonic waves in fluid media was performed by Vanhille and Campos-Pozuelo [70]. They found reasonable agreement between the two schemes. A numerical model for quasi-standing nonlinear standing waves in a viscous fluid, based on a second order Taylor expansion of the state equation was presented by Vanhille and Campos-Pozuelo [71]. Their second order accurate model is valid for any viscous fluid but for a limited range of amplitudes. In a later work, they proposed a nonlinear equation based on conservation laws (written in Lagrangian coordinates) and the isentropic state equation, and numerically solved the equation using a second-order accurate implicit FDM [72]. They did not impose any restriction on the nonlinearity level in the momentum equation. However, they used a simplified form of continuity equation which is only valid for finite-amplitude waves. Furthermore, they considered the fluid to be viscous but thermally non-conducting.

The FEMs have also been used for the study of nonlinear standing waves in an rigid-walled air-filled and water-filled tubes [73]. The comparison between the results of different methods developed in these studies shows that, although the FEM and FVM may have some advantages over the FDM to simulate 3-D nonlinear fields and irregular geometries, for simple geometries in 1-D and 2-D, the FDM is preferred because of its lower computational cost.

Numerical analysis of the effect of the tube shape on the pressure and resonant frequency of an axisymmetric tube has been performed by Chun and Kim [74]. They found that the half cosine-shape tube is more suitable to induce high compression ratio than the other shapes. Optimized shapes of resonators for generating high-amplitude pressure waves has been numerically investigated by Li *et al.* [75]. They used a quasi-Newton type numerical scheme and validated the numerical results with the experimental ones. They found the optimized shape parameters, resonance frequency and excitation amplitude for cone, horn-cone and cosine shaped resonators.

A large numbers of studies dealing with the numerical solution of the highly

nonlinear acoustic standing waves can be also found in the literature. A study of nonlinear acoustic waves in homentropic ,i.e. uniform and constant entropy, perfect gas was presented by Christov *et al.* [76]. They solved the unsteady nonlinear wave equation using a Godunov-type FDM which is second-order accurate in space and time. They however, did not consider the effect of thermoviscous attenuation. Bednařík and Červenka [77] developed a model for finite-amplitude standing waves in acoustical resonators of variable cross-section. Their model takes into account external driving force, gas dynamic nonlinearities and thermoviscous dissipation. They solved the model numerically using central semi-discrete difference scheme developed by Kurganov and Tadmor [78]. Later, they extended their method to nonlinear standing waves in two-dimensional acoustic resonators [79]. Their model is second-order accurate in space and third-order accurate in time. They however, did not present any details about their numerical scheme. Periodic gas oscillations in closed tubes has been investigated experimentally and numerically by Alexeev and Gutfinger [80]. A two-dimensional numerical model of turbulent gas oscillations is developed and verified by a comparison with experiments. They observed that at resonance, gas oscillations are accompanied by shock waves traveling back and forth along the tube. They found that the gas temperature changes substantially along the tube. They also found that the experimental data of temperature and pressure inside the resonance tube are well correlated by the numerical model.

Experimental studies

As the literature review of section 1.2.1 indicates, all previous studies related to the acoustic velocity measurement have been performed in the linear range and consequently, no experimental study has reported the spatial and temporal variations of the velocity field inside a nonlinear acoustic standing wave resonator. The

previous experimental studies about nonlinear standing waves focused on the acoustic pressure measurement only. Historically, these studies may be traced back to Coppens and Sanders [65]. They presented experimental analysis and perturbation model of complicated modes in realistic cavities. A rectangular cavity was experimentally studied in this reference. Another notable work was performed by Maa and Liu [66]. They reported the gradual spectral variation of the standing wave with increasing excitation. They measured the sound pressure only at the ends of the standing wave tube. Measurements of macrosonic standing waves in oscillating closed cavities of four axisymmetric shapes: cylinder, cone, horn-cone and bulb, have been reported by Lawrenson *et al.* [81]. Cavities were filled with nitrogen, propane and refrigerant R-134a. They concluded that, for a given gas and a fixed power delivery, the dominant factor affecting the peak pressure amplitude is the geometry of the resonator. A recent experimental study in this field has been reported by Vanhille and Campos-Pozuelo [82]. They developed an experimental setup to measure high-amplitude pressures inside a rigid axisymmetric cylindrical resonator and compared the experimental results with the numerical ones. They measured the pressure at the tube end and compared the frequency spectrum of pressure obtained from experimental and numerical data. They found a good agreement between the numerical and experimental values of pressure in the frequency domain. However, they did not provide any comparison between the instantaneous numerical and experimental data in time domain. Furthermore, they measured the pressure at only the end of the tube and did not study the pressure dynamics along the channel. Good agreement between the numerical and experimental data in the frequency domain and only at the tube end wall is not enough for the validation of the model.

Summary

As seen in the above literature review, the accuracy of all previously developed numerical schemes for solving highly nonlinear standing wave equation is of second order in space and of second or third order in time. In the experimental part, no experimental study has reported the spatial and temporal variations of the velocity field inside a nonlinear acoustic standing wave resonator. Furthermore, regarding to the nonlinear acoustic pressure, no study provided any comparison between the instantaneous numerical and experimental data in time domain at different locations along the resonator.

1.2.3 Acoustic streaming

Acoustic streaming is a second-order, steady, circulatory fluid motion generated by mechanically driven sound waves. Acoustic streaming can be classified on the basis of the different mechanisms by which the streaming is generated [83]:

Rayleigh streaming is a vortex-like structure generated outside the boundary layer in a standing wave resonator. The interaction between the acoustic waves in viscous fluids and solid boundaries is responsible for this kind of streaming [84]. Rayleigh streaming can be referred to as *boundary layer driven streaming* as well as *outer streaming.*

Schlichting streaming (also known as *inner streaming*) is the mean fluid motion inside the boundary layer of a standing wave field [85, 86]. The length and width of Schlichting streaming vortices are estimated to be $\lambda/4$ and $1.9\delta_v$, respectively. Inner and outer streaming can be formed inside a channel where the acoustic wave propagates longitudinally (see Fig. 1–3).

Eckart streaming is driven by the dissipation within the fluid volume and is predominant in the high frequency range. This kind of streaming has been used in ultrasonic applications and can be referred to as bulk dissipation driven streaming

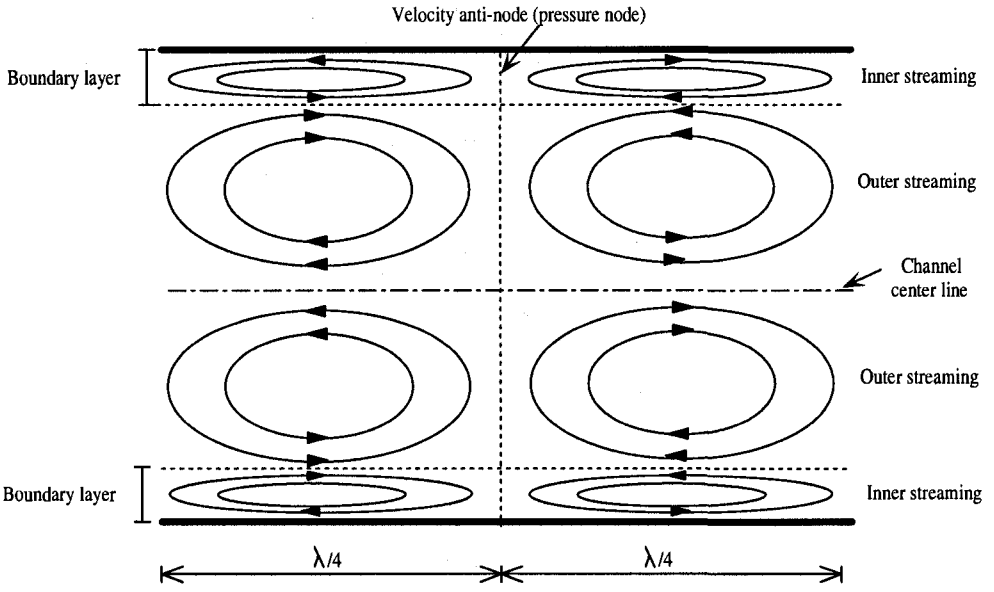

Figure 1–3: Schematic of acoustic streaming in a channel.

[87].

Jet-driven streaming is associated with the periodic suction and ejection of a viscous fluid through an orifice or a change in resonator cross section. The mechanism of jet-driven streaming relies on the fact that a viscous fluid behaves quite differently during the suction and ejection periods. During suction, the flow in the orifice comes effectively from all directions. However, in the ejection period, a jet is generated that induces a mean flow in a certain direction. The vortices in the jet shear layer in the vicinity of the orifice or change in cross sectional area are responsible for this kind of streaming.

Finally, *traveling wave streaming* occurs in the presence of a progressive wave and exhibits certain unique features. A perspective on the several different classes of acoustic streaming has been provided by Boluriaan and Morris [88].

Rayleigh or outer streaming can be classified to *regular* (*classical*) and *irregular* streaming patterns. The classical streaming structure is typically comprised of two

outer streaming vortices per quarter-wavelength of the acoustic wave which are symmetric about the channel center line (see Fig. 1–3). In irregular streaming, the shape and number of the streaming vortices are different from the regular case.

Analytical and numerical studies

The phenomenon of acoustic streaming has been extensively studied using the analytical methods. Lord Rayleigh [84] was the first to consider the streaming that occurs in the case of the imposition of an acoustic field on a channel consisting of two plane-parallel plates. He used a successive approximation technique to study the vortex flows occurring in a long pipe as a result of the presence of a longitudinal standing wave. In the successive approximation technique, the governing equation (i.e. the momentum equation) is scaled to the first-order linear equation and the second-order nonlinear equation. The solution for the first-order linear equation provides the forcing function for the second-order streaming equation [84]. This approach has become a dominant analytical tool for the study of acoustic streaming. Westervelt [89] evaluated the streaming velocity induced by acoustical disturbances by developing and solving a general vorticity equation. Andres and Ingard [90, 91] analytically investigated acoustic streaming around a cylinder and discussed the distortion of the streaming flow patterns as a function of sound intensity, under different Reynolds numbers. Lee and Wang [92] studied the effect of compressibility on the streaming patterns. They concluded that compressibility can affect the inner but not the outer streaming for the flow between parallel plates, however, for two or three dimensional objects such as cylinder or sphere, the compressibility also affects the outer streaming pattern. They used the limiting velocity at the edge of the inner streaming layer as a slip boundary condition to solve for the large outer streaming for different geometries.

The compressibility is a necessary condition for the propagation of acoustic waves.

However, previous studies on acoustic streaming were limited to incompressible fluids. This inconsistency is due to adapting the incompressible boundary layer solutions obtained by Schlichting [85] to solve acoustic streaming near rigid boundaries. Qi [93] investigated the effect of compressibility on acoustic streaming near a rigid boundary to resolve this inconsistency. Qi's results showed that the consideration of compressibility leads to a larger streaming velocity outside the boundary layer. The effect was found to be significant in gases, but not in liquids. The study was extended to investigate acoustic streaming in a circular tube [94]. By fully including the effects of compressibility and heat conduction, they made corrections to their earlier work. The leading order acoustic wave solution was analyzed using matched asymptotic expansions. The matching gave the dispersion relation and from this a model propagation equation was proposed. Their results agreed with earlier ones derived quite differently.

Menguy and Gilbert [95] studied nonlinear acoustic streaming in a guide with a perturbation calculation using asymptotic expansions. A notable distortion of the acoustic field due to the fluid inertia was demonstrated and a comparison of slow and nonlinear acoustic streaming was presented. Hamilton *et al.* [96] derived an analytic solution for acoustic streaming generated by a standing wave in two-dimensional channel of arbitrary width, filled with a viscous fluid. Their solution showed the inner streaming vortex confined to the boundary layer, in addition to the outer Rayleigh streaming. Moreover, it showed that the Rayleigh streaming disappears when the channel is sufficiently narrow. In their study, both the streaming structure and streaming velocity were described for various channel widths. They found that the inner vortices increase in size relative to the outer vortices as channel width is reduced, and the outer vortices disappear when the width of channel is less than about 10 times the boundary layer thickness. Hamilton *et al.* extended their method to a gas in which heat conduction and dependence of viscosity on temperature were taken

into account [97]. They found that for channel widths 10-20 times the viscous velocity penetration depth, thermal effects may alter the streaming velocity substantially. For significantly wider or narrower channels, thermal effects influence the streaming velocity by only a few percent. Carlsson *et al.* [98] performed an analytical study of the steady streaming flow induced by vibrating solid walls and argued that both vibrational frequency and normalized channel width affect the streaming flow.

The classical theory of acoustic streaming is restricted to *slow* or *linear streaming* . It is assumed that in the second-order governing equations (continuity and momentum equations), any nonlinear term that involves a second-order quantity is negligible. As a result, the second-order equations are linear in the dependent variables. This is why it is usually referred to as linear streaming. The numerical methods that directly solve the Navier-Stokes equations provide new approaches to overcome this limit. The two-dimensional numerical analysis of acoustic streaming induced by finite amplitude oscillation of air in a closed duct has been performed by Kawahashi and Arakawa [99]. They concluded that the structure of acoustic streaming changes with the oscillation amplitude. When the amplitude is very small, the theoretically predicted circulatory streaming does not occur. As the amplitude increases, circulatory streaming develops and is then distorted to a complicated and irregular structure at very large oscillation amplitude. Aktas and Farouk [100] simulated the acoustic streaming motion in a compressible gas-filled two-dimensional rectangular enclosure by direct solving the compressible Navier-Stokes equations using the LCPFCT (Laboratory for Computational Physics Flux-Corrected Transport) scheme. They numerically investigated the effects of sound field intensity on the formation process of streaming structures. They found that up to a certain value of the enclosure height to wavelength ratio, the vibrational motion causes classical and steady streaming flows that usually appear as two streaming rolls per half-wavelength, as reported in the previous studies. However, when the enclosure height is increased beyond this limit, the streaming structures

become irregular and complex. Yano [101] used an upwind TVD (Total Variation Diminishing) scheme to solve the full Navier-Stokes equation to investigate the turbulent acoustic streaming in a resonator. When $M << 1$ ($M = \chi_{max}\omega/c_0$), shock waves are formed and the gas oscillation attains a quasi-steady state, where the magnitude of the streaming velocity is linearly proportional to the acoustic Mach number.

Experimental studies

The acoustic streaming in a resonator has also been investigated experimentally by several researchers. Acoustic streaming at resonance was observed experimentally by Gulyaev and Kuznetzov [102]. The authors tracked the motion of small oil droplets on the inner tube wall and found that they migrated along the tube from its middle part toward the ends. They assumed that the migration is caused by acoustic streaming and, therefore, concluded that the presence of periodic shock waves does not prevent the formation of streaming patterns. Coppens and Sanders [64] measured the acoustic pressure in a resonator. They found that the microphone output waveforms become irregular when the sound intensity increases. This kind of nonharmonic wave shape was believed to be the non-linear source of the acoustic streaming. A similar measurement was carried out by Cruikshank [103]. On the basis of these experimental observations, a qualitative argument was presented to explain the disagreement between theory and experiment due to presence of acoustic streaming. Alexeev and Gutfinger [80] reproduced the Gulayev and Kuznetzov's experiment using a resonance tube. They argued that, when a tube is driven at the resonance frequency, shock waves traveling along the tube affect strongly the motion of particles suspended in the gas [104]. In particular, the shocks cause particle drift toward the tube ends. Using the analytical model proposed by Goldshtein *et al.* [104], for their experimental conditions, a shock induced drift velocity of about 8 m/s can be calculated. On the other hand, the streaming velocity obtained in the numerical

simulation is about 2 m/s. Hence, drift due to periodic shock waves dominates and they conclude that in their experiment, as well as in the experiments of Gulayev and Kuznetzov [102], the drift of droplets was caused by periodic shock waves, rather than by acoustic streaming, as was assumed by Gulayev and Kuznetzov.

PIV and LDA techniques have been used to measure acoustic streaming. Arroyo and Greated [105] used stereoscopic PIV technique to measure all three components of the streaming velocity field. They however, measured the streaming velocity field only in a region within 2 cm around the velocity node (in a 62.5 cm long tube). Hann and Greated [58] measured two components of both acoustic and streaming velocity fields simultaneously in the vicinity of a velocity node in a 70 cm long resonator excited by 1616 Hz sinusoidal signal. Thompson *et al.* [55] used LDA to study the acoustic streaming generated in a cylindrical standing-wave resonator filled with air. They observed that as the excitation amplitude increases, the difference between the experimental acoustic velocity and theoretical ones increases due to the fluid inertial effect. Recently, Moreau *et al.* [106] have used LDA for measurements of inner and outer streaming vortices at different streaming Reynolds numbers and frequencies (f=88, 113 and 150 Hz). They observed that for high values of streaming Reynolds number, the axial streaming velocity starts to depart from the theoretical slow streaming. It should be noted that their experiments have been performed at uncontrolled thermal boundary conditions. However, the LDA measures velocity at one spatial location at a time is not capable of simultaneously mapping the flow in a two-dimensional region. Due to the large magnitude of acoustic velocity which is superimposed on the streaming velocity, the previous PIV measurements were conducted only in the vicinity of a velocity node, where the magnitude of the acoustic velocity is negligible.

Influence of temperature gradient on streaming shape and velocity

The influence of the axial temperature gradient (i.e. the temperature gradient in the direction of the acoustic wave propagation) on acoustic streaming has been extensively studied analytically, numerically and experimentally. Rott [107] derived a simplified analytical formula for the acoustic streaming including the effect of variable tube wall temperature. Aktas and Farouk [16] numerically investigated thermal convection in a 2-D resonator. In their model, the left and right sidewalls were kept at different temperatures, while the top and bottom walls were kept insulated. They reported that the influence of mechanically-induced periodic oscillations on the heat transfer characteristics of the system is significant only in the presence of steady streaming flows. Thompson *et al.* [108] experimentally investigated the influence of axial temperature gradient on the behavior of the streaming flow. They observed that as the magnitude of the axial temperature gradient increases, the shape of streaming vortices becomes distorted.

Unlike the axial temperature gradient, the influences of transverse temperature gradient (i.e. the temperature gradient orthogonal to the direction of acoustic wave propagation) on acoustic streaming have been scarcely investigated. Very recently, only one study has numerically investigated this behavior [109]. They considered the temperature dependent conductivity and viscosity in their model and conducted simulations at top-bottom wall temperature difference of 0°C, 20°C and 60°C. At 20°C and 60°C, they found that the classical two symmetric streaming vortices are distorted to one vortex. However, they did not study the transition behavior of streaming vortices due to the gradual increase in the temperature gradient. Furthermore, they did not provide any validation of their numerical model.

Summary

As seen in the above literature review, all of the reported measurements of streaming velocity fields are either point measurement or have been performed in the vicinity of a velocity node. There is no reported study on the measurement of two-dimensional streaming patterns along the resonator. Furthermore, no experimental study investigated the formation process of the regular and irregular acoustic streaming, as well as, the effects of transverse temperature gradient on acoustic streaming.

1.2.4 Acoustic standing wave pump and micropump

In recent years, intensive efforts have been made to design an efficient ASWP. These efforts can be traced back to Mandorian [22]. The pump invented by Mandorian works based on the principle described in section 1.1. Due to the pressure differential between the pressure node and the pressure antinode, fluid outside the chamber at the pressure node will be forced into the chamber and fluid outside the chamber at the pressure antinode will be forced out, thus achieving a pumping action. Later, Lucas [110] and Bishop [111, 10] reported the similar devices for refrigeration and air-conditioning compressors. Recently, Kawahashi *et al.* [112] claimed to invent an acoustic fluid machine that works similar to the previous inventions except that they used a chamber with the optimized shape to achieve more pumping flow rate. The pumping action of the above-mentioned pumps requires one check valve at inlet and outlet, and therefore, moving mechanical parts are involved.

1.3 Motivation and objectives

1.3.1 Motivation

Although, there are several studies dealing with the numerical investigation of linear and nonlinear acoustic standing waves, there is still need to more accurate numerical schemes for solving both linear and nonlinear standing wave equations.

The experimental investigations of acoustic velocity fields of linear and nonlinear standing wave are scarce and there is no two-dimensional velocity measurement of nonlinear standing wave using PIV system. Furthermore, all of the reported measurements of acoustic streaming velocity fields are either point measurements or have been performed in the vicinity of a velocity node only. There is no reported study about measuring the two-dimensional streaming patterns along the resonator. Moreover, there is no experimental study about the influences of transverse temperature gradient on acoustic streaming.

Another motivation of this research is that, in spite of the importance of the ASWP as a unique solution for many applications, there is no academic investigation of the standing wave pump. Only a few patents regarding to fabrication of the standing wave pump with no numerical and experimental analysis can be found in the open literature. Thus, the design and development of such pump would be challenging. Furthermore, the waves inside the pump could be nonlinear. The dynamics of nonlinear waves even in simple cavities is still not well understood. This makes the analysis and design of standing wave pump, even more challenging. Furthermore, the existing ASWPs have one main drawback. They need one or more check valves for their operation. The significant problems associated with these pumps include the fatigue of moving valves, clog, high pressure loss of valves and low driving frequency. Therefore, developing a valveless version of the ASWP would be a great step forward in the field of valveless pumping.

Since the valveless ASWP needs no check valve, its driving frequency can be increased to high frequencies (20 kHz or more). Therefore, the length of the pump chamber can be decreased to the order of millimeter. Thus, the *acoustic standing wave micropump* (ASWMP) could be able to pump fluids at micro scale and it can be consider as a new pumping actuation mechanism for micropumps.

For the characterization of acoustic resonators, thermoacoustic devices, the valveless ASWP and ASWMP, and to obtain some knowledge closer to the practical needs, a thorough knowledge of linear and nonlinear acoustic standing wave and acoustic streaming dynamics is essential.

1.3.2 Objectives

The main objectives of the proposed research are:

- To understand the linear and nonlinear acoustic standing wave and acoustic streaming dynamics through numerical and experimental investigations.
- To design and development of a valveless acoustic standing wave pump and micropump.

In order to achieve these objectives, linear and nonlinear standing wave equations have been solved numerically using the new schemes. The variation of the nonlinear pressure and velocity have been measured. The nonlinear behaviors of the temporal and axial pressure and velocity waveforms have been described and highlighted. The two-dimensional pattern of the nonlinear phenomenon of acoustic streaming has been measured using a novel technique. The formation process of regular and irregular acoustic streaming, as well as, the effects of transverse temperature gradient on acoustic streaming have been investigated. The application of the acoustic standing wave in fluid pumping has been studied. New valveless acoustic standing wave pump and micropump have been introduced and the velocity fields inside this novel pumps have been analyzed.

1.4 Scope of the thesis

In this context, the research is focused on the study of acoustic standing wave and streaming as well as acoustic standing wave pump and micropump. In chapter 2, the linear standing wave is investigated using a new sixth-order accurate numerical scheme. New numerical models for nonlinear standing wave equation are presented in

chapter 3. The experimental investigations of the acoustic pressure and velocity fields are described in chapters 4 and 5, respectively. The experimental investigations of the acoustic streaming are presented in chapter 6. Finally, the novel valveless ASWP and ASWMP are described in chapters 7 and 8, respectively.

CHAPTER 2
Sixth-order Accurate Compact Solver for the Helmholtz Equation

2.1 Introduction

Linear standing wave is governed by the Helmholtz equation. Intensive research has been performed in recent years to develop efficient and accurate numerical schemes to solve the Helmholtz equation. A key study work in this field has been performed by Singer and Turkel [41]. They developed a sixth-order compact FDM for the two-dimmensional Helmholtz equation. They used the Helmholtz equation to calculate higher-order correction terms. Sutmann [42] extended the same scheme for the three-dimmensional Helmholtz equation. However, for both papers, the authors implemented their schemes only with Dirichlet boundary conditions. Whereas, some practical problems such as acoustic scattering and structural acoustic interactions, need to be solved with Neumann boundary conditions [113, 114]. In the present study, a new 9-point stencil, sixth-order accurate compact FDM has been developed and implemented for solving the Helmholtz equation in one-dimensional and two-dimensional domains with Dirichlet and/or Neumann boundary conditions. To the best of our knowledge, this study is the first that developed a sixth-order compact FDM with the Neumann boundary conditions.

2.2 Helmholtz equation

Linear wave propagation in a lossless medium is described by the wave equation,

$$(\frac{1}{c^2}\frac{\partial^2}{\partial t^2} - \nabla^2)\Psi(\mathbf{r}, t) = F(\mathbf{r}, t), \tag{2.1}$$

where $\Psi(\mathbf{r},t)$ is the velocity potential at any time t and any point $\mathbf{r} = (x,y,z)$ and $F(\mathbf{r},t)$ is a prescribed source function. The time harmonic linear acoustic wave propagation is governed by the Helmholtz equation. That is, the Helmholtz equation is obtained from the wave equation when the solution is time-harmonic. For instance, we might have

$$F(\mathbf{r},t) = f(\mathbf{r})e^{i\omega t}. \tag{2.2}$$

Assuming function of this type, we can look for time-harmonic solutions of the forms of the Helmholtz equation,

$$\Psi(\mathbf{r},t) = \varphi(\mathbf{r})e^{i\omega t}. \tag{2.3}$$

Substituting equations (2.2) and (2.3) into (2.1) give the following forms

$$\begin{aligned}
\left(\frac{1}{c^2}\frac{\partial^2}{\partial t^2} - \nabla^2\right)\varphi(\mathbf{r})e^{i\omega t} &= f(\mathbf{r})e^{i\omega t}, \\
-\frac{\omega^2}{c^2}\varphi(\mathbf{r})e^{i\omega t} - \nabla^2\varphi(\mathbf{r})e^{i\omega t} &= f(\mathbf{r})e^{i\omega t}, \\
(k^2 + \nabla^2)\varphi(\mathbf{r}) &= -f(\mathbf{r}),
\end{aligned} \tag{2.4}$$

where $k = \omega/c$ is wave number [115].

The solution of Eq. (2.4) requires boundary conditions. Dirichlet and Neumann boundary conditions for the Helmholtz equation are common in acoustics. The Dirichlet boundary condition $\varphi = \varphi_0$ is associated with the known pressure amplitude on vibrating boundaries. Homogeneous Neumann boundary condition $\partial\varphi/\partial n = 0$ (n is the unit vector normal to the boundary surface) is associated with zero velocity on a boundary, which occurs on rigid walls.

2.3 Nine-point sixth-order accurate compact finite difference scheme

The proposed method is based on a sixth-order accurate approximation to the derivative calculated from the Helmholtz equation. The scheme has been developed

for both one-dimensional and two-dimensional uniform Cartesian grids with grid spacing $\Delta x = \Delta y = h$. The notation δ_x^0 is used to denote the first order central difference with respect to x, which is defined as

$$\delta_x^0 u_i = \frac{u_{i+1} - u_{i-1}}{2h}, \tag{2.5}$$

where $u_i = u(x_i)$. The standard second-order central difference is denoted by δ_x^2 and is defined as

$$\delta_x^2 u_i = \frac{u_{i+1} - 2u_i + u_{i-1}}{h^2}. \tag{2.6}$$

The other difference operators δ_y^0 and δ_y^2 are defined in a similar manner.

2.3.1 One dimensional case

In one dimensional case, the Helmholtz equation becomes the following ordinary differential equation

$$u'' + k^2 u = f(x) \quad \text{for } x \in [a, b]. \tag{2.7}$$

A sixth-order accurate finite difference estimate of Eq. (2.6) is

$$\delta_x^2 u_i = u_i'' + \frac{h^2}{12} u_i^{(4)} + \frac{h^4}{360} u_i^{(6)} + O(h^6). \tag{2.8}$$

Both $O(h^2)$ and $O(h^4)$ terms are included in Eq. (2.8), because we want to approximate all of them in order to construct a sixth order accurate scheme. Applying δ_x^2 to $u_i^{(4)}$, we get

$$u_i^{(6)} = \delta_x^2 u_i^{(4)} + O(h^2). \tag{2.9}$$

Substitution of Eq. (2.9) into Eq. (2.8) yields

$$\delta_x^2 u_i = u_i'' + \frac{h^2}{12} u_i^{(4)} + \frac{h^4}{360} (\delta_x^2 u_i^{(4)} + O(h^2)) + O(h^6). \tag{2.10}$$

To get a compact $O(h^6)$ approximation, we simply take the appropriate derivative of Eq. (2.7), that is

$$u_i^{(4)} = -k^2 u_i'' + f_i'', \tag{2.11}$$

where $f_i = f(x_i)$ and $f_i'' = f''(x_i)$. Inserting Eq. (2.11) into Eq. (2.10), we get

$$\delta_x^2 u_i = u_i'' + \left(\frac{h^2}{12} + \frac{h^4}{360}\delta_x^2\right)(-k^2 u_i'' + f_i'') + O(h^6). \tag{2.12}$$

Then, a compact (implicit) approximation for u_i'' with a sixth-order accuracy will be given as

$$u_i'' = \frac{\delta_x^2 u_i - \frac{h^2}{12}\left(1 + \frac{h^2}{30}\delta_x^2\right) f_i''}{\left(1 - \frac{k^2 h^2}{12}\left(1 + \frac{h^2}{30}\delta_x^2\right)\right)} + O(h^6). \tag{2.13}$$

Using this estimate and considering the discrete solution of Eq. (2.7) which satisfies the approximation, we get

$$\delta_x^2 U_i + k^2\left(1 - \frac{k^2 h^2}{12}\left(1 + \frac{h^2}{30}\delta_x^2\right)\right) U_i = \left(1 - \frac{k^2 h^2}{12}\left(1 + \frac{h^2}{30}\delta_x^2\right)\right) f_i + \frac{h^2}{12}\left(1 + \frac{h^2}{30}\delta_x^2\right) f_i'', \tag{2.14}$$

$$k^2\left(1 - \frac{k^2 h^2}{12}\right) U_i + \left(1 - \frac{k^4 h^4}{360}\right)\delta_x^2 U_i = \left(1 - \frac{k^2 h^2}{12}\right) f_i - \frac{k^2 h^4}{360}\delta_x^2 f_i + \frac{h^2}{12} f_i'' + \frac{h^4}{360}\delta_x^2 f_i'', \tag{2.15}$$

where U_i is the discrete approximation to u_i satisfying the discrete formulation of Eq. (2.7) which implies,

$$u_i = U_i + O(h^6). \tag{2.16}$$

Using Eq. (2.6) and

$$\delta_x^2 f_i'' = (f_{i+1}'' - 2f_i'' + f_{i-1}'')/h^2, \tag{2.17}$$

we can express the scheme in the following form

$$d_{10} U_i + d_{11}(U_{i+1} + U_{i-1}) = b_{10} f_i + b_{11}(f_{i+1} + f_{i-1}) + b_{12} f_i'' + b_{13}(f_{i+1}'' + f_{i-1}''), \tag{2.18}$$

where,

$$\begin{aligned} d_{10} &= -2 + k^2 h^2\left(1 - \frac{28 k^2 h^2}{360}\right) \quad , \quad d_{11} = 1 - \frac{k^4 h^4}{360}, \\ b_{10} &= \left(1 - \frac{28 k^2 h^2}{360}\right) h^2 \quad , \quad b_{11} = \frac{-k^2 h^4}{360} \quad , \quad b_{12} = \frac{28 h^4}{360} \quad , \quad b_{13} = \frac{h^4}{360}. \end{aligned} \tag{2.19}$$

Since f and f'' are known at every grid point, the right hand side of Eq. (2.18) is known for all nodes. The system equations given by Eq. (2.18) can be written for each node and a resultant linear system of equation is obtained. In the cases where f is not known analytically, only a fourth-order accurate approximation of f'' is required, which can be obtained using

$$f_i'' = (-f_{i+1} + 16f_{i+1/2} - 30f_i + 16f_{i-1/2} - f_{i-1})/12h^2. \tag{2.20}$$

2.3.2 Two dimensional case

Consider the two-dimensional Helmholtz equation

$$\frac{\partial^2 u}{\partial x^2} + \frac{\partial^2 u}{\partial y^2} + k^2 u(x,y) = f(x,y) \quad \text{for } x \in [a,b] \text{ and } y \in [c,d]. \tag{2.21}$$

We want to have a 9-point stencil which is symmetric in both x and y directions. The central difference scheme for Eq. (2.21) in two dimensions can be written as

$$\delta_x^2 u_{i,j} + \delta_y^2 u_{i,j} + k^2 u_{i,j} + T_{i,j} = f_{i,j}, \tag{2.22}$$

where $u_{i,j} = u(x_i, y_j), f_{i,j} = f(x_i, y_j)$ and

$$T_{i,j} = -\frac{h^2}{12}\Big[\frac{\partial^4 u}{\partial x^4} + \frac{\partial^4 u}{\partial y^4}\Big]_{i,j} - \frac{h^4}{360}\Big[\frac{\partial^6 u}{\partial x^6} + \frac{\partial^6 u}{\partial y^6}\Big]_{i,j} + O(h^6). \tag{2.23}$$

The appropriate derivatives of Eq. (2.21) are,

$$\frac{\partial^4 u}{\partial x^4} = \frac{\partial^2 f}{\partial x^2} - k^2\frac{\partial^2 u}{\partial x^2} - \frac{\partial^4 u}{\partial x^2 \partial y^2} \quad , \quad \frac{\partial^4 u}{\partial y^4} = \frac{\partial^2 f}{\partial y^2} - k^2\frac{\partial^2 u}{\partial y^2} - \frac{\partial^4 u}{\partial y^2 \partial x^2} \tag{2.24}$$

Using Eq. (2.24) in Eq. (2.23), we get

$$T_{i,j} = -\frac{h^2}{12}\Big(\nabla^2 f_{i,j} - 2\Big[\frac{\partial^4 u}{\partial x^2 \partial y^2}\Big]_{i,j} - k^2\Big[\frac{\partial^2 u}{\partial x^2} + \frac{\partial^2 u}{\partial y^2}\Big]_{i,j}\Big) - \frac{h^4}{360}\Big[\frac{\partial^6 u}{\partial x^6} + \frac{\partial^6 u}{\partial y^6}\Big]_{i,j} + O(h^6). \tag{2.25}$$

In our derivation of a sixth order accurate scheme, we need a fourth-order approximation of $\partial^4 u/\partial x^2 \partial y^2$ in Eq. (2.25) which can be written as

$$\Big[\frac{\partial^4 u}{\partial x^2 \partial y^2}\Big]_{i,j} = \delta_x^2 \delta_y^2 u_{i,j} - \frac{h^2}{12}\Big[\frac{\partial^6 u}{\partial x^4 \partial y^2} + \frac{\partial^6 u}{\partial x^2 \partial y^4}\Big]_{i,j} + O(h^4). \tag{2.26}$$

Substituting Eq. (2.26) into Eq. (2.25), we get

$$\begin{aligned} T_{i,j} = \frac{h^2}{12}\big(&- \nabla^2 f_{i,j} + 2\delta_x^2 \delta_y^2 u_{i,j} + k^2 f_{i,j} - k^4 u_{i,j}\big) \\ &- \frac{h^4}{360}\Big[\frac{\partial^6 u}{\partial x^6} + 5\frac{\partial^6 u}{\partial x^4 \partial y^2} + 5\frac{\partial^6 u}{\partial x^2 \partial y^4} + \frac{\partial^6 u}{\partial y^6}\Big]_{i,j} + O(h^6). \end{aligned} \tag{2.27}$$

Eq. (2.27) clearly shows that a compact sixth-order approximation requires compact expressions of the four derivatives of order six, which can be obtained by further differentiating Eq. (2.21). That is

$$\frac{\partial^4 f}{\partial x^2 \partial y^2} = \frac{\partial^6 u}{\partial x^4 \partial y^2} + \frac{\partial^6 u}{\partial x^2 \partial y^4} + k^2 \frac{\partial^4 u}{\partial x^2 \partial y^2} \tag{2.28}$$

$$\frac{\partial^6 u}{\partial x^6} + \frac{\partial^6 u}{\partial y^6} = \nabla^4 f - k^2\Big(\frac{\partial^4 u}{\partial x^4} + \frac{\partial^4 u}{\partial y^4}\Big) - \Big(\frac{\partial^6 u}{\partial x^4 \partial y^2} + \frac{\partial^6 u}{\partial x^2 \partial y^4}\Big). \tag{2.29}$$

Substituting Eqs. (2.24,2.28) into Eq. (2.29), we get

$$\frac{\partial^6 u}{\partial x^6} + \frac{\partial^6 u}{\partial y^6} = \nabla^4 f - \frac{\partial^4 f}{\partial x^2 \partial y^2} - k^2 \nabla^2 f + k^4(-k^2 u + f) + 3k^2 \frac{\partial^4 u}{\partial x^2 \partial y^2}. \tag{2.30}$$

Using Eqs. (2.28,2.30), we can eliminate all derivatives of u in Eq. (2.27), that is

$$\begin{aligned} T_{i,j} = \frac{h^2}{12}\big(&- \nabla^2 f_{i,j} + 2\delta_x^2 \delta_y^2 u_{i,j} + k^2 f_{i,j} - k^4 u_{i,j}\big) \\ &- \frac{h^4}{360}\big(\nabla^4 f_{i,j} + 4\Big[\frac{\partial^4 f}{\partial x^2 \partial y^2}\Big]_{i,j} - k^2 \nabla^2 f_{i,j} + k^4 f_{i,j} - k^6 u_{i,j} - 2k^2 \delta_x^2 \delta_y^2 u_{i,j}\big) + O(h^6). \end{aligned} \tag{2.31}$$

The compact sixth-order approximation of the two-dimensional Helmholtz equation can thus be obtained as

$$\frac{h^2}{6}\big(1+\frac{k^2h^2}{30}\big)\delta_x^2\delta_y^2U_{i,j}+(\delta_x^2+\delta_y^2)U_{i,j}+k^2\big(1-\frac{k^2h^2}{12}+\frac{k^4h^4}{360}\big)U_{i,j}= \\ \big(1-\frac{k^2h^2}{12}+\frac{k^4h^4}{360}\big)f_{i,j}+\big(\frac{h^2}{12}\big(1-\frac{k^2h^2}{30}\big)\big)\nabla^2f_{i,j}+\frac{h^4}{360}\nabla^4f_{i,j}+\frac{h^4}{90}\big[\frac{\partial^4f}{\partial x^2\partial y^2}\big]_{i,j}, \tag{2.32}$$

where $U_{i,j}$ is the discrete approximation to $u_{i,j}$ satisfying the discrete formulation of Eq. (2.21) which means that $u_{i,j}=U_{i,j}+O(h^6)$. As it is seen, we can express the equation in the form of

$$d_{20}U_{i,j}+d_{21}D_1+d_{22}D_2=b_{20}f_{i,j}+b_{21}\nabla^2f_{i,j}+b_{22}\nabla^4f_{i,j}+b_{23}\big[\frac{\partial^4f}{\partial x^2\partial y^2}\big]_{i,j}, \tag{2.33}$$

where,

$$\begin{aligned} D_1&=U_{i+1,j}+U_{i-1,j}+U_{i,j+1}+U_{i,j-1},\\ D_2&=U_{i+1,j+1}+U_{i-1,j+1}+U_{i+1,j-1}+U_{i-1,j-1},\\ B_1&=f_{i+1,j}+f_{i-1,j}+f_{i,j+1}+f_{i,j-1},\\ B_2&=f_{i+1,j+1}+f_{i-1,j+1}+f_{i+1,j-1}+f_{i-1,j-1}, \end{aligned} \tag{2.34}$$

then we get

$$\begin{aligned} d_{20}&=-\frac{10}{3}+k^2h^2\big(\frac{46}{45}-\frac{k^2h^2}{12}+\frac{k^4h^4}{360}\big)\ ,\ d_{21}=\frac{2}{3}-\frac{k^2h^2}{90}\ ,\ d_{22}=\frac{1}{6}+\frac{k^2h^2}{180},\\ b_{20}&=h^2\big(1-\frac{k^2h^2}{12}+\frac{k^4h^4}{360}\big),\ b_{21}=\frac{h^4}{12}\big(1-\frac{k^2h^2}{30}\big),\ b_{22}=\frac{h^6}{360},\ b_{23}=\frac{h^6}{90}. \end{aligned} \tag{2.35}$$

If we write the system equations given by Eq. (2.33) for each node, we can obtain the final linear system of equations. In the cases where f is not known analytically, only a fourth-order accurate approximation of ∇^2f and a second-order accurate approximation of ∇^4f and $\frac{\partial^4f}{\partial x^2\partial y^2}$ are required.

2.3.3 Sixth-order accurate approximation of the Neumann boundary condition

We like to approximate the boundary conditions with the same accuracy as the interior nodes. For the Dirichlet boundary condition, we can simply put the boundary for every node on the boundary. For the Neumann boundary condition, the sixth-order approximation is conducted for both one dimensional and two dimensional cases.

One dimensional case

For a Neumann boundary condition in one dimension, we assume

$$u'(x_0) = \beta \ \ (\beta \text{ a constant}). \tag{2.36}$$

The sixth-order approximation of Eq. (2.36) is

$$\delta_x^0 u_i = u_i' + \frac{h^2}{6}u_i''' + \frac{h^4}{120}u_i^{(5)} + O(h^6), \tag{2.37}$$

$$\delta_x^0 u_i = u_i' + \frac{h^2}{6}u_i''' + \frac{h^4}{120}\left(\delta_x^2 u_i''' + O(h^2)\right) + O(h^6). \tag{2.38}$$

Differentiating Eq. (2.7) will result in

$$u_i''' = -k^2 u_i' + f'. \tag{2.39}$$

Using Eq. (2.39) in Eq. (2.38), we get

$$\delta_x^0 u_i = (1 - \frac{k^2h^2}{6})u' - \frac{k^2h^4}{120}\delta_x^2 u_i' + \frac{h^2}{6}(1 + \frac{h^2}{20}\delta_x^2)f_i' + O(h^6). \tag{2.40}$$

Using

$$\delta_x^2 u_i' = u_i''' + O(h^2) \tag{2.41}$$

and Eq. (2.39) in Eq. (2.40) gives

$$\delta_x^0 u_i = (1 - \frac{k^2h^2}{6} + \frac{k^4h^4}{120})u_i' + \frac{h^2}{6}\left(1 - \frac{h^2}{20}\right)f_i' + \frac{h^4}{120}\delta_x^2 f_i' + O(h^6). \tag{2.42}$$

Using

$$\delta_x^2 f_i' = (f_{i+1}' - 2f_i' + f_{i-1}')/h^2 + O(h^2) \tag{2.43}$$

and Eq. (2.5) in Eq. (2.42), we get

$$\frac{u_{i+1} - u_{i-1}}{2h} = (1 - \frac{k^2h^2}{6} + \frac{k^4h^4}{120})u' + \frac{h^2}{6}(\frac{9}{10} - \frac{k^2h^2}{20})f_i' + \frac{h^2}{120}(f_{i+1}' + f_{i-1}') + O(h^6). \tag{2.44}$$

Considering discrete formulation and using Eq. (2.36) for $i = 0$, we get

$$d_{11}(U_1 - U_{-1}) = 2h\beta d_{11}(1 - \frac{k^2h^2}{6} + \frac{k^4h^4}{120}) + \frac{h^3}{3}d_{11}(\frac{9}{10} - \frac{k^2h^2}{20})f_0' + \frac{h^3}{60}d_{11}(f_1' + f_{-1}'). \tag{2.45}$$

U_{-1} should be eliminated from Eq. (2.45) as there is no equation at point x_{-1}. Using Eq. (2.18) for $i = 0$, we get

$$d_{11}(U_1 + U_{-1}) + d_{10}U_0 = b_{10}f_0 + b_{11}(f_1 + f_{-1}) + b_{12}f_0'' + b_{13}(f_1'' + f_{-1}'') \tag{2.46}$$

Eqs. (2.45,2.46) can be used to eliminate U_{-1} and get the desired approximation for the boundary point x_0, that is

$$\begin{aligned} 2d_{11}U_1 + d_{10}U_0 = {} & 2h\beta d_{11}(1 - \frac{k^2h^2}{6} + \frac{k^4h^4}{120}) + b_{10}f_0 + b_{11}(f_1 + f_{-1}) \\ & + \frac{h^3}{3}d_{11}(\frac{9}{10} - \frac{k^2h^2}{20})f_0' + \frac{h^3}{60}d_{11}(f_1' + f_{-1}') + b_{12}f_0'' + b_{13}(f_1'' + f_{-1}''). \end{aligned} \tag{2.47}$$

All parameters on the right hand side of Eq. (2.47) are known. In the cases where f is not known analytically, only a fourth-order accurate approximation of f' is required.

Two dimensional case

For a Neumann boundary condition in two dimensions, we assume

$$\frac{\partial u}{\partial x}|_{x=0} = \beta(y). \tag{2.48}$$

The sixth-order approximation of Eq. (2.48) is

$$\delta_x^0 u_i = [\frac{\partial u}{\partial x}]_{i,j} + \frac{h^2}{6}[\frac{\partial^3 u}{\partial x^3}]_{i,j} + \frac{h^4}{120}[\frac{\partial^5 u}{\partial x^5}]_{i,j} + O(h^6). \tag{2.49}$$

Using the appropriate derivatives of Eq. (2.21), we get

$$\frac{\partial^3 u}{\partial x^3} = \frac{\partial f}{\partial x} - k^2\frac{\partial u}{\partial x} - \frac{\partial^3 u}{\partial x \partial y^2} \quad , \quad \frac{\partial^5 u}{\partial x^5} = \frac{\partial^3 f}{\partial x^3} - k^2\frac{\partial^3 u}{\partial x^3} - \frac{\partial^5 u}{\partial x^3 \partial y^2}, \tag{2.50}$$

For the sixth order accurate scheme, a fourth-order approximation of $(\partial^3 u/\partial x \partial y^2)$ is needed in Eq. (2.50) which can be written as

$$[\frac{\partial^3 u}{\partial x \partial y^2}]_{i,j} = \delta_x \delta_y^2 u_{i,j} - \frac{h^2}{12}[\frac{\partial^5 u}{\partial x \partial y^4} + 2\frac{\partial^5 u}{\partial x^3 \partial y^2}]_{i,j} + O(h^4). \tag{2.51}$$

Substituting Eq. (2.51) into Eq. (2.50), we get

$$[\frac{\partial^3 u}{\partial x^3}]_{i,j} = [\frac{\partial f}{\partial x}]_{i,j} - k^2[\frac{\partial u}{\partial x}]_{i,j} - \delta_x \delta_y^2 u_{i,j} + \frac{h^2}{12}[\frac{\partial^5 u}{\partial x \partial y^4} + 2\frac{\partial^5 u}{\partial x^3 \partial y^2}]_{i,j} + O(h^4). \tag{2.52}$$

The second-order approximation of $(\partial^3 u/\partial x^3)$ can be written as

$$[\frac{\partial^3 u}{\partial x^3}]_{i,j} = [\frac{\partial f}{\partial x}]_{i,j} - k^2[\frac{\partial u}{\partial x}]_{i,j} - \delta_x \delta_y^2 u_{i,j} + O(h^2). \tag{2.53}$$

Using Eqs. (2.50,2.53), the second-order approximation of $(\partial^5 u/\partial x^5)$ can be written as

$$[\frac{\partial^5 u}{\partial x^5}]_{i,j} = [\frac{\partial^3 f}{\partial x^3}]_{i,j} - k^2[\frac{\partial f}{\partial x}]_{i,j} + k^4[\frac{\partial u}{\partial x}]_{i,j} + k^2\delta_x \delta_y^2 u_{i,j} - [\frac{\partial^5 u}{\partial x^3 \partial y^2}]_{i,j} + O(h^2). \tag{2.54}$$

The appropriate derivatives of Eq. (2.21) gives

$$\frac{\partial^3 f}{\partial x \partial y^2} = \frac{\partial^5 u}{\partial x^3 \partial y^2} + \frac{\partial^5 u}{\partial x \partial y^4} + k^2\frac{\partial^3 u}{\partial x \partial y^2} \quad \Rightarrow \quad \frac{\partial^5 u}{\partial x^3 \partial y^2} + \frac{\partial^5 u}{\partial x \partial y^4} = \frac{\partial^3 f}{\partial x \partial y^2} - k^2\frac{\partial^3 u}{\partial x \partial y^2}. \tag{2.55}$$

Substituting Eqs. (2.52,2.54,2.55) into Eq. (2.49), and after some modifications we get

$$\delta_x^0 u_i - \frac{k^4h^4}{120}[\frac{\partial u}{\partial x}]_{i,j} + \frac{h^2}{6}(1+\frac{k^2h^2}{30})\delta_x\delta_y^2 u_{i,j} =$$
$$(1-\frac{k^2h^2}{6})[\frac{\partial u}{\partial x}]_{i,j} + \frac{h^2}{6}(1-\frac{k^2h^2}{20})[\frac{\partial f}{\partial x}]_{i,j} + \frac{h^4}{120}[\frac{\partial^3 f}{\partial x^3}]_{i,j} + \frac{h^4}{72}[\frac{\partial^3 f}{\partial x \partial y^2}]_{i,j} + O(h^6). \tag{2.56}$$

For $(\partial u/\partial x)_{i,j}$ on the right hand side of Eq. (2.56), we use the approximation

$$[\partial u/\partial x]_{i,j} = \delta_x^0 u_i + \vartheta h^2 \delta_x \delta_y^2 u_{i,j}, \tag{2.57}$$

where ϑ is an arbitrary number. Using Eq. (2.57) in Eq. (2.56), multiplying by $2h$ and setting $i = 0$, we get

$$\hat{d}_{21}(U_{1,j} - U_{-1,j}) + \hat{d}_{22}(U_{1,j+1} + U_{1,j-1} - U_{-1,j+1} - U_{-1,j-1}) =$$
$$(1-\frac{k^2h^2}{6})\beta_j + \frac{h^2}{6}(1-\frac{k^2h^2}{20})[\frac{\partial f}{\partial x}]_{0,j} + \frac{h^4}{120}[\frac{\partial^3 f}{\partial x^3}]_{0,j} + \frac{h^4}{72}[\frac{\partial^3 f}{\partial x \partial y^2}]_{0,j}. \tag{2.58}$$

where $\beta_j = \beta(y_j)$ and

$$\hat{d}_{21} = 1 - \frac{k^4h^4}{120}(1-2\vartheta) - \frac{1}{6h}(1+\frac{k^2h^2}{30}) \quad , \quad \hat{d}_{22} = -\frac{k^4h^4}{120}\vartheta + \frac{1}{12h}(1+\frac{k^2h^2}{30}). \tag{2.59}$$

Setting $i = 0$ in Eq. (2.33), we get

$$d_{20}U_{0,j} + d_{21}(U_{1,j} + U_{-1,j} + U_{0,j+1} + U_{0,j-1}) + d_{22}(U_{1,j+1} + U_{-1,j+1} + U_{1,j-1} + U_{-1,j-1})$$
$$= b_{20}f_{0,j} + b_{21}\nabla^2 f_{0,j} + b_{22}\nabla^4 f_{0,j} + b_{23}[\frac{\partial^4 f}{\partial x^2 \partial y^2}]_{0,j}. \tag{2.60}$$

In order to eliminate all elements with $i = -1$, we define a constant η such that $\eta = d_{21}/\hat{d}_{21} = d_{22}/\hat{d}_{22}$, which can be obtained by

$$\eta = \frac{1}{1 - \frac{k^4h^4}{120}}. \tag{2.61}$$

If we multiply Eq. (2.58) with η and add to Eq. (2.60) we will get the final equation for boundary nodes. That is,

$$d_{20}U_{0,j} + d_{21}(2U_{1,j} + U_{0,j+1} + U_{0,j-1}) + d_{22}(U_{1,j+1} + U_{1,j-1}) =$$
$$b_{20}f_{0,j} + b_{21}\nabla^2 f_{0,j} + b_{22}\nabla^4 f_{0,j} + b_{23}[\frac{\partial^4 f}{\partial x^2 \partial y^2}]_{0,j} +$$
$$\eta\big((1 - \frac{k^2h^2}{6})\beta_j + \frac{h^2}{6}(1 - \frac{k^2h^2}{20})[\frac{\partial f}{\partial x}]_{0,j} + \frac{h^4}{120}[\frac{\partial^3 f}{\partial x^3}]_{0,j} + \frac{h^4}{72}[\frac{\partial^3 f}{\partial x \partial y^2}]_{0,j}\big). \quad (2.62)$$

All parameters on the right hand side of Eq. (2.62) are known. In the cases where f is not known analytically, only a fourth-order accurate approximation of $\frac{\partial f}{\partial x}$ and a second-order approximation of $\frac{\partial^3 f}{\partial x^3}$ and $\frac{\partial^3 f}{\partial x \partial y^2}$ are required.

2.4 Numerical results

In order to validate our sixth-order accurate scheme and examine its behavior, we develop the scheme on two model problems in two dimensions. These problems are selected because they have exact solution to compare with the numerical results. In *problem A*, we solve

$$\frac{\partial^2 u}{\partial x^2} + \frac{\partial^2 u}{\partial y^2} + k^2 u(x,y) = (k^2 - 2\pi^2)\sin(\pi x)\sin(\pi y) \quad 0 \le x \le 1 \text{ and } 0 \le y \le 1, \quad (2.63)$$

with the pure Dirichlet boundary conditions on all sides of a unit square, that is

$$u(0,y) = u(1,y) = u(x,0) = u(x,1) = 0, \quad (2.64)$$

and in *problem B*, we solve

$$\frac{\partial^2 u}{\partial x^2} + \frac{\partial^2 u}{\partial y^2} + k^2 u(x,y) = (k^2 - 2\pi^2)\cos(\pi x)\sin(\pi y) \quad 0 \le x \le 1 \text{ and } 0 \le y \le 1, \quad (2.65)$$

with the Neumann boundary condition on the left side of a unit square and Dirichlet boundary conditions on the remaining three sides, that is

$$u_x(0,y) = 0 \quad u(1,y) = -\sin(\pi y) \quad u(x,0) = u(x,1) = 0. \tag{2.66}$$

The exact solutions for problems A and B are

$$u(x,y) = \sin(\pi x)\sin(\pi y) \tag{2.67}$$

and

$$u(x,y) = \cos(\pi x)\sin(\pi y), \tag{2.68}$$

respectively.

The next step is to solve the resultant linear set of equations. We use LU-decomposition by Gaussian elimination with pivoting for each set of equations to find values of u at $N \times N$ nodes. The code is written in MATLAB environment using version 7.1. The code is executed on a Pentium 4, 3 GHz PC.

In order to compare the numerical solution $U_{i,j}$ with the exact solution $u_{i,j}$, we use two performance metrics namely l_2-*norm* and *order*. The metric l_2-*norm* of the error vector e, is defined as,

$$\|e\|_2 = \frac{1}{N}\sqrt{\sum_{i,j=0}^{N} e_{i,j}^2}, \tag{2.69}$$

where $e_{i,j} = u_{i,j} - U_{i,j}$ and N is the number of nodes. The metric *order* is defined as

$$Order(n, n+1) = \log_2 \frac{\|e\|_\infty(n)}{\|e\|_\infty(n+1)}. \tag{2.70}$$

It measures the order of accuracy of numerical solutions. $\|e\|_\infty$ in Eq. (2.70) is called l_∞-*norm* of the error vector and is defined as

$$\|e\|_\infty = \max_{0 \le i,j \le N} e_{i,j} \tag{2.71}$$

The l_2-norm of the error and the order of accuracy, for different values of N and for k=10, are presented in tables 2–1 and 2–2 for problems A and B, respectively. It is clearly seen that the norm of the error behaves like the order of the scheme. As we multiply N by two, the error decreases by $2^6 = 64$. It shows that the present scheme has the accuracy of order six. This trend can also be seen in Figs. 2–1 and 2–2, where the $\log_2 \|e\|_\infty$ is plotted versus $\log_2 N$ for both problems A and B, respectively. The slope of the line is -6 which means that the order of accuracy is 6.

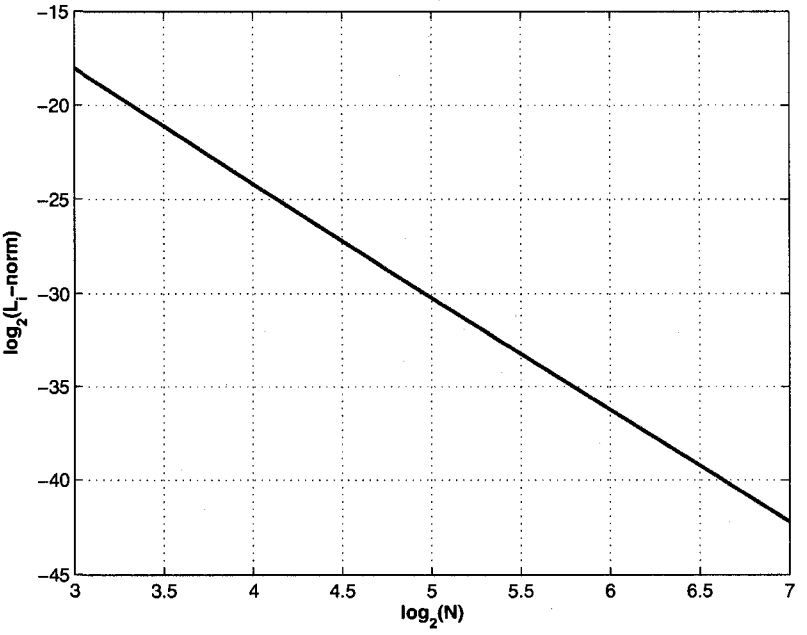

Figure 2–1: $\log_2 \|e\|_\infty$ versus $\log_2 N$ for problem A

The behavior of the present scheme is also examined for different values of k. Figs. 2–3 and 2–4 show $\log_2 \|e\|_2$ versus k with three different value of N for both problems A and B, respectively. Fig. 2–3 shows that for problem A, except for $4 \leq k \leq 5$ in which the scheme is more sensitive to the value of k, the method behaves robustly with respect to the wave number. Fig. 2–4 shows that in comparison with to problem A, the scheme for problem B is more sensitive to the value of k. However, for any given value of N, the overall error does not increase with an increase in k. As Figs.

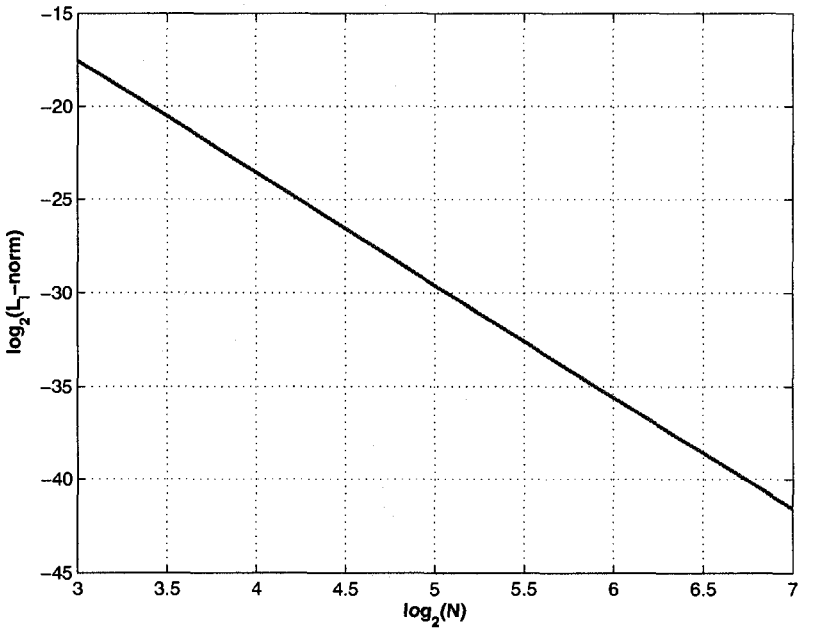

Figure 2–2: $\log_2 \|e\|_\infty$ versus $\log_2 N$ for problem B

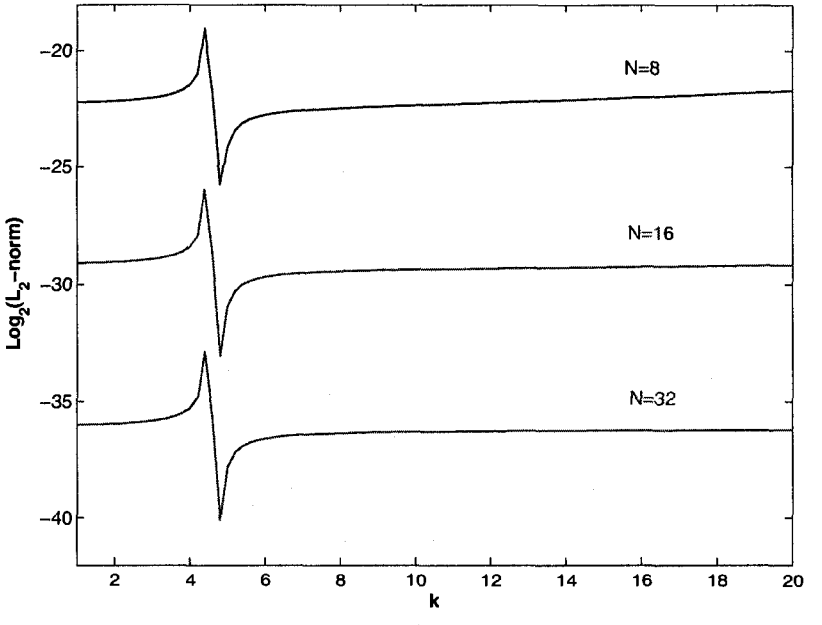

Figure 2–3: $\log_2 \|e\|_2$ versus k for problem A for N=8,16 and 32; k varies in units of 0.2.

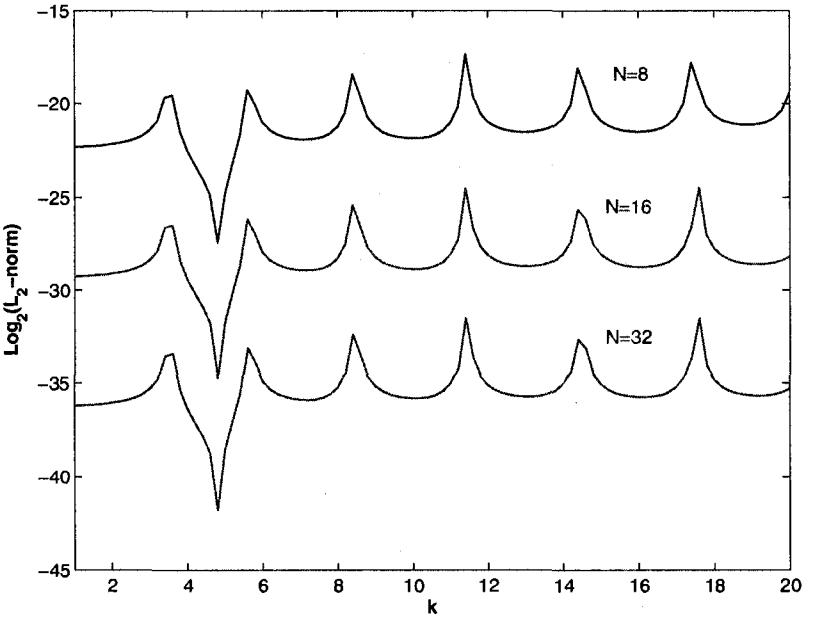

Figure 2–4: $\log_2 \|e\|_2$ versus k for problem B for N=8,16 and 32; k varies in units of 0.2.

2–3 and 2–4 indicate, at some particular values of k in both problems, the accuracy of the method is poor. This fact can be explained through eigenvalue analysis. The approximate eigenvalues for problems A and B are given as,

$$\Lambda_{Am,n} = k^2 - \pi^2(m^2 + n^2) \tag{2.72}$$

and,

$$\Lambda_{Bm,n} = k^2 - \pi^2\big((m + 1/2)^2 + n^2\big) \tag{2.73}$$

respectively [40]. For example, near $k = 4.44$ where $\Lambda_{A1,1} \rightarrow 0$, problem A is unstable and near $k = 5.663$ where $\Lambda_{B1,1} \rightarrow 0$, problem B is unstable and the scheme has poor accuracy.

One of the important advantages of the proposed scheme is that in comparison with the finite element, boundary element or spectral element methods, this method is very fast. A quantitative comparison in terms of the execution time between the

present scheme and the fourth-order FEM is presented in the last two columns of tables 2–1 and 2–2. The results show that for large number of nodes, the present scheme is more that 100 times faster than the fourth-order FEM.

The behavior of the proposed sixth-order accurate scheme is also investigated for the case where the wave resolution (kh) is kept constant. Fig. 2–5 shows the comparison of $\log_2 \|e\|_2$ between the fourth-order CFDM and the fourth-order FEM for $kh = 0.5$ at different values of $10 \leq k \leq 20$. As expected, error of the CFDM is smaller at higher wave numbers than that of the FEM which means that the performance of the CFDM is better than the FEM at higher wave numbers. The behavior of the six-order CFDM for the same conditions is plotted in Fig. 2–6.

2.5 Conclusions

In this chapter, a new 9-point sixth-order accurate compact FDM for solving the Helmholtz equation is presented. A sixth-order accurate symmetrical representation for the Neumann boundary condition is also developed. Numerical results show that our scheme has the expected accuracy and is more than 100 times faster than the fourth-order FEM. The results also show that the overall error does not increase with an increase in the wave number.

Table 2–1: Numerical results for problem A, $k = 10$

N	$\|e\|_2$	$\|e\|_\infty$	*Order*	*Execution time of the proposed scheme (sec)*	*Execution time of the 4-order FEM (sec)*
8	1.8561E-7	3.7586E-6		0.021	0.84
16	1.4556E-9	5.2585E-8	6.16	0.031	3.66
32	1.1750E-11	7.9975E-10	6.04	0.094	15.86
64	9.4278E-14	1.2433E-11	6.00	0.50	84.14
128	9.5151E-016	1.9691E-013	5.98	4.18	502.84

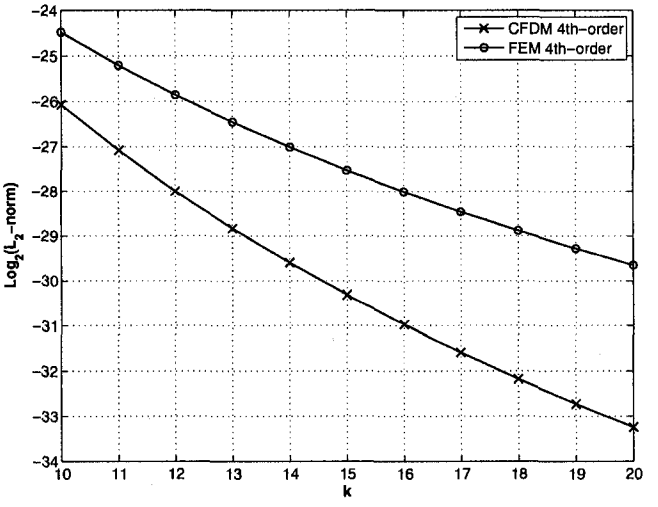

Figure 2–5: $\log_2 \|e\|_2$ of the fourth-order CFDM and the fourth-order FEM versus k for problem A at kh=0.5.

Table 2–2: Numerical results for problem B, $k = 10$

N	$\|e\|_2$	$\|e\|_\infty$	*Order*	*Execution time of the proposed scheme (sec)*	*Execution time of the 4-order FEM (sec)*
8	2.611E-7	3.368E-6		0.021	0.86
16	2.048E-9	8.112E-8	6.05	0.031	3.71
32	1.653E-11	1.2337E-9	6.04	0.11	17.47
64	1.3264E-13	1.9248E-11	6.00	0.58	95.11
128	1.0560E-015	3.0507E-013	5.98	4.42	541.15

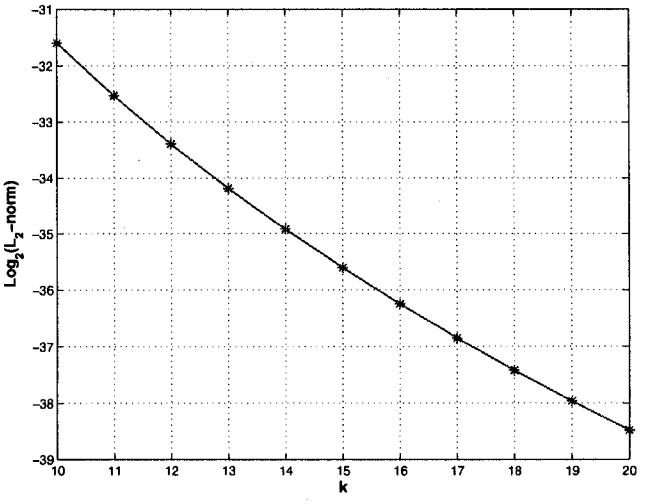

Figure 2-6: $\log_2 \|e\|_2$ of sixth-order CFDM versus k for problem A at kh=0.5; ; k varies in units of 1.

CHAPTER 3
Fourth-order Accurate Compact Solver for the 1-D Nonlinear Standing Wave Equation

3.1 Introduction

Recently, there has been a growing and renewed interest in numerical solvers for nonlinear standing waves. All the proposed numerical methods for solving the nonlinear standing wave equation can be categorized in two main groups of finite-amplitude and high-amplitude nonlinear standing wave which have been defined in section 1.1. A notable study in the finite-amplitude field has been reported by Vanhille and Campos-Pozuelo [82]. They proposed a nonlinear axisymmetric wave equation written in Lagrangian coordinates. A time domain numerical model, based on a finite difference algorithm, was developed to solve it. From the good agreement between numerical and experimental results the validity of the model was established.

In this chapter, the behavior of finite-amplitude nonlinear standing waves in an air-filled rigid-wall square tube is investigated numerically in section 3.2. The mathematical model of the finite-amplitude nonlinear standing wave is solved numerically using an effective finite difference method. The model can be used for any other thermoviscous medium. The model is then validated in both space and time domains using the experimentally obtained pressure measurements.

As the literature review (section 1.2.2) indicates, the accuracy of all previously developed schemes for solving highly nonlinear standing wave equation is of second order in space and of second or third order in time. In section 3.4, a three-dimensional exact wave equation is presented for acoustic standing waves of arbitrary amplitude in a tube excited by a vibrating diaphragm and filled with a thermoviscous fluid. The

effect of both thermoviscous attenuation and wall absorbtion have been considered in this equation. A high-order numerical scheme is described for solving highly nonlinear standing waves equation in one-dimension with no restriction on the nonlinearity level and type of fluid. The numerical scheme is fourth-order accurate in both time and space.

3.2 Finite-amplitude nonlinear standing wave

When the amplitude of the acoustic standing wave is infinitesimal, the acoustic wave can be described by linear laws. When the acoustic wave is driven into higher amplitude oscillations, the equations of motion are nonlinear.

3.2.1 Mathematical equations

For a viscous, compressible, heat-conducting fluid, the description of nonlinear acoustic waves is obtained using the basic equations of fluid mechanics along with the appropriate state equation.

Equation of continuity :

$$\rho_t + \nabla(\rho \mathbf{v}) = 0 \tag{3.1}$$

Navier-Stokes equation :

$$\rho\big(\partial \mathbf{v}/\partial t + (\mathbf{v}.\nabla)\mathbf{v}\big) = -\nabla p + \mu\nabla^2\mathbf{v} + (\mu_B + \frac{1}{3}\mu)\nabla(\nabla.\mathbf{v}) \tag{3.2}$$

A simpler form of this equation can be found using the vector identities, $\nabla\times(\nabla\times\mathbf{v}) = \nabla(\nabla.\mathbf{v}) - \nabla^2\mathbf{v}$ and $\frac{1}{2}\nabla\mathbf{v}^2 = (\mathbf{v}.\nabla\mathbf{v}) + \nabla\times(\nabla\times\mathbf{v})$ and assuming the motion to be irrotational, that is

$$\rho(\partial \mathbf{v}/\partial t + \frac{1}{2}\nabla\mathbf{v}^2) = -\nabla p + (\mu_B + \frac{4}{3}\mu)\nabla(\nabla\mathbf{v}), \tag{3.3}$$

or

$$\rho\big(\partial \mathbf{v}/\partial t + (\mathbf{v}.\nabla)\mathbf{v}\big) = -\nabla p + (\mu_B + \frac{4}{3}\mu)\nabla(\nabla\mathbf{v}). \tag{3.4}$$

Neglecting $\nabla \mathbf{v}^2$ and substituting $\rho = \rho_0 + \rho'$ and $p = P_0 + p'$ and assuming the disturbances to be small compared to the static values ($|\rho'| \ll \rho_0, |p'| \ll P_0$) and dropping the second and third order terms, the continuity and Navier-Stokes equations in one-dimension can be written as

$$\rho'_t + \rho u_x = 0, \tag{3.5}$$

$$\rho_0 u_t = -p_x + \mu b u_{xx}. \tag{3.6}$$

State equation: An equation of state particularly useful in acoustic is the one that relates pressure to density and entropy i.e., $p = p(\rho, s)$ [116]. We can write

$$p' = (\frac{\partial p}{\partial \rho})_s \rho' + (\frac{\partial p}{\partial s})_\rho s'. \tag{3.7}$$

Using $\rho_0 T_0 \frac{\partial s'}{\partial t} = \kappa \nabla T', (where, T' = \left(\frac{\partial T}{\partial p}\right)_s p')$ and the simplified version of the momentum equation, $\rho_0 \partial \mathbf{u}/\partial t = -\nabla p'$, we get $s' = -\frac{\kappa}{T_0}\left(\frac{\partial T}{\partial p}\right)_s \nabla.\mathbf{u}$, and using $\frac{1}{T_0}\left(\frac{\partial p}{\partial s}\right)_\rho \left(\frac{\partial T}{\partial p}\right)_s = \frac{1}{c_V} - \frac{1}{c_p}$, we obtain,

$$(\frac{\partial p}{\partial s})_\rho s' = -\kappa(\frac{1}{c_V} - \frac{1}{c_p})\nabla.\mathbf{u}, \tag{3.8}$$

Regarding the first term on right-hand side of Eq. (3.7), the sound speed c can be introduced as

$$c^2 \equiv \frac{\partial p'}{\partial \rho}|_{s=const}, \tag{3.9}$$

The sound speed may be thought of as a new thermodynamic variable, since it is derived from other thermodynamic quantities. In the limit of vanishing condensation ($\rho \rightarrow \rho_0$ or $|\rho'| \ll \rho_0$), c^2 becomes constant, which we denote c_0^2 ($c_0 = \sqrt{\gamma P_0/\rho_0}$). Thus, a modified equation of state in one-dimension can be written as,

$$p' = c_0^2 \rho' - \kappa(\frac{1}{c_V} - \frac{1}{c_p})u_x. \tag{3.10}$$

To eliminate ρ in Eq. (3.10), by substituting $u = \partial\chi/\partial t$ (χ is particle displacement), and integrating Eq. (3.5), we get

$$\rho' + \rho\chi_x = 0 \rightarrow \frac{\rho_0 - \rho}{\rho} = \chi_x \rightarrow \frac{\rho}{\rho_0} = \frac{1}{1+\chi_x}. \tag{3.11}$$

Substituting Eqs. (3.10,3.11) in Eq. (3.6), we get the final equation of 1-D finite-amplitude acoustic field in a thermoviscous fluid

$$\rho_0\chi_{tt} = \gamma P_0 \frac{1}{(1+\chi_x)^{\gamma+1}}\chi_{xx} + \mu b\chi_{txx}, \tag{3.12}$$

where,

$$b = \frac{\kappa}{\mu}\left(\frac{1}{c_V} - \frac{1}{c_p}\right) + \frac{4}{3} + \frac{\mu_B}{\mu}, \tag{3.13}$$

is the so-called viscosity number which shows the total effect of viscosity and heat conduction [117].

Consider progressive plane waves with a source at $x = 0$. The fluid is assumed to be initially at rest ,that is, particle displacement and velocity at $t = 0$ are zero. The fluid is excited by the harmonic motion of a diaphragm at $x = 0$ at frequency of f ($\omega = 2\pi f$). Assuming L to be the length of the tube, the following initial and boundary conditions are applicable,

$$\begin{aligned} &\chi(0,t) = \chi_0 \sin(wt) \ , \ \chi(L,t) = 0, \\ &\chi(x,0) = 0 \ , \ \chi_t(x,0) = 0. \end{aligned} \tag{3.14}$$

It must be noted that any time dependent excitation function and any position and shape of the diaphragm can be modeled using appropriate boundary conditions. The acoustic pressure p', can be evaluated from χ using the following equation,

$$p' = \frac{P_0}{(1+\chi_x)^{\gamma}} - P_0. \tag{3.15}$$

Eq. (3.15) can be derived by combining Eq. (3.11) and simplified version of Eq. (3.10) which is $p' = P_0(\rho/\rho_0)^\gamma$.

3.2.2 Numerical model

The mathematical formulation outlined in section 3.2.1 is solved numerically using the finite difference approach. This numerical scheme is based on a second-order accurate finite difference approximation for both x and t to evaluate $\chi(x,t)$ in Eq. (3.12). p' is then calculated using equation Eq. (3.15). The first step involves the discretization of Eq. (3.12). The x and t axes are subdivided into M and K uniform elements, respectively. Therefor, $h = \Delta x = L/M$ and $\tau = \Delta t = T/K$ denote the uniform spatial and temporal step sizes respectively, where T is the total simulation time. The mesh points (x_m, t_k) are given by $x_m = mh$, for $m = 0, 1, ..., M$, and $t_k = k\tau$, for $k = 0, 1, ..., K$. The second step is to replace the first and second order derivatives with centered-difference quotients. Substituting these values in Eq. (3.12) and after some manipulations, the following implicit and conditionally stable equation is obtained

$$
\begin{aligned}
&-A\chi_{m+1}^{k+1} + (2A+1)\chi_m^{k+1} - A\chi_{m-1}^{k+1} = \\
&B(m,k)\chi_{m+1}^{k} + 2(1-B(m,k))\chi_m^{k} + B(m,k)\chi_{m-1}^{k} - A\chi_{m+1}^{k-1} + (2A-1)\chi_m^{k-1} - A\chi_{m-1}^{k-1},
\end{aligned}
\tag{3.16}
$$

where, $\chi_m^k = \chi(x_m, t_k) + O(h^2, \tau^2)$ and

$$
A = (\nu b\tau)/(2h^2) \;\;,\;\; B(m,k) = \frac{c_0^2\tau^2/h^2}{\left(1 + \frac{\chi_{m+1}^k - \chi_{m-1}^k}{2h}\right)^{\gamma+1}}. \tag{3.17}
$$

The third step is to solve the resultant linear set of equations. LU-decomposition by Gaussian elimination with pivoting is used for each set of $M-1$ equations at each time step $2 \leq k \leq K$ to find values of χ at $M-1$ nodes.

As mentioned earlier, this implicit scheme is conditionally stable. The stability analysis of this scheme using Fourier or von Neumann method [118] shows that the stability condition is

$$\tau^2 \leq \frac{h^2}{c_0^2}\left(1 - \left(\frac{\nu b}{c_0 h}\right)^2\right). \tag{3.18}$$

Comparison of the numerical and experimental results of pressure signal for the finite-amplitude nonlinear case in time, space and frequency domains will be presented later in section 4.3.

3.3 Acoustic and streaming Reynolds numbers

Before continuing the investigation of the nonlinear standing waves, it is useful to introduce two important non-dimensional parameters which are used to discriminate linear and nonlinear acoustic and streaming flow fields. These parameters are *acoustic Reynolds number* and *streaming Reynolds number*. Generally, the *Reynolds number* (Re) is the ratio of the inertial force to the viscous force and defined as

$$Re = \frac{L_s U_s}{\nu}. \tag{3.19}$$

Assuming L_s to be the length of the tube and U_s to be the maximum acoustic velocity (u_{max}), the acoustic Reynolds number is defined as

$$Re_{a1} = \frac{c_0 u_{max}}{\nu\omega}. \tag{3.20}$$

Considering the total effect of viscosity and heat conduction, another definition of the acoustic Reynolds number is

$$Re_{a2} = \frac{c_0 u_{max}}{b\nu\omega}. \tag{3.21}$$

For $Re_{a2} \ll 1$, the acoustic waves are considered to be linear, whereas, nonlinear acoustical theory must be used when the amplitude of the oscillations of the medium is sufficiently large, so that Re_{a2} is close to unity or greater [119].

Choosing L_s as the length of the tube and U_s as the maximum streaming velocity (which is proportional to u_{max}^2/c_0), the streaming Reynolds number (Re_{s1}) is defined as

$$Re_{s1} = \frac{u_{max}^2}{\nu\omega}. \tag{3.22}$$

Choosing L_s as the width of the tube (H) and U_s as the maximum streaming velocity, the second definition of the streaming Reynolds number (Re_{s2}) would be [120],

$$Re_{s2} = \frac{3}{8}\frac{u_{max}^2 H}{c_0\nu}. \tag{3.23}$$

The third definition of the streaming Reynolds number which includes the ratio of channel width to the thickness of the viscous boundary layer is,

$$Re_{s3} = \frac{1}{2}\left(\frac{u_{max}}{c}\right)^2\left(\frac{H}{\delta_\nu}\right)^2, \tag{3.24}$$

[108]. According to Thompson *et al.* $Re_{s3} \ll 1$ corresponds to the relatively *slow streaming*, whereas $Re_{s3} \gg 1$ is referred to as *nonlinear streaming* [108].

3.4 Highly nonlinear standing wave

Strongly nonlinear acoustics is devoted to waves of amplitude high enough that the finite-amplitude assumption, $|\rho'| \ll \rho_0, |p'| \ll P_0$, does not hold. When nonlinear terms in the conservation equations are retained, great mathematical difficulty is encountered and the analytical solution even in special cases is very difficult or nearly impossible. Therefore, numerical approaches are frequently used.

3.4.1 Mathematical equations

In order to derive the wave equation for the high-amplitude nonlinear acoustic waves in a viscous, heat-conducting fluid, using Eqs. (3.10,3.9), we can express ρ and p' in terms of c as,

$$\rho = \rho_0\left(\frac{c}{c_0}\right)^{2/(\gamma-1)}, \tag{3.25}$$

$$p' = P_0\left(\frac{c}{c_0}\right)^{2\gamma/(\gamma-1)}. \tag{3.26}$$

[119]. Now the continuity and Navier-Stokes equations (Eqs. 3.1 and 3.4) can be written as,

$$\frac{\partial c}{\partial t} + \mathbf{v}\nabla c + \frac{\gamma-1}{2}c\nabla\mathbf{v} = 0, \tag{3.27}$$

$$\frac{\partial \mathbf{v}}{\partial t} + \mathbf{v}\nabla\mathbf{v} + \frac{2}{\gamma-1}c\nabla c = \nu b\left(\frac{c}{c_0}\right)^{-2/(\gamma-1)}\nabla(\nabla\mathbf{v}), \tag{3.28}$$

where b indicates the total effect of viscosity and thermal conductivity of the fluid as well as the wall absorbtion, and can be obtained as,

$$b = \frac{2c_0^3\alpha}{\omega^2\nu}, \tag{3.29}$$

where α is the total absorbtion coefficient which is the sum of thermoviscosity absorbtion coefficient and wall absorbtion coefficient [121]. We write,

$$\alpha = \alpha_{tv} + \alpha_{wall}, \tag{3.30}$$

where,

$$\alpha_{tv} = \frac{\omega^2\nu}{2c_0^3}\left(\frac{4}{3} + \frac{\mu_B}{\mu} + \frac{\gamma-1}{P_r}\right), \quad \alpha_{wall} = \sqrt{\frac{\omega\nu}{8c_0^2}}\left(1 + \frac{\gamma-1}{\sqrt{P_r}}\right)\frac{\wp}{\Gamma}, \tag{3.31}$$

where $P_r = \frac{\mu c_p}{\kappa}$ is the Prandtl number [122].

Eqs. (3.27,3.28) are the exact highly nonlinear wave equations in a thermoviscous fluid. In one-dimension they can be written as,

$$c_t + uc_x + \frac{\gamma-1}{2}cu_x = 0, \tag{3.32}$$

$$u_t + uu_x + \frac{2}{\gamma-1}cc_x = \nu b(c/c_0)^{-2/(\gamma-1)}u_{xx}. \tag{3.33}$$

Eqs.(3.32, 3.33) can be combined in the conservative form as,

$$U_t + AU_x = BU_{xx}, \tag{3.34}$$

where,

$$U = \begin{bmatrix} c \\ u \end{bmatrix}, A = \begin{bmatrix} u & \frac{\gamma-1}{2}c \\ \frac{2}{\gamma-1}c & u \end{bmatrix}, B = \begin{bmatrix} 0 & 0 \\ 0 & \nu b(c/c_0)^{-2/(\gamma-1)} \end{bmatrix}.$$

This unsteady nonlinear equation must be solved using an appropriate numerical scheme. The acoustic pressure p', can be evaluated from c using Eq. (3.26). The following initial and boundary conditions for the variables u and c are applicable,

$$\begin{aligned} u(0,t) &= u_0 \sin(wt) \ , \ u(L,t) = 0, \\ c_x(0,t) &= 0 \ , \ c_x(L,t) = 0 \\ u(x,0) &= 0 \ , \ c(x,0) = c_0. \end{aligned} \tag{3.35}$$

3.4.2 Numerical model of highly nonlinear standing waves

The mathematical formulation outlined in section 3.4.1 is solved numerically using the fourth-order compact finite difference method (CD4) in space and the fourth-order Runge-Kutta time stepping scheme. Explicit finite difference schemes express the nodal derivatives as an explicit weighted sum of the nodal values of the function. Whereas, implicit or compact schemes (also called Padé schemes) equate a weighted sum of the nodal derivatives to a weighted sum of the nodal values of the function. Using CD4 scheme, the spatial derivatives can be expressed as,

$$u'_{i+1} + 4u'_i + u'_{i-1} = 3(u_{i+1} - u_{i-1})/h, \tag{3.36}$$

and

$$u''_{i+1} + 10u''_i + u''_{i-1} = 12(u_{i+1} - 2u_i + u_{i-1})/h^2, \tag{3.37}$$

or as,

$$(u_x)_i = \left(1 + \frac{h^2}{6}\delta_x^2\right)^{-1} \delta_x^0 u_i + O(h^4), \tag{3.38}$$

and

$$(u_{xx})_i = \left(1 + \frac{h^2}{12}\delta_x^2\right)^{-1} \delta_x^2 u_i + O(h^4), \tag{3.39}$$

where $\delta_x^0 u_i$ and $\delta_x^2 u_i$ have been defined in Eqs. (2.5, 2.6) and $h = \Delta x$. With the same stencil width, compact schemes are more accurate than explicit ones [123].

For the time evolution equation,

$$\frac{\partial U}{\partial t} = F(U), \tag{3.40}$$

where,

$$F(U) = -A U_x + B U_{xx}. \tag{3.41}$$

An explicit, p-stage Runge-Kutta scheme advances the solution from time level $t = t_n$ to $t_n + \tau$ as,

$$U^{n+1} = U^n + \sum_{i=1}^{p} \zeta_i R_i, \tag{3.42}$$

where

$$R_1 = \tau F(U^n) \ , \ R_i = \tau F(U^n + \sigma_{i-1} R_{i-1}). \tag{3.43}$$

For four-stage Runge-Kutta scheme, $\zeta = [\frac{1}{6}, \frac{1}{3}, \frac{1}{3}, \frac{1}{6}]$ and $\sigma = [\frac{1}{2}, \frac{1}{2}, 1]$.

3.4.3 Discretization of the nonlinear wave equation

Using Eqs. (3.38, 3.39, (3.41), we can write,

$$\left(1 + \frac{h^2}{6}\delta_x^2\right)\left(1 + \frac{h^2}{12}\delta_x^2\right) F_i = -A_i\left(1 + \frac{h^2}{12}\delta_x^2\right)\delta_x^0 U_i + B_i\left(1 + \frac{h^2}{6}\delta_x^2\right)\delta_x^2 U_i, \tag{3.44}$$

The stencil on the left-hand side of Eq. (3.44) is five node and requires the system of equations with penta-diagonal coefficient matrix to be solved. The reason for the increased stencil is that the denominators of the Padé approximation for U_x and U_{xx} (Eqs. 3.38 and 3.39) are not equal. In order to obtain small-stencil with the same fourth-order accuracy, following Lele [123], we can write,

$$(u_{xx})_i = \left(1 + \frac{h^2}{6}\delta_x^2\right)^{-1}\left(\frac{1}{3}\hat{\delta}_x^2 + \frac{2}{3}\delta_x^2\right) u_i + O(h^4), \tag{3.45}$$

where

$$\hat{\delta}_x^2 u_i = \frac{u_{i+2} - 2u_i + u_{i-2}}{h^2}. \tag{3.46}$$

Using Eq. (3.45), Eq. (3.41) can be discretized as,

$$\left(1 + \frac{h^2}{6}\delta_x^2\right) F_i = -A_i \delta_x^0 U_i + \frac{1}{3} B_i \left(\hat{\delta}_x^2 + 2\delta_x^2\right) U_i, . \tag{3.47}$$

This is a tri-diagonal system which can be solved efficiently using the fourth-order Runge-Kutta time stepping scheme. Since tri-diagonal matrices can be inverted quite efficiently, this method is very attractive and efficient. This invertibility also proves the solvability of Eq. (3.47).

3.4.4 Stability analysis

The choice of the time step τ is an important issue in solving unsteady equations. One criterion for the time step is that the time integration must be stable. Following Jameson and Baker [124], the amplification factor of the four-step Runge-Kutta method is given as,

$$\xi = 1 + Z + Z^2/2 + Z^3/6 + Z^4/24, \tag{3.48}$$

where Z is the Fourier symbol of the discretized $F(U)$ (Eq. 3.41). Applying von Neumann stability analysis method [118] to Eq. (3.47) we can obtain,

$$Z = \frac{r(4\cos(\beta) + 2\cos(2\beta) - 6) - 3\sqrt{-1}s\sin(\beta)}{\cos(\beta) + 2}, \tag{3.49}$$

where $s = \Lambda_A \tau/h$ and $r = \Lambda_B \tau/h^2$, Λ_A and Λ_B are the eigenvalues of matrices A and B which can be obtained as, $\Lambda_A = v \pm c$ and $\Lambda_B = \nu b(c/c_0)^{-2/(\gamma-1)}$, $\beta = 2\pi m h/L$, $m = 0, 1, ..., N$ and N is the number of nodes in the x direction. Applying von Neumann stability method to large-stencil scheme (Eq. 3.44), we get

$$Z = \frac{12r(\cos(2\beta) + 2\cos(\beta) - 3) - 15\sqrt{-1}s(\sin(2\beta) + 2\sin(\beta))}{\cos(2\beta) + 14\cos(\beta) + 21}, \tag{3.50}$$

The magnitude of the amplification factor is related to the artificial dissipation. When $|\xi| \geq 1$, the method is unstable. For unsteady cases, $|\xi|$ is desired to be as close as possible to unity to ensure stability with minimum artificial dissipation.

The stability footprints (imaginary part of ξ versus its real part) of the small-stencil scheme (Eq. 3.47) for different values of s and r are depicted in Fig. 3–1. The stability region of the given scheme is: $s \leq 1.2$ and $r \leq 0.274$. Fig. 3–1(a) shows that, to get $|\xi|$ as close as possible to unity, we need smaller values for s and r, which implies that the node numbers must be increased in both x and t directions. As seen in Figs. 3–1(a-c), for $s > 1.2$, regardless the value of r, the scheme is unstable. Fig. 3–1(d) shows that for $r > 0.274$, regardless the value of s, the scheme is unstable. The stability footprint for the marginal values of s and r (s=1.2 and r=0.274) is included in Fig. 3–1(c). The stability region of the large-stencil scheme (Eq. 3.44) is: $s \leq 1.345$ and $r \leq 0.46$.

3.4.5 Results and discussion

Numerical calculations are performed using the small-stencil scheme (Eq. 3.47) for two thermoviscous gases, air and CO_2 at 0°C. For both cases, the cross-sectional area of the resonator is set equal to 16 cm^2 and the excitation frequency is 1024 Hz. The length of the resonator is set equal to half of the wavelength of the acoustic standing wave, which for the given frequency and temperature is 16.2 cm for air and 12.6 cm for CO_2. The values of physical parameters of these gases for the given conditions are presented in table 3–1. Also presented in table 3–1 are the values of the absorbtion coefficient and corresponding values of b, computed from Eqs. (3.29,3.30). The values of μ_B/μ have been obtained from Pan *et al.* [125].

For the numerical simulation, the spatial and temporal step sizes are set as h=0.81 mm and τ=0.244 μsec, respectively. The corresponding values of s and r are 0.121 and 0.098, respectively, which satisfy the stability condition with low artificial

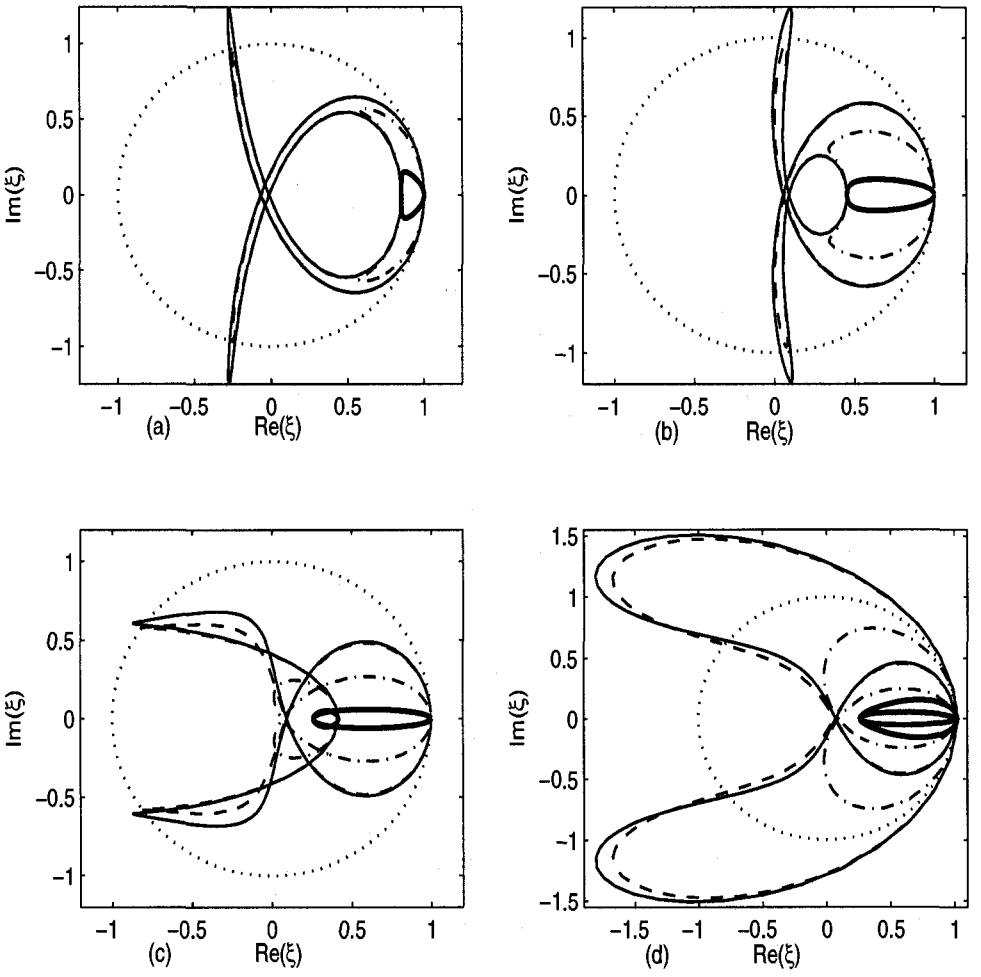

Figure 3–1: The stability footprints of the given scheme for s=0.1 (thick-solid); 0.5 (dash-dotted), 1.2 (dashed) and 1.25 (thin solid) and different values of r (a) $r = 0.02$, (b) $r = 0.1$, (c) $r = 0.274$ and (d) $r = 0.35$; dotted line is $|\xi| = 1$ circle.

dissipation. One advantage of the given numerical scheme is that no additional attenuation is required to get numerical stability.

Fig. 3–2 represents the variation of the pressure and particle velocity over one standing wave period for air subjected to the boundary conditions given in Eq. 5.8. The maximum velocity of the diaphragm is u_0=10 m/s that corresponds to the acoustical Reynolds number (Eq. 3.21) of Re_{a2}=14.23. Fig. 3–2(a) shows that in the highly

Table 3–1: Values of parameters for air and CO_2 at 0°C.

	Air	CO_2
$\mu\ (kg/ms)$	0.0000181	0.0000145
μ_B/μ	0.6	1000
$\rho_0\ (kg/m^3)$	1.293	1.98
$c_0\ (m/s)$	331.6	258
γ	1.402	1.289
$\kappa\ (J/Kms)$	0.026	0.017
$c_p\ (J/kgK)$	1005	846
$\alpha\ (m^{-1})$	0.1196	0.0916
b	15050	10373

nonlinear standing wave case, the pressure waveform distorts from the pure sinusoidal waveform which is observed in the linear case. Fig. 3–2(b) shows that nonlinearity significantly influences the particle velocity profile. The particle velocity waveform is also deviated from the sinusoidal behavior. For the linear case, the velocity profile is symmetric about the pressure node (i.e. at $L/2$). However, for the highly nonlinear case, the plot shows a steep wavefront traveling along the resonator.

To get a better insight into the pressure and velocity dynamics of highly nonlinear waves, the pressure waveform at $x = L$ (i.e. pressure antinode) and particle velocity waveform at $x = L/2$ (i.e. velocity antinode) are plotted in Figs. 3–3(a) and (b), respectively, for air and CO_2. The maximum velocity of the diaphragm for both cases is $u_0 = 10$ (m/s) that corresponds to the Re_{a2} of 14.23 and 27.45 for air and CO_2, respectively. The plots show that the shape of pressure and velocity waveforms for both gases are similar. However, for air, the pressure amplitude is lower and the particle velocity amplitude is higher than that for CO_2. This is due to the reason that the absorbtion coefficient of CO_2 for the given frequency and other conditions is less than that of air, resulting in higher pressure amplitude.

Fig. 3–3(a) also shows another important difference between the temporal pressure waveforms for air and CO_2. The asymmetry of the pressure wave for CO_2 is higher than that for air. This phenomenon can be explained using the acoustic

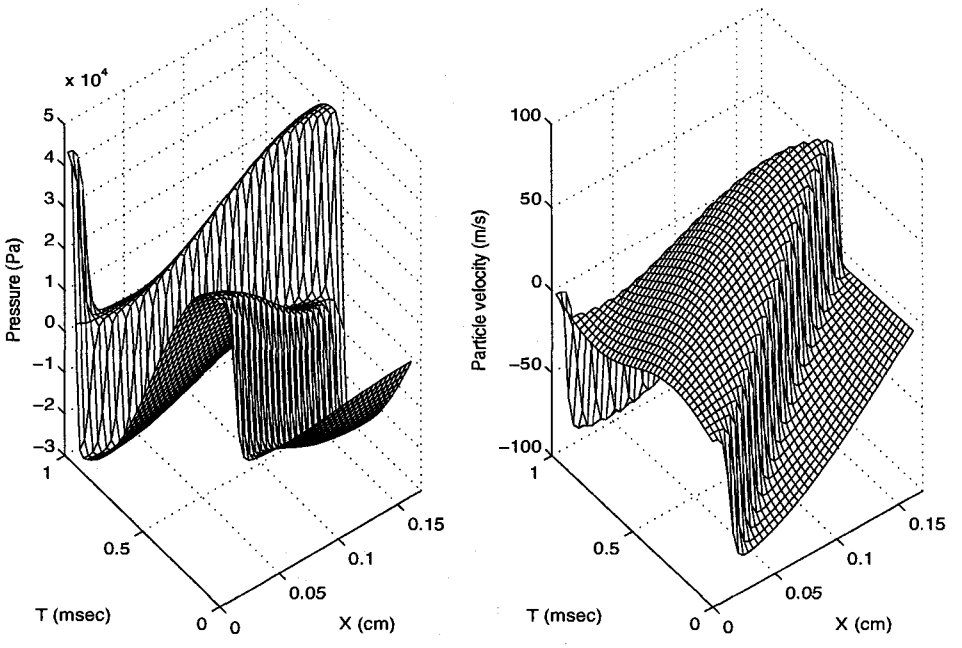

Figure 3–2: (a) Pressure and (b) particle velocity over a standing wave period for air. Maximum velocity of the diaphragm is $u_0 = 10$ (m/s).

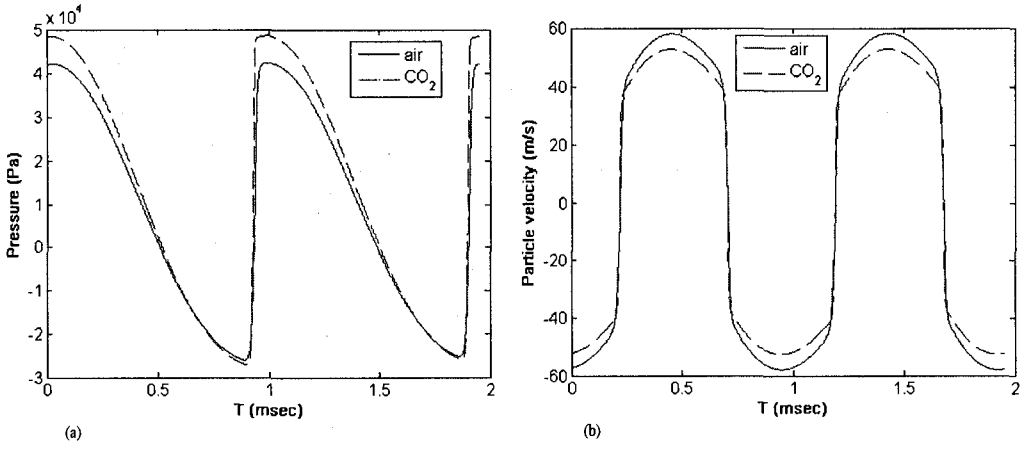

Figure 3–3: (a) Pressure waveform at $x = L$ and (b) particle velocity waveform at $x = L/2$ from the center of the diaphragm over two standing wave periods for air (solid line) and CO_2 (dashed line). Maximum velocity of the diaphragm is $u_0 = 10$ (m/s).

Reynolds number. Due to lower values of b and ν for CO_2 than those for air, the acoustic Reynolds number is higher for CO_2 than that for air. The higher value of the acoustic Reynolds number for CO_2 means that the degree of nonlinearity is higher for CO_2 than that for air. As the degree of nonlinearity increases, more energy will transfer to distortion components of the wave [6, 63]. Table. 3–2 shows the relative harmonic amplitudes ($p_n/p_1; n = 0, 2, 3, 4$) of the pressure waveforms for air and CO_2, where p_1 is the amplitude of the fundamental frequency. The relative amplitude of the dc component (P_0) is higher for CO_2 than that for air. The higher dc pressure gives the upward shift in the pressure waveform and is responsible for the higher asymmetry in the pressure wave for CO_2 compare to that for air.

In order to study the influence of nonlinearity on the pressure and particle velocity, the pressure variations at $x = L$ (pressure anti-node) and particle velocity variations at $x = L/2$ (velocity anti-node) are depicted in Fig. 3–4 for air over two standing wave periods for $u_0 = 0.1, 0.5, 1$ and 5 (m/s). The corresponding values of the acoustical Reynolds numbers for the given cases are $1.04, 3.05, 4.4, 6.3$ and 10.04. These cases cover a range from linear to highly nonlinear standing waves. Fig. 3–4(a) shows that the shape of pressure waveform changes from sinusoidal in the linear case to saw-tooth in the highly nonlinear case. The plot also shows that as the nonlinearity effect increases, the pressure waveform becomes asymmetric about the static pressure and the pressure peaks shift towards the pressure antinodes. The shift in the pressure

Table 3–2: Relative harmonic amplitudes of the pressure waveforms (p_n/p_1) for air and CO_2.

Harmonic	Air	CO_2
dc	0.55	0.67
2	0.38	0.4
3	0.26	0.28
4	0.22	0.23

peaks is due to increase in the amplitudes of second and higher harmonics with nonlinearity. Fig. 3–4(b) shows that as the nonlinearity increases, high velocity gradients are observed around $T/4$ and $3T/4$ and the waveform changes to near-rectangular form. Similar waveforms for pressure and particle velocity are reported by Bednařík and Červenka [77]. However, for their simulations, the acoustical Reynolds number is around 4, which is in the moderate nonlinearity range.

Fig. 3–2 shows that nonlinearity influences the spatial waveforms of pressure and particle velocity. To analyze this impact, the pressure and particle velocity waveforms along the resonator are plotted for the highly nonlinear ($u_0 = 10$ m/s) case in Figs. 3–5(a) and (b), respectively. The waveforms in the figure are plotted with a time step of $T/8$, and cover a total of half wave period. The axial distribution of pressure shows that in the highly nonlinear case, the pressure node is not fixed in time and space. That is, during a wave period, the pressure node oscillates about the theoretical pressure node. Whereas, in the linear case a pressure node is present in the middle of the resonator that is fixed in time and space. In case of particle velocity, the nodes are fixed at both ends of the resonator, and the plots show that for the highly nonlinear case, the velocity peaks move across the resonator with time, whereas they are almost fixed at the middle of the resonator in the linear case. The plot in Fig. 3–5(b) also indicates the presence of an additional node inside the resonator whose position changes with time. The plot also shows a wavefront with high velocity gradient, which also corresponds to the high pressure gradient. The ratio between the positive and negative peaks of the wavefront changes with propagation. Such wavefront is not observed in the linear case. Thus, it can be concluded that for highly nonlinear standing waves, a wavefront with very high velocity and pressure gradients travels along the resonator.

Fig. 3–5 also shows the effect of the filled gas on the axial pressure and particle velocity waveforms. The slopes of the traveling velocity and pressure gradients are

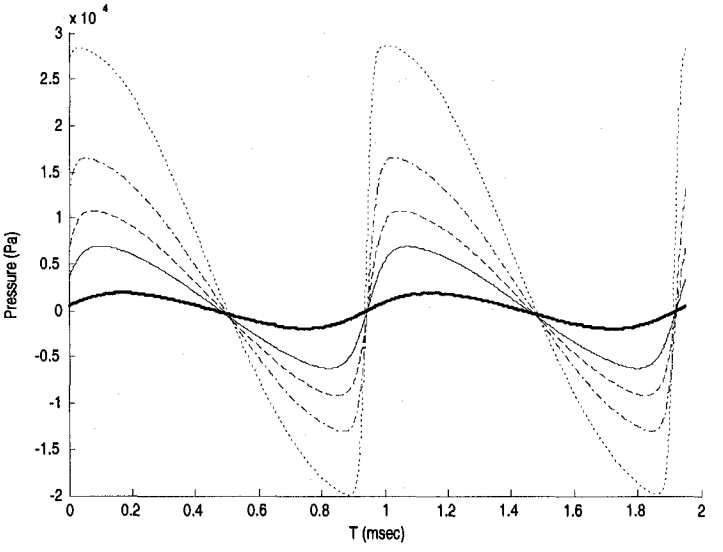

(a)

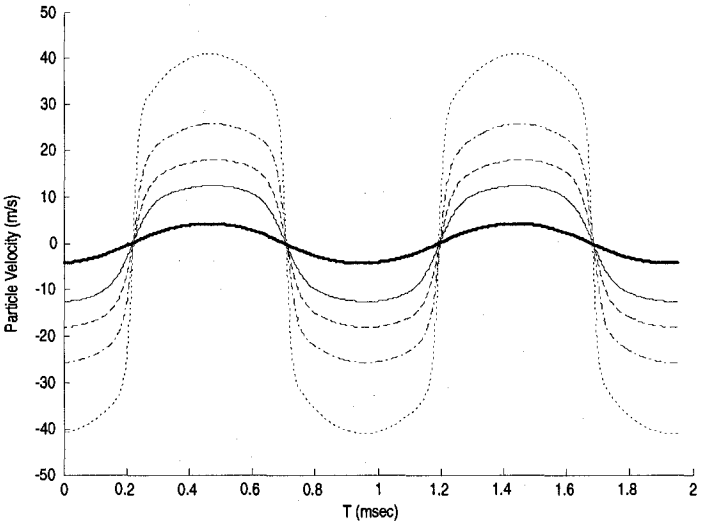

(b)

Figure 3–4: (a) Pressure waveforms at $x = L$ and (b) particle velocity waveforms at $x = L/2$ from the center of the diaphragm for $u_0 = 0.1$ m/s (thick solid); $u_0 = 0.5$ m/s (thin solid); $u_0 = 1.0$ m/s (dashed); $u_0 = 2.0$ m/s (dash-dotted) and $u_0 = 5.0$ m/s (dotted).

higher for CO_2 than those for air. It means that the shock waves generated in the resonator are more intense for CO_2 compare to air which is due to the higher level of nonlinearity for CO_2.

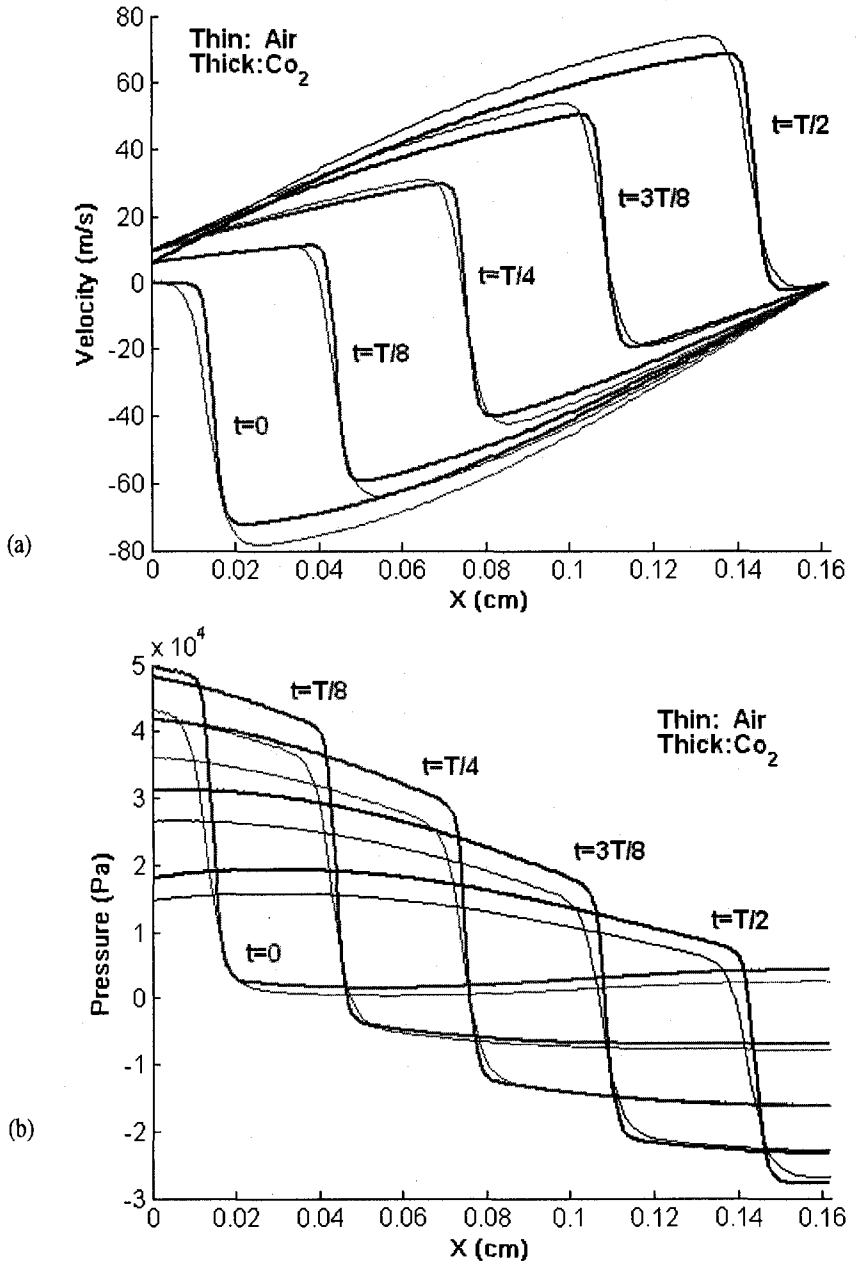

Figure 3–5: Axial distributions of the (a) pressure and (b) particle velocity for air (thin) and CO_2 (thick) for $u_0 = 10$ (m/s) at different times; $t = 0$, $t = T/8$, $t = T/4$, $t = 3T/8$, and $t = T/2$ (solid).

3.5 Conclusions

A set of two nonlinear equations for highly nonlinear standing waves in a thermoviscous fluid is derived from the basic equations of fluid mechanics along with the appropriate state equation. The set of equations is solved numerically using a combination of a fourth-order compact finite difference scheme and a fourth-order Runge-Kutta time stepping scheme. The result is an accurate and fast-solver numerical model which can predict the pressure, particle velocity and density along the highly nonlinear standing wave resonator filled with a thermoviscous fluid with no restriction on nonlinearity level and type of fluid. The results show that the pressure and particle velocity waveforms of highly nonlinear waves are significantly different from that of the linear waves, in both time and space. As the waves become highly nonlinear, the pressure waveform changes from sinusoidal to saw-tooth form and the particle velocity waveform changes from sinusoidal to near-rectangular form. For highly nonlinear waves, the results also indicate the presence of a wavefront that travels along the resonator with very high pressure and velocity gradients. The slopes of the traveling velocity and pressure gradients are higher for CO_2 than those for air. Another important observation is that the asymmetry in pressure waveform for CO_2 is higher than that for air.

CHAPTER 4
Experimental Study of the Nonlinear Pressure Field in a Closed Tube

4.1 Introduction

One of the objectives of the present research is to improve our understanding of the acoustic standing wave characteristics in a closed tube by performing different experimental investigations of linear and nonlinear pressure and particle velocity fields. A notable study in the finite-amplitude field has been reported by Vanhille and Campos-Pozuelo [82]. They conducted experiments in a rigid axisymmetric cylindrical resonator whose transverse dimension was bigger than the longitudinal dimension. They measured the pressure at the tube end and compared the frequency spectrum of the pressure obtained from experimental and numerical data. However, neither this study nor the other works discussed in the literature review (section 1.2.2) presented the time variation of the experimental pressure waveform. Furthermore, they did not provide any comparison between the instantaneous numerical and experimental data in the time domain. The spectral analysis provides information about the pressure amplitudes at the fundamental and higher harmonics, however, it does not provide any information about the shape of the pressure waveform in time. Similarly, the distribution of fundamental and second-harmonic pressure amplitudes along the tube axis may not be sufficient to describe the spatial nonlinear behavior inside the tube. Furthermore, for a nonlinear wave model that describes the spatial and temporal variations of pressure and velocity, a good agreement between numerical and experimental data sets in the frequency domain may not be a good indicator of the accuracy of the model.

As the literature review (sections 1.2.1 and 1.2.2) indicates, none of the previous

experiments related to the acoustic pressure measurement presented the time variation of the pressure amplitude and similarly, did not provide any comparison between the instantaneous numerical and experimental data in the time domain. The spectral analysis provides information about the pressure amplitudes at the fundamental and higher harmonics, however, it does not provide any information about the shape of the pressure oscillations in time. Similarly, the distribution of fundamental and second-harmonic pressure amplitudes along the tube axis may not be sufficient to describe the spatial nonlinear behavior inside the tube. Furthermore, for a nonlinear wave model that describes the spatial and temporal variations of pressure and velocity, a good agreement between numerical and experimental datasets in the frequency domain may not be a good indicator of the accuracy of the model.

In this chapter, different components of the experimental setup for the pressure measurement are described first. In section 4.3, we investigate the behavior of nonlinear pressure signal in an air-filled rigid-wall square tube experimentally. The pressure is measured temporally and spatially along the channel axis to obtain a better insight into the temporal and spatial dynamics of nonlinear standing waves. As mentioned earlier, for a nonlinear wave model, the validation in both time and space is vital. The experimentally obtained pressure measurements are compared with the numerical ones obtained in section 3.2.2 in both space and time.

4.2 Experimental setup and instrumentation

Before describing different parts of the experimental setup, it must be noted that all experiments are conducted in air at 20°C. The static pressure inside the tube is atmospheric. The thermo-physical properties of air at this condition are, $c_0 = 344$ m/s, $\rho_0 = 1.2$ kg/m^3, $\mu = 1.81 \times 10^{-5}$ N.s/m^2, $\mu_B = 0.6 \times \mu$ and $\gamma = 1.401$.

4.2.1 Acoustic chamber and driver

As mentioned in section 1.1, to establish the standing wave, a chamber and an acoustic driver are required. As shown in Fig. 4–1, the acoustic chamber is a Plexiglas channel with a square cross-sectional area. The inner cross-section of the channel is 7 cm×7 cm. The walls of the channel are 6 mm thick, and therefore, the assumption of rigid walls held for this channel. A special loudspeaker driver is used to excite the acoustic standing wave inside the tube. The driver has a maximum power of 200 watts and DC resistance of 8 Ω. The use of loudspeaker driver for the source makes it easy to vary the frequency and intensity of excitation continuously and precisely. A Function generator (model Agilent 33120A) is used to generate the sinusoidal wave. The accuracy of the generated frequency and amplitude are 1 μHz and 0.1 mV, respectively. The signal from the function generator is amplified by a 220-W amplifier (Pioneer SA-1270). The loudspeaker is driven by this amplified signal.

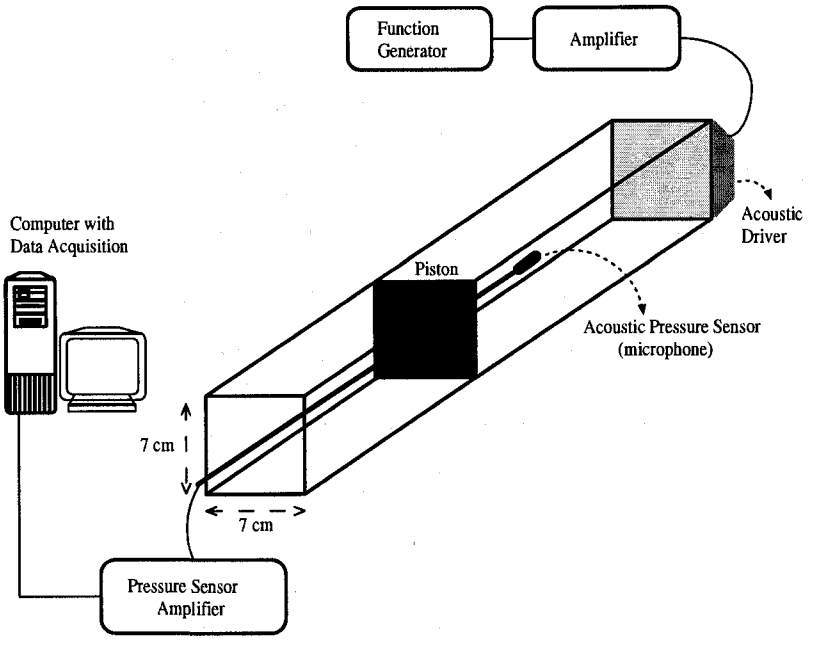

Figure 4–1: The schematic of the experimental setup developed to measure pressure inside the standing wave tube.

4.2.2 Pressure measurement and data acquisition

A quarter-inch condenser microphone cartridge Model 377A10 PCB Piezotronics is used to measure the sound intensity level and the dynamic pressure amplitude inside the resonator when the loudspeaker is excited. The microphone consists of a microphone cartridge and a microphone preamplifier. A preamplifier Model 426B03 is used in order to measure the sound intensity. The cartridge screws directly onto the preamplifier housing. The frequency response is almost flat between 5 Hz and 100 kHz. For the pressure measurement along the channel, the microphone is attached to a rigid plastic rod and slid into the channel through a hole in the piston wall. The measurements are made at five different locations along the channel center axis, at different excitation voltages. During velocity measurements, the microphone is placed inside the hole in the adjustable piston and flushed with the piston inner surface. Thus, the microphone and piston are always at the same position i.e. at the pressure antinode, and the microphone measures the maximum pressure. In all experiments, the pressure signal from the microphone is acquired via a 16-channel data acquisition card (PCI-6036E, National Instruments) using the LabView data acquisition software. For each experimental run, the data are sampled at a sampling rate of 32 kHz for a duration of 20 sec.

4.2.3 Laser vibrometer

A Brüel & Kjær laser vibrometer is used to measure maximum diaphragm displacement for different loudspeaker driver intensities. The laser vibrometer consists of three components: A Helium-Neon laser velocity transducer type 8323, a power supply type 2815 and a signal analyzer unit type 2035. Unlike traditional contact vibration transducers, the laser vibrometer requires no physical contact with the test object. The measurement principle of a laser vibrometer is based on the Doppler

effect. When monochromatic laser light is scattered back from a vibrating target, it undergoes a frequency shift proportional to the velocity of the target. If the target is vibrating, the frequency of the back-scattered beam will be modulated at the so-called Doppler frequency. The Doppler frequency is directly proportional to the velocity of the target. In order to confirm that the assumption of rigid walls holds for the channel used in this study, the wall vibration has also been measured using the laser vibrometer. The maximum wall displacement is found to be approximately 0.5% of the maximum displacement.

4.3 Finite-amplitude nonlinear standing waves

The experimental setup developed to measure pressure inside the standing wave tube is shown in Fig. 4–1. For the given experiments, the position of the piston is so adjusted to create a full wavelength acoustic standing wave inside the channel.

The numerical model presented in section 3.2.2 requires maximum diaphragm displacement for the boundary condition (see Eq. 5.8). Fig. 4–2 shows the maximum vibration displacement at the center of the driver's diaphragm as a function of the excitation voltage of driver for different excitation frequencies. The plot shows that for a given excitation frequency, the diaphragm displacement and excitation voltage are linearly related. The plot also shows that the sensitivity of the diaphragm displacement to the excitation voltage increases with an increase in the excitation frequency. Vanhille and Campos-Pozuelo [82] also observed linear relationship between the vibration velocity of the transducer at the fundamental mode and the excitation voltage. Using Fig. 4–2, for a given excitation frequency we can estimate the amplitude of diaphragm displacement at all excitation voltages over the range of our practical interest.

An accurate empirical evaluation of the attenuation coefficient α is essential to

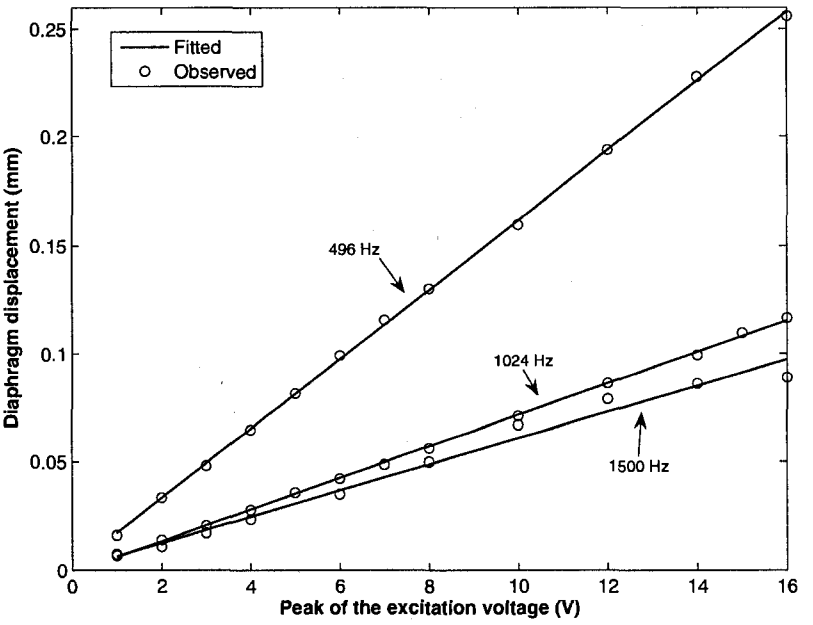

Figure 4–2: Maximum displacement at the center of the driver diaphragm versus excitation voltage for different excitation frequencies. Solid line, fitted; o, experimental

get a good correlation between the experimental and the numerical data (The comparison between the experimental and the numerical results will be discussed later in this chapter). The attenuation coefficient can be calculated from the pressure measurements when the length of the tube is varied near the resonance length [126].

In the present case, experiments and simulations are conducted for $f = 1024$ Hz. The length of the channel is set equal to 33.6 cm that corresponds to one full wavelength of the standing wave, that is, $L = \lambda$. To estimate the attenuation coefficient α, the length of the channel is changed from 33.6 to 33.9 cm with an increment of 0.1 cm. The pressure is measured at each length and the data are then used to estimate the resonance pressure amplitudes. The attenuation coefficient (α) is then estimated using the method described by Campos-Pozuelo *et al.*[127] as

$$\alpha = \frac{n\pi}{2Q_s L}, \tag{4.1}$$

Table 4–1: Experimental spatial resonance values of the pressure

L(cm)	*Output of the pressure transducer (V)*
33.6	7.2
33.7	6.0
33.8	5.0
33.9	4.0

where $n = 1, 2, 3, ...$ and Q_s is the spatial quality factor defined as $Q_s = L/2\Delta L$, where L is the tube length at resonance (maximum pressure) and $2\Delta L$ is the spatial bandwidth, that is the difference between the two values of the tube length at which the pressure is equal to 70.7% of the resonance pressure. After evaluation of the attenuation coefficient, the viscosity number b in Eq. (3.12) can be calculated for the same frequency using the following equation,

$$\alpha = \frac{\nu b \omega^2}{2c_0^3}. \tag{4.2}$$

[121]. Table 4–1 shows the resonant pressure amplitudes for different tube lengths for the excitation frequency is $f = 1024$ Hz and resonant length of $L = 33.6$ cm. From this data, we obtained $Q_s = 84$ and using Eqs. (4.1,4.2) the attenuation coefficient is found to be $\alpha = 0.1087$ m^{-1} and the viscosity number $b = 14059$. This value of the viscosity number and the value of the excitation displacement (χ_0), evaluated from Fig. 4–2, are used in the given numerical model to obtain the particle displacement and pressure.

4.3.1 Results and discussion

The results from experiments and numerical simulations for $f = 1024$ Hz and $b = 14059$ ($\alpha = 0.1087$), for various diaphragm amplitudes ranged from 28 to 175 μm, are presented and discussed in this section. The range of diaphragm amplitudes is set in a way that it covers linear to nonlinear waves. For the numerical simulation

described in section 3.2.2, the spatial and temporal step sizes are set as $h = 0.00247$ m and $\tau = 5.08 \times 10^{-6}$ sec, respectively, which satisfies the stability condition in Eq. (3.18). The simulation results showed that starting from rest, the standing wave is fully established after approximately 30 wave periods. Thus, the total time for each simulation is set equal to 100 periods.

Fig. 4–3 shows the time variation of pressure waveform inside the tube for different diaphragm vibration amplitudes at $x = 17$ and 13 cm from the diaphragm end along the channel axis. The plots show that as the diaphragm vibration amplitude increases, the pressure waveform distorts from the pure sinusoidal waveform. The numerically simulated pressure waveform for the same conditions and location are also plotted in Fig. 4–3 for comparison. The results show that the experimentally obtained pressures are slightly lower than that from the numerical model. Taking into account the experimental uncertainties, the agreement between the numerical and experimental data in time domain for the lower diaphragm vibration amplitudes is excellent and the difference between the numerical and experimental results for the higher diaphragm vibration amplitudes is on average less than 5%. This small difference between the two results can be due to inaccuracy in the empirical evaluation of the attenuation coefficient and the position of the pressure sensor during the experiments, which has the uncertainty of ± 1 mm. Another important factor that leads to the discrepancy between the experimental and numerical results is the assumption in the mathematical model that pressure and density perturbations are small compared to the static values. As the diaphragm vibration amplitude gets larger, the validity of this assumption decreases.

An important parameter in practical applications is the RMS pressure level. Fig. 4–4 shows the numerically simulated and experimentally measured RMS pressure inside the tube at different points along the channel axis for different diaphragm vibration amplitudes. The plot shows that the pressure amplitude is maximum at the

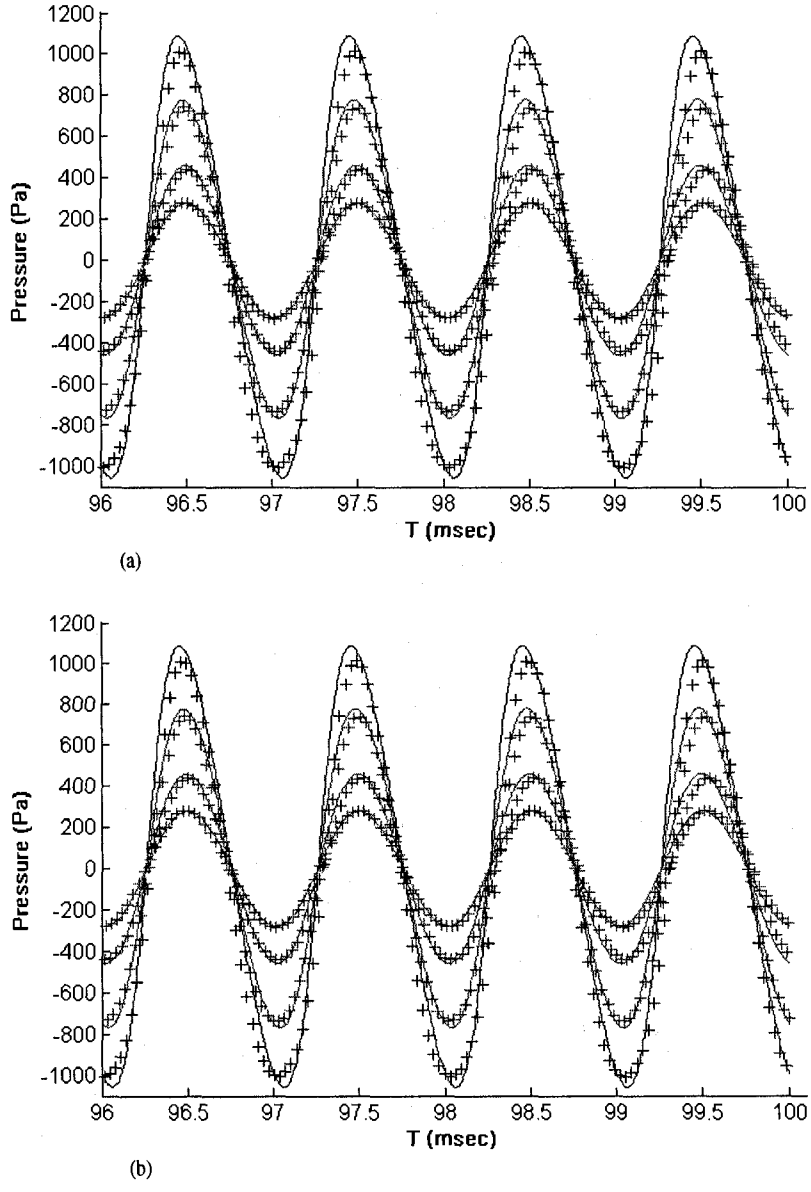

Figure 4–3: The time series of the experimental and numerical results for the pressure amplitudes for $\chi_0 = 28, 45, 90$ and 175 μm at (a) $x = 17$ cm and (b) $x = 13$ cm, where x is measured from the diaphragm end along the channel axis. Solid line, numerical; +, experimental. The acoustical Reynolds numbers for the given cases are 1.14, 1.96, 3.97 and 7.64. The pressure amplitude increased monotonically with χ_0.

pressure anti-nodes (x=0 and 16.8 cm), and minimum at the pressure node (x=8.4 cm). For linear acoustic standing wave, the RMS pressure at the pressure node should be zero, but the plot shows that because of nonlinearity, the RMS pressure is not zero

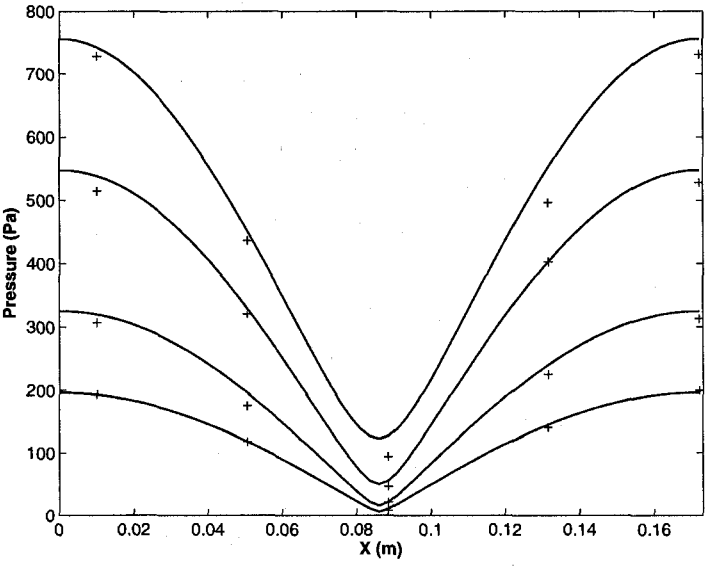

Figure 4–4: RMS pressure for $\chi_0 = 28, 45, 90$ and 175 μm at different distances along the channel axis. The RMS pressure increased monotonically with χ_0. Solid line, numerical; +, experimental.

at this location and as the nonlinearity increases, its magnitude increases. The plot also shows good agreement between the experimental and numerical RMS values at different axial locations along the channel at different nonlinearity level. On average, the difference between the experimental and numerical values is 5%.

The frequency spectra for the numerical and experimental pressure at different axial distances for $\chi_0 = 175$ μm ($Re_{a2} = 7.64$) and resonance frequency of $f = 1024$ Hz are shown in Fig. 4–5. It can be seen that there is a good agreement between the numerical and experimental data in frequency domain as well. The plot shows that the fundamental mode is dominant at all spatial locations except at x = 8.5 cm (the location of the theoretical pressure node), where the second harmonic is dominant. The reason for this trend will be discussed later. The plot also shows that except at x = 8.5 cm, the magnitude of second harmonic from experimental results is higher than the numerical results. Vanhille and Campos-Pozuelo [82] studied the pressure amplitude at different harmonics at the center of the reflector. They also

observed that the experimentally obtained pressure amplitude at second harmonic is higher than the numerical one. The results in Figs. 4–3, 4–4 and 4–5 show the pressure variations over a range of diaphragm vibration amplitudes that covers weakly nonlinear to moderately nonlinear waves. Good agreement between numerical and experimental data in both time and frequency domains confirms that the present numerical model accurately predicts the particle displacement and pressure of nonlinear standing waves inside a tube.

The verified model is then used to study the nonlinearity effects in both space and time domains in more details. For this purpose, simulations are conducted for $\chi_0 = 20$ and 800 μm. At $\chi_0 = 20$ μm the acoustical Reynolds number is 0.73 and the nonlinearity effects are very small. Whereas, at $\chi_0 = 800$ μm the acoustical Reynolds number is 27.8 and the phenomena is highly nonlinear. Fig. 4–6 shows the spatial and temporal variations of the particle displacement for the two cases. For a clear depiction of the waveforms, the time series of the particle displacement at $x = L/2$ for both cases is shown in Fig. 4–7. The plot clearly shows the change in the particle displacement behavior when the wave becomes highly nonlinear. The waveform of the particle displacement is changed from the typical sinusoidal behavior for weakly nonlinear case to an almost triangular form for the highly nonlinear case.

The spatial and temporal variations of pressure are shown in Fig. 4–8 for the two cases. The plots show a significant change in the pressure waveform as the waves become highly nonlinear. To obtain a better insight into the impact of nonlinearity on the pressure waveform in space and time, spatial and temporal data are extracted for both cases. To investigate the temporal variations, the time series of pressure amplitude at $x = L/2$ (pressure node) and $x = L$ (pressure anti-node) are depicted in Fig. 4–9. For the first case (i.e. χ_0=20μm) which is almost linear, the well-known half cosine distribution for the pressure is observed. At $x = L/2$, the pressure amplitude is almost negligible (less than 2 percent of that at the pressure

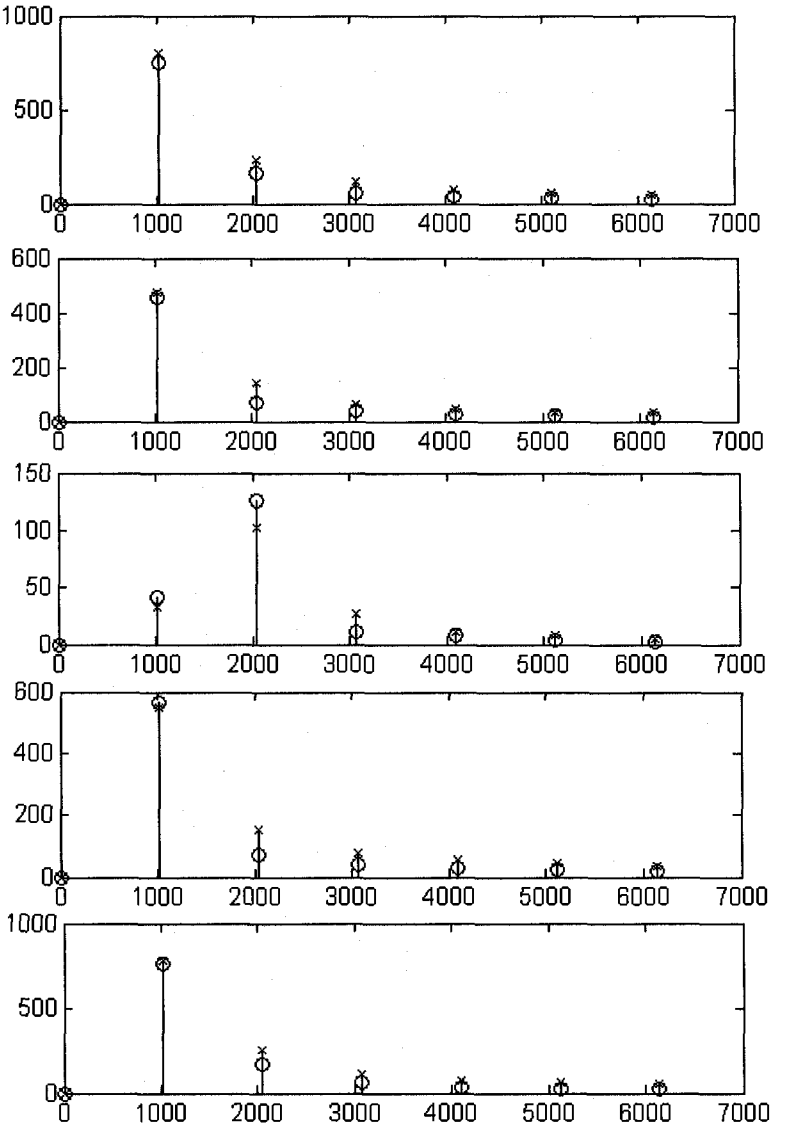

Figure 4–5: The frequency spectrum for the numerical and experimental waveforms of the pressure for $\chi_0 = 175$ μm at (a) $x = 17$cm, (b) $x = 13$ cm, (c) $x = 8.5$ cm, (d) $x = 5$ cm and (e) $x = 1$ cm. $\circ$, numerical; $\times$, experimental. The horizontal axes are frequency in Hz and the vertical axes are pressure in Pa.

antinode). The plot however, shows that presence of the second harmonic, although its magnitude is significantly less that that of the fundamental. For the second case

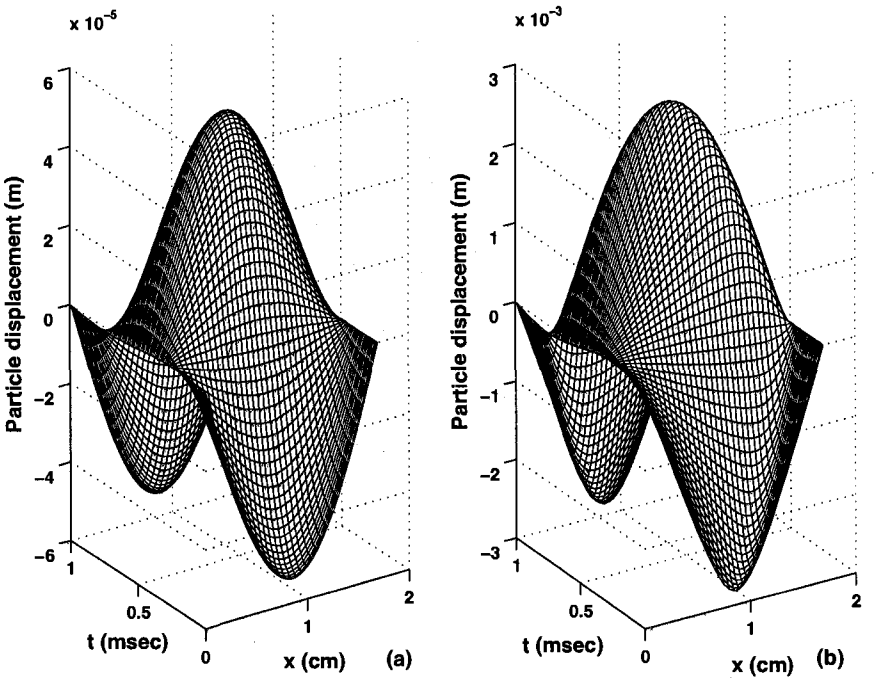

Figure 4–6: The variation of the simulated particle displacement over a standing wave period for (a) $\chi_0 = 20$ μm and (b) $\chi_0 = 800$ μm.

which is highly nonlinear (χ_0=800μm), the plot shows that the pressure waveform is significantly distorted from the classical sinusoidal form. At $x = L/2$, the pressure amplitude is significantly large indicating that there is no fixed node for the pressure at this location. It means that instead of a standing wave, that is a 'quasi-standing' wave. The plot also shows that for the highly nonlinear case, the second harmonic dominates over the fundamental mode. Vanhille and Campos-Pozuelo [68] solved the nonlinear wave equation by decomposing it into linear and second-order correction forms. Their second-order correction pressure also indicated the disappearance of the pressure node at the center of the tube. However, they did not explore this issue.

The axial distribution of pressure during a standing wave period along the channel axis for $\chi_0 = 20$ and 800 μm is shown in Fig. 4–10. The comparison of these

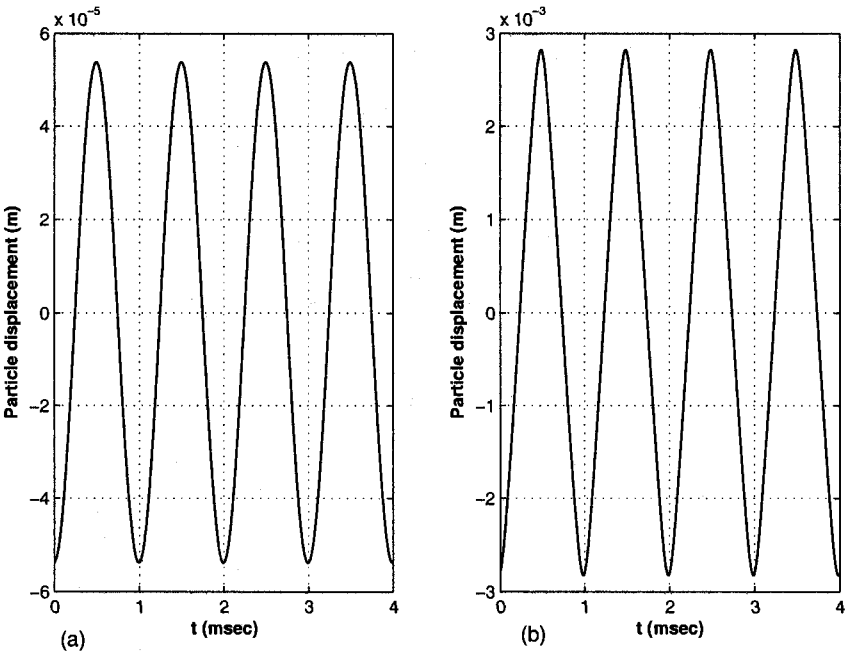

Figure 4–7: The simulated particle displacement amplitudes at $x = L/2$ from the center of diaphragm for (a) $\chi_0 = 20$ μm and (b) $\chi_0 = 800$ μm.

two distributions shows that the axial distribution of pressure for the highly nonlinear case is significantly different from that of the linear or weakly nonlinear case. The latter shows a pressure node at the middle of the channel that is fixed in time and space. However, for the highly nonlinear case, the pressure node is not fixed in time and space. That is, during a wave period, the pressure node oscillates about the theoretical pressure node. The frequency of oscillation is twice the resonance frequency. It is because of this oscillation that the large amplitude second harmonic mode of pressure manifested at the location of theoretical pressure node in Figs. 4–5 and 4–9b. The analysis also showed that the amplitude of this oscillation increases with an increase in the excitation voltage. For a linear or weakly nonlinear case, the pressure magnitude at any instant of time is symmetric about the pressure node (see Fig. 4–10a). However, for the highly nonlinear case, due to the oscillation of

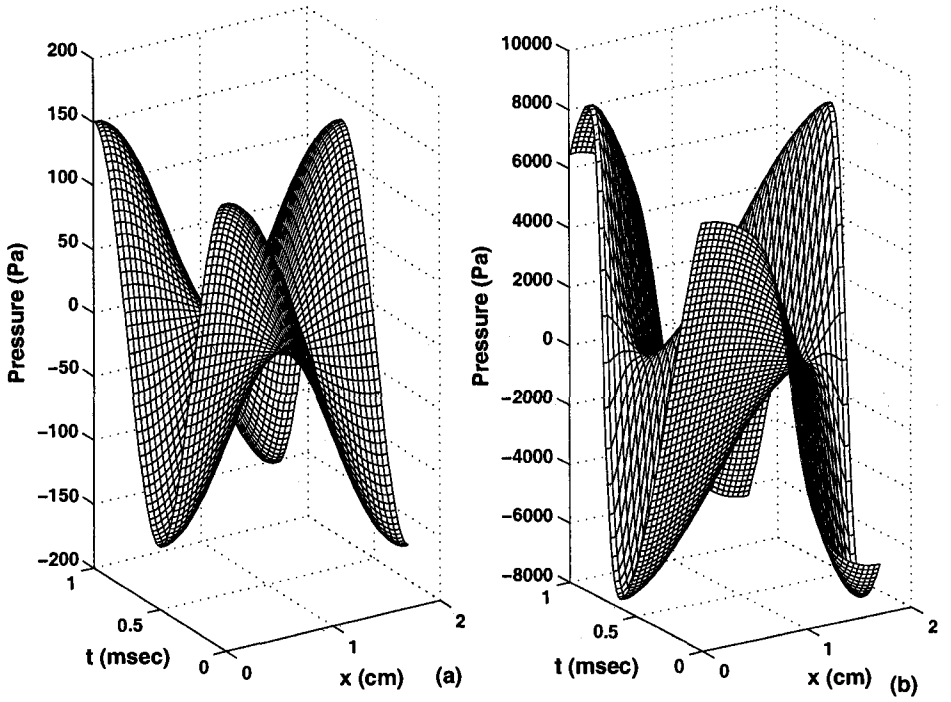

Figure 4–8: The variation of the simulated pressure over a standing wave period for (a) $\chi_0 = 20$ μm and (b) $\chi_0 = 800$ μm.

the pressure node, the pressure magnitude is not symmetric. This asymmetry in the pressure magnitude increases with an increase in the distance of the actual pressure node from that of the theoretical pressure node at any particular instant of time.

4.3.2 Conclusions

Nonlinear pressure inside an acoustic resonator is numerically and experimentally investigated. A good agreement between the experimental and numerical results is observed in time, space and frequency domains. The analysis showed that the shape of the particle displacement and pressure waveforms of highly nonlinear waves are significantly deviated from the sinusoidal form in both time and space. It is also observed that for highly nonlinear waves, the pressure node is not fixed in time and space and oscillates about the theoretical pressure node at a frequency twice that of

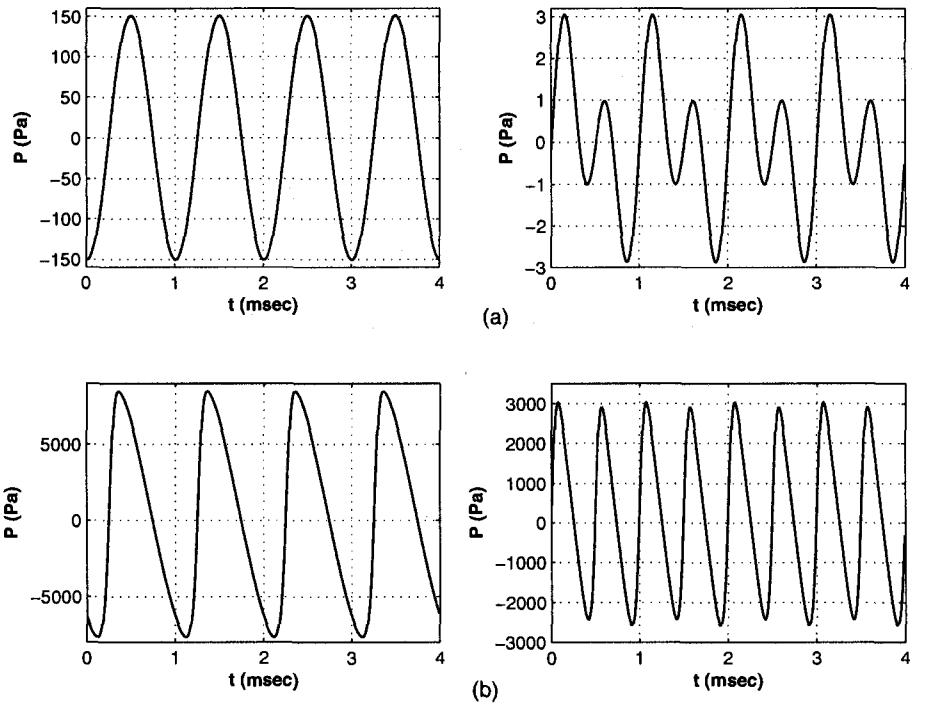

Figure 4–9: The simulated pressure amplitudes at $x = L$ (left pane) and $x = L/2$ (right pane) from the center of diaphragm for (a) $\chi_0 = 20$ μm and (b) $\chi_0 = 800$ μm.

the resonance frequency. This resulted in the manifestation of large amplitude second harmonic mode of pressure at the location of the theoretical pressure node.

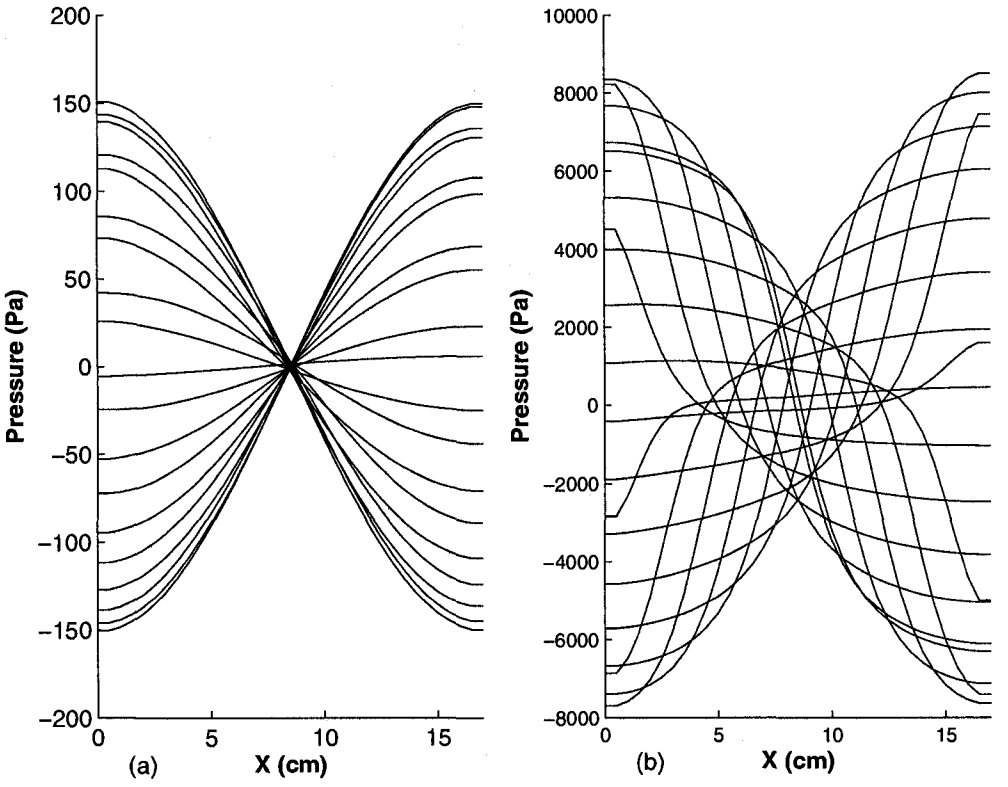

Figure 4–10: The axial distribution of the pressure during a standing wave period along the channel axis for (a) $\chi_0 = 20$ and, (b) 800 μm. Each profile reports a different time, which cover one wave period.

CHAPTER 5
Experimental Study of the Nonlinear Velocity Field in an Acoustic Resonator

5.1 Introduction

As the literature review (sections 1.2.1 and 1.2.2) indicates, all previous experimental studies related to the acoustic velocity measurement have been performed in the linear range and consequently, no experimental study has reported the spatial and temporal variations of the velocity field inside a nonlinear acoustic standing wave resonator. Very recently, Berson *et al.* [128] used PIV ti characterize the flow field at the end of the stack plates of the thermoacoustic refrigeration system in order to understanding and optimization of heat transfer between the stack and the heat exchangers.

In this chapter, a brief explanation of the principle of the PIV and synchronized PIV used to measure the acoustic velocity fields comes first. Then, the behavior of acoustic velocity fields of nonlinear standing waves is investigated temporally and spatially using the synchronized PIV technique (section 5.4). To compare the experimental velocities with the theoretical ones, two finite-amplitude nonlinear cases are considered which have the analytical solution for the particle velocity variations. After the validation of the technique, it is used to measure the velocity fields of nonlinear standing waves. To the best of our knowledge, this work is the first experimental investigation of the spatial and temporal particle velocity inside a nonlinear acoustic standing wave tube.

5.2 PIV principle

PIV is an optical technique that measures two-dimensional velocity fields with high spatial resolution. The principe of PIV technique is illustrated in Fig. 5–1. In this technique, the fluid under investigation is seeded with tracer particles that

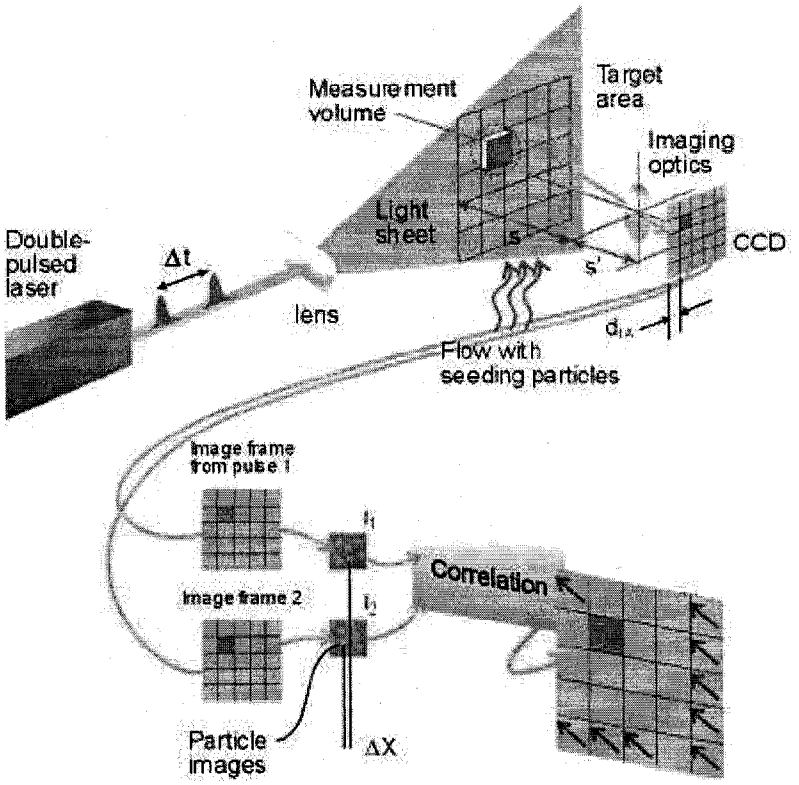

F

Figure 5–1: Particle Image Velocimetry measurement principles (taken from Dantec Dynamics A/S).

follow the flow field. The PIV system consists of a light source, CCD camera, pulse generator and a PC equipped with a frame grabber. The laser light sheet produced by spherical and cylindrical lenses illuminates a plane in the flow and the camera records the position of the particles. The laser light sheet is pulsed twice with a known time separation between the two pulses (Δt in Fig. 5–1). The CCD camera captures the images of the tracer particles at each pulse in the flow field of interest. Each image pair is then processed to obtain the corresponding velocity field based on the particle shift. The images are divided into small subsections called interrogation

areas (IA). The interrogation areas from first and second images (I_1 and I_2 in Fig. 5–1), are cross-correlated pixel by pixel. It produces a correlation peak, identifying the average particle displacement in a given interrogation area from first image to second image, i.e. during the time interval Δt. An accurate measure of the displacement is achieved with sub-pixel interpolation. A map of displacement vectors over the whole target area is obtained by cross-correlating each corresponding interrogation area in the two image frames captured by the camera. The displacement of particles between the two images (Δx in Fig. 5–1) divided by Δt provides the velocity field.

5.2.1 Seeding particles

BIS(2-ETHYLHEXYL) SEBACATE mist with the mean diameter of 0.5 μm is used as the tracer particles. An aerosol generator (Lavision Inc., Ypsilanti, MI) is used to generate the mist. An important issue related to the tracer particles is their response time. That is, how quickly the particles respond to any change in the flow behavior. In the present study, the density of the tracer particles is much higher than that of the air; therefore, it is important to find the response time of the particles. Furthermore, as the particles oscillate under the action of the standing wave, this issue becomes even more critical. The characteristic response time of the seed particles is computed by

$$T_p = u_T/g. \tag{5.1}$$

[129], and the terminal velocity is computed by

$$u_T = \frac{(\gamma - 1)D^2 g}{18\nu}. \tag{5.2}$$

[130]. Using the above equations, for D=0.5 μm, u_T=6.5 μm/s, and the particle response time is found to be T_p=0.67 μs. For example, for the driver frequency of 1400 Hz, the particle response time is more than 1000 times smaller than the wave time period. Thus, we conclude that, for the frequency range used in this study, the

tracer particles accurately follow the flow.

5.2.2 Laser and camera

A New Wave Research 120 mJ Nd:YAG is used as a light source for the PIV measurements. A digital 2 Megapixel progressive scan CCD camera (JAI CV-M2) with the resolution of 1600×1200 pixels is used to image the flow. The camera is connected to a PC equipped with a frame grabber (DVR Express, IO Industries, London, ON, Canada) that acquired 8-bit images at a rate of 30 Hz. A four-channel digital delay generator (555-4C, Berkeley Nucleonics Corporation, San Rafael CA) is used to control the timing of the laser pulses.

5.2.3 Correlation of fixed interrogation areas

The vector grid spacing h_{vec} is given in terms of the interrogation cell size D_I and the percentage overlap O by $h_{vec} = D_I(1 - O/100)$. To increase the apparent resolution and make more effective use of the data, it is common to have an overlap of 50%. At any grid point (k, l), the location of the center of the interrogation areas, and hence the vector locations, are given by $x_I(k) = (k+0.5)h_{vec}$ and $y_I(l) = (l+0.5)h_{vec}$, where x_I and y_I are the distances from the left and upper image boundary respectively (see Fig. 5–2). The discrete cross-correlation of two interrogation areas $IA_1(i, j)$ and $IA_2(i, j)$ is defined by

$$R(r, s) = \sum_{i=0}^{D_I-1} \sum_{j=0}^{D_I-1} IA_1(i, j)IA_2(i + r, j + s), \tag{5.3}$$

where $r, s = -D_I/2, ..., D_I/2-1$. This could be computed with fast Fourier transform (FFT) as,

$$R(r, s) = \Re[FFT^{-1}(FFT^*(IA_1).FFT(IA_2))], \tag{5.4}$$

where * denotes the complex conjugate [131]. The advantage of using Eq. (5.4) instead of Eq. (5.3) is that the computation with FFT is faster than the direct

computation, but it also requires that the interrogation cell size $D_I = 2^n$, where n is an integer, e.g. D_I = 8, 16, 32, 64 or 128. The highest value in the correlation plane identifies the average displacement in the given interrogation region. Smaller interrogation window size gives higher spatial resolution. However, particles may move out of this small region and cause erroneous vectors, when a small interrogation window is taken. The use of a larger window causes the velocity distribution to become of low spatial resolution. Therefore, an optimum window size should be chosen [132].

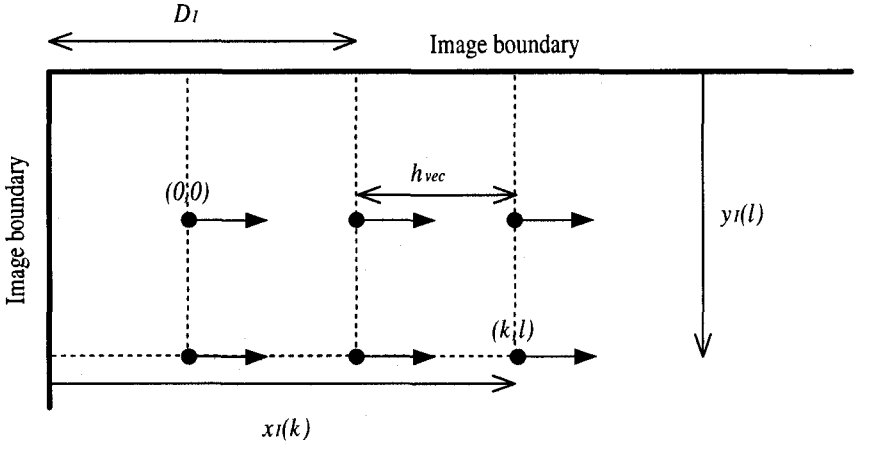

Figure 5–2: Vector locations at the center of the interrogation areas for a case with O = 50%, i.e. $h_{vec} = 0.5 \times D_I$.

Since the image consists of the discrete function in pixel units, the displacement vector (r, s) is discrete. Thus, the location of the peak on the correlation plane is also in pixel units. Several methods for improving the dynamic range have been developed, such as sub-pixel analysis. One of the approaches is peak fitting, in which the correlation peak is fitted to some functions with a sub-pixel accuracy. The three-point Gaussian peak fitting is widely used for sub-pixel analysis in which, the sub-pixel displacement ε is estimated from

$$\varepsilon = \frac{1}{2} \frac{\ln R(\xi - 1) - \ln R(\xi + 1)}{\ln R(\xi - 1) + \ln R(\xi + 1) - 2 \ln R(\xi)}, \tag{5.5}$$

where ξ denotes the position of the peak in the one dimensional case [133]. Keane and Adrian [134] have reported the effects on the RMS error of parameters such as the relative in-plane displacement, the velocity gradient, the particle image density and so on.

5.2.4 Post-processing of displacement field

Even if all steps of the image acquisition and processing are optimized there is a finite probability that the highest correlation peak does not correspond to the true displacement. This results in a spurious or false vector. Reasons for the occurrence of spurious vectors can be for example, a local region of low particle image density, disturbing background noise from reflections, or low signal-to-noise ratio.

The recommended method for detecting spurious vectors is to use a local median test [135], which means that each displacement vector is compared to the median displacement in a local neighborhood of the given vector. If the displacement vector deviates more than an accepted range from the local median value, it is considered as a spurious vector. Other methods for detecting spurious vectors include global mean, local mean and detectability tests. The global mean test is similar to confining the range of acceptable displacements in the correlation plane, as described above. It only gives a sort-out of the completely unlikely vectors. The local mean test is similar to the local median test, but since the local mean value is more sensitive to neighboring spurious vectors than the local median, it is less robust. The detectability is defined as the ratio of the highest to the next highest peak in the correlation plane. It has been shown as the least efficient method of all the above methods [135].

The local median test used in the present work, is explained as follows: The local median displacement (r_{med}, s_{med}), i.e. the middle value in an ordered list, is computed for each vector for the x- and y-directions separately. The median is based on the vector itself and the eight closest neighbors. If a close neighbor is non-existing, e.g.

at the image boundary or if the vector has been discarded by a previous median test, that neighbor is excluded from the computation of the median. If either the x- or the y-component of the tested displacement vector deviates more than a prescribed amount e from the median value, i.e. if $|r_p - r_{med}| > e$, or $|s_p - s_{med}| > e$, the vector is not accepted, and is replaced by the median value. An improved performance of the local median test has been found by repeating the test a few times (typically three). Since spurious vectors are removed after each pass of the test, the median values of the next pass will be more reliable.

5.3 Synchronized PIV technique

In the conventional PIV setup, the laser pulses are synchronized with the camera frames. Typically these signals are not synchronized with any flow characteristics as for steady flows it is not necessary. However, for velocity measurements in the presence of an acoustic standing wave, these signals should be synchronized with the excitation signal to capture velocity fields at a desired phase [60]. The block diagram of the synchronized PIV system is shown in Fig. 5–3. It includes components grouped in these categories: System control, Flow imaging, Image capture and Image analysis.

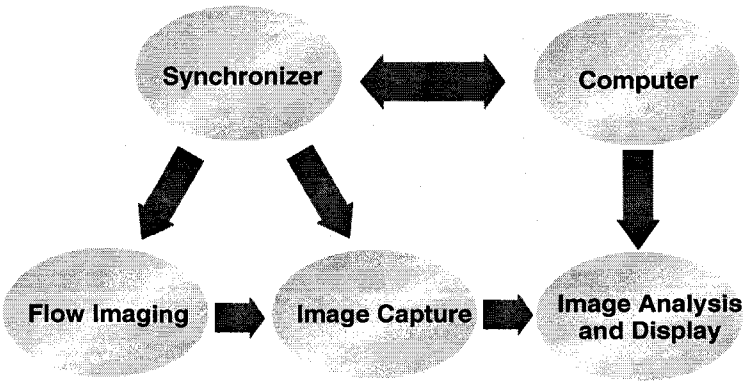

Figure 5–3: Block diagram of the synchronization circuit.

In this study, an electronic circuit is developed to generate a trigger signal which

could synchronize the laser pulses and camera frame with any particular phase of the excitation signal. This phase can be adjusted from 0 to 2π and therefore covers the whole period of the excitation waveform. The basic principal of this scheme is shown in Fig. 5–4.

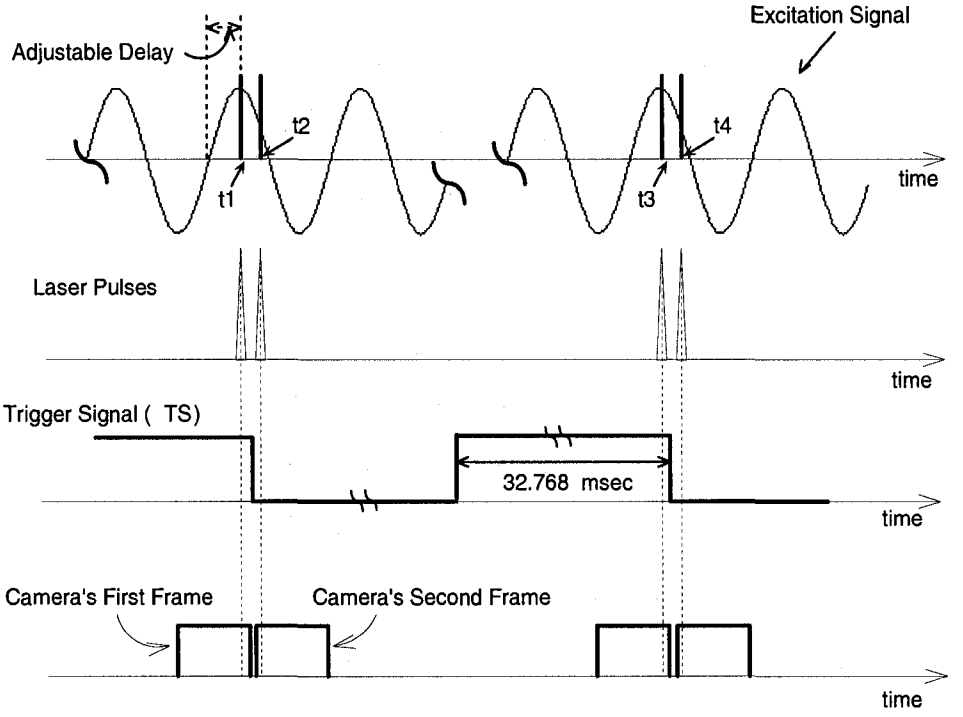

Figure 5–4: The triggering sequence that shows the simultaneous measurement of the acoustic and streaming velocity fields at a particular phase of the excitation signal. t_1 and t_2 correspond to the times at which the first and second images of an image pair are captured. t_3 and t_4 are the times associated with the first and second images of the consecutive image pair.

The block diagram and the output waveforms of each block of the developed synchronization circuit are shown in Fig. 5–5. The excitation voltage (TP1) which is used to excite the standing wave inside the tube, is sent to the sync generator to produce a rectangular wave synchronized with the zero crossing points of the excitation signal (TP2). The delay generator provides a train of pulses with adjustable duty cycle (TP3) which is synchronized with the rising edge of TP2. The rising edge of the trigger output signal (TP4) is synchronized with the falling edge of TP3. By

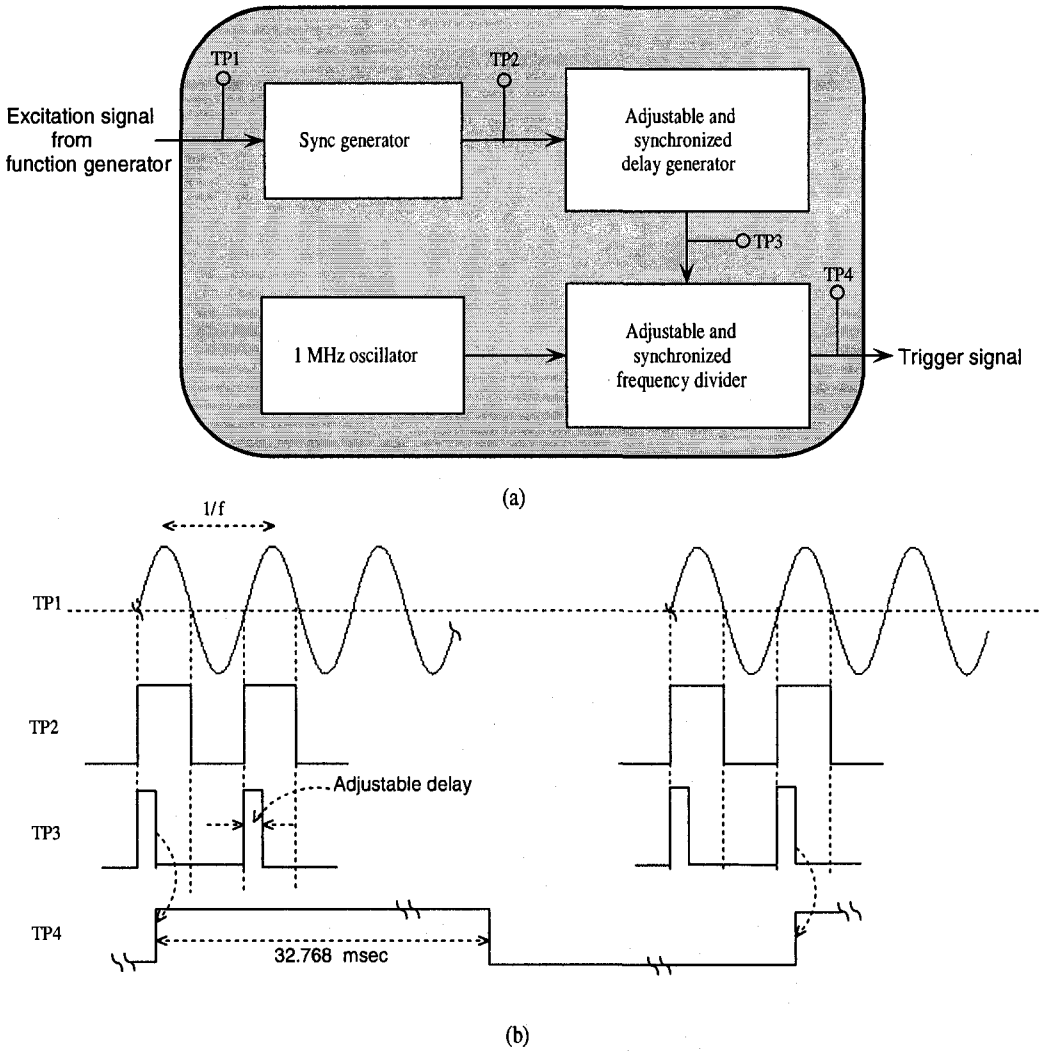

Figure 5–5: (a) Block diagram of the synchronization circuit, (b) The waveforms at different test points (TP) of the synchronization circuit.

adjusting the duty cycle of TP3, we can select the phase at which PIV images have to be acquired. In the conventional PIV setup, a fixed unsynchronized 15 Hz signal is used as a trigger for both laser and camera. However, in the present synchronized PIV technique, TP4 is used to trigger both laser and CCD camera of the PIV system. That is, both the laser and the camera are synchronized with the acoustic signal via TP4. Although, the high state duration of TP4 is fixed (32.768 msec), The low state duration is not fixed because the rising edge of TP4 is synchronized with the excitation signal. Therefore, the frequency of TP4 is not exactly but close to 15 Hz and

it is automatically adjusted according to the excitation frequency. For example, the frequency of TP4 for the excitation frequency of 1000 Hz is 15.15 Hz and for 1330 Hz is 15.11 Hz. The frame rate of camera is twice the frequency of TP4. Furthermore, we can measure the streaming velocity field at any arbitrary excitation frequency, because the acoustic frequency is not forced to be a multiple of the frame rate. Rather, the frame rate is forced to be an exact divisor of the acoustic frequency. For a given acoustic frequency, the frame rate is automatically adjusted to a frequency close to 30 Hz. Since the time delay, the width of the trigger signal (TP4), the frequency of the excitation signal and the time separation between two laser pulses are accurately known, the phase where two laser pulses are located in the excitation signal can be calculated.

5.4 Particle velocity in the nonlinear standing wave resonator

The schematic of the experimental setup to measure the acoustic velocity fields inside the standing wave tube using the synchronized PIV technique is shown in Fig. 5–6. A photograph of the setup is shown in Fig. 5–7. The two-dimensional velocity fields inside the channel are measured using the synchronized PIV technique. The measurements are made in a plane parallel to the channel length at the mid-channel location as shown in Fig. 5–6. The driver frequency (f) is set equal to 935 Hz. The corresponding wavelength (λ) of the acoustic standing wave is 36.4 cm. The length of the channel (L) is adjusted with the movable piston to allow the formation of two full standing waves inside the channel (i.e. $L = 2\lambda$=72.8 cm). The field of view of the CCD camera is set in a way to map the flow field in the half wavelength section. That is, the field of view of the camera is set equal to 19 cm in horizontal and 14.25 cm in vertical.

In order to accurately measure the periodic particle velocity, the separation time between two images must be adjusted appropriately. Due to the oscillation of the

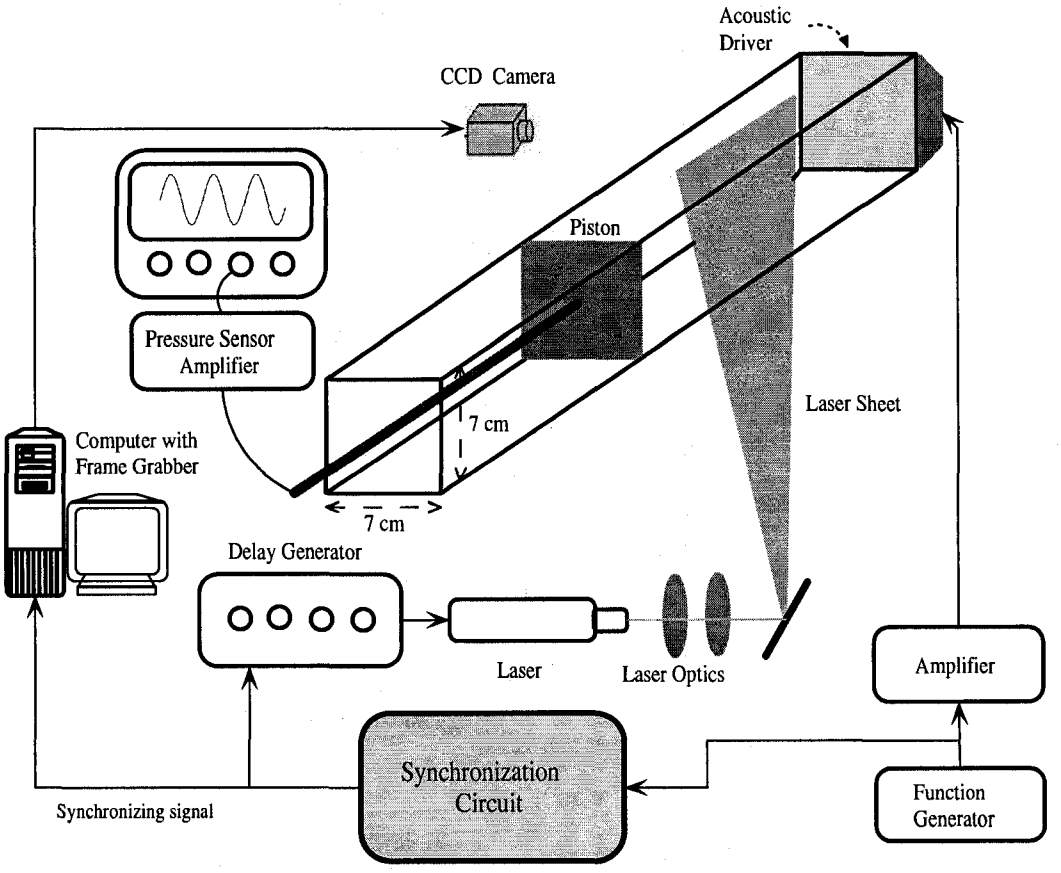

Figure 5–6: Schematic of the experimental setup and instrumentation.

seed particles, the time separation between the two images of an image pair should be much less than the quarter of the wave period. Otherwise, the particle displacement computed by cross-correlating the PIV images will be smaller than the actual displacement of the particles. This will result in the under estimation of the acoustic velocities. On the other hand, for a very short separation time, the particle shift between the two images of an image pair will be too small and will increase uncertainty in the velocity measurements. The vertical dimension of the camera field of view is larger than the channel height. Therefore, before computing the velocity vectors, the images are preprocessed to remove the regions outside the channel from the images. A PIV algorithm developed by Marxen [136] is used for velocity computation by cross-correlating the interrogation region in the first image with the corresponding

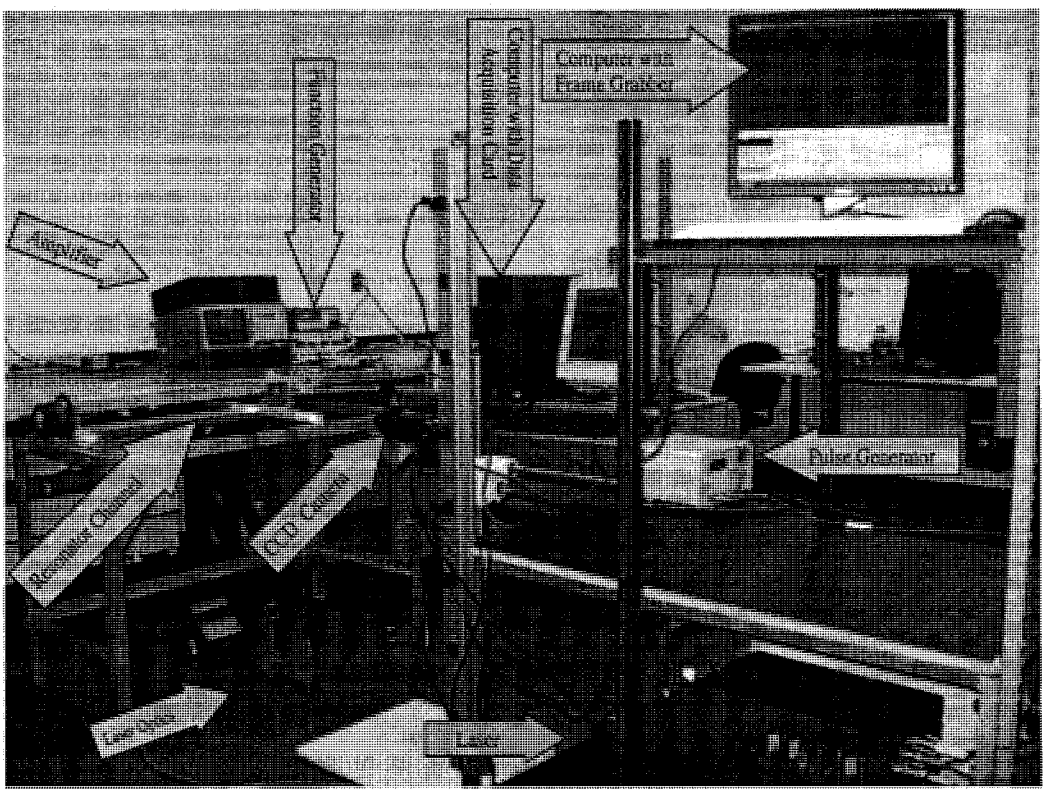

Figure 5–7: Photograph of the experimental setup and instrumentation.

search region in the second image. The size of the interrogation region is set equal to 32×32 pixels and the size of the search region is set equal to 64×64 pixels. A three-point Gaussian sub-pixel fit scheme is used to obtain the correlation peak with sub-pixel accuracy. A 50% window overlap is used in order to increase the nominal resolution of the velocity field to 16 × 16 pixels. This resulted in a spatial resolution of 1.9 × 1.9 mm of the velocity field. A scheme is used to identify the spurious velocity vectors and then correct them using a local median test [137].

The maximum diaphragm velocity is also measured for each excitation amplitude using the laser vibrometer. Fig. 5–8 shows the maximum vibration velocity at the center of the driver's diaphragm as a function of the excitation voltage of the driver for different excitation frequencies. The plot shows that for a given excitation frequency, the diaphragm velocity and excitation voltage are almost linearly related. Using Fig. 5–8 for a given excitation frequency, we can estimate the amplitude of

diaphragm velocity at all excitation voltages over the range of our practical interest. By adjusting the time delay in the synchronization circuit, the measurements have been conducted at 18 different phases of the excitation signal. It should be noted that the first image of the image pair is taken at the desired phase. For each phase of the excitation voltage, 200 PIV images are captured. From these images, 100 acoustic velocity fields are computed.

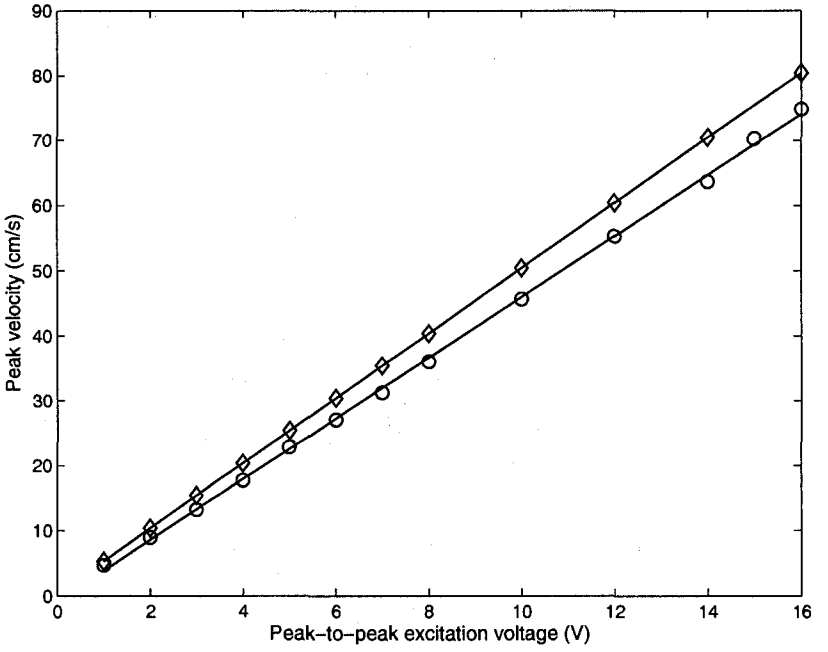

Figure 5–8: Maximum velocity at the center of the driver diaphragm (u_0) versus excitation voltage at different excitation frequencies; o, 496 Hz; $\diamond$, 1024 Hz. Solid line, linear fit. The overall bias error between the measured and fitted velocities for f =496 and 1024 Hz is 0.36 and 0.49 cm/s, respectively.

5.4.1 Validation of the synchronized PIV technique

Before measuring the velocity field of highly nonlinear standing wave using the synchronized PIV technique, we present the results for the finite-amplitude nonlinear cases that have analytical solution in order to compare the experimental data with

the theoretical results and validate the accuracy of the synchronized PIV technique.

Mathematical formulation

To validate the experimental velocity fields obtained from the synchronized PIV, the experimental data are compared with the analytical solution of the one-dimensional finite-amplitude nonlinear wave equation. This equation in a thermoviscous fluid can be written as

$$u_{tt} - c_0^2 u_{xx} = \left(\nu b u_{tx} - \frac{1}{2}(u^2)_t\right)_x, \tag{5.6}$$

where b is defined in Eq. (3.29).

Both the nonlinear term $(\frac{1}{2}(u^2)_t)$ and dissipative term $(\nu b u_{tx})$ in the righthand side of Eq. (5.6) play a role in the deviation of the velocity from the pure sinusoidal waveform observed in the linear standing wave. Under certain condition (which will be found later in this section), the nonlinear term can be neglected in comparison with the dissipative term. Thus, Eq. (5.6) can be simplified as,

$$u_{tt} - c_0^2 u_{xx} - \nu b u_{txx} = 0. \tag{5.7}$$

We call this equation as *quasi-nonlinear* wave equation to differentiate it from the finite-amplitude nonlinear case (Eq. 5.6) and linear wave equation in lossless medium $(u_{tt} = c_0^2 u_{xx})$.

The fluid is excited by the harmonic motion of a diaphragm at $x = 0$ with the frequency of f. Assuming L to be the length of the tube (equal to 2λ in the present case), the following boundary conditions are applicable,

$$u(0,t) = u_0 \cos(wt) \quad , \quad u(L,t) = 0. \tag{5.8}$$

A solution of the form $u(x,t) = U(x)e^{-j\omega t}$ is sought for Eq.(5.7). We write,

$$U'' + \frac{\omega^2}{c_0^2 - j\nu b\omega}U = 0. \tag{5.9}$$

Defining the dissipation parameter $\delta \equiv \frac{\nu b\omega}{2c_0^2}\frac{\omega L}{c_0} \ll 1$ [119], we get,

$$U'' + \big(\frac{\omega}{c_0}(1 + j\frac{c_0}{\omega L}\delta - \frac{3c_0^2}{2\omega^2 L^2}\delta^2)\big)^2 U = 0. \tag{5.10}$$

Solving Eq.(5.10) and using the boundary conditions (5.8) we obtain,

$$\begin{aligned} u(x,t) = {} & \frac{u_0}{(1+\frac{\delta^2}{2})\sin^2\frac{\omega' L}{c_0} + \delta^2\cos^2\frac{\omega' L}{c_0}} \times \Big(\Big[(1 + \frac{\delta^2(L-x)^2}{2L^2})\sin\frac{\omega' L}{c_0}\sin\frac{\omega'(L-x)}{c_0} \\ & + \delta^2\frac{L-x}{L}\cos\frac{\omega' L}{c_0}\cos\frac{\omega'(L-x)}{c_0}\Big]\cos\omega t \; + \; \delta\Big[\frac{L-x}{L}\sin\frac{\omega' L}{c_0}\cos\frac{\omega'(L-x)}{c_0} \\ & - \cos\frac{\omega' L}{c_0}\sin\frac{\omega'(L-x)}{c_0}\Big]\sin\omega t\Big), \end{aligned} \tag{5.11}$$

where $\omega' = \omega(1 - \frac{3c_0^2\delta^2}{2\omega^2 L^2})$.

Eq. (5.11) represents the analytical solution for the one-dimensional acoustic velocity of quasi-nonlinear case. In order to find the condition when Eq. (5.7) (from which Eq. (5.11) is obtained) is valid, the nonlinear and dissipative terms on the righthand side of Eq. (5.6) are estimated. Assuming $\delta \ll 1$, we can write $u(x,t) \simeq \big(u_0 \sin\frac{\omega'(L-x)}{c_0} / \sin\frac{\omega' L}{c_0}\big)\cos\omega t$. Then, it is found that $\frac{1}{2}(u^2)_t \sim \omega u_0^2$, and $\nu b u_{tx} \sim \nu b u_0\omega^2/c_0$. Therefore, the condition when nonlinear effects can be neglected in comparison with dissipation effects can be found as, $\eta \equiv \frac{u_0 c_0}{\nu b\omega} \ll 1$. This condition can be written in terms of the acoustical Reynolds number ,Re_{a2} (Eq. 3.21), as

$$Re_{a2} \ll \frac{u_{max}}{u_0}. \tag{5.12}$$

Therefore, as long as the acoustic intensity is not very large, Eq. (5.12) is satisfied, and Eq. (5.11) can be considered as a valid solution for the finite-amplitude nonlinear wave in an enclosure.

The axial distribution of the analytical axial velocity (Eq. 5.11) over the entire

tube for $u_0 = 34$ cm/s at different phases is plotted in Fig. 5–9. The phases at which the velocity is plotted are $t/T = 0$, 0.05, 0.1, 0.25, 0.4, 0.45, 0.5, 0.55, 0.6, 0.75, 0.9, and 0.95. As expected the maximum velocity at the vibrator end is u_0 and at the other end is zero. The variation of the velocity fields especially near the vibrator end and when the velocity magnitude is low, are deviated from the pure sinusoidal waveform.

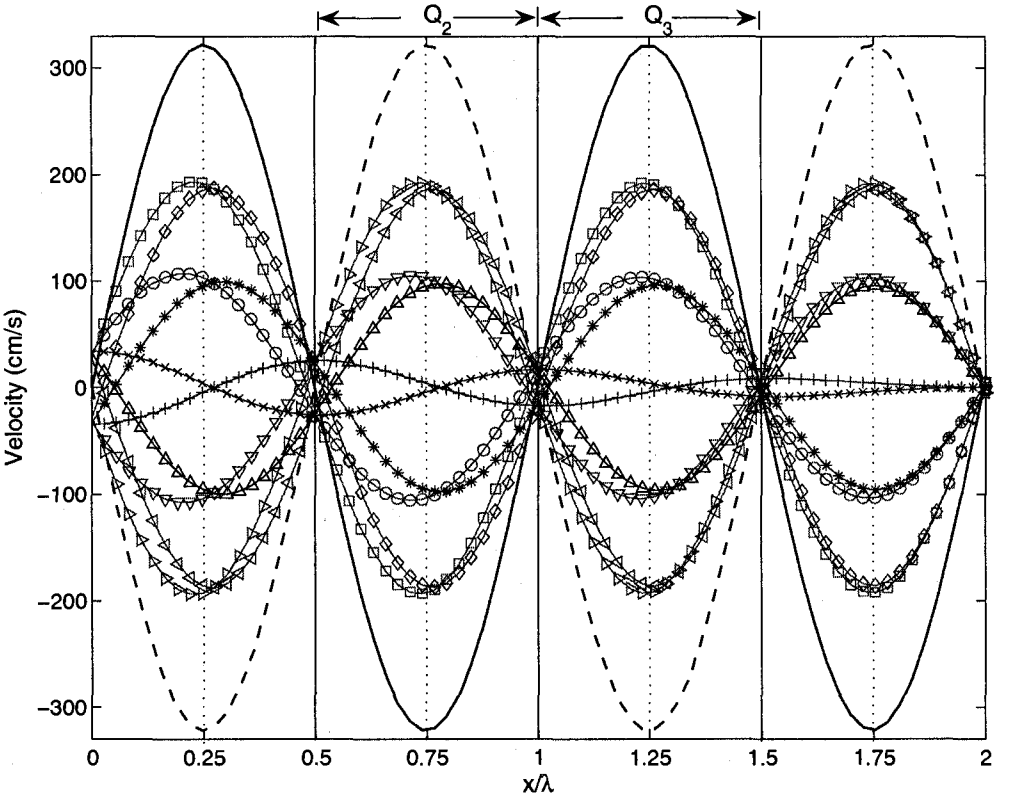

Figure 5–9: The axial variation of the analytical axial velocity for $u_0 = 34$ cm/s at different phases: t/T=0, $\times$; t/T=0.05,$\circ$; t/T=0.1, $\square$; t/T=0.25, solid line; t/T=0.4, $\diamond$; t/T=0.45, $*$; t/T=0.5, $+$; t/T=0.55, $\triangledown$; t/T=0.6, $\triangleright$; t/T=0.75, dashed line; t/T=0.9, $\triangleleft$; t/T=0.95, $\triangle$.

5.4.2 Results and discussion

As mentioned in section 5.4.1, the first set of experiments has been performed for the quasi-nonlinear condition. The reason is that the analytical solution for the quasi-nonlinear case is available (Eq. 5.11) and thus, the experimental results can

be compared with the analytical ones in order to validate the measured data. The results are presented for two excitation amplitudes that correspond to the maximum diaphragm velocity (u_0) of 34 and 40 cm/s, hereinafter referred to as cases A and B, respectively. The maximum acoustic velocity for cases A and B is approximately 3.2 and 3.8 m/s, respectively. Thus, the acoustical Reynolds number is 0.57 for case A and 0.66 for case B, which lie in the quasi-nonlinear range. For both cases, u_{max}/u_0 = 9.5, which implies that for the validity of Eq. (5.11), we must have $Re_{a2} \ll 9.5$, which is true for both cases. Therefore, we conclude that the validation condition (Eq. 5.12) is satisfied and Eq. (5.11) is a valid solution for both cases.

The experimental velocity vectors along with the transversely averaged axial velocities for cases A and B are shown in Figs. 5–10 and 5–11 at four different phases. The measurements have been done over the second half wavelength (Q_2 in Fig. 5–9) for case A and over the third half wavelength (Q_3 in Fig. 5–9) for case B. Two steps were taken to obtain the transversely averaged axial velocities. First, the average two dimensional velocity field is obtained first by averaging 100 PIV fields i.e. average velocity is computed at each grid point. In the next step, at each axial location, the axial velocities are transversally averaged. The corresponding axial velocities obtained from the analytical formula (Eq. 5.11) are also plotted for comparison. A good agreement in both shape and amplitude between the experimental and analytical values of the axial velocity along the channel is observed at all phases for both cases. At all phases (especially the phases at which the velocity amplitude is low), the velocity profiles differ from a perfect sinusoidal wave field which is expected due to attenuation caused by viscous and nonlinear effects. At phases that correspond to the lower velocity magnitudes, i.e. t/T=0.476 and 0.980 (see Figs. 5–10b, 5–10d, 5–11b and 5–11d), it is observed that the maximum and minimum peaks are not located at the middle of the Q_2 and Q_3 sections, rather they are shifted slightly in the direction away from the driver end.

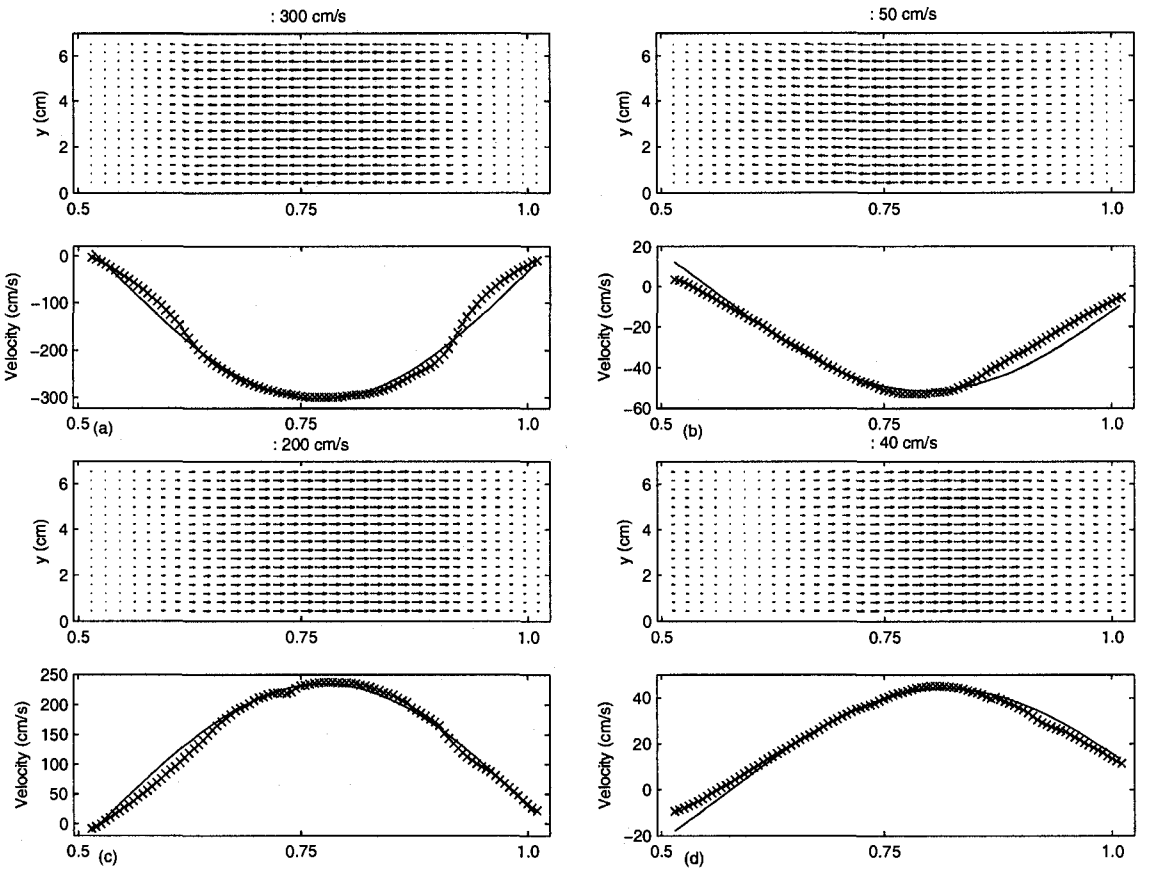

Figure 5–10: The particle velocities at u_0 = 34 cm/s at four different phases, (a) t/T=0.308, (b) t/T=0.476, (c) t/T=0.868, (d) t/T=0.980; (top) two-dimensional velocity field from PIV measurements, (bottom) corresponding transversely averaged axial velocity ($\times$). The analytical axial velocities are also plotted with solid line. Horizontal axis is x/λ, measured from the driver end. Note that the resolution of the velocity vectors was reduced in the plot for better visualization.

Furthermore, as shown in Figs. 5–10, and 5–11, the peaks of the experimental and analytical data at all phases are almost coincident, indicating that these phase-dependent shifts are also predicted by the mathematical solution of the quasi-nonlinear case. As shown in Fig. 5–9, the peaks of velocity at, for example, t/T= 0.05 do not occur at x/λ= 0.75 and 1.25. These phase-dependent shifts are not predicted by the linear wave equation in lossless medium. Aktas *et al.* found similar shapes for the axial velocity at different phases using a numerical model (see Fig. 2a in [100]).

The difference between the experimental transversely averaged velocity (Ue) and

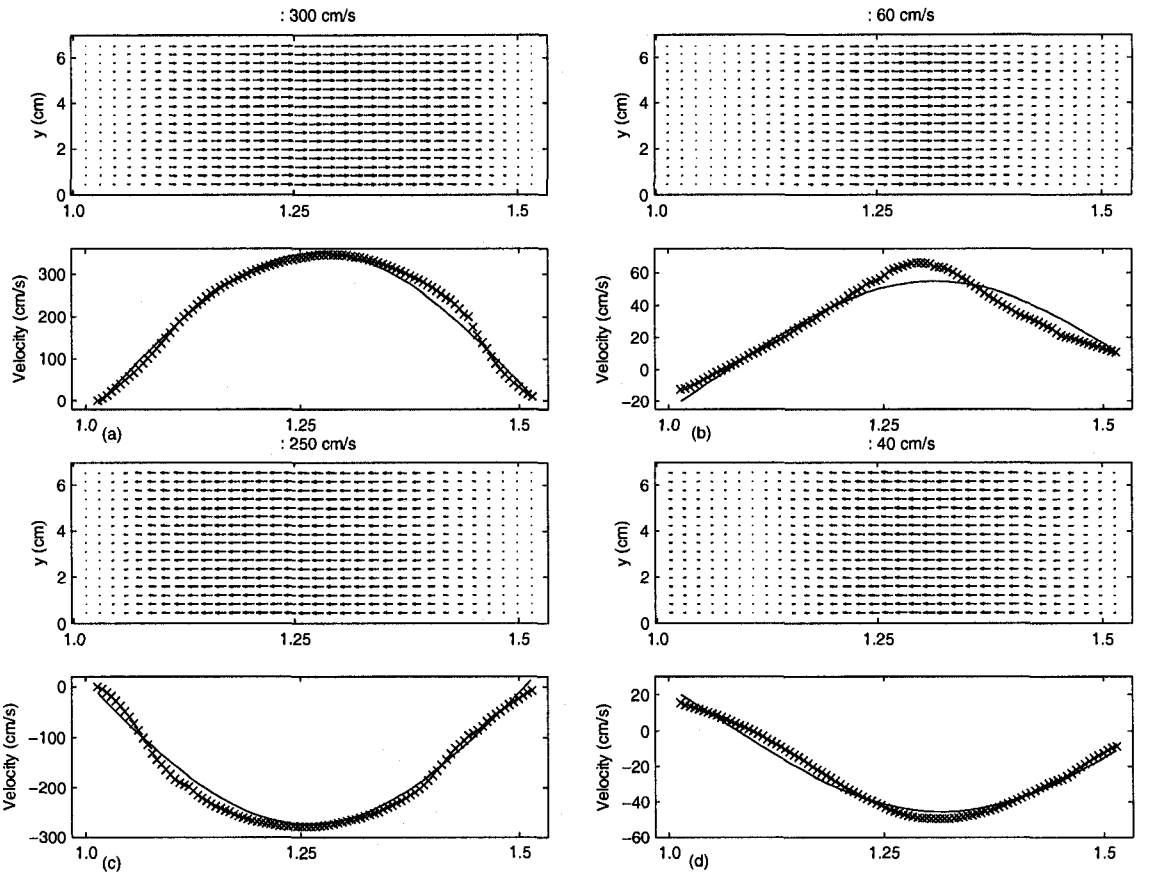

Figure 5–11: The particle velocities at $u_0 = 40$ cm/s at four different phases, (a) t/T=0.308, (b) t/T=0.476, (c) t/T=0.868, (d) t/T=0.980; (top) two-dimensional velocity field from PIV measurements, (bottom) corresponding transversely averaged axial velocity ($\times$). The analytical axial velocities are also plotted with solid line. Horizontal axis is x/λ, measured from the driver end. Note that the resolution of the velocity vectors was reduced in the plot for better visualization.

the analytical velocity (Ua) at any particular phase is compared in terms of the relative error (e) defined as,

$$e = \frac{e_{bias}}{u_m} \quad , \quad e_{bias} = \frac{1}{N} \sum_{i=1}^{N} \left| Ue_i - Ua_i \right| \tag{5.13}$$

where e_{bias} is the mean of the deviations between the measured and analytical velocities, N is the number of data points in the axial direction and u_m is the maximum magnitude of the analytical axial velocity at that particular phase. In order to obtain the uncertainty in the experimental transversal-averaged velocities, we use the

Table 5–1: Percentage of the relative error for the axial velocity (e_u), bias error for the transversal velocity ($e_{u\,bias}$) and the average of the standard deviation for both velocities ($mstd_u$ and $mstd_v$) in spatial variation at different phases for cases A and B.

	case A				case B			
t/T	e_u (%)	$mstd_u$ (cm/s)	$e_{u\,bias}$ (cm/s)	$mstd_v$ (cm/s)	e_u (%)	$mstd_u$ (cm/s)	$e_{u\,bias}$ (cm/s)	$mstd_v$ (cm/s)
0.028	16.26	2.2	0.51	0.2	15.71	2.9	0.48	0.4
0.084	6.54	0.6	0.60	0.4	9.82	1.1	1.44	0.7
0.140	11.77	1.4	1.07	0.7	7.61	2.7	0.83	0.7
0.196	7.62	1.6	1.01	0.9	3.17	1.4	0.98	0.8
0.252	4.79	1.6	1.38	1.1	4.86	1.9	1.40	1.0
0.308	3.88	1.9	0.86	0.7	3.68	1.5	2.04	0.8
0.364	5.69	2.1	0.95	0.7	6.09	2.0	1.27	0.6
0.420	7.29	2.0	2.78	0.9	9.98	2.0	1.74	0.6
0.476	5.49	1.2	2.13	0.8	7.12	1.6	0.63	0.5
0.532	4.60	0.7	1.02	0.5	9.51	0.7	1.48	0.4
0.588	7.38	0.8	2.07	0.5	7.49	1.4	1.54	0.6
0.644	6.49	1.6	1.88	0.9	7.07	1.6	3.83	0.8
0.700	4.40	2.3	1.76	0.9	3.61	1.9	3.22	1.1
0.756	3.05	2.6	1.43	1.0	6.06	2.2	2.98	1.0
0.812	7.07	2.5	3.05	1.0	8.19	2.7	2.60	0.9
0.868	9.47	2.4	1.3	0.9	8.31	3.5	2.26	1.1
0.924	10.9	1.8	1.21	0.8	12.56	2.3	1.10	0.7
0.980	4.54	0.7	0.52	0.5	6.76	0.5	0.91	0.3

average of the standard deviation ($mstd$) defined as,

$$mstd = \frac{1}{N}\sum_{i=1}^{N} std_i \ , \ std_i = \sqrt{\frac{1}{M}\sum_{j=1}^{M}(Ue_{i,j} - Ue_i)^2} \tag{5.14}$$

where M is the number of measured velocity fields at each phase (M=100 in the present cases). The values of relative error e for the axial velocity, e_{bias} for the transversal velocity and $mstd$ for both velocities, at different phases for both cases A and B are presented in table 5–1.

The results show that the overall relative error of the axial velocity for cases A and B is 7.07% and 7.68%, respectively. At some phases where the amplitude of the axial velocity is low, the relative error is higher than the overall relative error.

Table 5–2: Percentage of the overall relative error (e_t) and the average of the standard deviation ($mstd_t$) in the temporal variation of the axial velocity over all 18 phases for cases A and B at two different locations.

case A			case B		
x/λ	e_t (%)	$mstd_t$ (cm/s)	x/λ	e_t(%)	$mstd_t$ (cm/s)
3/4	4.26	1.7	5/4	4.30	1.9
5/8	5.04	1.8	9/8	6.32	2.2

The overall bias error of the measured transversal velocity is about 1.4 and 1.6 cm/s for cases A and B, respectively, which is negligible compared to the magnitude of the axial velocity. The differences between the experimental and analytical results for both axial and transversal velocities are partially related to the existence of the acoustic streaming associated with a standing wave resonator. The streaming velocity is superimposed on the acoustic velocity and its magnitude is much smaller than that of the acoustic velocity. The small values of the uncertainty in the measured axial and transversal velocities indicated by $mstd_u$ and $mstd_u$ in table 5–1, show that the experimental transversal-averaged velocity are accurate.

The synchronized PIV technique enables us to resolve the temporal variation of the particle velocity. Fig. 5–12 shows the temporal variations of the experimental and analytical axial velocities at x=$3\lambda/4$ (velocity anti-node) and x=$5\lambda/8$ for case A and x=$5\lambda/4$ (velocity anti-node) and x=$9\lambda/8$ for case B. A good agreement is observed between the experimental and analytical results for both cases. The values of the overall relative error (e_t) and the average of the standard deviation ($mstd_t$) in the temporal variation of the axial velocity over all 18 phases for cases A and B are shown in table 5–2. The results show that the relative error is on average 5%.

The good agreement between the measured and analytical acoustic velocities in both time and space domains proves the ability of the synchronized PIV technique to accurately measure both temporal and spatial acoustic velocities in a nonlinear

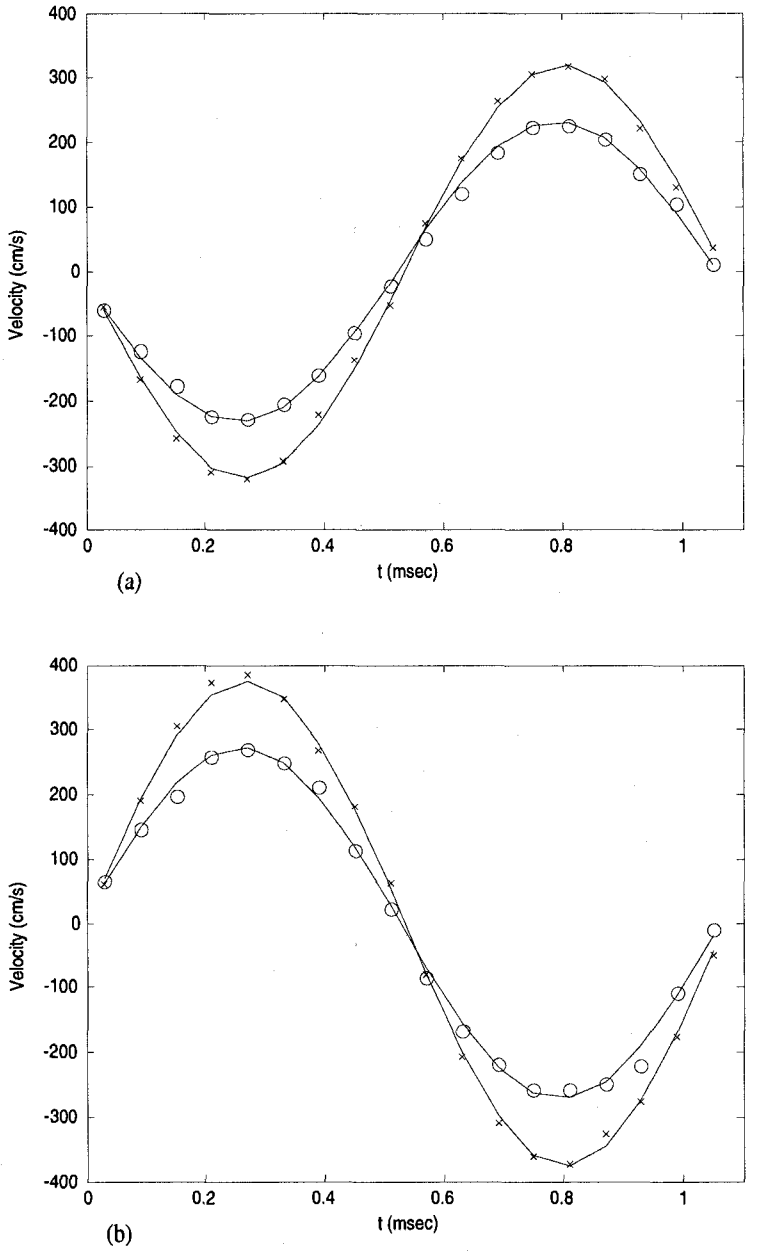

Figure 5–12: Temporal variation of the experimental (symbols) and analytical (solid line) axial velocities for **a** $u_0 = 34$ cm/s ($\times; x = 3\lambda/4$, $\circ; x = 5\lambda/8$) and **b** $u_0 = 40$ cm/s ($\times; x = 5\lambda/4$, $\circ; x = 9\lambda/8$).

standing wave tube.

5.4.3 Nonlinear standing wave case

We have presented the results for two quasi-nonlinear cases that have analytical solution in order to compare the experimental data with the theoretical results and validate the accuracy of the measurement technique. In the next set of experiment, we used the verified synchronized PIV technique to measure the acoustic velocity field of finite-amplitude nonlinear standing wave. Fig. 5–13 shows the axial variation of the particle velocity profile at four different phases. The maximum vibrational amplitude of the driver is u_0=95 (cm/s). The maximum acoustic velocity (u_{max}) in this case is 7.28 (m/s) and the corresponding Reynolds number is 1.27. Aktas and Farouk have reported the similar shape for the spatial variation of the acoustic velocity using a numerical scheme (see Fig. 2b in Ref. [100]). Fig. 5–13 also shows that for the nonlinear case, the velocity peaks move across the resonator with time, whereas they are almost fixed at the middle of the resonator in the linear case. The peak of the wave (where u has its greatest value) travels fastest and the trough (where u is least) travels slowest. Consequently, the peak tends to catch up with the trough [138]. Since in the present case the nonlinearity effects are relatively small, a slight shift in the peak locations is observed. The maximum difference between the position of the velocity peaks is about 0.1λ. This difference is also observed in the quasi-nonlinear cases (Figs. 5–10 and 5–11), although its value is smaller. The plot also shows a wavefront with high velocity gradient, which also corresponds to the high pressure gradient. The ratio between the positive and negative peaks of the wavefront changes with propagation. Such wavefront is not observed in the linear case. Thus, it can be concluded that for highly nonlinear standing waves, a wavefront with very high velocity and pressure gradients travels along the resonator.

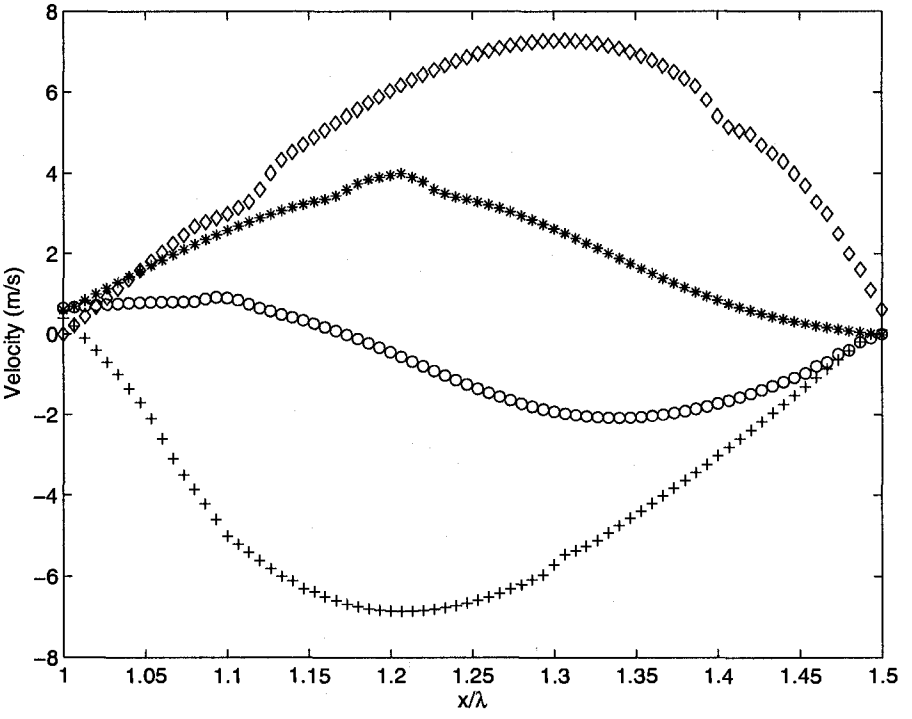

Figure 5–13: Spatial variation of the experimental axial velocities for $u_0 = 95$ cm/s at different phases, $\diamond$; t/T=0.25, $*$; t/T=0.45, $\circ$; t/T=0.55, $\times$; t/T=0.75.

5.5 Conclusions

Spatial and temporal variations of the particle velocity inside an air-filled rigid-walled square channel in the presence of finite-amplitude nonlinear standing waves are experimentally investigated. The synchronized PIV technique has been used to measure the acoustic velocity fields at 18 different phases over the excitation signal period for two different acoustic intensities. A good agreement between the experimental and analytical results in time and space domains confirms the accuracy of the method. The analysis showed that the difference between the experimental and analytical values of axial velocity is on average less than 7.68%. The verified technique is then used to measure the acoustic velocity fields of the nonlinear case at four different phases. Finally, the present study, for the first time, presents an accurate technique to measure the two-dimensional variations of the particle velocity inside

the nonlinear standing wave resonator at different phases of the excitation signal. The result shows a wavefront with high velocity gradient inside the resonator.

CHAPTER 6
Experimental Investigation of Acoustic Streaming

6.1 Introduction

The measured velocity field inside a standing-wave resonator is the superposition of acoustic and streaming velocities. The acoustic velocity is typically one to two orders of magnitude larger than the streaming velocity. As a result, in a given velocity measurement, the streaming velocity component is suppressed by the acoustic velocity component. The streaming velocity can be obtained by either removing the acoustic velocity component or conducting the velocity measurements at a location where the acoustic velocity is negligible. As the literature review (section 1.2.3) indicates, all of the reported PIV measurements of streaming velocity fields have been performed in the vicinity of a velocity node, at which the amplitude of the acoustic velocity is almost zero. In order to measure the streaming velocity fields at different locations along the resonator where the magnitude of the acoustic velocity is significant, it is necessary to find a way to remove the acoustic velocity component. In this chapter, we present a novel approach that we have developed to simultaneously measure two-dimensional acoustic and streaming velocity fields at a given wave phase using the synchronized PIV technique. Using this technique, we investigate the formation of acoustic streaming as well as the regular (classical) and irregular streaming patterns inside a standing-wave resonator. The influence of differentially heated horizontal walls on streaming shape and velocity has also been investigated.

6.2 A novel technique to simultaneously measure the acoustic and streaming velocities

The idea behind our novel technique to measure acoustic and streaming velocities simultaneously is illustrated in Fig. 6–1. This figure shows the triggering sequence used to sample velocity fields at a particular phase of the excitation signal. Consider the image taken at time t_1 as the first image and the image taken at time t_2 as the second image, with the time separation of $t_2 - t_1$. The cross-correlation of this image pair provides the acoustic velocity field at time t_1. Now, consider the image taken at time t_1 as the first image and the image taken at time t_3 as the second image, with the time separation of $t_3 - t_1$. Since the images at t_1 and t_3 are acquired exactly at the same phase, the acoustic velocity components at these instances will be the same and therefore, the particle shift between these two images will only be due to streaming velocity. Thus, the cross-correlation of this image pair will provide the streaming velocity field at time t_1. Hence, by using this novel approach, both acoustic and streaming velocity fields can be obtained simultaneously at any wave phase.

6.2.1 Measurement of high gradient streaming velocities

In the approach reported in section 6.2, the separation time between two images utilized for the streaming velocity measurement ($\delta t = t_3 - t_1$ in Fig. 6–1) is fixed and equal to inverse of the camera frame rate. However, to resolve the streaming velocity fields of high magnitudes and gradients, this value of δt might be too large. As a result, the particle shift between the first and second images of the image pair will also be large. Thus, larger interrogation window size needs to be selected which significantly reduce the spatial resolution of the measured velocity vectors. Hence, in cases where the streaming velocity fields are highly rotational or the velocity gradients are very high, the shape of the streaming patterns can not be correctly captured. Therefore, in such cases, δt needs to be adjusted accordingly.

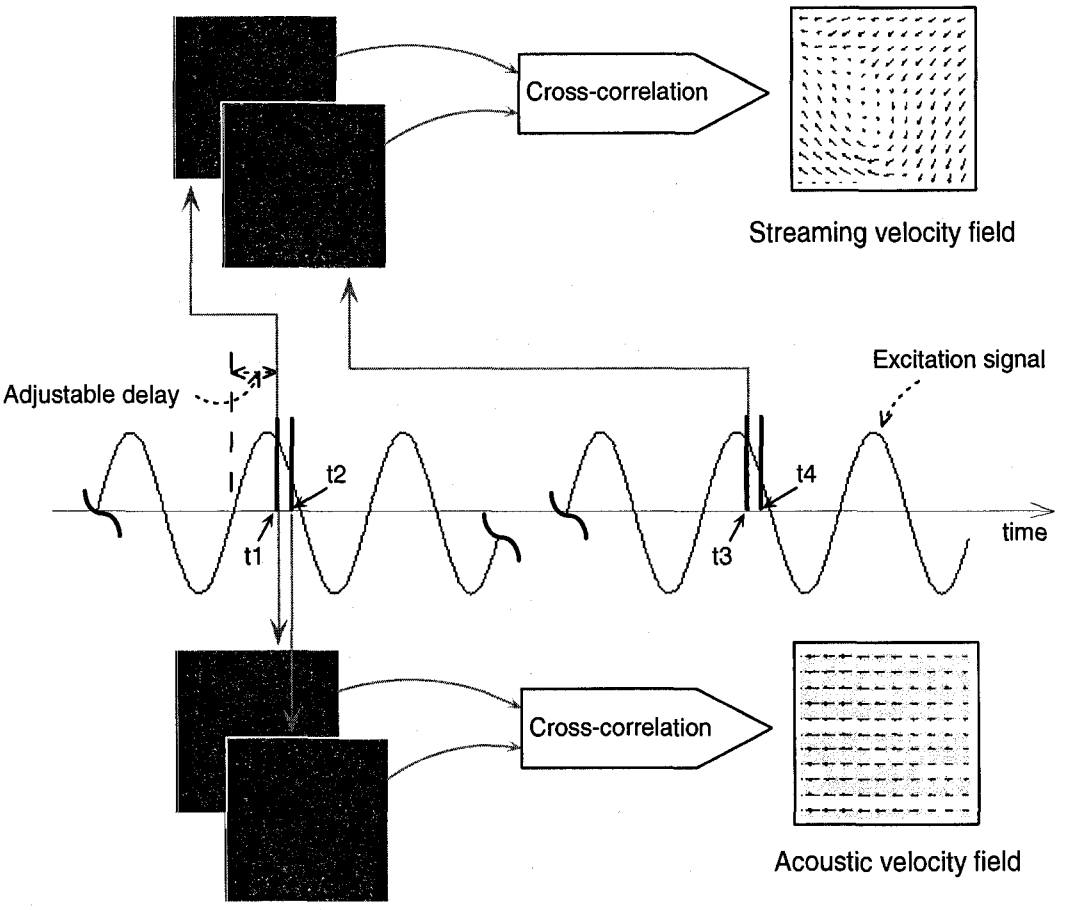

Figure 6–1: The triggering sequence that shows how the acoustic and streaming velocity fields at a particular phase of the excitation signal are extracted. t_1 to t_4 are the times at which the laser light sheet is pulsed and the flow field is imaged.

In the case of high velocity amplitude or gradient, the separation time is chosen to be an integer multiplication of the wave period (T), that is, $\delta t = nT, \;\; n = 1, 2, ..., N$ (see Fig. 6–2). N should be chosen so that $1/nT \leq$ frame rate of the CCD camera. The appropriate value of N should be determined for each experiment based on the maximum amplitude and gradient of the streaming velocity. For example, at the excitation frequency of f=1000 Hz (T= 1 msec) and camera frame rate of 30 fps, N can be varied from 1 to 33. For very high amplitude or gradient streaming flows, a small number should be chosen for N in order to reduce δt, so that the streaming patterns can be correctly captured. Whereas, for slow streaming flows, a large number should be chosen for N in order to increase the signal to noise ratio and reduce error in the

velocity measurement.

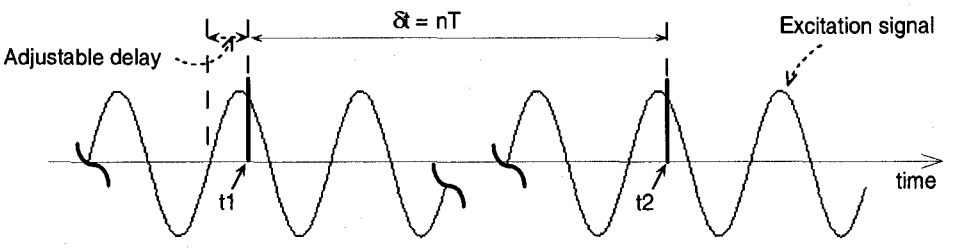

Figure 6–2: The triggering sequence that shows the measurement of the streaming velocity field at a particular phase of the excitation signal. t_1 and t_2 correspond to the times at which the first and second images of an image pair are captured.

It must be noted that the modified synchronized PIV technique described in this section is capable of measuring streaming flow of different amplitudes and gradients. The modified technique can not measure the acoustic and streaming velocity fields simultaneously, which is not matter of interest in some cases.

6.2.2 Experimental setup

The experimental setup developed to measure the streaming velocity fields inside the standing wave tube is shown in Fig. 6–3. The acoustic chamber is a Plexiglas channel with a square cross-sectional area. The channel is 74 cm long with the inner cross-section of 7 cm×7 cm. The walls of the channel are 10 mm thick. The resonator is filled with air. As shown in Fig. 6–3, the resonator is placed inside a large water tank of 50×50×90 cm dimensions, in order to completely isolate the resonator from the temperature gradients within the laboratory that can cause ambient convection velocities and affect the streaming patterns. The water temperature is $T = 22.5°C$. This allows to maintain isothermal boundary condition at the channel walls.

Although for the measurement of streaming velocity vectors, the separation time between two images is about 1/15 second ($t_3 - t_1$ in Fig. 6–1), for the acoustic velocity measurement, the separation time between two images ($t_2 - t_1$ in Fig. 6–1) must be adjusted appropriately. Due to the oscillation of the particles, the time separation

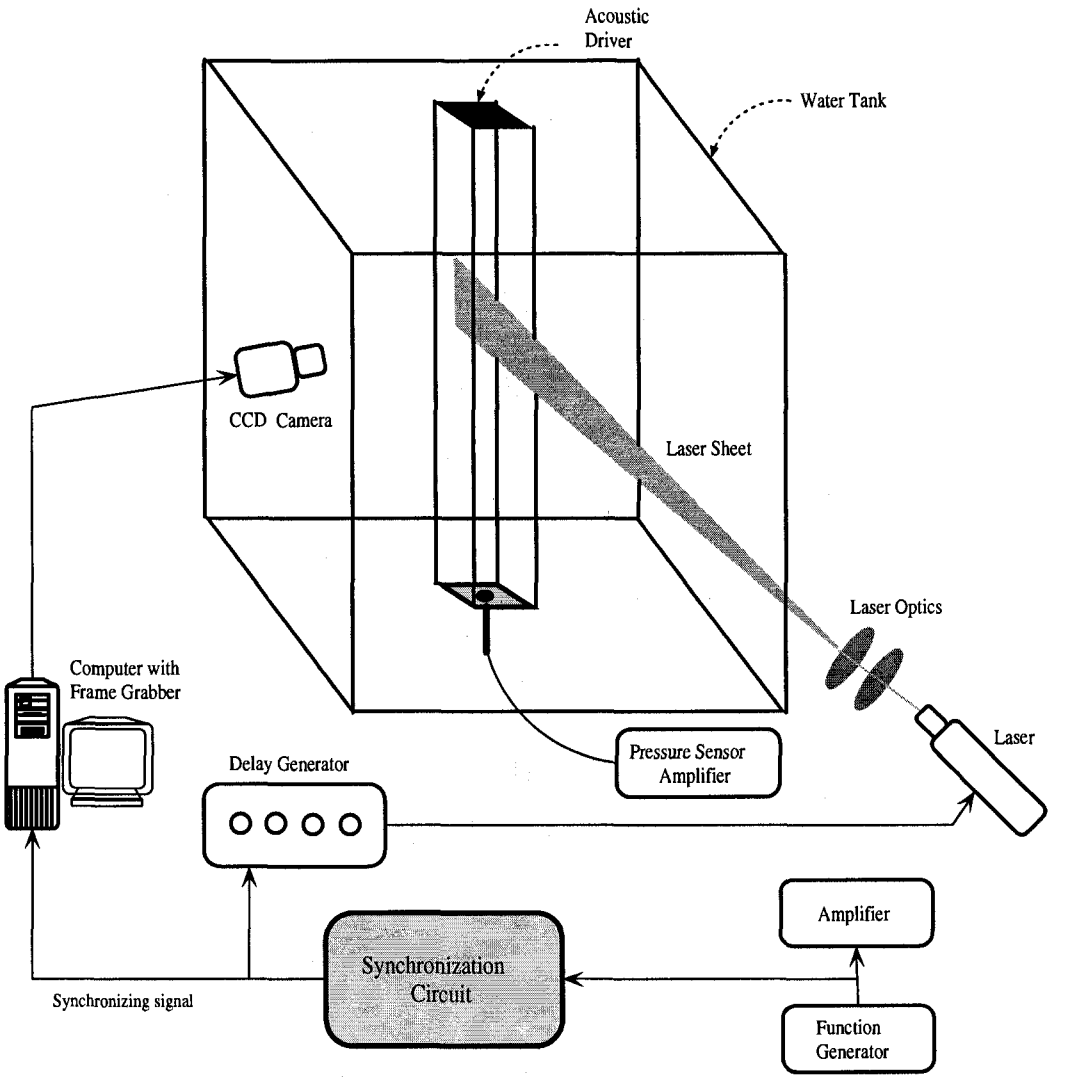

Figure 6–3: Schematic of the experimental setup and instrumentation.

between the two images of an image pair should be much less than the quarter of the time period. Otherwise, the particle displacement computed by cross-correlating the PIV images will be smaller than the actual displacement of the particles. This will result in underestimating the acoustic velocities. On the other hand, for very short separation time, the particle displacement will be too small, which will significantly increase the uncertainty in the velocity measurements. In the present case, the time separation is set equal to 50 μs, which is about four times smaller than the quarter wave period. The vertical dimension of the camera field of view is larger than the

channel height. Therefore, before computing the velocity vectors, the images are preprocessed to chop off the regions outside the channel. For PIV cross-correlation, the size of the interrogation region is set equal to 32×32 pixels and the size of the search region is set equal to 64×64 pixels. A 50% window overlap is used in order to increase the nominal resolution of the velocity field to 16 × 16 pixels. A three-point Gaussian sub-pixel fit scheme is used to obtain the correlation peak with sub-pixel accuracy.

For each set of measurements, 200 PIV images are captured. From these images, 100 acoustic velocity fields and 50 streaming velocity fields are computed using the technique described in section 5.3. A scheme is used to identify the spurious velocity vectors and then correct them using a local median test [137]. All experiments are conducted in air at 25°C. The properties of air at this condition are, $c_0 = 344$ m/s, $\rho_0 = 1.29$ kg/m^3 and $\nu = 1.56 \times 10^{-5}$ m^2/s.

6.2.3 Simultaneous measurement of acoustic and streaming velocities

In order to confirm that the velocities obtained from the given approach are accurate, the velocity characteristics from the experimental data are compared with that obtained from the analytical solution of the linear wave equation. The amplitude of the axial component of the acoustic velocity field in the linear case is given as,

$$u = u_{max} \sin(2\pi x/\lambda), \tag{6.1}$$

where $u_{max} = P_0/\rho_0 c_0$. The axial component (u_{st}) and transverse component (v_{st}) of the streaming velocity field are,

$$u_{st} = \frac{3}{8}\frac{u_{max}^2}{c}\left(1 - \frac{2y^2}{(H/2)^2}\right)\sin(\pi x/\ell), \tag{6.2}$$

$$v_{st} = -\frac{3}{8}\frac{u_{max}^2}{c}\frac{2\pi y}{\lambda}\left(1 - \frac{y^2}{(H/2)^2}\right)\cos(\pi x/\ell), \tag{6.3}$$

where $(-H/2 \leq y \leq H/2)$, H is the height of tube and $\ell = \lambda/4$ [55].

The experimental and theoretical instantaneous streaming velocity vectors for the excitation frequency of 1400 Hz and node pressure of 897 Pa, in quarter of the wavelength in which the acoustic velocity varies from zero at the velocity node ($x = 0$) to the maximum at $x = \lambda/4 = 6.125$ cm, is shown in Fig. 6–4. The streamlines are also depicted in Fig. 6–4 for better flow visualization. The plot shows that present scheme captures the streaming velocity fields very well. All 50 measurements of the streaming velocity at this phase are consistent and all streaming velocity fields at different phases are found to be similar. The instantaneous two-dimensional acoustic velocity vectors for this case over the half of the wavelength is shown in Fig. 6–5. The plot as expected, shows the maximum acoustic velocity at the velocity anti-node located at $x = \lambda/4 = 6.125$.

In order to evaluate the performance of the present approach, the theoretical and experimental values of the mean acoustic velocity and RMS streaming velocities along the resonator are quantitatively compared in Fig. 6–6. In order to compute the RMS streaming velocity, the velocity data at each axial location is extracted in the region occupied by one streaming vortex and the RMS velocity at each axial location is computed from this data. Fig. 6–6 shows that the magnitude of the streaming velocities are considerably smaller than the magnitude of the horizontal acoustic velocities which is also reported by Thompson *et al.* [55]. The plot also shows that the variation of the axial and transverse components of the streaming velocity with respect to the axial coordinate are sinusoidal. Good agreement between the theoretical and experimental results for both acoustic and streaming velocities proves the ability of the present method to measure acoustic and streaming velocities, simultaneously and accurately at any phase of the acoustic standing wave.

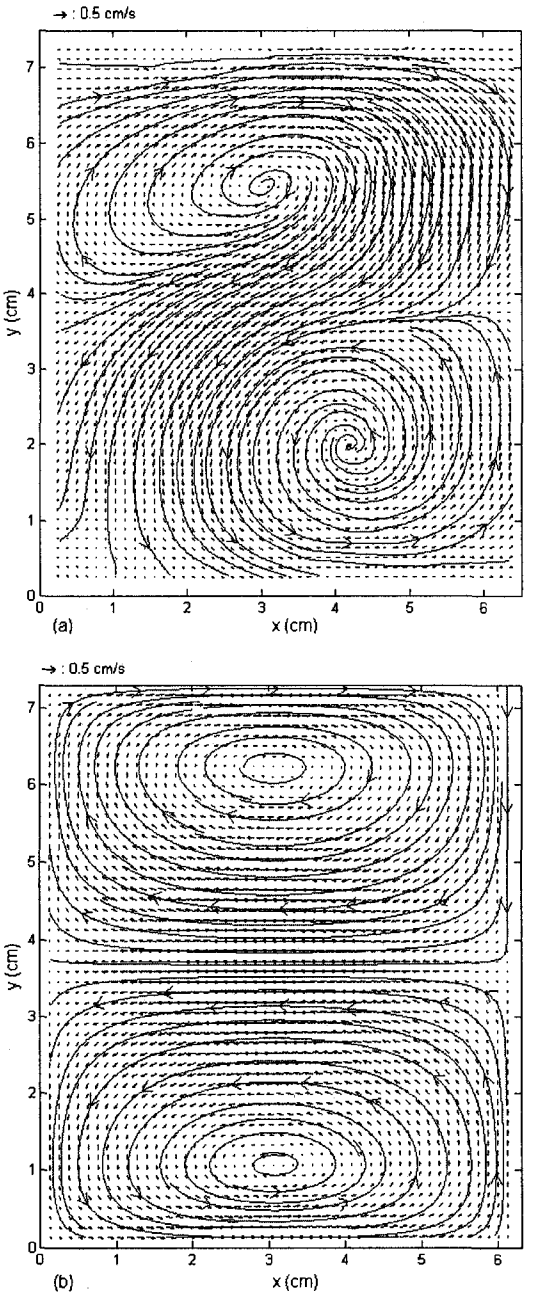

Figure 6–4: Instantaneous streaming velocity fields for the excitation frequency of 1400 Hz and node pressure of 897 Pa (Re_{s1}=30, Re_{s2}=20, and Re_{s3}=6.0) in the quarter of the wavelength at time t/T = 0.9134, where T is the period of the excitation sinusoidal signal. $x = 0$ corresponds to the velocity node and $x = 6.125$ cm corresponds to the velocity anti-node at $\lambda/4$; (a) experimental and (b) theoretical.

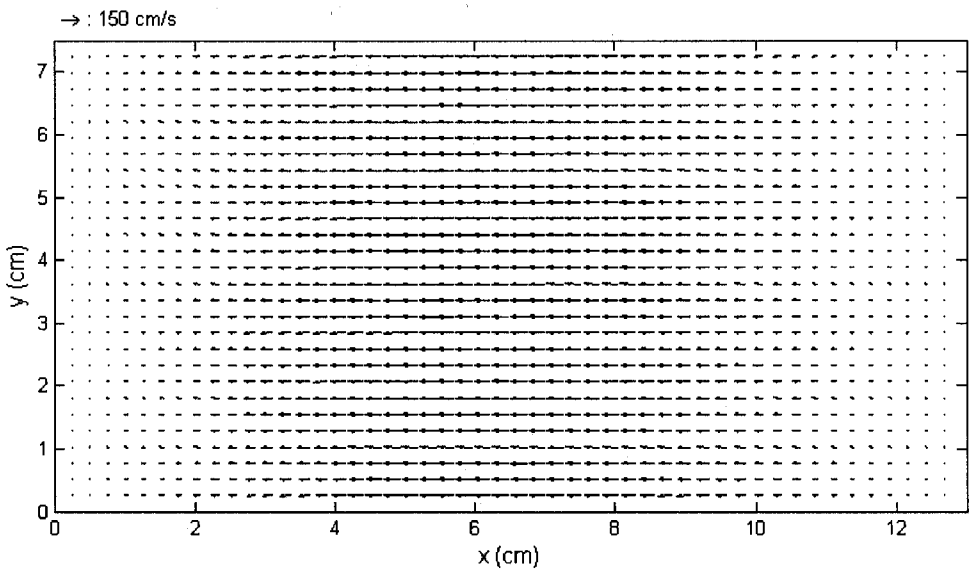

Figure 6–5: Experimental instantaneous acoustic velocity vectors for the excitation frequency of 1400 Hz and the node pressure of 897 Pa at time t/T = 0.9134. $x = 0$ and $x = 12.25$cm correspond to the velocity nodes and $x = 6.125$ cm corresponds to the velocity anti-node. Note that the resolution of the velocity vectors was reduced to half in the plot for better visualization.

6.3 Onset of acoustic streaming

As mentioned in section 6.2 and verified in section 6.2.3, two-dimensional streaming velocity fields at location along the resonator can be measured using our novel technique. In this section, for the first time, the onset (formation process) of acoustic streaming generated in an air-filled rigid-walled square channel subjected to acoustic standing waves of different frequencies and intensities is investigated experimentally using the aforementioned technique. The measurements have been performed in a Plexiglas channel of 104 cm long with the inner cross-section of 4 cm×4 cm. The walls of the channel are 10 mm thick.

For this investigation, three different excitation frequencies (f) and four different maximum vibrational displacements (X_{max}) of the acoustic driver for each frequency (i.e. 12 different cases) are considered which are summarized in Table 6–1. The half-wavelength of the acoustic standing wave (ℓ), normalized channel width (H/ℓ) and

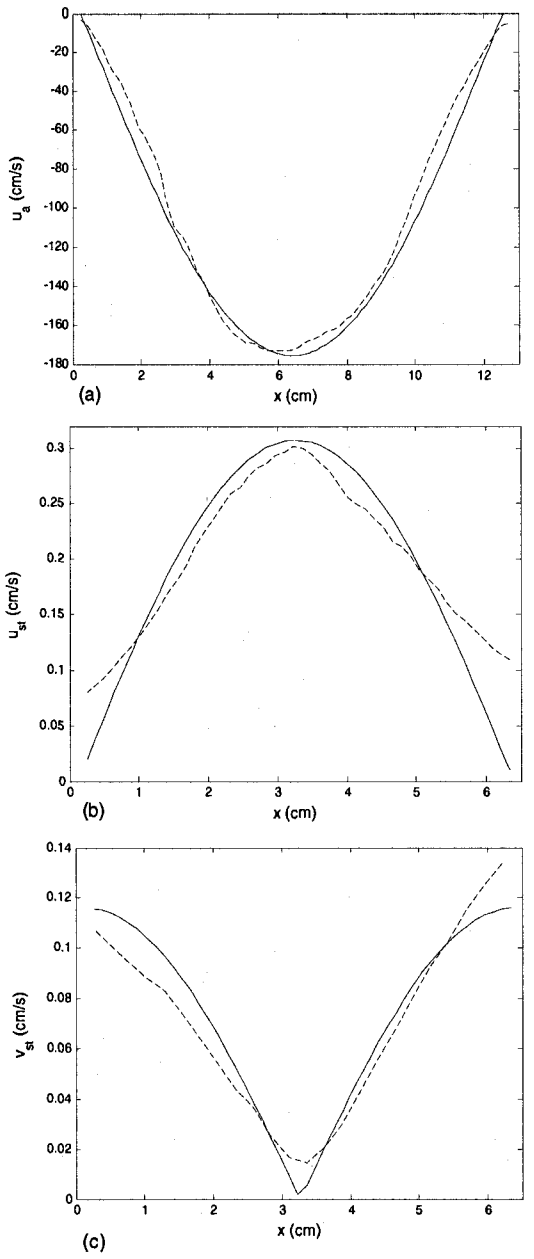

Figure 6–6: The theoretical (solid line) and experimental (dashed line) values of (a) mean acoustic velocity (u_a), (b) RMS u_{st} and (c) RMS v_{st}, along the resonator for the excitation frequency of 1400 Hz and the node pressure of 897 Pa at time t/T = 0.9134. $x = 0$ and $x = 12.25$cm correspond to the velocity nodes and $x = 6.125$ cm corresponds to the velocity anti-node. The RMS streaming velocities are computed from the upper vortex in Fig. 6–4(a).

normalized maximum vibrational displacement (X_{max}/ℓ) are also listed in Table 6–1.

In cases A-1 to A-4, the frequency of the acoustic driver is set equal to 666 Hz.

Table 6–1: The cases considered for the acoustic streaming experiments along with the details of parameters for each case. f, frequency; ℓ, half-wavelength; H/ℓ, normalized channel width; X_{max}, maximum vibrational displacement of the driver.

Case	f (Hz)	$\ell = \lambda/2$ (cm)	H/ℓ	X_{max} (μm)	X_{max}/ℓ
A-1	666	25.8	0.15	12	4.65×10^{-5}
A-2	666	25.8	0.15	23	8.91×10^{-5}
A-3	666	25.8	0.15	35	1.36×10^{-4}
A-4	666	25.8	0.15	120	4.65×10^{-4}
B-1	976	17.6	0.23	20	1.13×10^{-4}
B-2	976	17.6	0.23	28	1.58×10^{-4}
B-3	976	17.6	0.23	43	2.44×10^{-4}
B-4	976	17.6	0.23	96	5.45×10^{-4}
C-1	1310	13.1	0.3	12	9.14×10^{-5}
C-2	1310	13.1	0.3	20	1.52×10^{-4}
C-3	1310	13.1	0.3	42	3.20×10^{-4}
C-4	1310	13.1	0.3	80	6.09×10^{-4}

The half-wavelength (ℓ) of the acoustic standing wave corresponding to this frequency is 25.8 cm. It allows the formation of two full standing waves inside the channel. The field of view of the CCD camera is set in a way to map the flow field in the half wavelength section. That is, the field of view of the camera is set equal to 13.1 cm in horizontal and 9.8 cm in vertical. The maximum vibrational displacement (X_{max}) is 12 μm, 23 μm, 35 μm and 120 μm, for cases A-1 to A-4, respectively. The corresponding maximum peak-to-peak pressure amplitudes at pressure anti-node (P_{ac}) are 375, 575, 720 and 2187 Pa.

The streaming flow patterns for cases A-1 to A-4 are shown in Fig. 6–7. The streamlines are also depicted in the figure for better flow visualization. The sequence shows the impact of excitation amplitude on the structure of the streaming flow as it increases from case A-1 to case A-4. As mentioned in section 1.2.3, the classical streaming structure is typically comprised of two streaming vortices per quarter-wavelength of the acoustic wave which are symmetric about the channel center line. The plot in Fig. 6–7(a) shows that at smaller excitation amplitude (case A-1), some

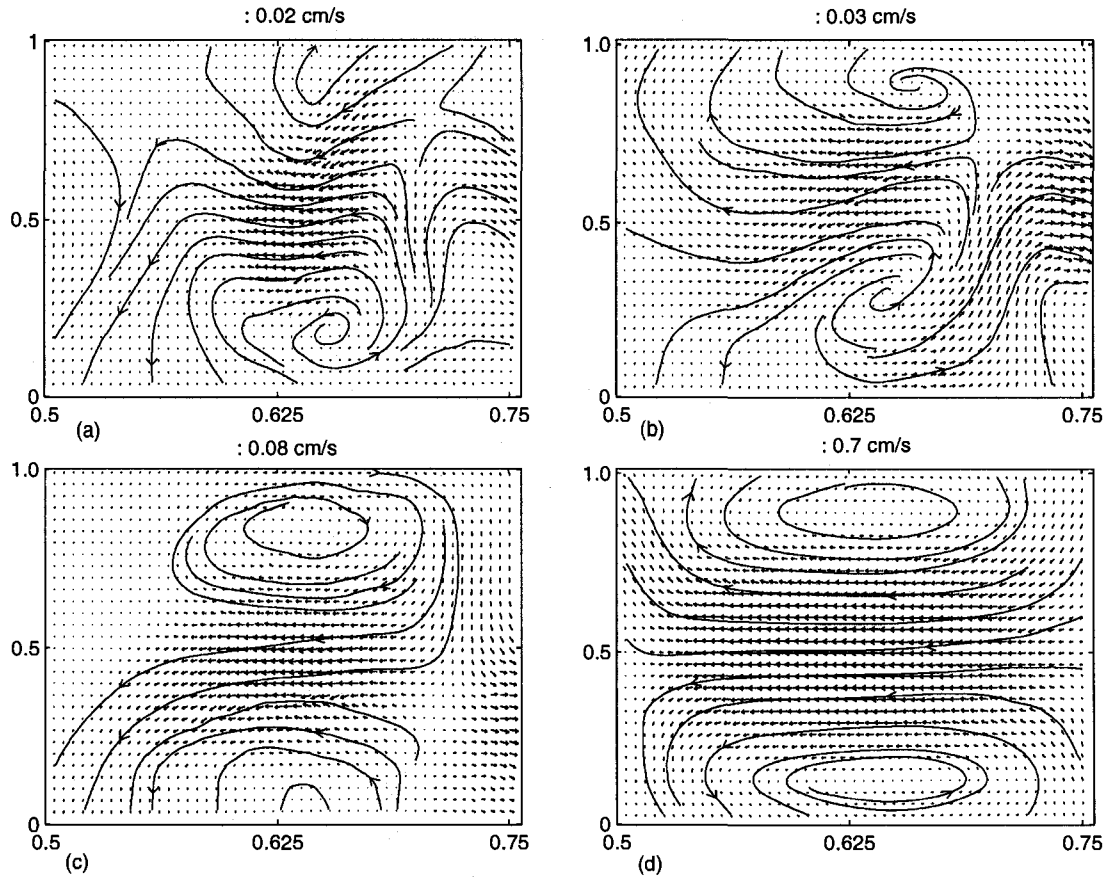

Figure 6–7: The streaming structures in the half-wavelength region for (a) case A-1, (b) case A-2, (c) case A-3, (d) case A-4. The horizontal axes are x/λ and the vertical axes are y/H. Note that the resolution of the velocity vectors was reduced to half in the plot for better visualization.

flow circulations are visible but they are not similar to the classical streaming structure. As the excitation magnitude further increased (Fig. 6–7b, case A-2), two vortices appear to be establishing themselves in the quarter wavelength. However, they are not symmetric and fully developed. At a higher excitation magnitude (Fig. 6–7c, case A-3), two classical and symmetric streaming patterns are almost established. At a further higher excitation magnitude (case A-4), the classical outer streaming vortices are fully established (see Fig. 6–7d). Kawahashi *et al.* [99] argued that the maximum vibrational displacement of the acoustic driver plays an important role in the formation of classical streaming vortices. The present results confirm their

argument. As Fig. 6–7 shows, for cases A-1 and A-2, the maximum vibrational displacement of the driver is not large enough to generate perfect classical streaming structure.

For a better qualitative observation of the streaming patterns, a sample PIV image for case A-4 is shown in Fig. 6–8. The image clearly shows two symmetric and developed Rayleigh or outer streaming vortices.

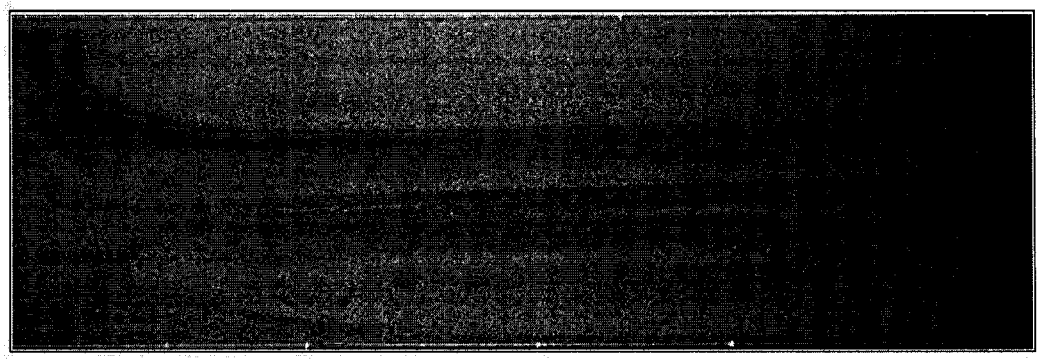

Figure 6–8: A sample PIV image for case A-4. The image dimensions are 18 cm $\times$ 4 cm.

For the next experimental set, the frequency of acoustic driver is increased to 976 Hz. This results in the formation of three full standing waves inside the channel. The field of view of the camera is set equal to 10.6 cm in horizontal and 8 cm in vertical to map the flow field in the quarter wavelength section of the channel. Four cases are considered in this set (cases B-1 to B-4) that correspond to the maximum vibrational displacement of the acoustic driver (X_{max}) equal to 20 μm, 28 μm, 43 μm and 96 μm, respectively. The maximum peak-to-peak pressure amplitudes at pressure anti-node (P_{ac}) are 500, 690, 962 and 2300 Pa for cases B-1 to B-4, respectively.

Fig. 6–9 depicts the streaming velocity fields for these four cases. As mentioned above, in the present set, the camera field of view covered the quarter wavelength. The plots show that the classical streaming structure, i.e. two symmetric vortices

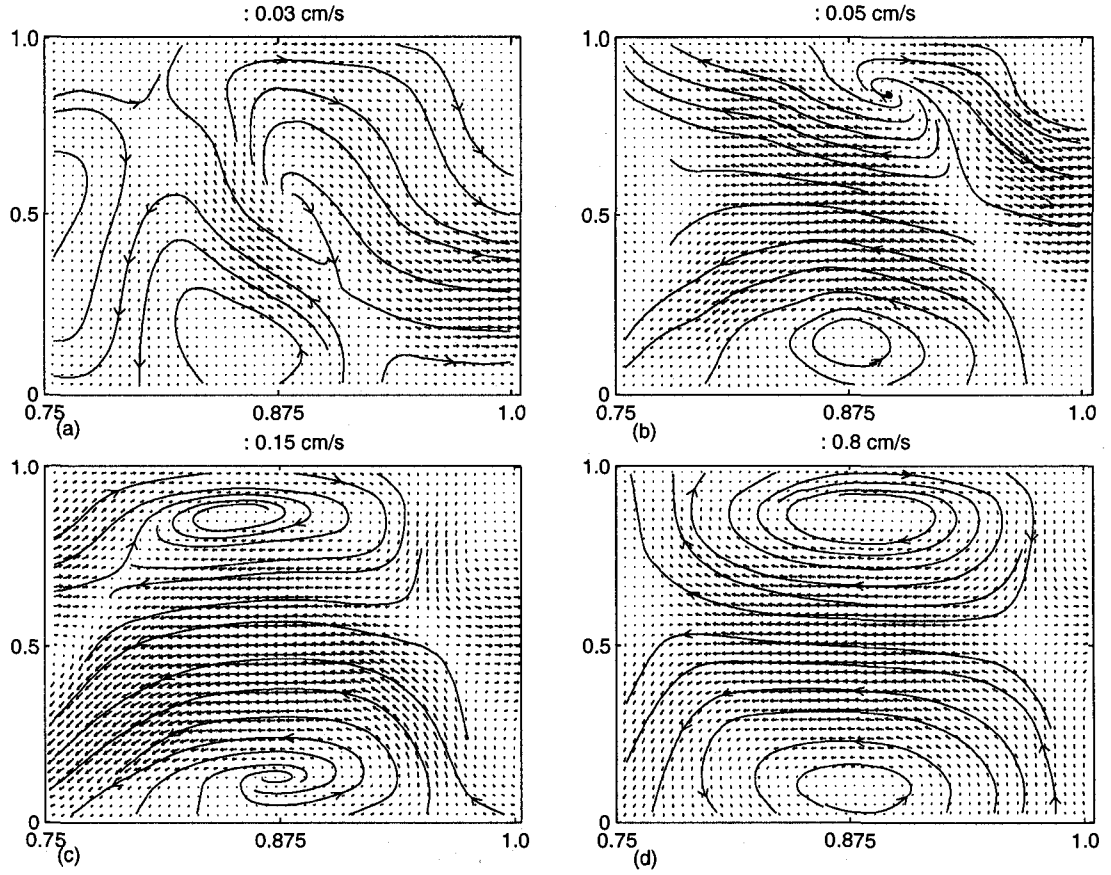

Figure 6–9: The streaming structures in the quarter-wavelength region for (a) case B-1, (b) case B-2, (c) case B-3, (d) case B-4. The horizontal axes are x/λ and the vertical axes are y/H. Note that the resolution of the velocity vectors was reduced to half in the plot for better visualization.

in quarter-wavelength is clearly observed for cases B-3 and B-4. For cases B-1 and B-2, the plot shows that the classical streaming vortices are not completely developed which would be due to the reason that the acoustic intensity is not strong enough at these cases.

The final set of experiments is conducted at the driver frequency of 1310 Hz resulting in the formation of four complete standing waves inside the channel. Four cases are considered in this set, cases C-1 to C-4 that correspond to $X_{max} = 12$ μm, 20 μm, 42 μm and 80 μm, respectively. The camera field of view is set equal to 13.1 cm in horizontal and 9.8 cm in vertical that allows to capture the streaming velocity

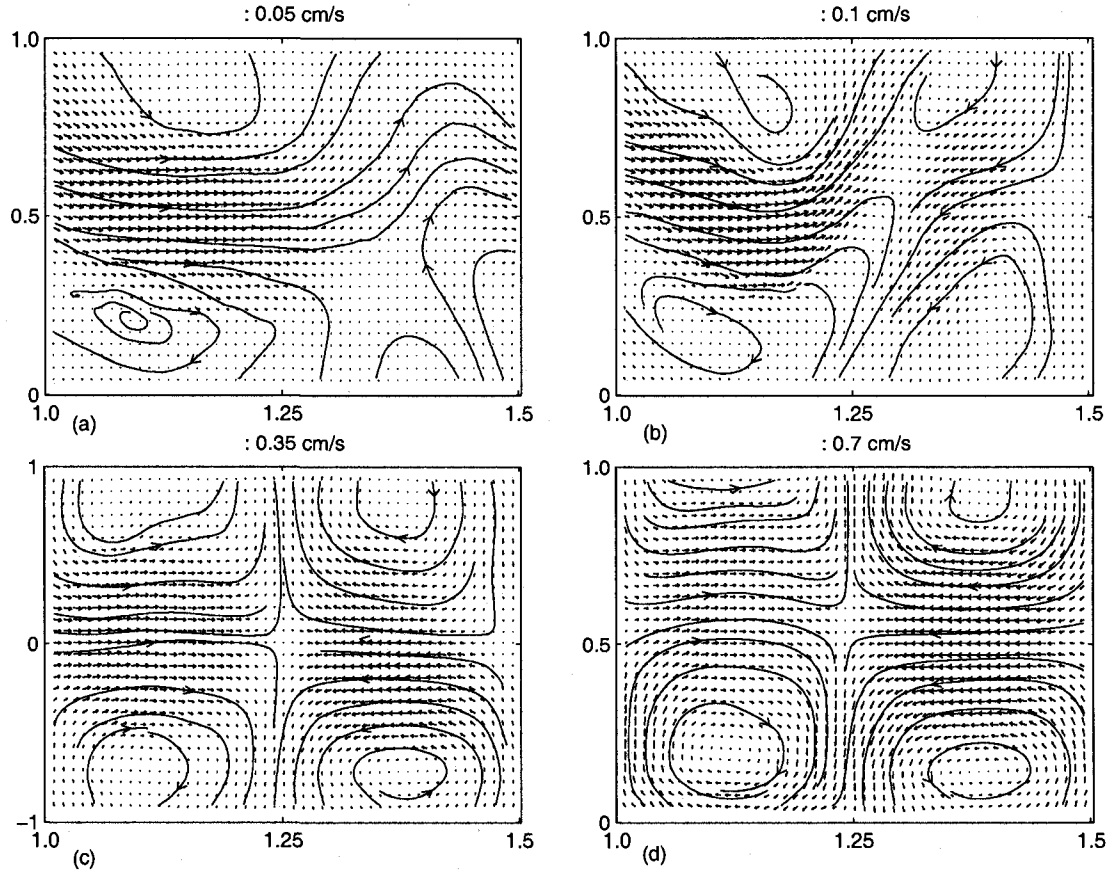

Figure 6–10: The streaming structures in the quarter-wavelength region for (a) case C-1, (b) case C-2, (c) case C-3, (d) case C-4. The horizontal axes are x/λ and the vertical axes are y/H. Note that the resolution of the velocity vectors was reduced to half in the plot for better visualization.

field in half wavelength region. The maximum peak-to-peak pressure amplitudes at pressure anti-node (P_{ac}) are 513, 812, 1375 and 2188 Pa for cases C-1 to C-4, respectively.

The streaming flow structures for cases C-1 to C-4 are shown in Fig. 6–10. The plots show that for cases C-1 and C-2, the streaming flow patterns are not developed, whereas, for cases C-3 and C-4, the classical streaming patterns are observed i.e. four vortices per half-wavelength of the standing wave which are symmetric about the channel center line. The reason for underdeveloped streaming patterns for cases C-1 and C-2 would be the same as for previous cases, i.e. X_{max} is not large enough.

The accuracy of the synchronized PIV technique to measure the streaming velocities inside the acoustic resonator has already been verified in section 6.2.3. To further confirm that the experimental streaming velocities are accurate enough, the axial component of the streaming velocities are compared with the analytical ones, defined in Eq. (6.2). The theoretical and experimental RMS axial streaming velocity (u_{strms}) along the resonator for cases A-4, B-4 and C-4 (in which the classical streaming patterns are established) are compared in Fig. 6–11. The relative error between the experimental and analytical mean values of u_{strms} for cases A-4, B-4 and C-4 are 11% and 6.5% and 10.5%, respectively. Good agreement between the analytical and experimental results confirms that the presented streaming patterns are accurate. The plots also show that the variation of the axial component of the streaming velocity with respect to the axial coordinate is sinusoidal.

We have presented the results for different excitation frequencies and amplitudes of the acoustic driver. It should be noted that for all cases considered in this study, the streaming patterns are found to be stationary and time-invariant. In the following, we have attempted to generalize the results obtained in the present study. Two frequently used definitions of the streaming Reynolds number (Re_{s1} and Re_{s3}) have been defined in Eqs. (3.22, 3.24). Aktas and Farouk [100] have used Re_{s1} in their numerical study of acoustic streaming and Thompson *et al.* [55, 108] have used Re_{s3} in their acoustic streaming measurements. Menguy *et al.* [95] have also used Re_{s3} in their numerical study of streaming. Re_{s1} and Re_{s3} for all cases considered in the present study are presented in Table 6–2. The results show that for cases A-1 to A-4 (f=666 Hz), the classical streaming is observed at $Re_{s1} > 6.43$. At f=976 Hz (cases B-1 to B-4) the classical streaming is observed at $Re_{s1} > 6.28$, whereas at f=1310 Hz (cases C-1 to C-4), it is observed at $Re_{s1} > 6.53$. Therefore, for all cases considered, the classical streaming is not developed for $Re_{s1} < 6.5$. Furthermore, as observed in Table 6–2, Re_{s3} does not appear to be an appropriate parameter to

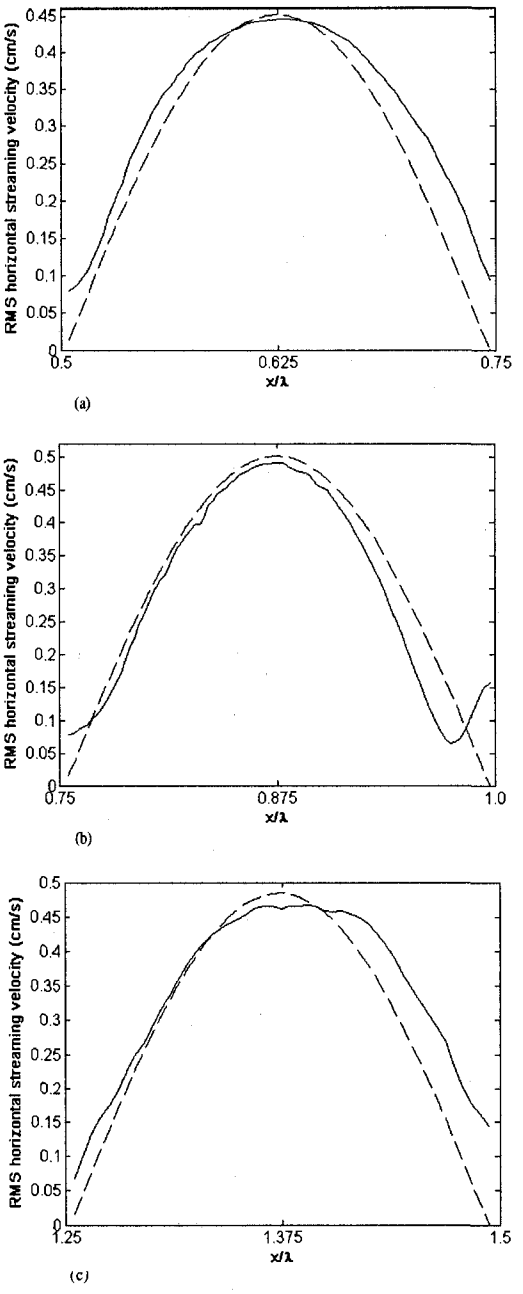

Figure 6–11: The theoretical (dashed line) and experimental (solid line) RMS of the axial component of the streaming velocity (u_{strms}) along the resonator for cases (a) A-4, (b) B-4 and (c) C-4 in which the classical streaming patterns are established.

classify non-developed and classical streaming patterns. While classical streaming is observed in case A-3 for Re_{s3}=0.91, the streaming patterns are still in developing stage at Re_{s3}=1.49 for case C-2. Thus, based on the present experimental results, it

Table 6–2: Different experimentally obtained parameters for the cases studied. P_{ac}, maximum peak-to-peak pressure; u_{max}, maximum acoustic velocity; Re_{s1} and Re_{s2}, two definitions of acoustic Reynolds number.

Case	P_{ac} (Pa)	u_{max} (m/s)	Re_{s1}	Re_{s3}	Streaming pattern
A-1	375	0.42	2.73	0.16	Non-developed
A-2	575	0.65	6.43	0.38	Non-developed
A-3	720	0.81	10.04	0.91	Classical
A-4	2187	2.46	93.0	5.51	Classical
B-1	500	0.56	3.29	0.42	Non-developed
B-2	690	0.78	6.28	0.80	Non-developed
B-3	962	1.08	12.3	1.56	Classical
B-4	2300	2.59	70.2	8.92	Classical
C-1	513	0.60	2.79	0.64	Non-developed
C-2	812	0.92	6.53	1.49	Non-developed
C-3	1375	1.55	18.7	4.28	Classical
C-4	2188	2.47	47.3	10.83	Classical

can be concluded that the streaming patterns can be classified based Re_{s1} and that the classical streaming patterns are not established at Re_{s1} <6.5.

Thompson *et al.* [55] have measured classical streaming in a channel with H=4.8 cm, u_{max}=0.81 m/s and f= 311 Hz. Based on Eq. (3.22), the streaming Reynolds number for their case is Re_{s1}=21.5. This is in agreement with the present results. Furthermore, the lowest value of Re_{s1} at which Aktas and Farouk [100] predicted classical streaming using their numerical scheme is 6.6, which is very close to our conclusion that for the classical streaming Re_{s1} should be greater than 6.53. Therefore, our experimental results are in agreement with the numerical predictions of Aktas and Farouk [100] and experimental measurements of Thompson *et al.* [55].

Finally, using the results summarized in Table 6–2, the non-developed and classical streaming flow patterns can also be classified based on the normalized channel width (H/ℓ) and the normalized maximum vibrational displacement (X_{max}/ℓ). The normalized channel width (related to the vibrational frequency) versus the normalized maximum vibrational displacement (related to both vibrational displacement and frequency) is plotted in Fig. 6–12. The symbol ($\diamond$) indicates the streaming structures

which are not developed. The classical streaming patterns are symbolized by (○). Fig. 6–12 clearly shows that both the vibrational amplitude and frequency affect the classical streaming structure. Using numerical simulations, Kawahashi *et al.* [99] and Aktas and Farouk [100] also found that the streaming structure can be affected by the vibrational amplitude and frequency. As shown in Fig. 6–12, for H/ℓ=0.15 (f=666 Hz, cases A-1 to A-4), if the normalized maximum vibrational displacement (X_{max}/ℓ) is greater than about 0.0001, we observe classical streaming structures, and for the values of X_{max}/ℓ less than this number, streaming flow patterns are in developing state and they are not completely developed. This threshold number for H/ℓ=0.23 (f=976 Hz, cases B-1 to B-4) and H/ℓ=0.3 (f=1310 Hz, cases C-1 to C-4) is about 0.00016.

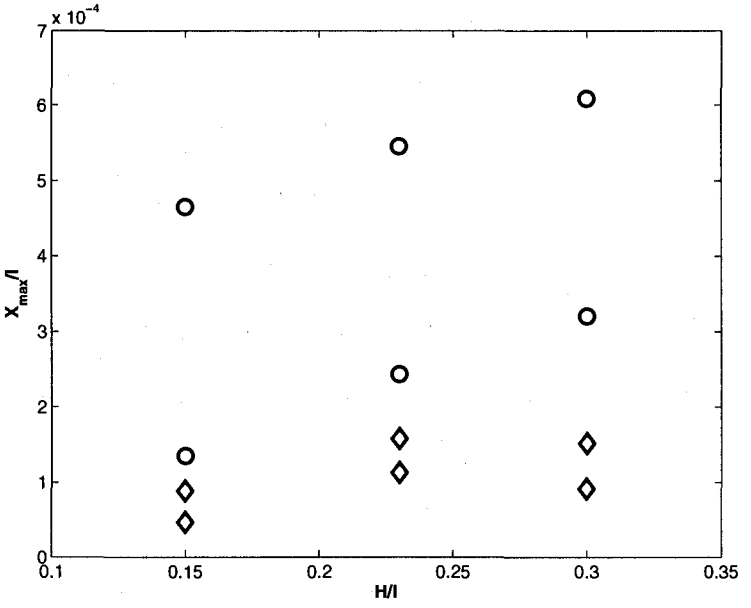

Figure 6–12: The normalized channel width (H/ℓ) versus the normalized maximum vibrational displacement (X_{max}/ℓ) for all cases; ◇, non-developed streaming structures; ○, classical streaming structures.

Table 6–3: The cases considered for the acoustic streaming experiments along with the details of parameters for each case. f, frequency; ℓ, half-wavelength; H/ℓ, normalized channel width; X_{max}, maximum vibrational displacement of the driver.

Case	f (Hz)	$\ell = \lambda/2$ (cm)	H/ℓ	X_{max} (μm)	X_{max}/ℓ
A-5	666	25.8	0.15	510	1.97×10^{-3}
A-6	666	25.8	0.15	640	2.48×10^{-3}
A-7	666	25.8	0.15	850	3.29×10^{-3}
A-8	666	25.8	0.15	1040	4.03×10^{-3}
B-5	976	17.6	0.23	120	6.81×10^{-4}
B-6	976	17.6	0.23	143	8.11×10^{-4}
B-7	976	17.6	0.23	235	1.33×10^{-3}
B-8	976	17.6	0.23	350	1.99×10^{-3}
C-5	1310	13.1	0.3	80	6.09×10^{-4}
C-6	1310	13.1	0.3	102	7.77×10^{-4}
C-7	1310	13.1	0.3	145	1.10×10^{-3}
C-8	1310	13.1	0.3	190	1.45×10^{-3}

6.4 Regular and irregular acoustic streaming

This section is devoted to the experimental investigation of the regular (classical) and irregular flow patterns of acoustic streaming generated in an air-filled rigid-walled square channel subjected to the acoustic standing waves of different frequencies and intensities. Since the irregular streaming velocity fields studied in this section have high amplitude and gradient, the modified version of synchronized PIV technique discussed in section 6.2.1 has been used to measure the streaming velocity fields.

Three different excitation frequencies (f) and four different maximum vibrational displacements (X_{max}) of the acoustic driver at each frequency are considered. That is, a total of 12 different cases which are summarized in Table 6–3. The frequency, half-wavelength of the acoustic standing wave (ℓ), normalized channel width (H/ℓ) and field of view of the CCD camera for cases A-5 to A-8, B-5 to B-8 and C-5 to C-8 are the same as for cases A-1 to A-4, B-1 to B-4 and C-1 to C-4, respectively. The normalized maximum vibrational displacements (X_{max}/ℓ) are also listed in Table 6–3.

In cases A-5 to A-8, the separation time between two PIV images of the image

pair is set equal to 20 times the wave period (T=1.5 msec) i.e. δt=30.3 msec. For the values of δt much less than this number, the particle shift between two images is not large enough to get accurate streaming velocity. Choosing $\delta t \gg 30.4$ msec, will result in losing high velocity gradient components of the streaming flow. The maximum vibrational displacement (X_{max}) is 510 μm, 640 μm, 850 μm and 1040 μm, for cases A-5 to A-8, respectively. The corresponding maximum peak-to-peak pressure amplitudes (P_{ac}) are 2469, 3094, 3844 and 4844 Pa. We took average of all 50 streaming velocity fields at each particular amplitude for better suppression of the noise.

The time-averaged streaming flow patterns for cases A-5 to A-8 are shown in Figs. 6–13(a-d), respectively. The sequence shows the impact of excitation amplitude on the structure of the streaming flow as it increases from case A-5 to case A-8. The plot in Fig. 6–13(a) shows that at smaller excitation amplitude (case A-5), two streaming vortices per quarter-wavelength are observed which are symmetric about the center line of the channel. This verifies the establishment of the classical streaming flow structure for case A-5. As the excitation magnitude increases (Fig. 6–13b, case A-6), the circular and symmetric shape of the vortices starts to degrade and can not be assumed as classical streaming flow pattern. At a higher excitation magnitude (Fig. 6–13c, case A-7), another small vortex is initiated at the left-hand side of the two main vortices which indicates that the classical streaming is no longer exists for this case. At a further higher excitation magnitude (Fig. 6–13d, case A-8), the flow pattern consists of four streaming vortices which should be considered as irregular streaming flow pattern (see Figs. 6–13d).

Aktas and Farouk [100] argued that the maximum vibrational displacement of the acoustic driver plays an important role in the formation of regular and irregular streaming flow structures. They predicted that up to a certain value of the vibrational displacement, classical and steady streaming flows are established in the

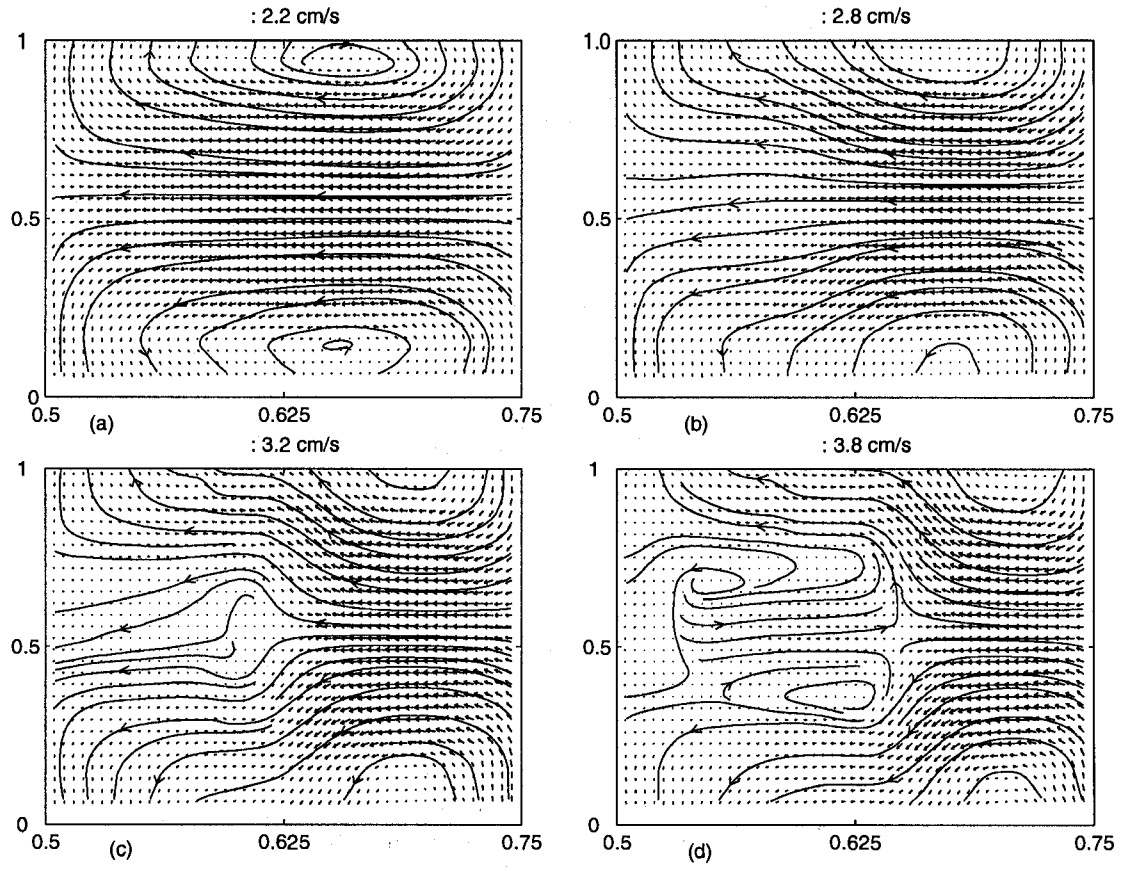

Figure 6–13: The streaming flow structures in the half-wavelength region for (a) case A-5, (b) case A-6, (c) case A-7, and (d) case A-8.The horizontal axes are x/λ and the vertical axes are y/H. Note that the resolution of the velocity vectors was reduced to half in the plot for better visualization.

acoustic resonator. However, when the vibrational displacement is increased beyond this limit, the streaming flow structures become irregular and complex. The present results confirm this by showing that the maximum vibrational displacement of the driver has a significant influence on the streaming flow patterns.

For the next experimental set (cases B-5 to B-8), the separation time between two PIV images of the image pair is set equal to 30 times the wave period (T=1.02 msec) i.e. δt=30.7 msec. Cases B-5 to B-8 correspond to the maximum vibrational displacement of the acoustic driver (X_{max}) equal to 120 μm, 143 μm, 235 μm and 350 μm, respectively. The maximum pressure amplitudes (P_{ac}) are 1437, 1780, 2844

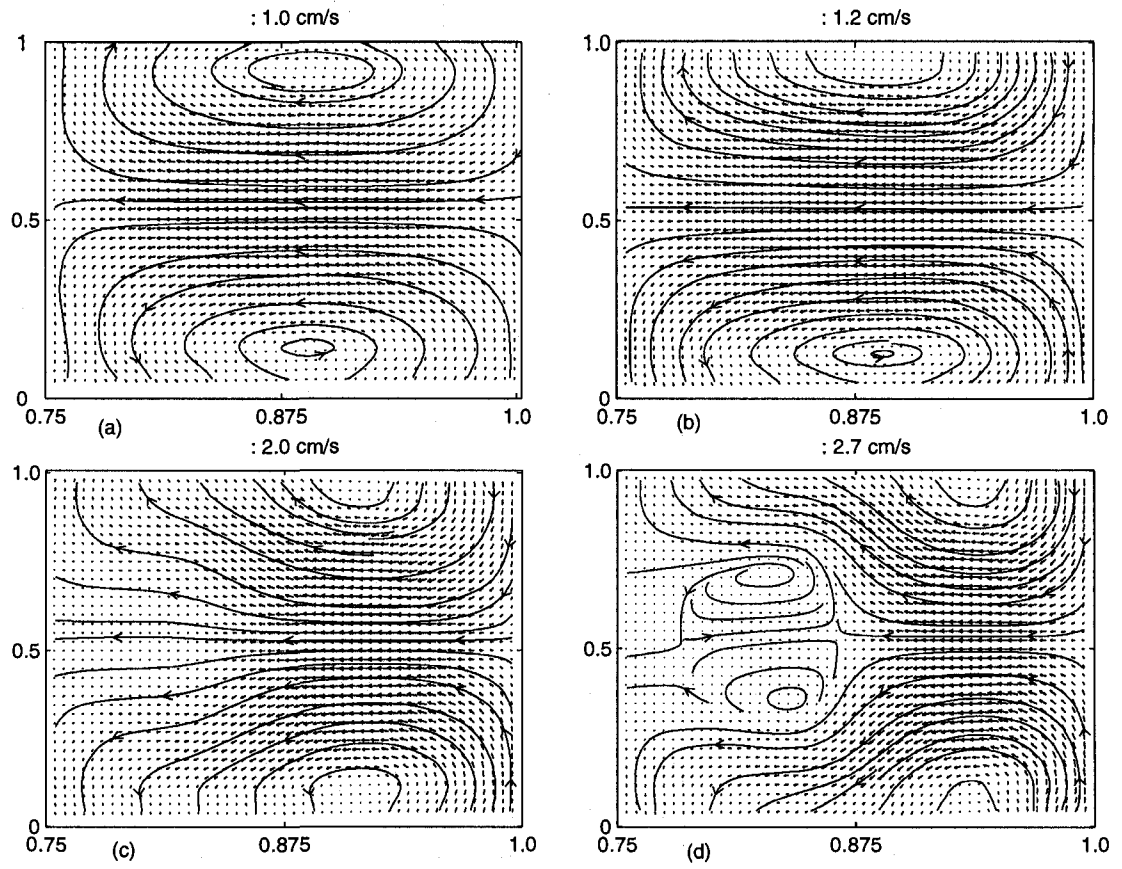

Figure 6–14: The streaming flow structures in the quarter-wavelength region for (a) case B-5, (b) case B-6, (c) case B-7, (d) case B-8. The horizontal axes are x/λ and the vertical axes are y/H. Note that the resolution of the velocity vectors was reduced to half in the plot for better visualization.

and 4375 Pa for cases B-5 to B-8, respectively.

Fig. 6–14 depicts the time-averaged streaming velocity fields for these four cases. As mentioned above, in the present set, the camera field of view covered the quarter-wavelength. The plots show that the classical streaming flow structure, i.e. two symmetric vortices in quarter-wavelength is clearly observed for case B-5. For case B-6, the plot shows that the classical streaming vortex is starting to deform into irregular shape although can still be considered as classical streaming. At a higher excitation magnitude (Fig. 6–14c, case B-7), the irregularity in the shape and number of the vortices is initiated and classical streaming is no longer exists for this case. At

further higher excitation magnitude (cases B-8, Fig. 6–14d), two small vortices are produced near the centerline which indicates that the flow pattern is clearly irregular.

The final set of experiments, cases C-5 to C-8, correspond to X_{max} = 80 μm, 102 μm, 145 μm and 190 μm, respectively. The maximum peak-to-peak pressure amplitudes at pressure anti-node (P_{ac}) reaches to 1094, 1500, 2281 and 2716 Pa for cases C-5 to C-8, respectively. The separation time between two PIV images of the image pair is set equal to 40 times the wave period (T=0.76 msec) i.e. δt=30.5 msec.

The streaming flow structure for cases C-5 to C-8 are shown in Fig. 6–15. The plots show that for cases C-5 and C-6, the classical streaming patterns are observed i.e. four vortices per half-wavelength of the standing wave which are symmetric about the channel center line. Whereas, for cases C-7 and C-8, the streaming flow patterns are clearly irregular.

The difference between the regular and irregular streaming patterns can also be examined by comparing with the theoretical streaming velocity which is valid for slow streaming. The variation of theoretical and experimental RMS of u_{st} (u_{strms}) with respect to the axial coordinate x for cases B-5 (Re_{s2}=16.1, regular streaming) and B-8 (Re_{s2}=149.7, irregular streaming) are quantitatively compared in Fig. 6–16(a). The variation of theoretical and experimental values of u_{st} with respect to the transverse coordinate y for cases B-5 and B-8 at three axial positions ($x = \lambda/4, \lambda/2$, and $3\lambda/4$) are shown in Figs. 6–16(c-d). For the classical streaming case (left-hand side plots in Fig. 6–16), the shape of experimental results is similar to the theoretical ones which confirms the presence of regular streaming patterns. However, the maximum amplitudes of the experimental velocities are lower than the theoretical ones. This is due to this fact that the theoretical values are valid only for slow streaming (Re_{s2} <1), whereas, for case B-5, Re_{s2}=16.1. Thompson *et al.* [108] used LDA to measure u_{strms} with respect to x and the u_{st} with respect to y in a resonator with isothermal boundary condition for Re_{s2}=4, 10, 20 and 40. They also observed that as the streaming

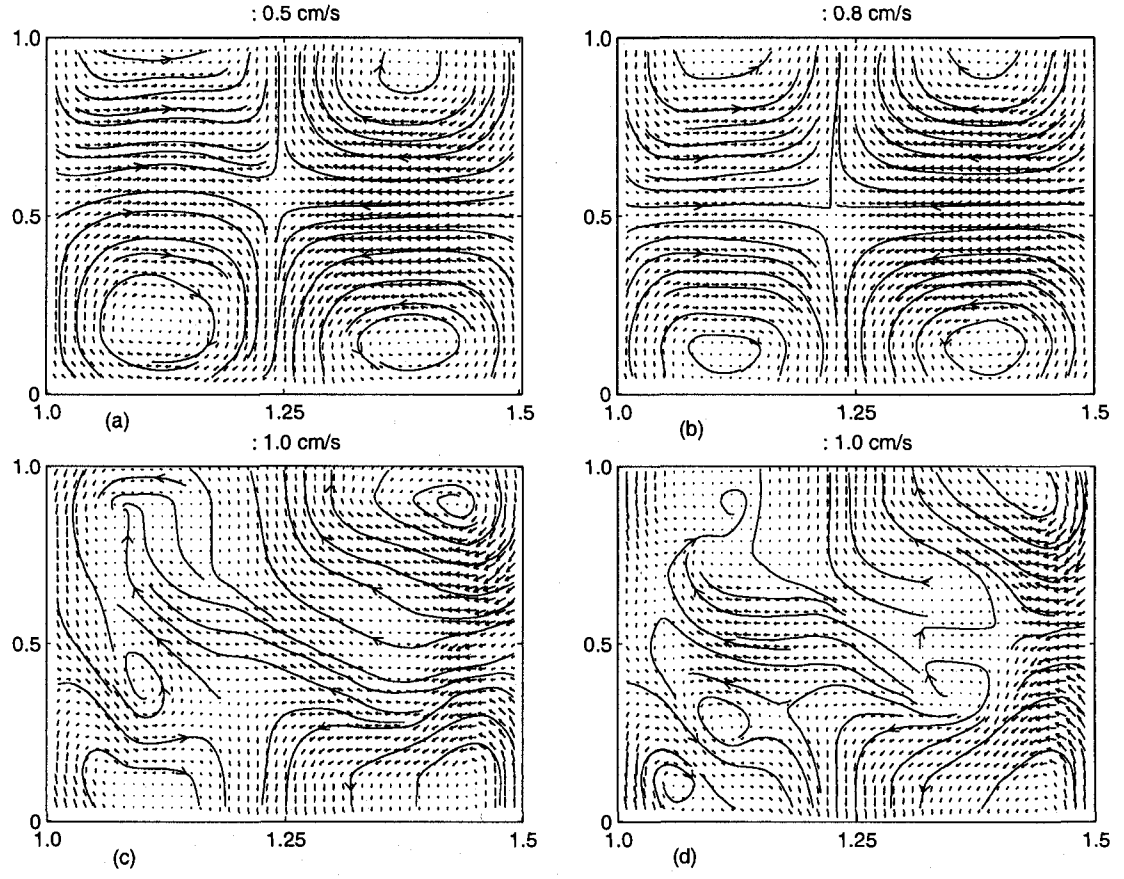

Figure 6–15: The streaming flow structures in the quarter-wavelength region for (a) case C-5, (b) case C-6, (c) case C-7, (d) case C-8. The horizontal axes are x/λ and the vertical axes are y/H. Note that the resolution of the velocity vectors was reduced to half in the plot for better visualization.

Reynolds number increases, the experimental acoustic velocities get smaller than the theoretical ones. The amplitudes of the experimental velocities close to the top and bottom walls are not in agreement with the theoretical ones. The reason is that the field of view of the camera is set to cover the whole quarter-wavelength (10.3 cm). Therefore, the resolution of PIV velocity vectors is not high enough to resolve the near wall region velocities.

For the irregular streaming case (case B-4, Re_{s2}=149.7, right pane of Fig. 6–16), the shape of experimental velocities with respect to x and y are significantly deviated from that of the theoretical ones which confirms the presence of irregular streaming

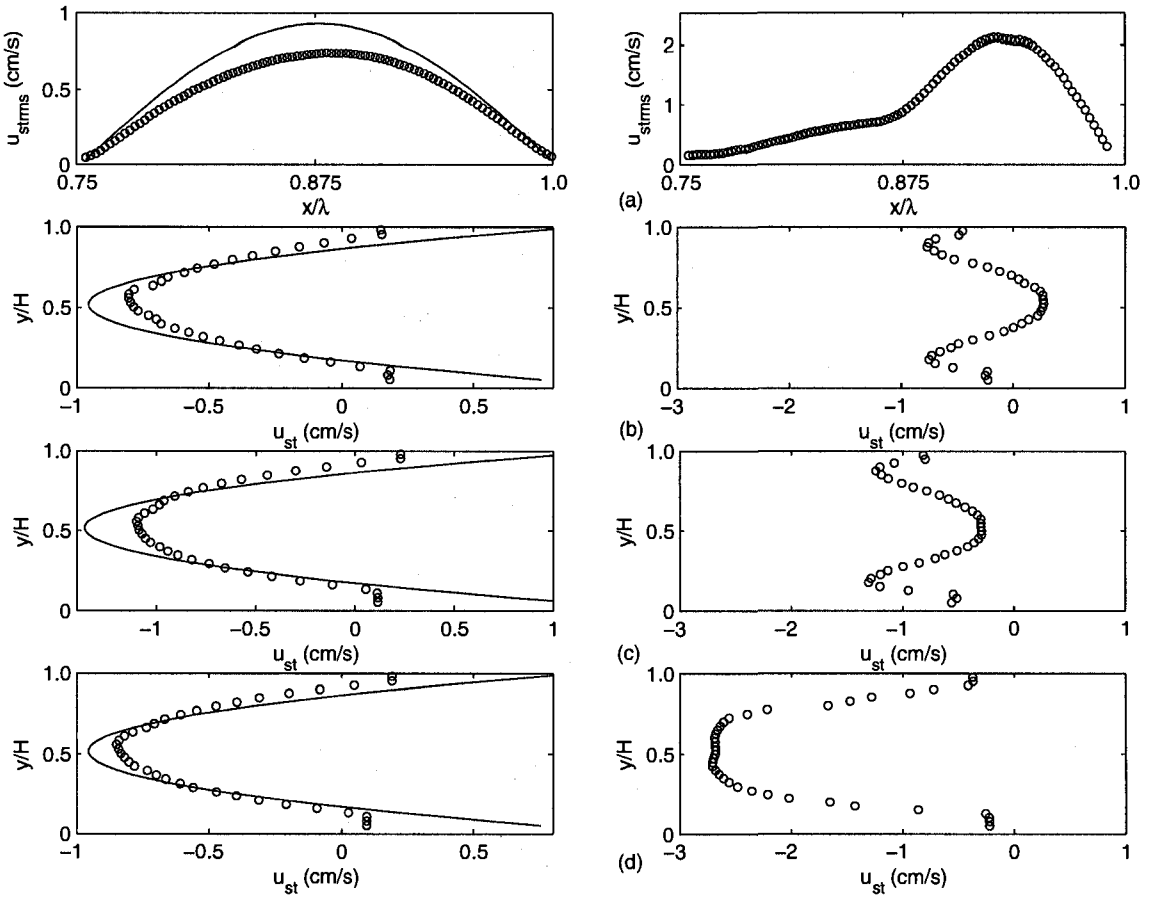

Figure 6–16: (a) The variation of theoretical (solid line) and experimental (○) root-mean-square (RMS) of u_{st} (u_{strms}) with respect to the axial coordinate x. The variation of theoretical and experimental values of u_{st} with respect to the transverse coordinate y for cases B-5 (Re_{s2}=16.1, regular streaming), left-hand side; and case B-8 (Re_{s2}=149.7, irregular streaming), right-hand side, at three axial positions (b) $x = \ell/4$ (c) $x = \ell/2$ and (d) $x = 3\ell/4$.

patterns. According to Fig. 6–16, the peak of u_{strms} with respect to x is shifted away from the typical location (see Figs. 6–13a,b), and the experimental values of u_{st} with respect to y tend to zero in the center of the the channel. Negative amplitudes of u_{st} with respect to y are observed at $x = \ell/4$ (see right pane of Fig. 6–16b). This is due to existence of two small vortices at this location (see Fig. 6–13d). In addition to shape, the amplitudes of the axial streaming velocities are much lower than the theoretical ones. Linear theory (Eq. 6.2) predicts 8.2 cm/s for the maximum of u_{strms} with respect to x and 9 cm/s, 12.5 cm/s and 9 cm/s for the the maximum of u_{st} with

Table 6–4: Different experimentally obtained parameters for the cases studied. P_0, maximum pressure; u_{stmax}, maximum streaming velocity; u_{max}, maximum acoustic velocity; Re_{a1}, acoustic Reynolds number; Re_{s1} and Re_{s2}, streaming Reynolds numbers.

Case	P_0 (Pa)	u_{max} (m/s)	Re_{a1}	Re_{s1}	Re_{s2}	Streaming pattern
A-5	2469	5.98	31512	548	32.5	Regular
A-6	3094	7.49	39470	861	51.0	Irregular
A-7	3844	9.31	49060	1328	78.6	Irregular
A-8	4844	11.74	61856	2109	124.8	Irregular
B-5	1437	3.48	12514	127	16.1	Regular
B-6	1780	4.31	15498	194	24.7	Regular
B-7	2844	7.41	24692	496	64.1	Irregular
B-8	4375	10.6	38116	1174	149.7	Irregular
C-5	1094	2.66	7126	54	12.6	Regular
C-6	1500	3.63	9425	104	23.6	Regular
C-7	2281	5.53	14815	238	54.4	Irregular
C-8	2716	6.58	17628	337	77.2	Irregular

respect to y at $x = \ell/4, \ell/2$, and $3\ell/4$, respectively, which are significantly larger than the measured values. This behavior can not be explained by the linear theory of acoustic streaming.

Different experimentally measured parameters for the cases studied, along with the remarks that whether the regular or irregular streaming is observed for the corresponding cases, are presented in Table 6–4. Using the results summarized in Table 3–2, we can classify regular and irregular streaming flow patterns based on the normalized channel width (H/ℓ) and the normalized maximum vibrational displacement (X_{max}/ℓ).

The normalized channel width (related to the vibrational frequency) versus the normalized maximum vibrational displacement (related to both vibrational displacement and frequency) for the cases studied are plotted in Fig. 6–17. This figure clearly shows that both the vibrational amplitude and frequency affect the classical streaming structure. Using their numerical models, Kawahashi *et al.* [99] and Aktas

and Farouk [100] also found that the streaming structure can be affected by the vibrational amplitude and frequency. Fig. 6–17 also shows that as H/ℓ increases, the transition from regular to irregular streaming occurs at lower values of X_{max}/ℓ. It is also observed that the relationship between H/ℓ and X_{max}/ℓ at which the transition occurs is nonlinear. We have attempted to establish this relationship through best fit to the data points of the lower bound where the irregular streaming patterns form. The relationship is found to be $X_{max}/\ell = a(H/\ell)^2 + b(H/\ell) + c$, where a=0.0739, b=-0.0425, and c=0.0072 (dashed line in Fig. 6–17). Since this equation is based on three data points which is the minimum number of data points to establish nonlinear equation, more future experiments at different frequencies and amplitudes are needed to confirm the validity of this equation.

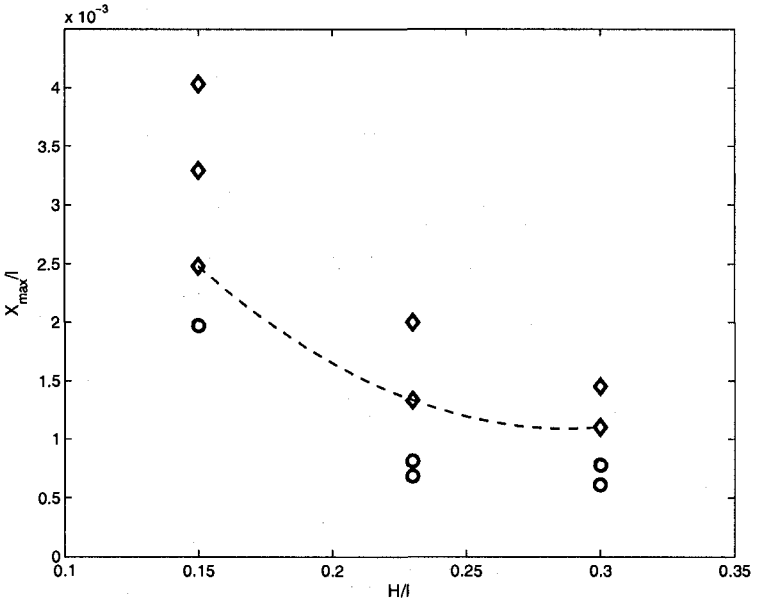

Figure 6–17: The normalized channel width (H/ℓ) versus the normalized maximum vibrational displacement (X_{max}/ℓ) for all cases; ○, regular streaming structures; ◇, irregular streaming structures.

In the following, we have attempted to generalize the results obtained in the present study in terms of a dimensionless parameter. The values of Re_{a1} and Re_{s1} (Eqs. 3.20 and 3.22) for all cases considered in the present study are presented in

Table 6–4. The results show that Re_{a1} and Re_{s1} are not appropriate parameters to classify the streaming flow patterns. Using their numerical simulation, Aktas and Farouk [100] also found that the regular and irregular streaming patterns can not be classified based on Re_{a1} and Re_{s1} which is consistent with the present experimental results.

The values of Re_{s2} (Eq. 3.23) for all cases are also presented in Table 6–4. The results show that at f=666 Hz (cases A-5 to A-8) the irregular streaming is observed at $Re_{s2} \geq$51. At f=976 (cases B-5 to B-8) Hz, the irregular streaming is observed at $Re_{s2} \geq$64. , whereas at f=1310 Hz (cases C-5 to C-8), it is observed at $Re_{s2} \geq$54. Therefore, it is inferred that whereas, Re_{a1} and Re_{s1} are not appropriate parameters to classify the regular and irregular streaming patterns, Re_{s2} can be used for this classification. Using their numerical model, Menguy *et al.* [95] also predicted that the nonlinear effect is controlled by the dimensionless number Re_{s2}. They argued that as Re_{s2} increases, the axial streaming velocity is distorted due to the inertia effect. Thompson *et al.* [108] measured streaming velocities for f=310 Hz for isothermal boundary condition using LDA. They observed classical streaming behavior for 4 $< Re_{s2} <$ 40. The results of these numerical and experimental studies are consistent with our experimental findings. Based on the results summarized in Table 6–4, it can be concluded that the irregular streaming patterns are observed at $Re_{s2} >$ 50.

6.5 Influence of differentially heated horizontal walls on streaming shape and velocity in a standing wave resonator

As mentioned in section 1.2.3, the influence of the axial temperature gradient on acoustic streaming has been extensively studied analytically [107], numerically [16] and experimentally [108]. However, the influence of transverse temperature gradient on acoustic streaming have been scarcely investigated. Very recently, only one study has numerically investigated this behavior [109]. In this section, the influence of differentially heated horizontal walls on shape and amplitude of acoustic streaming

velocity field inside a gas-filled rectangular enclosure subjected to acoustic standing wave are investigated experimentally. The synchronized PIV technique has been used to measure the streaming velocity fields.

The driver frequency is set equal to f=976 Hz. The maximum acoustic pressure is 775 Pa which corresponds to the maximum vibration displacement of 65 μm of the acoustic driver. In this study, we have considered four different thermal boundary conditions which are ΔT=0 (isothermal), $\Delta T = 0.3°C$, $\Delta T = 0.8°C$, and $\Delta T = 3°C$, where ΔT is the temperature difference between the bottom and the top walls. To achieve isothermal boundary condition, the resonator is placed inside a large water tank of dimensions 50×50×90 cm. In order to achieve differentially heated horizontal walls, the resonator is placed on top of an aluminum plate (150×10×2 cm). The surface of the aluminum plate of the test section is coated black with high temperature paint to minimize the laser reflection. Two electric strip heaters is attached to the bottom of the aluminum plate. Five thermocouples are placed along the aluminum plate to act as a feedback to the PID control system. This ensured constant and uniform wall temperature along the plate.

A sample PIV image for each of the four cases is shown in Fig. 6–18. The corresponding streaming flow patterns are shown in Fig. 6–19. The streamlines are also depicted in Fig. 6–19 for better flow visualization. For isothermal case (Fig. 6–19a), two streaming vortices per half-wavelength of the acoustic wave are observed which are symmetric about the channel center line. As the bottom wall is slightly heated ($\Delta T = 0.3°C$, Fig. 6–19b), the bottom vortex vertically expanded while the top vortex vertically contracted. As the temperature difference further increased ($\Delta T = 0.8°C$ Fig. 6–19c), the top vortex is completely disappeared. Once the top vortex is disappeared, it is found that a further increase in ΔT has no significant effect on the streaming flow structure. These results provided the first experimental

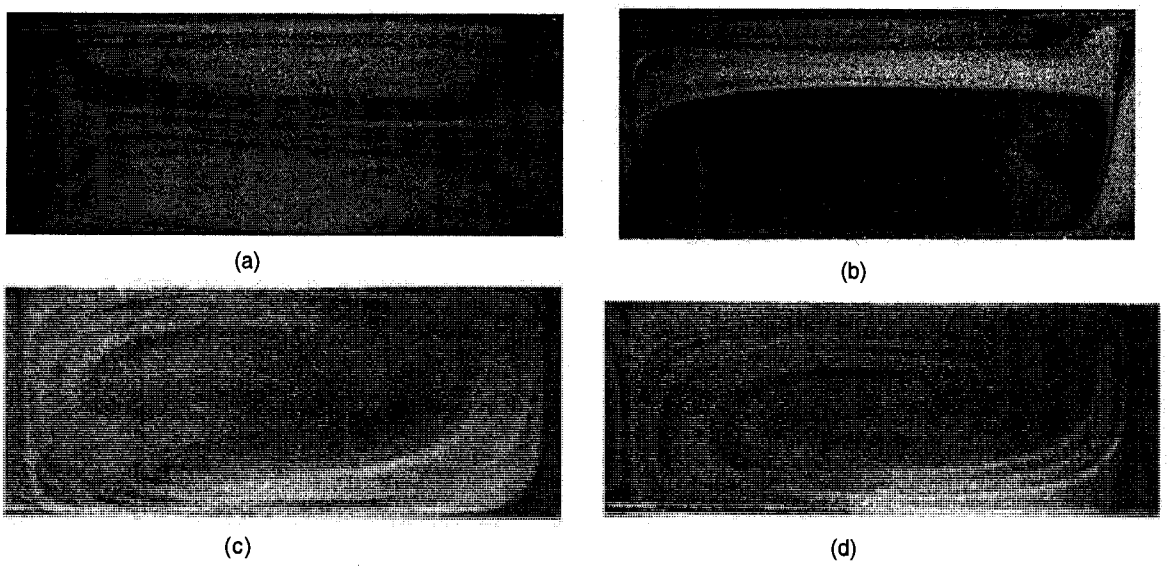

Figure 6–18: sample of PIV image for (a) $\Delta T = 0°C$, (b) $\Delta T = 0.3°C$, (c) $\Delta T = 0.8°C$, and (d) $\Delta T = 3°C$.

evidence of the influence of transverse temperature gradient on the transitional behavior of the streaming flow structure. The results also indicate that the transition could occur at small values of ΔT.

The influence of the transverse temperature gradient on the magnitude of the steaming velocity field is quantified in terms of the RMS axial streaming velocities. The results are plotted in Fig. 6–20 for all cases. The plot shows that as ΔT increases, the streaming velocity magnitude increases. The higher temperature at the bottom wall induces convective motion in the flow domain. Fig. 6–19 shows that once the transition occurred, the streaming patterns remains the same (for $\Delta T = 0.8°C$ and $3°C$), however, as shown in Fig. 6–20, the streaming velocity magnitude increased by 80%. These results indicate that the convective currents are aligned with the streaming flow patterns.

In summary, it is concluded that both structure and velocity amplitude of the acoustic streaming are changed drastically when one horizontal wall temperature is increased. Since this temperature difference causes nonuniform fluid properties, the symmetry of the acoustic streaming patterns is degraded by the differentially heated

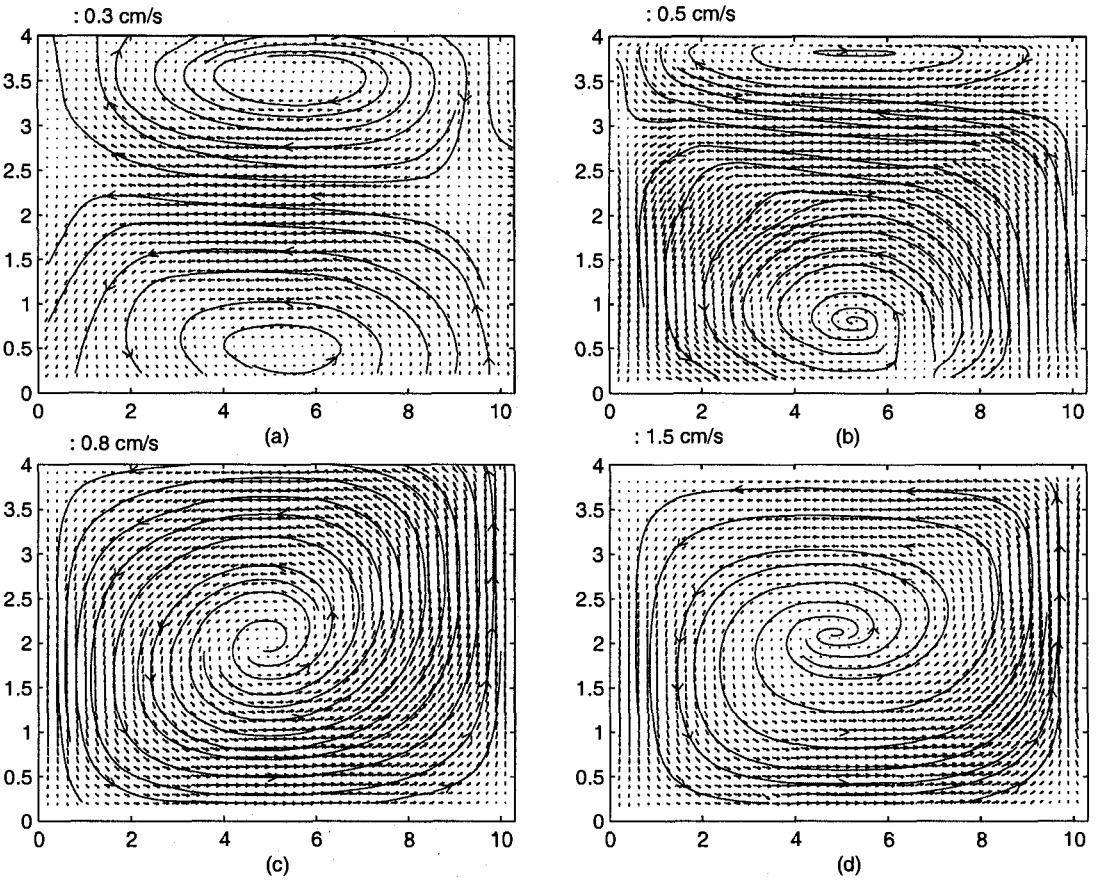

Figure 6–19: The streaming structures in the half-wavelength region of the resonator for (a) $\Delta T = 0°C$, (b) $\Delta T = 0.3°C$, (c) $\Delta T = 0.8°C$, and (d) $\Delta T = 3°C$. $x = 0$ corresponds to the velocity node and $x = 10.3$ cm corresponds to the velocity anti-node at $\lambda/4$.

horizontal walls. Therefore, the shape and velocity amplitude of the the acoustic streaming can be changed by both differentially heating of the walls and increasing the excitation amplitude of the driver.

6.6 Conclusions

Simultaneous measurement of the acoustic and streaming velocity vectors along a resonator is investigated. A novel approach is used for extracting the streaming velocity fields. In this approach, the velocity fields are sampled at a given phase of the excitation signal. This phase can be adjusted to covers the whole period of the

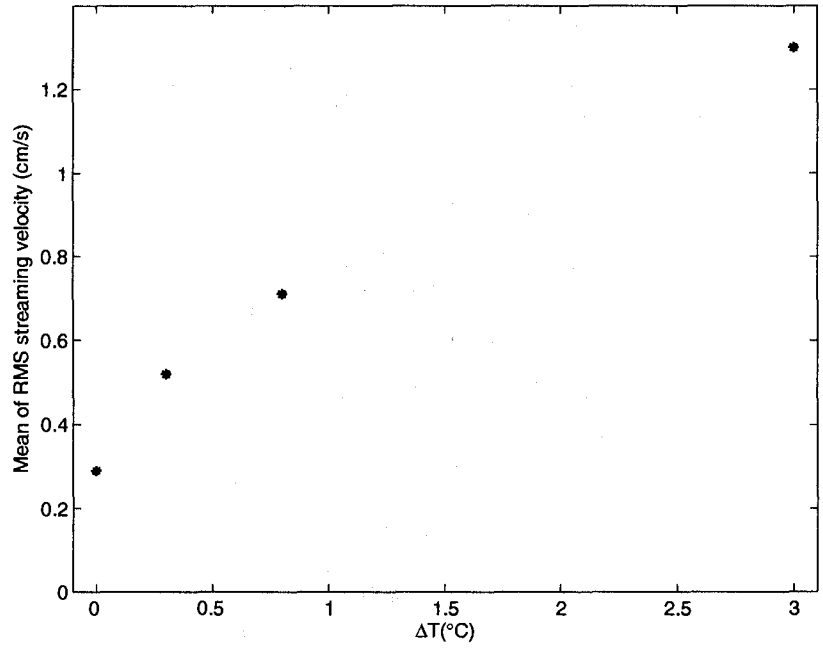

Figure 6–20: The experimental values of the RMS streaming velocities along the resonator versus ΔT.

excitation waveform. Despite all reported PIV measurements of streaming in which the measurements have been performed in the vicinity of the velocity node (where acoustic velocities are almost zero), the present technique enables the measurement of the streaming velocities at any location along the standing wave resonator in the presence of large amplitude acoustic wave. The results show that the given approach accurately captures the structure of the streaming velocity fields. The comparison of the experimental values of the mean acoustic velocity and RMS streaming velocities with the theoretical ones confirms the accuracy of the present approach.

The formation of acoustic streaming velocity fields in an air-filled rigid-walled square channel subject to acoustic standing waves is also investigated using the synchronized PIV technique. The resonator has been put inside a large water tank in order to completely isolate the resonator from the temperature gradients within the laboratory that can cause ambient convection velocities. The effects of the frequency

and maximum vibrational displacement of the acoustic driver on the streaming structure are studied. The results show that for a given vibrational frequency, classical streaming structures are only observed when the vibrational displacement of the acoustic driver is sufficiently large. The results also indicate that, whereas Re_{s3} does not appear to be an appropriate parameter to classify non-developed and classical streaming patterns, Re_{s1} can be used for this purpose. For all cases considered, the classical streaming is not developed for $Re_{s1} < 6.5$. It is also observed that the formation of classical streaming patterns depends on the frequency and vibrational displacement of the acoustic driver. The experimentally obtained structures of streaming vortices are found to be in good agreement with the theoretical ones and previously reported numerical predictions and experimental measurements.

Experimental investigation of regular and irregular acoustic streaming velocity fields are also performed using the synchronized PIV technique. A good correlation between the regular and irregular streaming flow patterns and the frequency and vibrational displacement of the acoustic driver is observed. The results also show that for the generation of irregular streaming flow patterns, Re_{s2} should be greater than 50.

Finally, the influences of differentially heated horizontal walls on the shape and amplitude of acoustic streaming velocity field are investigated experimentally using the synchronized PIV technique. The results indicate that the temperature difference between the top and bottom walls deforms the symmetric streaming vortices to the asymmetric form. As the temperature difference increases, the amplitude of streaming velocity increases.

CHAPTER 7
Valveless Acoustic Standing Wave Pump

7.1 Introduction

Valveless pumping is an attractive field of research due to the wide range of its applications in different areas of engineering and medicine. Two kinds of valveless pumps have been investigated extensively using experiments and numerical methods, which are *valveless impedance pumps* and *reciprocating valveless pumps.*

The impedance pump uses a mismatch in impedance to drive fluid. It comprises of an elastic tube connected at the ends to more rigid tubing. By compressing the elastic section periodically at an asymmetric position from the ends, traveling waves are emitted from the compression that can reflect at the impedance mismatch, and hence, generating a net flow [139] (see Fig. 7–1). Very recently, Bringley *et al.* [140] have constructed a prototype of the valveless impedance pump consisting of a section of elastic tube and a section of rigid tube connected in a closed loop and filled with water. They have studied the flow rates for various squeezing locations, frequencies, and elastic tube rigidities. They have also formulated a simple model that can be described by ordinary differential equations.

The reciprocating valveless pumps consist of two fluid diffuser-nozzle elements on each side of a chamber volume with an oscillating diaphragm. The vibrating diaphragm produces an oscillating chamber volume, which together with the two fluid-flow-rectifying diffuser-nozzle elements, creates a one-way fluid flow [141] (see Fig 7–2).

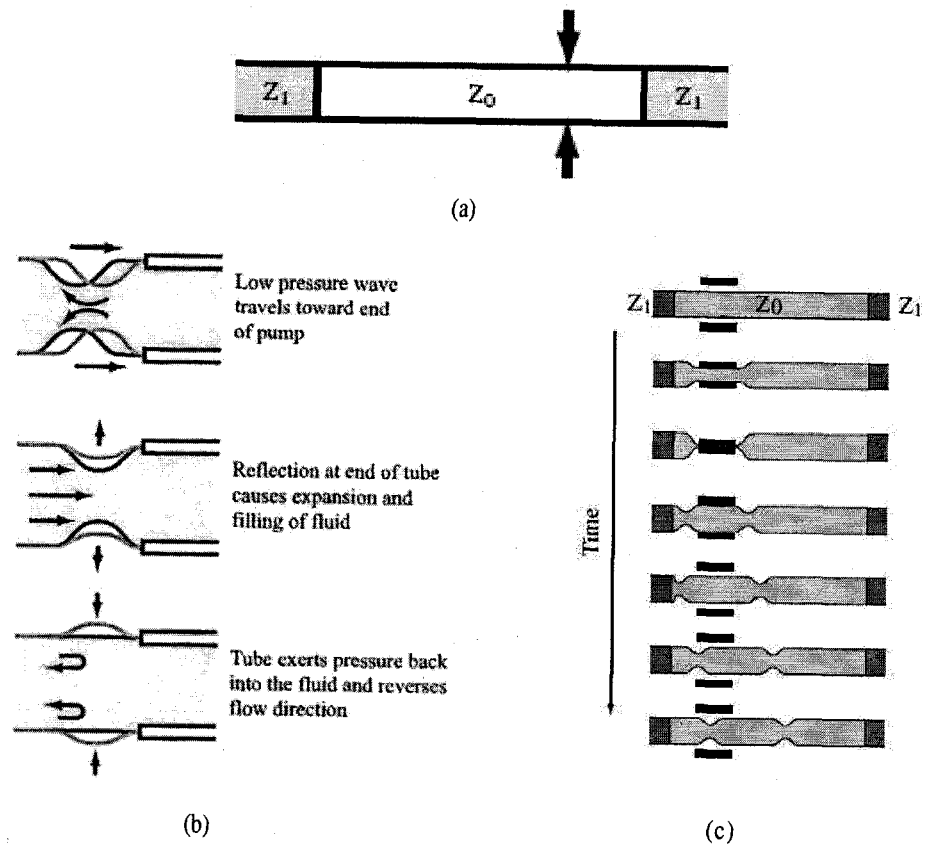

Figure 7–1: (a) A schematic of an impedance pump. The impedances are represented by Z0 and Z1. The two arrows show the pinch location. (b) Illustration of the pressure flow relationship close to one end of the elastic tube. (c) A schematic of an the wave motion on the elastic tube. The impedances are represented by Z0 and Z1.

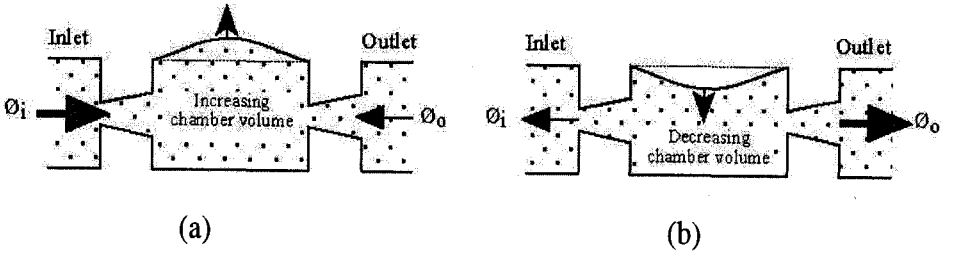

Figure 7–2: Operation of the diffuser-based pump (a) supply mode (b) pump mode.

7.2 Development of the valveless acoustic standing wave pump

In this study, we have developed a new valveless pumping mechanism called *valveless acoustic standing wave pump* (valveless ASWP) which achieves a pumping action using the properties of acoustic standing wave. It is a device that pumps both

gaseous and liquid fluids efficiently without any mechanical moving part and check valve. The device is simple and inexpensive to construct and operate. The valveless ASWP is suitable for a wide range of industrial and biomedical applications due to small power consumption, no moving parts, no frictional losses, no lubrication required, complete isolation of the fluid from the outside environment, no chance of fluid contamination and consequently, better biocompatibility. Furthermore, in the valveless ASWP there is no chance of mechanical failure and hence it is reliable. However, all of the previously-proposed ASWPs [22, 110, 111, 112] need one or more check valves for their operation and therefore, moving mechanical components are involved. The significant problems associated with these pumps include the fatigue of moving valves, clog, high pressure loss of valves and low driving frequency. Furthermore, no academic research has been conducted on these devices.

Of particular interest is the standing wave pump patented to Bishop [111], which claims to provide pumping action due to properties of acoustic standing wave. The pumping action of this pump requires a check valve at each inlet or outlet or both. It is also claimed in the above patent that the apparatus is able to pump fluids without check valve if operate at nonlinear standing wave region. Once the standing wave is established in the pump chamber, at the pressure anti-node the pressure is oscillating above and below the undisturbed pressure of the fluid (P_0). For linear standing wave, the pressure oscillations above and below P_0 are approximately equal and the average pressure at the pressure anti-node would be equal to P_0. However, in the nonlinear region, the pressure oscillations above and below P_0 become unequal. Consequently, an average pressure greater than the undisturbed pressure of the fluid can be obtained at the pressure anti-node. The small difference between the average pressure at pressure node and anti-node can pump the fluid without using the check valve. However, because of two main reasons this configuration of valveless pump is not practical and efficient. First of all, to obtain even a small pressure difference between

the average pressure at pressure node and anti-node (consequently very small net flow rate), the pressure amplitude at anti-node should rise to very large value, which is not efficient and practical. Secondly, at such high pressure fluctuations, several undesirable phenomena such as, large amplitude acoustic streaming, wave attenuation and wall vibration occur which degrade the pumping action and hence reduce the efficiency.

The valveless ASWP is able to pump fluids at both linear and nonlinear standing wave regions efficiently. In addition, unequal pressure oscillations above and below P_0 in the nonlinear region has a positive impact on the pumping action of the valveless ASWP. Like other reciprocating valveless pumps [141] (see Fig 7–2), in the valveless ASWP the difference of the flow resistance across the diffuser and the nozzle is used to direct the flow to a desired direction. In the previously-reported valveless pumps a moving diaphragm does pressure work on the working fluid in a periodic manner. However, in the valveless ASWP, pressure variation is achieved by the establishment of standing wave inside the pump chamber.

In this chapter, the operation principle of the proposed valveless ASWP is first described. Then, the behavior of the valveless ASWP is investigated experimentally using the synchronized PIV technique. The two-dimensional velocity field of the pump at the outlet at different phases of the excitation signal are measured.

7.2.1 Operating principle of the valveless ASWP

The valveless ASWP consists of a chamber, a vibrating object, a driver and a diffuser-nozzle element as illustrated in Fig. 7–3(a). The operating principle of the valveless ASWP is similar to the valved one (described in section 1.1). The main difference between the two devices is that, in the valveless ASWP instead of a check valve, a diffuser-nozzle element is placed at the outlet. A diffuser is characterized by a gradual widening of the fluidic cross-section in the sense of the flow and a smaller

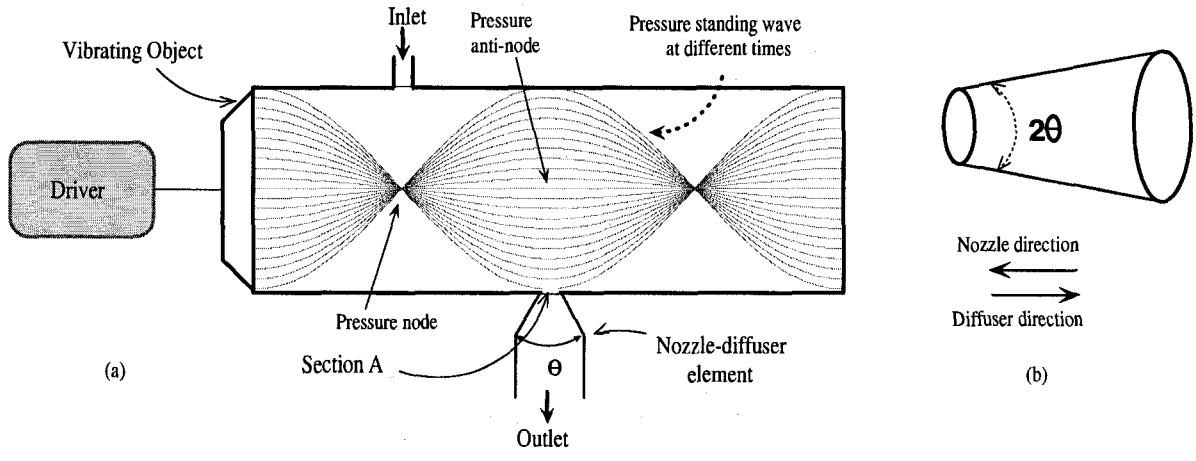

Figure 7–3: (a) Schematic illustration of the valveless ASWP, (b) The conical diffuser-nozzle element.

fluidic resistance. A nozzle is characterized by a gradual reduction of the fluidic cross-section in the sense of the flow and a higher fluidic resistance (see Fig. 7–3b). Thus, the diffuser-nozzle element has a higher pressure loss in the nozzle direction than in the diffuser direction.

In the linear range of the acoustic wave, the pressure at a pressure anti-node, $p(t)$, can be express by $p(t) = P_0 + p' \sin(\omega t)$ (see Fig. 7–4a). This time-varying pressure is applied at the diffuser-nozzle input (the narrowest part of the diffuser-nozzle element, section A in Fig. 7–4b,c). When $p(t) > P_0$, the pump is in the discharge mode and the fluid inside the pump chamber is discharged through the diffuser-nozzle element which acts as diffuser in this mode (see Fig. 7–4b). When $p(t) < P_0$, the pump is in the suction mode and the fluid will enter the pump chamber through the diffuser-nozzle element which acts as nozzle in this mode (see Fig. 7–4c). With the equal amplitude of pressure fluctuation in the discharge and suction modes, due to lower pressure loss (or lower flow resistance) in the diffuser direction than that in the nozzle direction, the volume of the outgoing flow through the outlet element in the pump mode is larger than the incoming flow in the suction mode. Therefore, there will be a net flow discharge through the diffuser-nozzle element, and hence, fluid pumping is

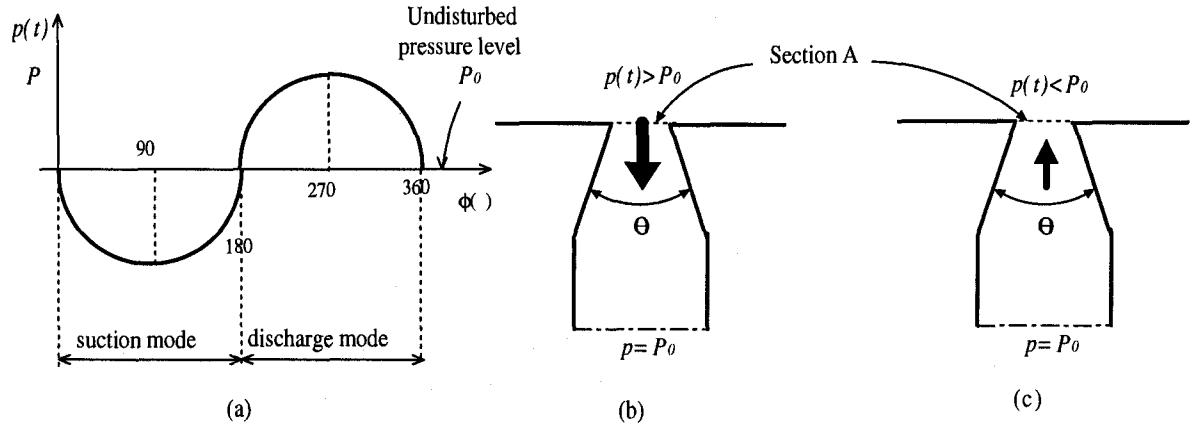

Figure 7–4: (a) Sinusoidal pressure fluctuation at the pressure anti-node in the linear region; Flow rectification of the valveless ASWP in (b) pump mode,(c) suction mode.

achieved by the valveless ASWP. As the fluid discharges, there is a reduction in the fluid mass inside the tube which will cause a reduction in the static pressure. The pressure will now be lower than the pressure at the inlet fluid. As a result the fluid will be sucked into the tube from the inlet located at the pressure node. The net flow discharge through this pump is related to the maximum pressure fluctuation inside the pump chamber. Larger the amplitude of pressure fluctuation, higher will be the net flow rate of the pump. Higher pressure fluctuation can be achieved using larger value of maximum vibrational displacement of the driver.

The pumping action of the valveless ASWP enhances in the nonlinear range of the standing wave. In the nonlinear range, the pressure oscillations above and below P_0 are asymmetric. The maximum amplitude of the pressure fluctuation above P_0 is greater than that below P_0 (see Fig. 7–5a). Consequently, the the net flow rate through the outlet element for nonlinear case is larger than that for the linear case (see Figs. 7–5b and c).

7.2.2 Diffuser-nozzle element

In order to achieve the best pump performance, the diffuser-nozzle element has to be designed for highest possible flow directing capability. The rectification capability

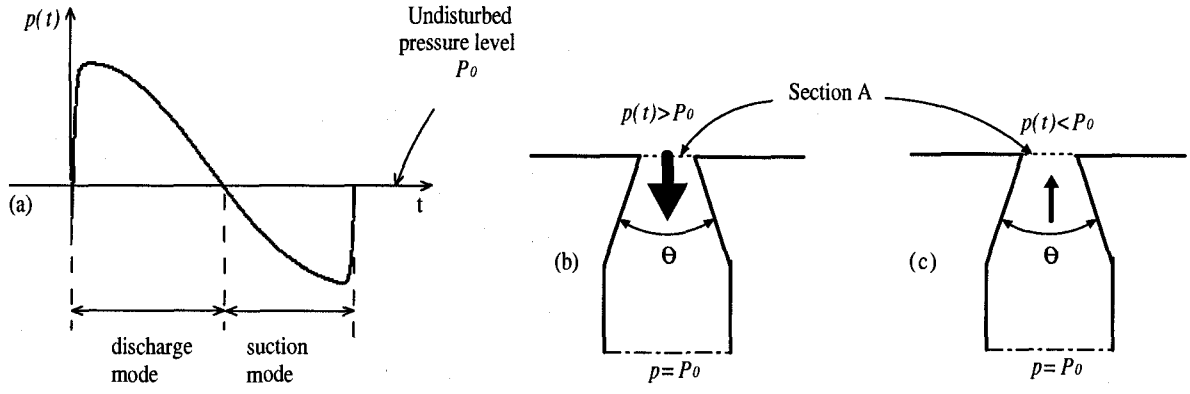

Figure 7–5: (a) Sinusoidal pressure fluctuation at the pressure anti-node in the non-linear region; Flow rectification of the valveless ASWP in (b) pump mode,(c) suction mode.

(η) of the diffuser-nozzle element can be defined as,

$$\eta = \frac{\xi_n}{\xi_d}, \tag{7.1}$$

where, ξ_n and ξ_d are measures of direction-dependent flow resistance and called pressure loss coefficients of the nozzle and diffuser, respectively. These parameters are defined as [141],

$$\xi_n = \frac{2\Delta p_n}{\rho u_n^2} \quad , \quad \xi_d = \frac{2\Delta p_d}{\rho u_d^2} \tag{7.2}$$

In order to increase the efficiency of the diffuser-nozzle element, η should be maximized.

7.3 Fabrication and experimental analysis of the valveless ASWP

A test apparatus is built to measure and analyze the behavior of the valveless ASWP. The pump chamber is a Plexiglas channel with a square cross-sectional area with the length of 74 cm and the inner cross-section of 7 cm×7 cm (see Fig. 7–6a). The inner diameter of the diffuser-nozzle element at the narrowest section is 5 mm and at the widest section is 13 mm. The half-angle of the diffuser-nozzle element (θ) is 14°. The inner diameter of the inlet is 13 mm. The inlet and outlet of the

pump are connected together to generate a circulation flow inside the pump (see Fig. 7–6b). This configuration make it possible to keep the seed particles inside the pump for PIV flow measurements.

The driver frequency (f) is set equal to 465 Hz. The corresponding wavelength (λ) of the acoustic standing wave is 74 cm. It allows the formation of one full standing waves inside the channel. The two-dimensional velocity fields inside the channel are measured using the synchronized PIV. The measurements are conducted in a plane parallel to the channel length at the mid-channel location as shown in Fig. 7–6 (a). The PIV measurements have been performed in a 3.4 cm $\times$ 2.5 cm region at outlet orifice (see Fig. 7–6b).

In order to accurately measure the periodic particle velocity, the separation time between two images must be adjusted appropriately. In the present cases, the time separation is set equal to $40\mu s$, which is more than 13 times smaller than the quarter wave period and still large enough to resolve the small displacements. The size of the interrogation region is set equal to 24×24 pixels and the size of the search region is set equal to 48×48 pixels. A three-point Gaussian sub-pixel fit scheme is used to obtain the correlation peak with sub-pixel accuracy. A 50% window overlap is used in order to increase the nominal resolution of the velocity field to 12 $\times$ 12 pixels. This resulted in a spatial resolution of 0.25 $\times$ 0.25 mm of the velocity field. A scheme is used to identify the spurious velocity vectors and then correct them using a local median test [137]. The percentage of the spurious velocity vectors is less than 0.5%. By adjusting the time delay in the synchronization circuit, the measurements are performed at 21 phases of the excitation signal equally-spaced in time. For each phase of the excitation voltage, 100 PIV images are captured. From these images, 50 acoustic velocity fields are computed. The experiments are conducted at two different maximum vibrational displacements (which result in two different maximum anti-node pressures, P_m) hereinafter called as cases A and B. The values of P_m are

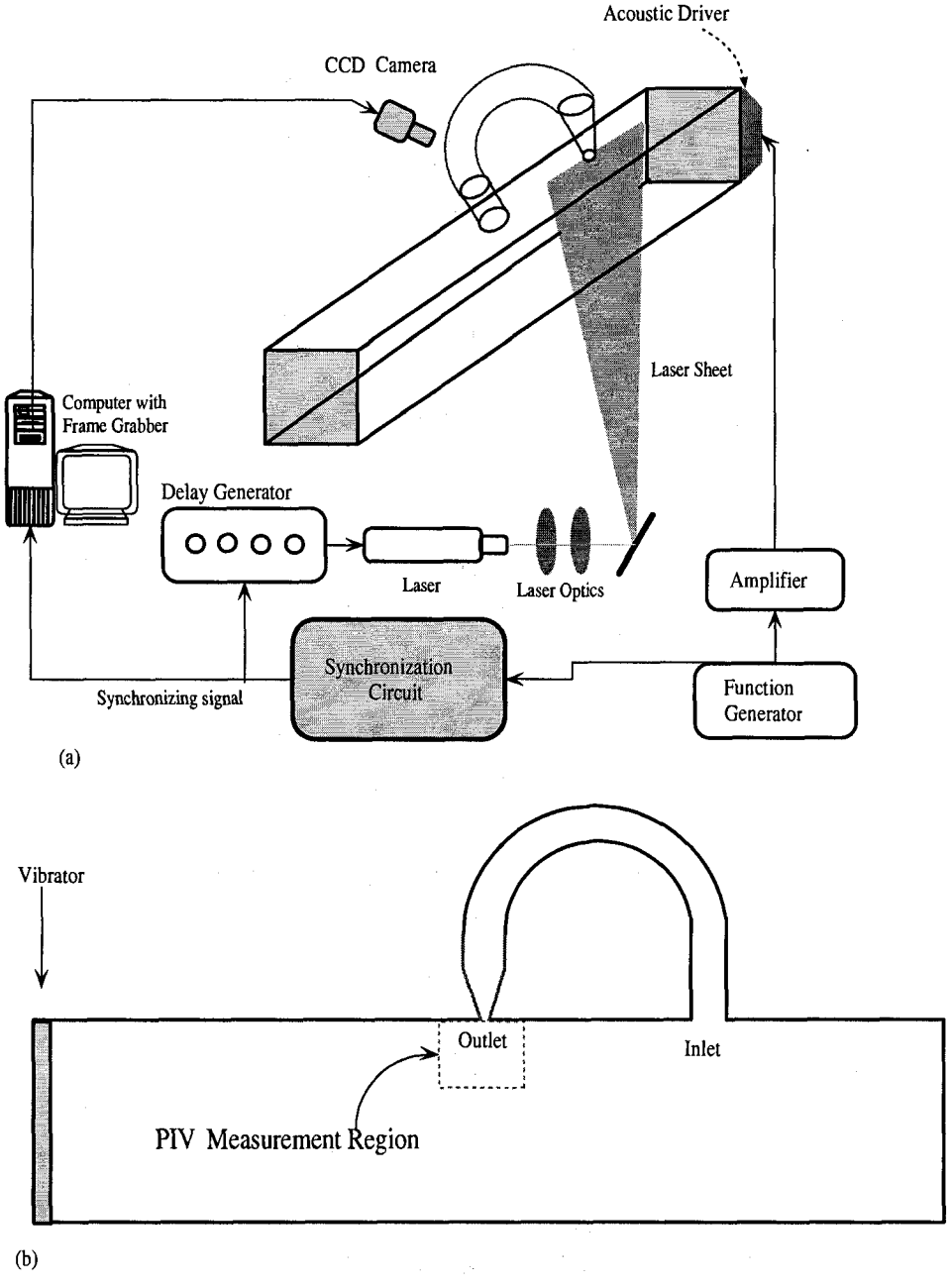

Figure 7–6: Experimental setup of the valveless ASWP.

295 Pa and 535 Pa, for cases A and B, respectively.

7.4 Results and discussion

The experimental velocity fields at six different phases of the anti-node pressure signal at outlet ($\phi = 100°, 133°, 167°, 200°, 233°, 267°$ in Fig. 7–4a) for cases A and

B are shown in Figs. 7–7 and 7–8, respectively. The mean velocities at the outlet

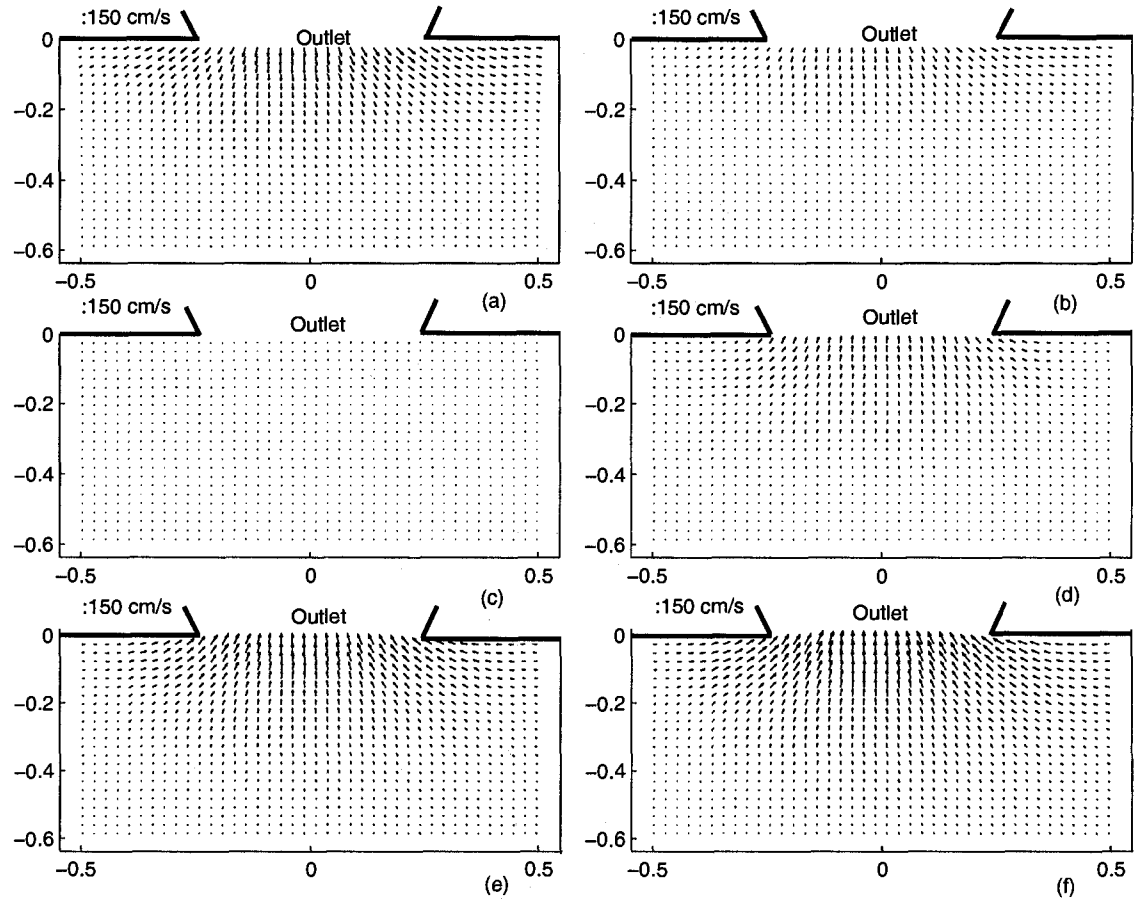

Figure 7–7: Two-dimensional velocity fields for case A at six different phases, (a) $\phi = 100°$, (b) $\phi = 133°$, (c) $\phi = 167°$, (d) $\phi = 200°$, (e) $\phi = 233°$, and (f) $\phi = 267°$. Horizontal axis is the axial location in cm, Vertical axis is the transverse location in cm; (0,0) coordinate corresponds to the middle of outlet orifice.

at different phases for cases A and B are plotted in Fig. 7–9. This parameter is computed by integrating the velocity amplitudes over the outlet sectional area.

The plots in Figs. 7–7 and 7–8, show the transitional behavior of the velocity fields inside the pump chamber and near the outlet over the half period of the excitation signal. Figs. 7–7(a,b) and 7–8(a,b) depict the transient flow rate at $\phi = 100°$ and 133°, where the pressure at the outlet (pressure anti-node) is below the undisturbed pressure. Therefore, the fluid is sucked into the pump chamber. At $\phi = 167°$ the pressure at the outlet is almost equal to P_0, which results in almost zero velocity

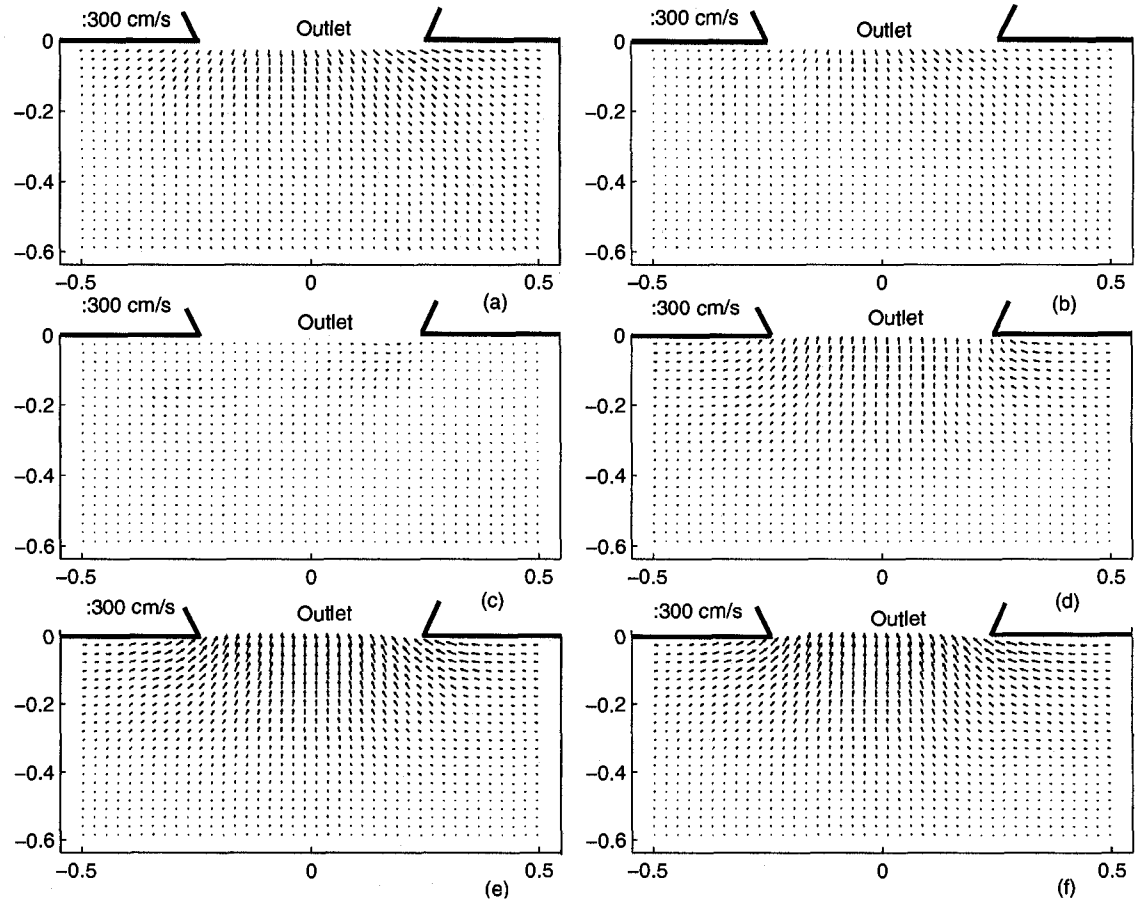

Figure 7–8: Two-dimensional velocity fields for case B at six different phases, (a) $\phi = 100°$, (b) $\phi = 133°$, (c) $\phi = 167°$, (d) $\phi = 200°$, (e) $\phi = 233°$, and (f) $\phi = 267°$. Horizontal axis is the axial location in cm, Vertical axis is the transverse location in cm; (0,0) coordinate corresponds to the middle of outlet orifice.

(see Figs. 7–7c and 7–8c). Whereas, at $\phi = 200°$, 233°, and 267° (Figs. 7–7d,e,f and 7–8d,e,f), the pressure at the outlet is larger than P_0, which makes the fluid pumped out of the pump chamber. However as shown in Fig. 7–9, due to less flow resistance in the diffuser than that of nozzle direction, the mean velocities in the diffuser direction (positive cycles) are larger than that of the nozzle direction (negative cycles). This means that a net flow is discharged through the outlet.

It must be noted that velocity fields depicted in Figs. 7–7 and 7–8 are the superposition of the pumping fluid flows and acoustic velocities. However, since the outlet is located at the velocity node (pressure anti-node), the amplitude of the acoustic

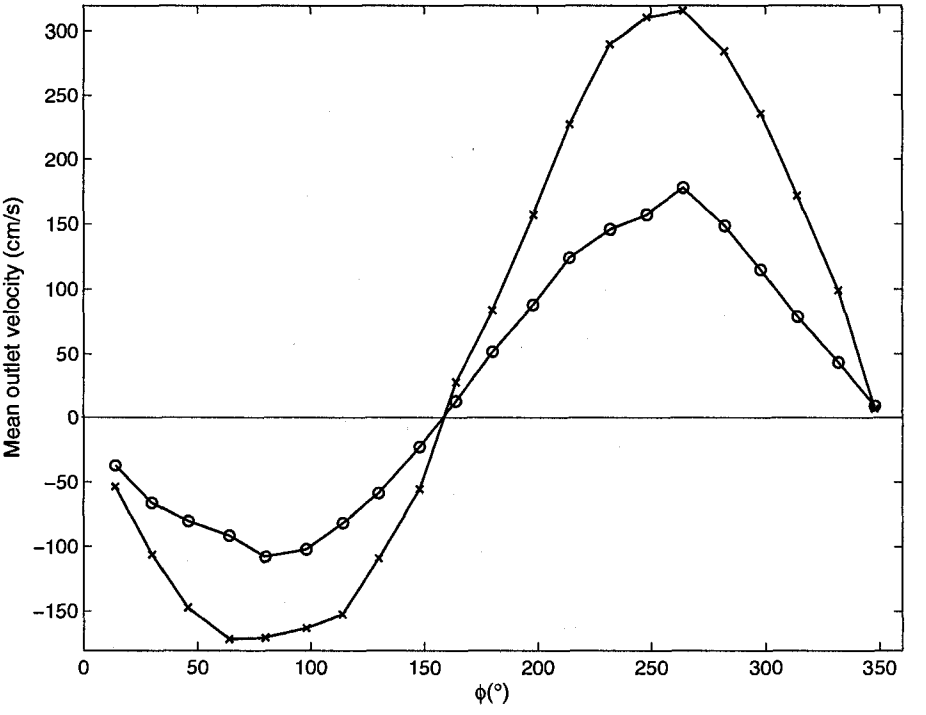

Figure 7–9: The mean velocity versus phase for case A (o), and case B (×).

velocities are almost zero.

In order to quantify the performance of the valveless ASWP, the values of the maximum, minimum and overall net velocities at the outlet, net flow rate (Q), pressure loss coefficients and rectification capability (Eqs. 7.2 and 7.1) for cases A and B are presented in Table 7–1. Q is simply computed by multiplication of the net velocity and the area of the outlet orifice of 5 mm diameter. The results in Table 7–1 show that the values of ξ_d are always smaller than those of ξ_n which is related to lower flow impedance in the diffuser direction than that in the nozzle direction. Table 7–1 also shows that the rectification capability and net flow rate increase with an increase in the maximum pressure (or Reynolds number). This observation is in agreement with the previous numerical and experimental analysis of the reciprocating valveless pumps [142, 143, 144, 145].

Table 7–1: Maximum anti-node pressure (P_m), maximum, minimum and overall net velocities at the outlet, maximum Reynolds number (Re_{max}), Pressure loss coefficients (ξ_n and ξ_d), rectification capability (η), and net flow rate (Q) of the tested valveless ASWP for cases A and B.

	case A	case B
$P_m(Pa)$	295	535
Maximum outlet velocity (cm/s)	177.8	315.8
Minimum outlet velocity (cm/s)	-107.8	-171.5
Net outlet velocity (cm/s)	24.0	51.5
$Remax$	588	1045
ξ_n	422	302
ξ_d	155	89
η	2.72	3.39
Q (mLit/min)	283	606

7.5 Conclusions

A valveless ASWP is developed and its operating principle is described. The behavior of this novel pump is investigated experimentally. The two-dimensional velocity field inside the pump chamber at the outlet at different phases of the excitation signal are measured using the synchronized PIV technique. The variation of the pump flow rate, pressure loss coefficients and rectification capability of the diffuser-nozzle element at two different pressure amplitudes are studied. The results show that the net flow rate of the pump increases with an increase in pressure amplitude (or Reynolds number).

CHAPTER 8
Numerical investigation of Acoustic Micropump

8.1 Introduction

Recently, micropumps have been extensively developed to manipulate fluids at small scales. With the increasing demand, micropumps have been applied to numerous applications in industrial and medical fields [146, 147, 148]. Various micropumps with different actuation principles, such as piezoelectric, shape memory alloys, electrostatics, thermal actuation and magnetics, have been investigated in the last decade [149].

Micropumps can be divided into two main categories, according to the way the fluid is displaced. *Hydrodynamic micropumps* continuously add energy to increase the fluid velocities such as Elctrohydrodynamic (EHD), Magnetohydrodynamic (MHD) and Electroosmotic (EO) micropumps. Whereas, in *positive displacement micropumps*, energy is periodically added by applying a force to one or more movable walls of pump chamber. Volume changes resulting from this diaphragm movement apply a direct pressure on the fluid and propel it to the outlet and produce a pulsating flow.

The reciprocating valveless micropumps are the most investigated micropumps in which the oscillation of a diaphragm excited by an actuator propels the flow and two micro diffuser-nozzle elements direct the flow. Olsson *et al.* [142] reported a numerical study of the valveless diffuser pump using lumped-mass model. Their results indicate that low chamber pressure is a limiting factor for the reciprocating valveless micropumps. An analytical model to investigate micropump characteristics has been proposed by Pan *et al.* [150]. Singhal *et al.* [144] analyzed the steady flow behavior of the micro diffuser-nozzle element using commercial software Fluent. They concluded

that contrary to past claims, flow rectification through micro diffuser-nozzle element is possible for very low Reynolds number laminar flows. Yang *et al.* [143] experimentally investigated the performance of the micro diffuser-nozzle element. They found that the pressure loss coefficients of the nozzle and diffuser decrease with the Reynolds number.

All of the above-mentioned studies about the flow pattern in micro diffuser-nozzle element have been performed in the steady flow regime. Sun *et al.* [151] presented a numerical study to characterize the unsteady behaviors of microdiffuser pumps. They found that diffusers with larger half angle show better rectification capability for $5° \leq \theta \leq 35°$. For $\theta > 35°$, the net flow rate is almost independent of θ. However, in their simulation, the excitation frequency was limited to 1 kHz. Very recently, experimental analysis of the unsteady flow in the micro diffuser-nozzle element was performed by Sheen *et al.* [145]. They measured the transient flow behaviors in an obstacle-type valveless PZT micropump using micro-PIV for the excitation frequency of 1 kHz$\leq f \leq$3 kHz. They concluded that the flow recirculation around the obstacle could enhance the flow-directing capability.

8.2 Acoustic standing wave micropump

Since the valveless ASWP (described in chapter 7) needs no check valve, its driving frequency can vary over a wide range (from less than 100 Hz to 20 kHz or more) depending on the application. Thus, the length of the pump chamber can be varied from millimeter to above meter (depending on the driving frequency) making it suitable for a wide range of application at macro and micro scales. Therefore, this device is capable of pumping fluids at micro scales and called *acoustic standing wave micropump* (ASWMP). It can be considered as a new pumping actuation mechanism for micropumps.

According to the operating principles of the ASWMP (similar to that of the valveless ASWP described in section 7.2.1), the minimum length of the micropump is $\lambda/2$. Therefore, the excitation frequency of this micropump should be higher than 20 kHz to keep the length of the micropump small (less than 8 mm for air). This range of frequency is significantly higher than that of the reciprocating valveless micropumps. The unsteady flow behavior in micro diffuser-nozzle element in the high frequency range is different from that at steady flow or at low frequency oscillations.

In this chapter, the time-variant flow structures through the micro diffuser-nozzle element in the ASWMP at a frequency of f=20 kHz for different values of the divergence angle of the element (θ) are numerically investigated.

8.3 Numerical simulation of the ASWMP

In this study, the commercial software FLUENT is used to simulate the unsteady flow behavior in the micro diffuser-nozzle element of the ASWMP. The working fluid is water with density of ρ=998.2 kg/m^3 and viscosity of μ=0.001003 kg/m. The flow is assumed to be laminar and incompressible. Transient axisymmetric solver is used, therefore, the mesh is created only for half of the domain. Fig. 8–1 shows the 2-D computational domain. No-slip condition is applied at the walls. Unsteady flow simulations are carried out for different values of θ in the range $15° \leq \theta \leq 60°$.

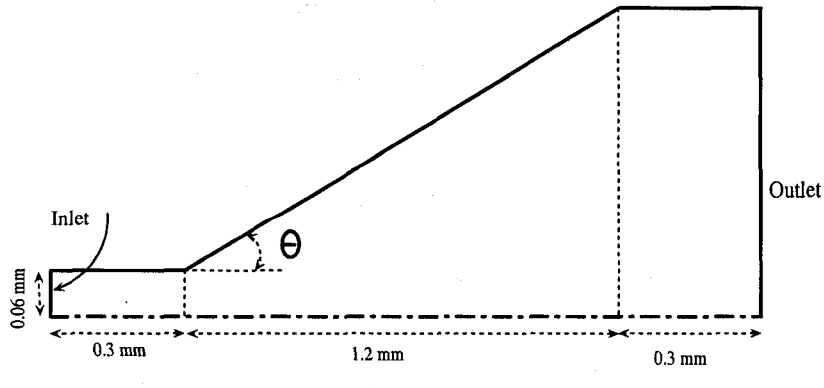

Figure 8–1: The 2-D computational domain.

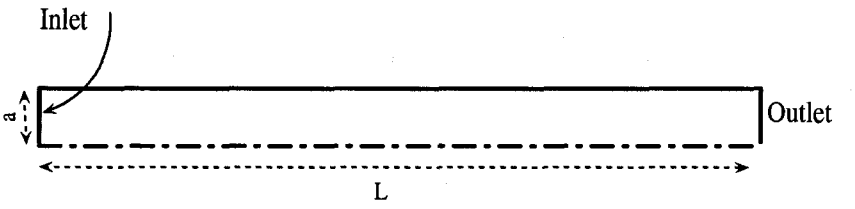

Figure 8–2: The 2-D computational domain used for the validation of the numerical model.

In order to minimize numerical diffusion, the first order up-wind differencing scheme is applied for the solution of momentum equation. The pressure-implicit with splitting of operators (PISO) is used for the pressure-velocity-coupling, which is recommended for usual transient calculations. According to FLUENT 6.2 User's Guide, PISO allows for a rapid rate of convergence without any significant loss of accuracy. Pressure is discretized with a PRESTO scheme. Other schemes (linear or second-order schemes) lead to strong divergence or to slow convergence (FLUENT 6.2 User's Guide). Under relaxation factors used for pressure and momentum are set equal to 0.6 and 0.4, respectively. A typical time step value of 100 times smaller than the wave period is used throughout the simulation.

8.3.1 Model validation

To validate the accuracy of our numerical model to simulate the oscillatory flow in microchannels, the numerical result of the unsteady, laminar oscillatory flow in a 2-D microchannel of width $2a$ and length L being driven by a sinusoidal pressure gradient $\partial p/\partial x = p^* e^{i\omega t}$ (see Fig. 8–2) is compared with the analytical solution. Following Cosgrove *et al.* [152], the final analytical expression of the y-dependent axial velocity in the microchannel is

$$u = \Re\{\frac{p^*}{i\omega\rho}[1 - \frac{\cosh[y(\alpha + i\alpha)/\sqrt{2}a]}{\cosh[(\alpha + i\alpha)/\sqrt{2}]}]e^{i\omega t}\}, \tag{8.1}$$

where $\alpha = a\sqrt{\omega/\nu}$, and $\Re$ denotes the real part of the solution. For large α, Eq. (8.1) reduces to

$$u \simeq u_m \sin \omega t, \tag{8.2}$$

where $u_m = \frac{p^*}{\omega\rho}$. Eq. (8.2) shows that the axial velocity is a time-oscillating flat profile across the microchannel. The analytical value of the mean absolute velocity ($\bar{u}$) is obtained as,

$$\bar{u} = \frac{1}{T}\int_0^T u(y,t)dt \simeq \frac{2p^*}{\pi\omega\rho}. \tag{8.3}$$

Considering a=60 μm, f=20 kHz and ν=1.004$\times 10^{-6}$ m^2/s, the value of α is found to be 21.2, which is large enough to consider Eqs. (8.2, 8.3) as the accurate solutions for u and $\bar{u}$.

The time variation of the analytical and numerical mean velocity over two periods of the pressure input for P=5000 Pa, (p^*= 2777777 Pa/m) are shown in Fig. 8–3. A good agreement in shape and amplitude between the analytical and numerical results of the mean velocity is observed, which confirms that the numerical model can predict the high-frequency oscillatory flow velocities accurately.

To gain more confidence, the numerical model used for the unsteady flow behavior in the micro diffuser-nozzle element, is validated against the 3-D numerical study performed by Sun *et al.* [151]. Using their geometry, but in 2-D, the time-dependent pressure and flow rate for $\theta = 25°$, f=100 Hz and P=200 Pa, are plotted in Fig. 8–4(a). It is observed that the variation of flow rate in time becomes periodic after the first cycle. The amplitude of flow rate signal and its phase difference with pressure are in good agreement with the 3-D simulation results of Sun *et al.* (see Fig. 8–4b).

8.4 Results and discussion

The excitation frequency and maximum pressure are set equal to f=20 kHz and P=5000 Pa. At these conditions, depending on the dimensions of computational domain (different values of θ), 200 to 300 cycles are required to drop the effect of the

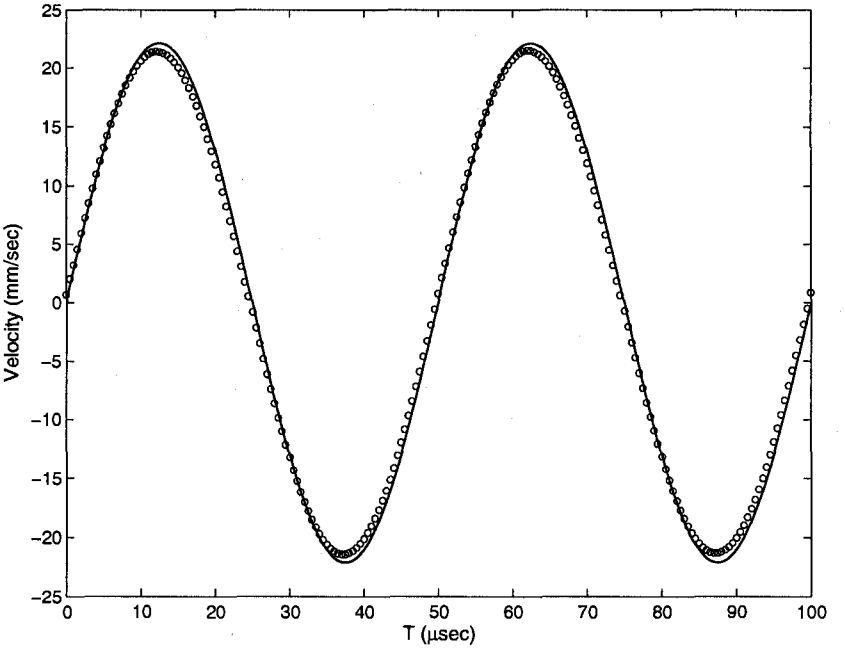

Figure 8–3: The time variation of the analytical (solid line) and numerical (○) mean velocity over two periods of the pressure input for f=20 kHz and P=5000 Pa in a microchannel of width 120 μm and length of 1800 μm.

initial state and to stabilize the velocity variations. This computational load takes 20 to 30 hours time on a Pentium 4, 3 GHz PC.

The time-dependent pressure and mean velocity at the inlet (see Fig. 8–1) for $\theta = 15°, 30°, 45°$, and 60° are plotted in Fig. 8–5. It is observed that for all cases, although the pressure variations are symmetric, the time-variant mean velocities are not symmetric. The mean velocities in the diffuser direction (positive cycles) are larger than that in the nozzle direction (negative cycles), which is due to less flow resistance in the diffuser direction than that in the nozzle direction. In Fig. 8–6, the time-dependent mean velocities are plotted for different values of θ to further highlight this trend.

One main difference between the unsteady flow behavior at high frequency and that at low frequency is that, the phase difference between pressure and velocity signals at high frequency is almost 90° (see Fig. 8–5). However, this value at low

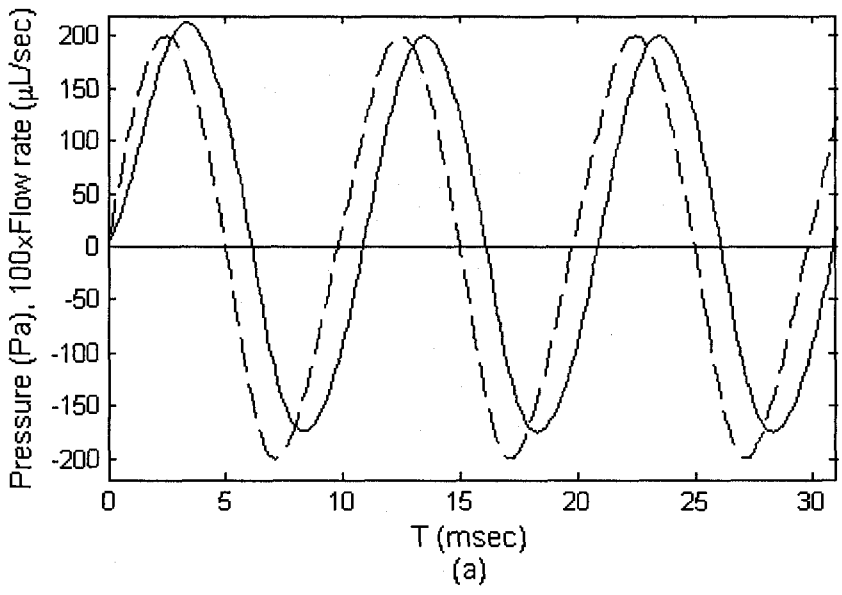

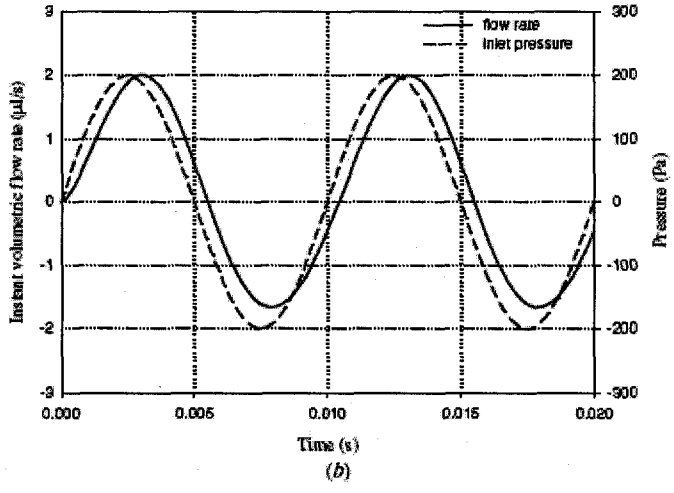

Figure 8–4: The time-dependent pressure (dashed line) and flow rate (solid line) for $\theta = 25°$, f=100 Hz and P=200 Pa, (a) our 2-D model, (b) 3-D model of Sun *et al.*.

frequency is considerably less than 90° (see Fig. 8–4). In order to explain this phenomenon, not only flow resistance (R) but also flow inductance (L) should be considered. A common model for harmonic incompressible viscous flow in a rigid channel is given by a series combination of a resistor R and an inductor I [153],

$$Z = \frac{\Delta P}{Q} = R + i\omega I, \tag{8.4}$$

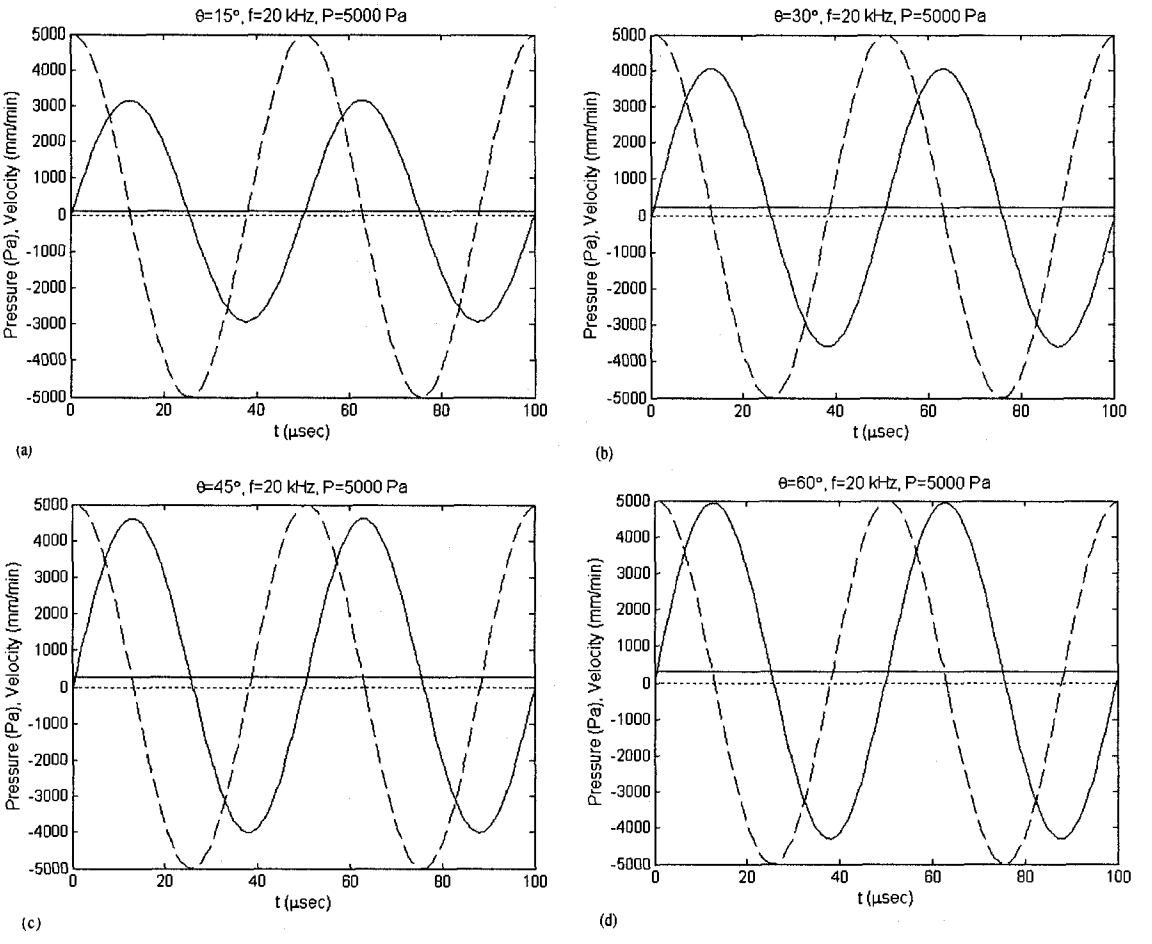

Figure 8–5: The time-dependent pressures (dashed line) and mean velocities (solid line) along with the net velocities (horizontal solid line) for P=5000 Pa and (a) $\theta = 15°$, (b) $\theta = 30°$, (c) $\theta = 45°$, and (d) $\theta = 60°$.

where, Z is the flow impedance, ΔP is the pressure drop, and Q is the volume flow rate. At high frequencies, the flow impedance is almost pure inductive, and the effect of resistive part on Z is almost negligible. Whereas at low frequencies, both resistive and inductive parts contribute to Z.

The maximum Reynolds number ($Re = \rho U D/\mu$, U is maximum velocity and D is width of the channel of the nuzzle/diffuser element) for these cases is about 10, which is much smaller than the critical Reynolds numbers (200-2300) reported in the literature for transition to turbulence in microchannels. Therefore, the assumption of laminar flow is valid for our simulations.

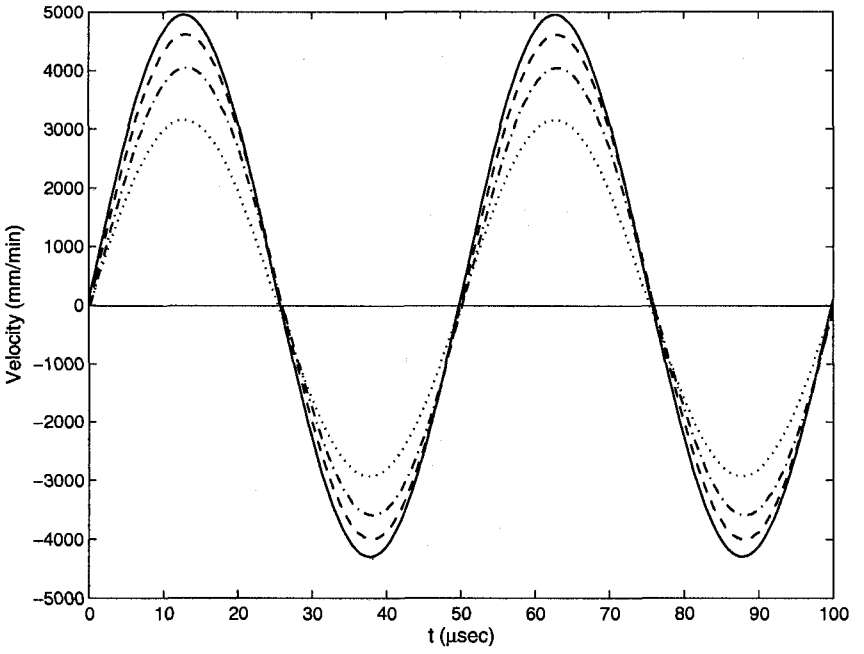

Figure 8–6: The time-dependent mean velocities for P=5000 Pa and $\theta = 15°$, dotted line; $\theta = 30°$, dot-dashed line; $\theta = 45°$, dashed line; $\theta = 60°$, solid line.

The net velocity (time-averaged velocity over a wave period) through the diffuser-nozzle element as a function of θ is shown in Fig. 8–7(a). It is observed that better pumping action is achievable at larger values of θ. However, increasing θ from 45° to 60° causes no significant increase in the net velocity. Using the values of mean velocity and pressure at the diffuser side of the diffuser-nozzle element (Fig. 8–5) and Eqs. (7.1, 7.2), the variations of ξ_d, ξ_n, and η as functions of θ are obtained and depicted in Figs. 8–7(b,c). Fig. 8–7(b) shows that the values of ξ_d are always larger than those of ξ_n, which is due to the less flow resistance in the diffuser than that of nozzle direction. ξ_d and ξ_n both decrease as θ increases which is related to lower flow impedance at higher values of θ. Fig. 8–7(c) shows that the maximum diffuser efficiency is achieved at θ approximately equal to 45°.

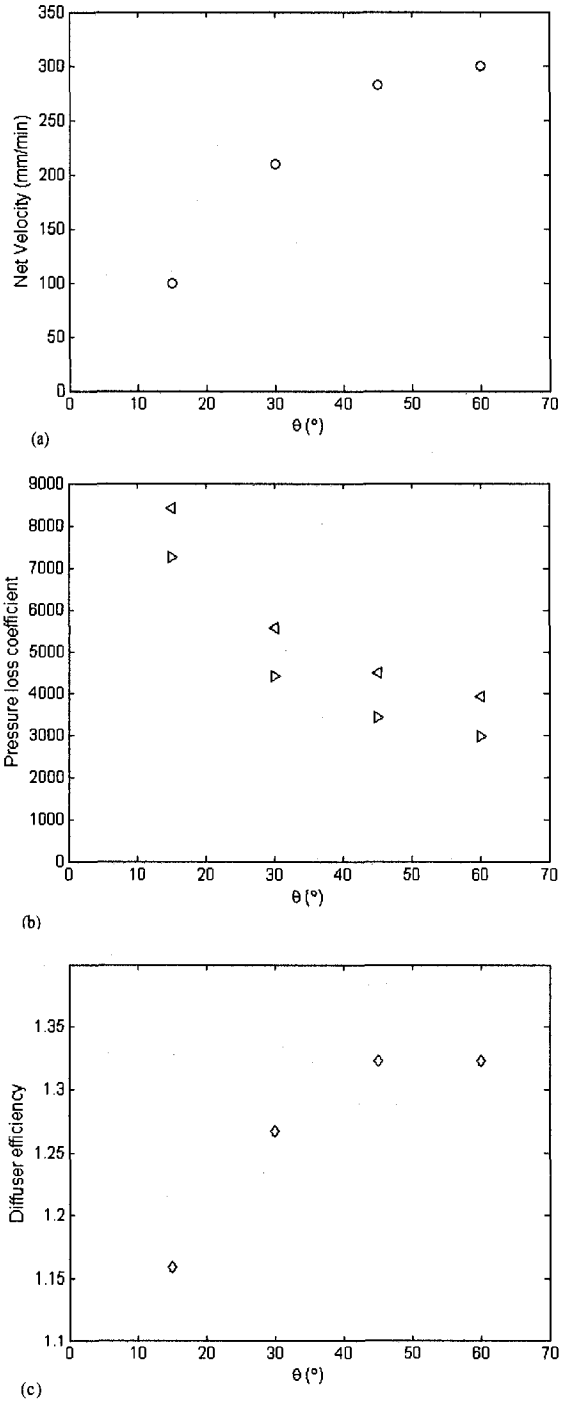

Figure 8–7: (a) The net velocity, (b) pressure loss coefficients ($\triangleright$, ξ_d; $\triangleleft$, ξ_n), (c) diffuser efficiency (η), as functions of θ.

8.5 Conclusions

In this chapter, the operating principle of the ASWMP is described. The variation of micropump flow rate, pressure loss coefficients of the nozzle and diffuser, and diffuser efficiency are shown as functions of θ. The differences between the unsteady flow behavior through the micro diffuser-nozzle element at high frequency (20 kHz) and that at low frequency are described. The results show that the higher micropump flow rate is obtained at larger values of θ. However, increasing θ from 45° to 60° shows no significant increase in the flow rate. The results also show that the maximum diffuser efficiency is achieved at θ approximately equal to 45°.

CHAPTER 9
Conclusions

9.1 Summary

In this study, different aspects of the interactions of acoustic waves and thermo-viscous fluids, such as linear and nonlinear acoustic standing waves, acoustic streaming and acoustic pump were investigated numerically and experimentally.

In chapter 2, a new 9-point sixth-order accurate compact FDM for the Helmholtz equation in one-dimensional and two-dimensional domains with Dirichlet and/or Neumann boundary conditions was developed. It was shown that the proposed scheme has better performance than the FEM at higher wave numbers and is more than 100 times faster than the fourth-order FEM.

In chapter 3, a new fourth-order numerical scheme was developed for solving highly nonlinear standing wave equations with no restriction on the nonlinearity level and type of fluid. In this scheme, the set of nonlinear equations was solved using a combination of a fourth-order compact finite difference scheme and a fourth-order Runge-Kutta time stepping scheme. The differences between the pressure and particle velocity waveforms of highly nonlinear waves and those of linear waves, in both time and space, were described. The effect of fluid type on the highly nonlinear waves were also explained for air and CO_2. It was observed that, as the waves become highly nonlinear, the pressure waveform changes from sinusoidal to saw-tooth form and the particle velocity waveform changes from sinusoidal to near-rectangular form. The results also indicated the presence of a wavefront that travels along the resonator with very high pressure and velocity gradients. The slopes of the traveling velocity and pressure gradients are higher for CO_2 than those for air. It was also observed

that the asymmetry in pressure waveform for CO_2 is higher than that for air.

In chapters 4 and 5, the experimental setup was fabricated for the measurements of the acoustic pressure using a pressure sensor, and the acoustic velocity field using the synchronized PIV technique. The spatial and temporal variations of the pressure and particle velocity fields inside an air-filled rigid-walled square channel in the presence of nonlinear standing waves of different frequencies and intensities were experimentally investigated. The experimental data were compared with the analytical and numerical results. Good agreements between the experimental results and analytical/numerical solutions for both pressure and particle velocity, in time and space domains, were observed.

In chapter 6, a novel technique was developed to simultaneously measure the acoustic and streaming velocity fields using the synchronized PIV technique. The accuracy of this technique was validated against the theoretical solution. Using this novel technique, the formation of acoustic streaming as well as regular and irregular streaming patterns were investigated. A good correlation was observed between the shape of the streaming flow patterns and the excitation frequency and maximum vibrational displacement of the acoustic driver. The formation process of streaming patterns was investigated. It was found that non-developed and classical streaming patterns can be classified based on Re_{s1}. For all cases considered, the classical streaming is not developed for $Re_{s1} < 6.5$. The regular and irregular streaming patterns are also analyzed and classified based on an appropriate streaming Reynolds number. It was found that the irregular streaming patterns are observed at $Re_{s2} > 50$. Furthermore, the influence of differentially heated horizontal walls on the shape and amplitude of acoustic streaming velocity field inside a gas-filled rectangular enclosure subjected to acoustic standing wave were investigated experimentally using the synchronized PIV. The results showed that the temperature difference between

the top and bottom walls deforms the symmetric streaming vortices about the channel centerline to the asymmetric form. As the temperature difference increases, the amplitude of streaming velocity increases.

In chapter 7, a valveless ASWP was developed. The performance of this novel valveless pump was investigated. The two-dimensional velocity field inside the pump chamber at the outlet orifice, at different phases of the excitation signal were measured using the synchronized PIV technique. The variation of the pump flow rate, pressure loss coefficients and rectification capability of the diffuser-nozzle element were studied. The results showed that the proposed pump is capable of pumping fluid without any moving part or check valve. The net flow rate of the pump increases with an increase in the pressure amplitude.

Finally, in chapter 8, the applicability of the valveless ASWP to pump fluid at microscale was numerically investigated. The behavior of the proposed valveless micropump in terms of flow rate, pressure loss coefficients of the nozzle and diffuser, and diffuser efficiency were analyzed at different values of the divergence angle of the element (θ). The results showed that the maximum diffuser efficiency is achieved at θ approximately equal to 45°. The differences between the unsteady flow behavior through the diffuser-nozzle element at high frequency (20 kHz) and that at low frequency were also described.

9.2 Research contributions

The main contributions of this research to the knowledge and techniques in the field of acoustic-fluid interactions can be listed as follows:

- Development of a new 9-point sixth-order accurate compact finite difference method for the Helmholtz equation in one-dimensional and two-dimensional domains with Dirichlet and/or Neumann boundary conditions.

- Development of a fourth-order accurate scheme for solving highly nonlinear standing wave equation in different thermoviscous fluids with no restriction on the nonlinearity level and type of fluid.
- Measurement of the two-dimensional acoustic velocity field of nonlinear standing wave using the synchronized PIV technique.
- Development of a novel technique to simultaneously measure the two-dimensional acoustic and streaming velocities at any location along the resonator and at any phase of the excitation signal.
- Investigation of the formation process of the acoustic streaming as well as the regular (classical) and irregular streaming patterns inside a standing-wave resonator. Establishment of the criteria based on the appropriate non-dimensional parameters to classify developed/non-developed and regular/irregular streaming patterns.
- Investigation of the influence of differentially heated horizontal walls on streaming shape and velocity.
- Development of the valveless acoustic standing wave pump and investigation of the time-variant flow structures inside this novel valveless pump.
- Numerical investigation of the time-variant flow structures through the micro diffuser-nozzle element in the acoustic standing wave micropump at high frequency.

9.3 Recommendations for future work

Several research problems in the field of acoustic-fluid interactions still remain unsolved which demand further numerical and experimental investigations. Some of these problems are:

1. Numerical and experimental investigations of the formation of acoustic streaming in resonators of arbitrary shapes such as, cone, horn-cone and cosine shapes.
2. Further experimental exploration of the interactions of the fluid flow and, acoustic and streaming velocity fields inside the valveless ASWP.
3. Numerical modeling of the valveless ASWP in order to optimize the shape of the diffuser-nozzle as well as the shape of pump chamber to achieve maximum net flow rate.
4. Investigation of the performance of valveless ASWP for incompressible fluids such as water.
5. Numerical and experimental analysis of the acoustic-fluid interactions in microchannels with application to the ASWMP.

List of Publications

Published or Accepted Journal Papers

1. M. Nabavi, K. Siddiqui and J. Dargahi, "A new 9-point sixth-order accurate compact finite difference method for the Helmholtz equation", *J. Sound and Vibration*, 307, 972-982, 2007.
2. M. Nabavi, K. Siddiqui and J. Dargahi, "Simultaneous measurement of acoustic and streaming velocities using a synchronized PIV technique", *Measurement Science and Technology*, 18, 1811-1817, 2007.
3. M. Nabavi, K. Siddiqui and J. Dargahi, "A fourth-order accurate scheme for solving highly nonlinear standing wave equation in different thermoviscous fluids", *J. Computational Acoustics*, In press, 2008.
4. M. Nabavi, K. Siddiqui and J. Dargahi, "Experimental investigation of the formation of acoustic streaming in a rectangular enclosure using a synchronized PIV technique", *Measurement Science and Technology*, 19, 065405 (9pp), 2008.
5. M. Nabavi, K. Siddiqui and J. Dargahi, "Influences of differentially heated horizontal walls on streaming shape and velocity in a standing wave resonator", *Int. Com. in Heat and Mass Transfer*, In press, Available online, 2008.
6. M. Nabavi, K. Siddiqui and J. Dargahi, "Measurement of the acoustic velocity field of nonlinear standing wave using a synchronized PIV technique", *Experimental Thermal and Fluid Science*, In press, 2008.
7. M. Nabavi, K. Siddiqui and J. Dargahi, "Effects of transverse temperature gradient on acoustic and streaming velocity fields in a resonant cavity", *Applied Physics Letters*, In press, Available online, 2008.

Submitted Journal Manuscripts

8. M. Nabavi, K. Siddiqui and J. Dargahi, "Regular and irregular acoustic streaming in a rectangular enclosure: An experimental study", submitted to *J. Acoustical Society of America*, under review.
9. M. Nabavi, K. Siddiqui and J. Dargahi, "Analysis of the flow structure inside the valveless standing wave pump", submitted to *Physics of Fluids*, under review.

Conference Articles

10. M. Nabavi, K. Siddiqui and J. Dargahi, "Valveless acoustic standing wave micropump for biomedical applications: Numerical study", *30th Annual International Conference of the IEEE Engineering in Medicine and Biology* (IEEE EMBC08), Vancouver, Canada, Aug. 2008, submitted.
11. M. Nabavi, K. Siddiqui and J. Dargahi, "A theoretical study on using PVDF in the acoustic micropump for biomedical applications", *Annual conference of the Canadian Acoustical Association (CAA 2007)*, Montreal, Canada, October 9-12, 2007.
12. M. Nabavi, K. Siddiqui and J. Dargahi, "A Numerical study on the effect of vibrator shape on the development of nonlinear standing waves in 2-D acoustical resonator", *Annual conference of the Canadian Acoustical Association (CAA 2007)*, Montreal, Canada, October 9-12, 2007.
13. M. Nabavi, K. Siddiqui and J. Dargahi, "Frequency analysis of the acoustic pressure of nonlinear standing waves", *Annual conference of the Canadian Acoustical Association (CAA 2007)*, Montreal, Canada, October 9-12, 2007.

14. M. Nabavi, K. Siddiqui and J. Dargahi, "Comparison between two numerical methods for modeling time-harmonic acoustic wave propagation in fluids", *21st Canadian Congress of Applied Mechanics (CANCAM 2007)*, Toronto, June 3-7, 2007.

15. M. Nabavi, K. Siddiqui and J. Dargahi, "Numerical and experimental analysis of finite-amplitude nonlinear standing waves in time and space domains", *Int. Congresses on Ultrasonics (ICU 2007)*, Vienna, Austria, April 9-11, 2007.

REFERENCES

[1] V. Gusev; H. Bailliet; P. Lotton and M. Bruneau. Asymptotic theory of nonlinear acoustic waves in a thermoacoustic prime-mover. *Acustica*, 86:25–38, 2000.

[2] M.F. Hamilton; Y.A. Ilinskii and E.A. Zabolotskaya. Nonlinear two-dimensional model for thermoacoustics engines. *J. Acoustical Society of America*, 111:2076–2086, 2002.

[3] I.S. Paek, L.G. Mongeau, and J.E. Braun. A method for estimating the parameters of electrodynamic drivers in thermoacoustic coolers. *J. Acoustical Society of America*, 117:185–193, 2005.

[4] M.A. Rotea, Y. Li, G.T.C. Chiu, L.G. Mongeau, and I.S. Paek. Extremum seeking control of tunable thermoacoustic cooler. *IEEE Transactions on Control Systems Technology*, 13:527–536, 2005.

[5] J.E. Braun, I.S. Paek, and L.G. Mongeau. Characterizing heat transfer coefficients for heat exchangers in standing wave thermoacoustic coolers. *J. Acoustical Society of America*, 118:2271–2280, 2005.

[6] Y.A. Ilinskii; B. Lipkens; T.S. Lucas and T.W. Van Doren. Nonlinear standing waves in an acoustical resonator. *J. Acoustical Society of America*, 104:2664–2674, 1998.

[7] V. Gusev; H. Bailliet; P. Lotton; S. Job and M. Bruneau. Enhancement of the Q of a nonlinear acoustic resonator by active suppression of harmonics. *J. Acoustical Society of America*, 103:3717–3720, 1998.

[8] J.A. Gallego-Juarez. New technologies in high-power ultrasonic industrial applications. *Ultrasonics Symposium*, 3:1343–1352, 1994.

[9] Y. Roha and J. Kwon. Development of a new standing wave type ultrasonic linear motor. *Sensors and Actuators A*, 112:196–202, 2004.

[10] A. Bishop and R. Patten. Standing wave pump. *J. Acoustical Society of America*, 109:447–448, 2001.

[11] Y. Lee and J. Kwon. Separation and concentration of particles in fluid using ultrasonic standing wave. *Key Engineering Materials*, 321:63–66, 2006.

[12] D.L. Taylor B. Bailey, D.L. Farkas and F. Lanni. Enhancement of axial resolution in fluorescence microscopy by standing-wave excitation. *Advanced in engineering software*, 366:44–48, 1993.

[13] M.D. Harpen. Basic nonlinear acoustics: An introduction tfor radiological physicists. *Medical Physics*, 33:3241–3247, 2006.

[14] G. Renaud, S. Calle, J.P. Remenieras, and M. Defontaine. Nonlinear acoustic measurements to assess crack density in trabecular bone. *International Journal of Non-Linear Mechanics*, 43:194–200, 2008.

[15] H. Bailliet; V. Gusev; R. Raspet and R.A. Hiller. Acoustic streaming in closed thermoacoustic devices. *J. Acoustical Society of America*, 110:1808–1821, 2001.

[16] M.K. Aktas and B. Farouk. Heat transfer enhancement by acoustic streaming in an enclosure. *J. Heat Transfer*, 127:1313–1321, 2005.

[17] Q. Wan; T. Wu; J. Castain; W. Roberts; L.A. Kuzvetov and P. Ro. Forced convective cooling via acoustic streaming in a narrow channel established by a vibrating piezoelectric bimorph. *Applied Scientific Research*, 74:195–206, 2005.

[18] E.H. Trinh and J.L. Robey. Experimental study of streaming flows associated with ultrasonic levitators. *Physics of Fluids*, 6:3567–3579, 1994.

[19] A.A. Busnaina and T.M. Elsawy. Post-cmp cleaning using acoustic streaming. *J. Electronic Materials*, 27:1095–1098, 1998.

[20] L.A. Kuznetsova and W.T. Coakley. Applications of ultrasound streaming and radiation force in biosensors. *Biosensors and Bioelectronics*, 22:1567–1577, 2007.

[21] G. Zauhar; H.C. Starritt and F.A. Duck. Studies of acoustic streaming in biological fluids with an ultrasound Doppler technique. *The British J. of Radiology*, 71:297–302, 1998.

[22] H. Mandorian. Standing wave pump, US Pat. No. 3743446, 1973.

[23] E. Luo; J. Hu; W. Dai and Y. Chen. An acoustical pump capable of significantly increasing pressure ratio of thermoacoustic heat engines. *Chinese Science Bulietin*, 51:1014–1016, 2006.

[24] I.S. Paek, J.E. Braun, and L.G. Mongeau. Evaluation of standing-wave thermoacoustic cycles for cooling applications. *Int. J. Refrigeration*, 30:1059–1071, 2007.

[25] A.H. Meng; N.T. Nguyen and R.M. White. Focused flow micropump using ultrasonic flexural plate waves. *Biomedical Microdevices*, 2, 2000.

[26] B.J. Grotberg and O.E. Jensen. Biofluid mechanics in flexible tubes. *Annual Review of Fluid Mechanics*, 36:121–147, 2004.

[27] I.E. Anar and A. Misir. Far-field patterns for time-harmonic acoustic plane waves in an inhomogeneous medium. *Applied Mathematics and Computation*, 111:103–119, 2000.

[28] Wagner J. Bouchal Z., Horak R. Propagation-invariant electromagnetic fields: Theory and experiment. *J. Modern Optics*, 43:1905–1920, 1996.

[29] R. Tezaur; A. Macedo; C. Farhat and R. Djellouli. Three-dimensional finite element calculations in acoustic scattering using arbitrarily shaped convex artificial boundaries. *Int. J. for Numerical Methods in Engineering*, 6:14611476, 2002.

[30] O. Mehdizadeh and M. Paraschivoiu. A three-dimensional finite element approach for predicting the transmission loss in mufflers and silencers with no mean flow. *Applied Acoustics*, 66:902918, 2005.

[31] K. Kashiyama and M. Sakuraba. Adaptive boundary-type finite element method for wave diffraction-reflection in harbours. *Computer methods in applied mechanics and engineering*, 112:185197, 1994.

[32] W.X. Wu; C. Shu and C.M. Wang. Vibration analysis of arbitrarily shaped membranes using local radial basis function-based differential quadrature method. *J. Sound and Vibration*, 306:252–270, 2007.

[33] J.R. Stewart and T.J.R. Hughes. Explicit residual-based a posteriori error estimation for finite element discretizations of the Helmholtz equation: computation of the constant and new measures of error estimator quality. *Computer methods in applied mechanics and engineering*, 131:335363, 1996.

[34] R.P. Shaw. Integral equation methods in acoustics. *Boundary elements*, 4:221–244, 1988.

[35] E. Giladi. Asymptotically derived boundary elements for the Helmholtz equation in high frequencies. *J. Computational and Applied Mathematics*, 198:52–74, 2007.

[36] I. Harari and T.J.R. Hughes. Finite element methods for the helmholtz equation in an exterior domain: model problem. *Computer methods in applied mechanics and engineering*, 87:59–96, 1991.

[37] F. Ihlenburg and I. Babuska. Finite element solution to the Helmholtz equation with high wavenumber part I: the h-version of the FEM. *Computers and Mathematics with applications*, 30:9–37, 1995.

[38] F. Ihlenburg and I. Babuska. Finite element solution to the Helmholtz equation with high wavenumber part II: the h-p-version of the FEM. *Computers and Mathematics with applications*, 34:315–358, 1997.

[39] O. Mehdizadeh and M. Paraschivoiu. Investigation of a two-dimensional spectral method for Helmholtz's equation. *J. computational physics*, 189:111–129, 2003.

[40] I. Singer and E. Turkel. High-order finite difference method for the Helmholtz equation. *Computer methods in applied mechanics and engineering*, 163:343–358, 1998.

[41] I. Singer and E. Turkel. Sixth order accurate finite difference schemes for the Helmholtz equation. *J. Computational Acoustics*, 3:339–351, 2006.

[42] G. Sutmann. Compact finite difference schemes of sixth order for the helmholtz equation. *J. Computational and Applied Mathematics*, 203:15, 2007.

[43] L.G. Copely. Fundamental results concerning integral representations in acoustic radiation. *J. Acoustical Society of America*, 44:28–32, 1968.

[44] A. Oberai and P. Pinsky. A numerical comparison of finite element methods for the Relmholtz equation. *J. computational Acoustics*, 8:211–221, 2000.

[45] I. Harari and C.L. Nogueria. Reducing dispersion of linear triangular elements for the helmholtz equation. *J. Engineering Mechanics*, 128:351–358, 2002.

[46] I. Harari. A survey of finite element methods for time-harmonic acoustics. *Computer methods in applied mechanics and engineering*, 195:1594–1607, 2006.

[47] K.S. Surana; P. Gupta and J.N. Reddy. Galerkin and least-squares finite element processes for 2D Helmholtz equation in h, p, k framework. *Int. J. for Computational Methods in Engineering Science and Mechanics*, 8:341–362, 2007.

[48] M.G. Blyth and C. Pozrikidis. A comparative study of the boundary and finite element methods for the Helmholtz equation in two dimensions. *Engineering Analysis with Boundary Elements*, 31:35–49, 2007.

[49] G. Bao; G.W. Wei and S. Zhao. Numerical solution of the Helmholtz equation with high wavenumbers. *Int. J. for Numerical Methods in Engineering*, 59:389–408, 2003.

[50] C. Shu and H. Xue. Solution of helmholtz equation by differential quadrature method. *Computer methods in applied mechanics and engineering*, 175:203–212, 1999.

[51] S.M. El-Sayed and D. Kaya. Comparing numerical method for helmholtz equation model problem. *Applied mathematics and computation*, 150:763–773, 2004.

[52] G. Huelsz and F. Lopez-Alquicira. Hot-wire anemometry in acoustic waves. *Experiments in Fluids*, 30:283–285, 2001.

[53] G. Huelsz and F. Lopez-Alquicira. Velocity measurements in the oscillatory boundary layer produced by acoustic waves. *Experiments in Fluids*, 32:612–615, 2002.

[54] J. Jarzynski J.F. Vignola, Y.H. Berthelot. Laser detection of sound. *J. Acoustical Society of America*, 90:1275–1286, 1991.

[55] M.W. Thompson and A.A. atchley. Simultaneous measurement of acoustic and streaming velocities in a standing wave using lase Doppler anemometry. *J. Acoustical Society of America*, 117:1828–1838, 2005.

[56] B. Gazengel and S. Poggi. Measurement of acoustic particle velocities in enclosed sound field: Assessment of two Laser Doppler Velocimetry measuring systems. *Applied Acoustics*, 66:15–44, 2005.

[57] D.B. Hann and C.A. Greated. Particle image velocimetry for the measurement of mean and acoustic particle velocities. *Measurement Science and Technology*, 8:656–660, 1997.

[58] D.B. Hann and C.A. Greated. The measurement of flow velocity and acoustic particle velocity using particle image velocimetry. *Measurement Science and Technology*, 8:1517–1522, 1997.

[59] M. Campbell; J.A. Cosgrove; C.A. Greated; S. Jack and D. Rockliff. Review of LDA and PIV applied to the measurement of sound and acoustic streaming. *Optics & laser technology*, 32:629–639, 2000.

[60] Y. Shin; C. Jaewon and G.A. Domoto. Compressible flow of liquid in a standing wave tube. *J. Fluid Mechanics*, 536:321–345, 2005.

[61] J.R. Castrejón-Pita; A.A. Castrejón-Pita; G. Huelsz and R. Tovar. Experimental demonstration of the rayleigh acoustic viscous boundary layer theory. *Physical Review E*, 73:036601–5, 2000.

[62] D.F. Gaitan and A.A. Atchley. Finite amplitude standing waves in harmonic and anharmonic tubes. *J. Acoustical Society of America*, 93:2489–2495, 1993.

[63] Y.A. Ilinskii; B. Lipkens and T.S. Lucas. Energy losses in an acoustical resonator. *J. Acoustical Society of America*, 109:1859–1870, 2001.

[64] A.B. Coppens and J.V. Sanders. Finite amplitude standing waves in rigid-walled tubes. *J. Acoustical Society of America*, 43:516–529, 1968.

[65] A.B. Coppens and J.V. Sanders. Finite amplitude standing waves within real cavities. *J. Acoustical Society of America*, 58:1133–1140, 1975.

[66] Dah-You Maa and Ke Liu. Nonlinear standing waves: Theory and experiments. *J. Acoustical Society of America*, 98:2753–2763, 1995.

[67] M. Bednařík and M.Červenka. Nonlinear waves in resonators. *Nonlinear Acoustics at the tern of Millennium*, 15:165–168, 2000.

[68] C. Vanhille and C. Campos-Pozuelo. A high-order finite difference algorithm for the analysis of standing acoustic waves with finite but moderate amplitude. *J. Computational Physics*, 165:334–353, 2000.

[69] C. Vanhille and C. Campos-Pozuelo. Numerical simulation of two-dimensional nonlinear standing waves. *J. Acoustical Society of America*, 116:194–200, 2004.

[70] C. Vanhille and C. Campos-Pozuelo. Finite difference and finite volume methods for nonlinear standing waves in fluid media. *Ultrasonics*, 42:315–318, 2004.

[71] C. Vanhille and C. Campos-Pozuelo. Three time-domain computational models for quasi-standing nonlinear acoustic waves, including heat production. *J. Computational Acoustics*, 14:143–156, 2006.

[72] C. Campos-Pozuelo C. Vanhille. Nonlinear ultrasonic resonators: A numerical analysis in the time domain. *Ultrasonics*, 44, 2006.

[73] L. Elvira-Segura and Riera-Franco de Sarabia. A finite element algorithm for the study of nonlinear standing waves. *J. Acoustical Society of America*, 103:2312–2320, 1998.

[74] Y. Chun and Y. Kim. Numerical analysis for nonlinear resonant oscillations of gas in axisymmetric closed tubes. *J. Acoustical Society of America*, 108:2756–2774, 2000.

[75] G. Raman C. Daniels X. Li, J. Finkbeiner and B. Steinetz. Optimized shapes of oscillating resonators for generating high-amplitude pressure waves. *J. Acoustical Society of America*, 116:2814–2821, 2004.

[76] I. Christov; P.M. Jordan and C.I. Christov. Nonlinear acoustic propagation in homentropic perfect gases: A numerical study. *Physics Letters A*, 353:273–280, 2006.

[77] M. Bednařík and M.Červenka. Description of finite-amplitude standing acoustic waves using convection-diffusion equations. *Czechoslovak J. of Physics*, 55:673–680, 2005.

[78] A. Kurganov and E. Tadmor. New high-resolution central schemes for nonlinear conservation laws and convectiondiffusion equations. *J. Computational Physics*, 160:241–282, 2000.

[79] M. Bednařík and M.Červenka. Nonlinear standing wave in 2D acoustic resonators. *Ultrasonics*, 44:773–776, 2006.

[80] A. Alexeev and C. Gutfingera. Resonance gas oscillations in closed tubes: Numerical study and experiments. *Physics of Fluids*, 15:3397–3408, 2003.

[81] C.C. Lawrenson; B. Lipkens; T.S. Lucas; D.K. Perkins and T.W. Van Doren. Measurements of macrosonic standing waves in oscillating closed cavities. *J. Acoustical Society of America*, 104:623–636, 1998.

[82] C. Vanhille and C. Campos-Pozuelo. Numerical and experimental analysis of strongly nonlinear standing acoustic waves in axisymmetric cavities. *Ultrasonics*, 43:652–660, 2005.

[83] L.K. Zarembo. *Acoustic streaming: High-intensity ultrasonic fields.* Plenum Press, New York, 1971.

[84] L. Rayleigh. On the circulation of air observed in Kundt's tubes. *Philosophical Transactions*, pages 1–21, 1884.

[85] H. Schlichting. Berechnung ebener periodischer grenzschichtstromungen (calculation of plane periodic boundary layer streaming). *Physikalische Zeitschrift*, 33:327–335, 1932.

[86] H. Schlichting. *Boundary Layer Theory.* McGraw-Hill, New York, 1968.

[87] C. Eckert. Vortices and streams caused by sound waves. *Physical Review*, 73:68–76, 1958.

[88] S. Boluriaan and P.J. Morris. Acoustic streaming: From Rayleigh to today. *International journal of aeroacoustics*, 2:255–292, 2003.

[89] P.J. Westervelt. The theory of steady rotational flow generated by a sound field. *J. Acoustical Society of America*, 25:60–67, 1953.

[90] J.M. Andres and U. Ingard. Acoustic streaming at low Reynolds numbers. *J. Acoustical Society of America*, 25:932–938, 1953.

[91] J.M. Andres and U. Ingard. Acoustic streaming at high Reynolds numbers. *J. Acoustical Society of America*, 25:928–932, 1953.

[92] C.P. Lee and T.G. Wang. Outer acoustic streaming. *J. Acoustical Society of America*, 88:2367–2375, 1990.

[93] Q. Qi. The effect of compressibility on acoustic streaming near a rigid boundary for a plane traveling wave. *J. Acoustical Society of America*, 94:1090–1098, 1993.

[94] Q. Qi; R.E. Johnson and J.G. Harris. Boundary layer attenuation and acoustic streaming accompanying plane-wave propagation in a tube. *J. Acoustical Society of America*, 97:1499–1509, 1995.

[95] L. Menguy and J. Gilbert. Nonlinear acoustic streaming accompanying a plane stationary wave in a guide. *Acustica*, 86:249–259, 2000.

[96] M.F. Hamilton; Y.A. Ilinskii and E.A. Zabolotskaya. Acoustic streaming generated by standing waves in two-dimensional channel of arbitrary width. *J. Acoustical Society of America*, 113:153–160, 2003.

[97] M.F. Hamilton; Y.A. Ilinskii and E.A. Zabolotskaya. Thermal effects on acoustic streaming in standing waves. *J. Acoustical Society of America*, 114:3092–3101, 2003.

[98] M. Sen F. Carlsson and L. Löfdahl. Steady streaming due to vibrating walls. *Physics of Fluids*, 16:1822–1825, 2004.

[99] M. Kawahashi and M. Arakawa. Nonlinear phenomena induced by finite amplitude oscillation of air-column in closed duct. *JSME*, 39:280–286, 1996.

[100] M.K. Aktas and B. Farouk. Numerical simulation of acoustic streaming generated by finite-amplitude resonant oscillations in an enclosure. *J. Acoustical Society of America*, 116:2822–2831, 2004.

[101] T. Yano. Turbular acoustic streaming excited by resonance gas oscillation with periodic shock waves in a closed tube. *J. Acoustical Society of America*, 106:L7–L12, 1999.

[102] I. Gulyaev and V.M. Kuznetsov. Large amplitude gas oscillations in a closed tube. *Inzh. Zh.*, 3:236–272, 1963.

[103] D.B. Cruikshank. Experimental investigation of finite-amplitude acoustic oscillations in closed tubes. *J. Acoustical Society of America*, 52:1024–1034, 1972.

[104] A. Goldshtein; K. Shuster; P. Vainshtein; M. Fichman and C. Gutfinger. Particle motion in resonance tubes. *J. Fluid Mechanics*, 360:1–20, 1998.

[105] M.P. Arroyo and C.A. Greated. Stereoscopic particle image velocimetry. *Measurement Science and Technology*, 2:1181–1186, 1991.

[106] H. Bailliet S. Moreau and J.C. Valiere. Measurements of inner and outer streaming vortices in a standing waveguide using lase Doppler anemometry. *J. Acoustical Society of America*, 123:640–647, 2008.

[107] N. Rott. The influence of heat conduction on acoustic streaming. *J. of Applied Mathematics and Physics*, 25:417–421, 1974.

[108] M.W. Thompson; A.A. atchley and M.J. Maccarone. Influences of temperature gradient and flow inertia on acoustic streaming in a standing wave. *J. Acoustical Society of America*, 117:1839–1849, 2005.

[109] Y. Lin and B. Farouk. Heat transfer in a rectangular chamber with differentially heated horizontal walls - effects of a vibrating sidewall. *Int. J. of Heat and Mass Transfer*, 51:3179–3189, 2008.

[110] T.S. Lucas. Standing wave compressor, US Pat. No. 5020977, 1991.

[111] R.P. Bishop. Standing wave pump, US Pat. No. 6079214, 2000.

[112] F. Tamotsu M. Kawahashi and M. Saito. Acoustic fluid machine, US Pat. No. 7252178 B2, 2007.

[113] P.A. Krutitskii. Acoustic scattering by several obstacles and screens with neumann boundary condition. *Mathematics and Computers in Simulation*, 52:345–360, 2000.

[114] I. Lasiecka and C. Lebiedzik. Asymptotic behaviour of nonlinear structural acoustic interactions with thermal effects on the interface. *Nonlinear Analysis: Theory, Methods and Applications*, 49:703–735, 2002.

[115] P. Filippi. *Acoustics: Basic physics, theory, and methods.* Academic Press, 1999.

[116] O.V. Rudenko and S.I. Soluyan. *Theoretical fundation of nonlinear acoustics.* Consultants bureau, New Tork, 1977.

[117] R.T. Beyer. *Nonlinear acoustics.* Academic Press, New Tork, 1965.

[118] J.C. Tannehill; A.A. Anderson and R.H. Pletcher. *Computational fluid mechanics and heat transfer, 2nd edition.* Taylor and Francis, Washington, DC, 1997.

[119] B.O. Enflo and C.M. Hedberg. *Theory of nonlinear acoustics in Fluids.* Kluwer Academic Publishers, Dordrecht, the Netherlands, 2002.

[120] H. Lei; D. Henry and H. BenHadid. Numerical study of the influence of a longitudinal sound field on natural convection in a cavity. *Int. J. Heat and Mass Transfer*, 49:3601–3616, 2006.

[121] M.F. Hamilton and D.T. Blackstock. *Nonlinear acoustics.* Academic Press, New York, 1998.

[122] A.D. Pierce. *Acoustics.* Acoustical Society of America, 1989.

[123] S.K. Lele. Compact finite difference schemes with spectral-like resolution. *J. Computational Physics*, 103:16–42, 1992.

[124] A. Jameson and T.J. Baker. Numerical solution of the euler equations by finite volume methods using Runge-Kutta time stepping schemes. *American Institute of Aeronautics and Astronautics*, 81:1259–1269, 1981.

[125] X. Pan; M.N. Shneider; Z. Zhang and R.B. Miles. Bulk viscosity measurements using coherent Rayleigh-Brillouin. *The 42nd Aerospace Sciences Meeting and Exhibit Conference AIAA*, 2004.

[126] L. Elvira-Segura and C. Campos-Pozuelo. Experimental study of 3-D finite amplitude ultrasonic standing waves. *Nonlinear Acoustics at the tern of Millennium*, 15:169–172, 2000.

[127] C. Campos-Pozuelo; L. Elvira-Segura and B. Dubus. Numerical and experimental analysis of second order effects and loss mechanisms in axisymmetric cavities. *J. Acoustical Society of America*, 115:1973–1981, 2004.

[128] A. Berson, M. Michard, and P. Blanc-Benon. Measurement of acoustic velocity in the stack of a thermoacoustic refrigerator using particle image velocimetry. *Heat and Mass Transfer*, 44:1015–1023, 2008.

[129] J.L. Lumley W.H. Snyder. Some measurements of particle velocity autocorrelation functions in a turbulent flow. *J. Fluid Mechanics*, 48:41–71, 1971.

[130] D.A. Siegel and A.J. Plueddemann. The motion of a solid sphere in an oscillating flow: an evaluation of remotely sensed doppler velocity estimates in the sea. *J. Atmos. Oceanic. Technol.*, 8:296–304, 1991.

[131] M. Raffel; C. Willert and J. Kompenhans. *Particle image velocimetry: a practical guide.* Springer-Verlag Berlin Heidelberg, 1998.

[132] J. Westerweel. Fundamentals of digital particle image velocimetry. *Measurement Science and Technology*, 8:1379–1392, 1994.

[133] J. Grue; P.L. Liu and G.K. Pedersen. PIV *and water waves.* World Scientific Pub. Co., Singapore, 2004.

[134] R.D. Keane and R.J. Adrian. Theory of cross-correlation analysis of PIV images. *Applied Science Research*, 49:191–215, 1992.

[135] J. Westerweel. Efficient detection of spurious vectors in particle image velocimetry data. *Experiments in Fluids*, 16:236–247, 1994.

[136] M. Marxen. *Particle Image Velocimetry.* PhD thesis.

[137] M.H.K. Siddiqui; M.R. Loewen; C. Richardson; W.E. Asher and A.T. Jessup. Simultaneous particle image velocimetry and infrared imagery of microscale breaking waves. *Physics of Fluids*, 13:1891–1903, 2001.

[138] D.T. Blackstock. *Fundamentals of physical acoustics.* John Wiley & Sons Inc., 2000.

[139] A.I. Hickerson; D. Rinderknecht and M. Gharib. Experimental study of the behavior of a valveless impedance pump. *Experiments in Fluids*, 38:534–540, 2005.

[140] T.T. Bringley, S. Childress, N. Vandenberghe, and J. Zhang. An experimental investigation and a simple model of a valveless pump. *Physics of Fluids*, 20:0336021–15, 2008.

[141] Sremme E. and Stemme G. A valveless diffuser/nozzle-based fluid pump. *Sensors and Actuators A*, 39:159–167, 1993.

[142] A. Olsson, G. Stemme, and E. Stemme. A numerical design study of the valveless diffuser pump using lumped-mass model. *J. Micromechanics Microengineering*, 9, 1999.

[143] K.S. Yang, I.Y. Chen, and B.Y. Shew C.C. Wang. Investigation of the flow characteristics within a micronozzle/diffuser. *J. Micromechanics Microengineering*, 14:26–31, 2004.

[144] V. Singhal, S.V. Garimella, and J.Y. Murthy. Low reynolds number flow through nozzle/diffuser elements in valveless micropumps. *Sensors and Actuators A*, 113:226–235, 2004.

[145] H.J. Sheen, C.J. Hsu, T.H. Wu, C.C. Chang, H.C. Chu, C.Y. Yang, and U. Lei. Unsteady flow behaviors in an obstacle-type valveless micropump by micro-piv. *Microfluid Nanofluid*, 4:331–342, 2008.

[146] L. Jang and W. Kan. Peristaltic piezoelectric micropump system for biomedical applications. *Biomedical Microdevices*, 9:619–626, 2007.

[147] Y. Hsu, S. Lin, and S. Hou. Development of peristaltic antithrombogenic micropumps for in vitro and ex vivo blood transportation tests. *Microsystem Technology*, 14:31–41, 2007.

[148] Q. Cui, C. Liu C., and X. Zha. Study on a piezoelectric micropump for controlled drug delivery system. *Microfluid Nanofluid*, 3:377–390, 2007.

[149] C. Zhang, D. Xing, and Y. Li. Micropumps, microvalves, and micromixers within pcr microfluidic chips: Advances and trends. *Biotechnology Advances*, 25:483–514, 2007.

[150] L.S. Pan, T.Y. Ng, G.R. Liu, K.Y. Lam, and T.Y. Jiang. Analytical solution for the dynamic analysis of a valveless micropump: A fluid-membrane coupling study. *Sensors and Actuators A*, 93:173–181, 2001.

[151] C.L. Sun and K.H. Huang. Numerical characterization of the flow rectification of dynamic microdiffusers. *J. Micromechanics Microengineering*, 16:1331–1339, 2006.

[152] J.A. Cosgrove, J.M. Buick, S.J. Tonge, C.G. Munro, C.A. Greated, and D.M. Champbell. Application of the lattice boltzmann method to transition in oscillatory channel flow. *J Phys. A: Math. Gen.*, 36:2609–2620, 2003.

[153] C.J. Morris and F.K. Forster. Oscillatory flow in microchannels: Comparison of exact and approximate impedance models with experiments. *Experiments in Fluids*, 36:928–937, 2004.

Index